NUREG-0264-3

SUPPRESSION POOL DYNAMICS

Annual Report
July 1, 1976 - June 30, 1977

C. K. Chan V. K. Dhir
H. H. Chiou C. Y. Liu
B. K. C. Lee I. Catton

University of California, Los Angeles

Prepared for
U. S. Nuclear Regulatory Commission

NOTICE

This report was prepared as an account of work sponsored by the United States Government. Neither the United States nor the United States Nuclear Regulatory Commission, nor any of their employees, nor any of their contractors, subcontractors, or their employees, makes any warranty, express or implied, nor assumes any legal liability or responsibility for the accuracy, completeness or usefulness of any information, apparatus, product or process disclosed, nor represents that its use would not infringe privately owned rights.

Available from
National Technical Information Service
Springfield, Virginia 22161
Price: Printed Copy $9.50 ; Microfiche $3.00

The price of this document for requesters outside of the North American Continent can be obtained from the National Technical Information Service.

NUREG-0264-3
R4

SUPPRESSION POOL DYNAMICS

Annual Report
July 1, 1976 - June 30, 1977

C. K. Chan V. K. Dhir
H. H. Chiou C. Y. Liu
B. K. C. Lee I. Catton

Manuscript Completed: December 1977
Date Published: February 1978

University of California, Los Angeles
School of Engineering and Applied Science
Los Angeles, CA 90024

Prepared for
Division of Reactor Safety Research
Office of Nuclear Regulatory Research
U. S. Nuclear Regulatory Commission
Under Contract No. AT(49-24)-0342

ABSTRACT

This report describes the work performed at UCLA to study the transient thermal-hydraulic phenomena induced by the motion of submerged air and steam bubbles in a boiling water reactor (BWR) pressure suppression pool, following a loss-of-coolant accident. The air transients, which include vent clearing, bubble growth, and pool swelling, were investigated by a series of air-water tests. These tests were performed in a cylindrical plexiglas test chamber. Gas was injected downward through different-diameter pipes, placed in the middle of the test chamber, which was filled with water at room temperature.

ACKNOWLEDGMENTS

The authors would like to express their appreciation to James Yaung and Mike Cherng for their help in reducing the data. They would also like to extend their thanks to Ibi Temes and Mike Gogins for their assistance with editing.

The authors are grateful to Mike Gogins and Linda Infeld for their patience in converting our scribbling into a typed manuscript.

SUMMARY

This report describes the work performed at UCLA to study the transient thermal-hydraulic phenomena induced by the motion of submerged air and steam bubbles in a boiling water reactor (BWR) pressure suppression pool, following a loss-of-coolant accident. The air transients, which include vent clearing, bubble growth, and pool swelling, were investigated by a series of air-water tests. These tests were performed in a cylindrical plexiglas test chamber. Gas was injected downward through different-diameter pipes, placed in the middle of the test chamber, which was filled with water at room temperature.

The factors affecting the vent clearing process and the hydrodynamical forces are examined, particularly the effects of virtual mass and the Taylor instability. The effects of submergence depth and the driving pressures are also investigated. Scaling laws for air and steam transients are established. The effects of orificing, to overcome certain scaling limitations, are also examined. Simple analytical models developed under this project are described, and some results of their application to BWR prototype performance are given. This report also describes the design of the steam transient test apparatus which has just been fabricated.

It is found that the governing similitude parameters during vent clearing are the Froude number, the Euler number, the Reynolds number, and the Weber number. Similitude in the Froude and the Euler numbers leads to a linear scaling relation for pressure and a square root scaling relation for velocity and time. During bubble growth, in addition to the Froude and Euler numbers, the similitude parameters also include the Mach number, which leads to temperature scaling, and the specific gas constant.

The problem of temperature simulation is circumvented in practice by means of an orifice in the vent pipe.

The similitude analysis for steam condensation shows that the steam transient should be divided into two periods. During steam jet condensation, maintaining the thermodynamical properties in the model as in the prototype would lead to similitude in the Jacob number, the Kelvin-Helmholtz instability number, the Mach number, and the Euler number, but not the Fourier number or the Weber number. During the later steam chugging period, two characteristic lengths are identified: one to characterise the acoustic effect in the pipe, and the other to scale the steam flow rate. At this stage, no convincing scaling algorithm has been achieved for steam chugging in the heat transfer-dominated regime.

It is observed that a simple slug model can accurately describe the vent clearing process as long as the submergence depths are small. For large submergence depths, the water spike left in the vent tube due to the Taylor instability, and also the virtual mass phenomenon, affect the vent clearing process. The Taylor instability tends to reduce the effective mass that can be accelerated during vent clearing, and hence leads to an earlier vent clearing time, while the virtual mass tends to prolong the vent clearing time and hence allows the pressure to attain a higher value when the vent does clear. The downward force is found to depend to a large extent on this vent clearing pressure. The downward force characteristics also depend on the initial bubble growth, which is in turn governed by the solid boundary, gravity force, inertial force and flow pattern in the surrounding liquid. The compression of the gas space above the free surface in the test chamber due to pool swelling was found to be a monotone function of time, and no bubble oscillation was

observed.

Tests with different gases (air, helium, and argon) showed the effects of the velocity of sound and the gas density on the compression of the gas medium between the water slug and the solenoid valve during vent clearing. When the position of the orifice is relatively far away from the downcomer exit, the orifice has little effect on the rate of vent clearing, the total time to clear the vent, or the magnitude of the downward force. The orifice inhibited the expansion of the bubble after vent clearing.

The steam test chamber is hexagonal in cross-section with provisions for visual observation, non-condensible gas control, and pressure measurement. Steam will be injected downward through pipes placed in the middle of the test chamber, which will be filled with water at different temperatures. The preliminary calibration of the pressure transducers indicated potential problems for pressure measurement under transient temperature conditions.

TABLE OF CONTENTS

TABLE OF CONTENTS (Continued)

LIST OF FIGURES

LIST OF FIGURES (Continued)

LIST OF FIGURES (Continued)

LIST OF FIGURES (Continued)

LIST OF TABLES

1. INTRODUCTION

Transient air-water tests were performed in a plexiglas vessel to investigate the vent-clearing and pool-swelling phenomena that may occur in a boiling water reactor (BWR) pressure suppression pool at the onset of a loss-of-coolant accident (LOCA). These tests are part of an ongoing program at UCLA, to investigate the thermal-hydraulic phenomena that might affect the structural integrity of the pressure suppression pool in the event of a LOCA. Fundamental understanding of the controlling physical processes of BWR system behavior is desired. The results of this program will be part of the Nuclear Regulatory Commission (NRC) data base, used for evaluating the adequacy of analytical models developed to predict system response during a LOCA. In addition, the results of these small-scale tests will also be valuable for comparisons with the data from larger geometries, and thereby will also be of use in evaluating the effects of physical size.

The air-water tests were conducted to investigate the vent-clearing and pool-swelling phenomena in a laboratory-scale test facility, and to determine whether these phenomena have been adequately described by current analytical models. These tests also involve hydrodynamical force measurement and structural wall effects on the fluid transient.

The steam-water tests to investigate steady-state and transient submerged steam flow in a water medium, where the condensation modes could produce undesirable forces, will be conducted in the second phase of the test program. The design and fabrication of the test apparatus has already been completed.

In addition to the test programs, extensive efforts were made in establishing the appropriate scaling laws for vent clearing, bubble

growth, bubble motion, and pool surface swelling for air injection and for pure steam condensation.

1.1 Program Objectives

Current BWR Mark I containment designs utilize a water pool for pressure suppression, see Figure 1-1. One of the characteristics of a BWR suppression pool is the compartmental arrangement within the containment boundaries. In the event of a LOCA, the steam from the primary coolant pressurizes the dry well. This pressure-rise pushes the water initially filling the vent pipe into the suppression pool. The vent clearing is followed by an air-steam mixture. The steam condenses in the pool, causing the air, which is initially at drywell pressure, to expand and to rise up in the pool. The water slug ejection due to air pressure produces a downward load on the torus, while the air expansion displaces the pool free surface upward. The accelerating free surface could cause an impact load on the structure, e.g. on the internal ring header and the support columns which are critical for pressure suppression. The continued inflow of air leads to the breakup of the bubble, creating a two-phase froth of air and water. The air is finally released into the wet well atmosphere, which then becomes pressurized. The fallback of the free surface causes more waves, and there is speculation that thereby the vent-opening might be uncovered. During the later stages of such an accident, when the steam-flow rate is low, water can re-renter the vent pipe when the steam bubble collapses. A cyclic phenomenon, or chugging, occurs, which leads to an oscillatory loading of the piping and the surrounding structures. In the Mark I design, the chugging force is applied to the downcomer pipe. Axisymmetric steam condensation at the exit would also impose a lateral loading on the downcomer.

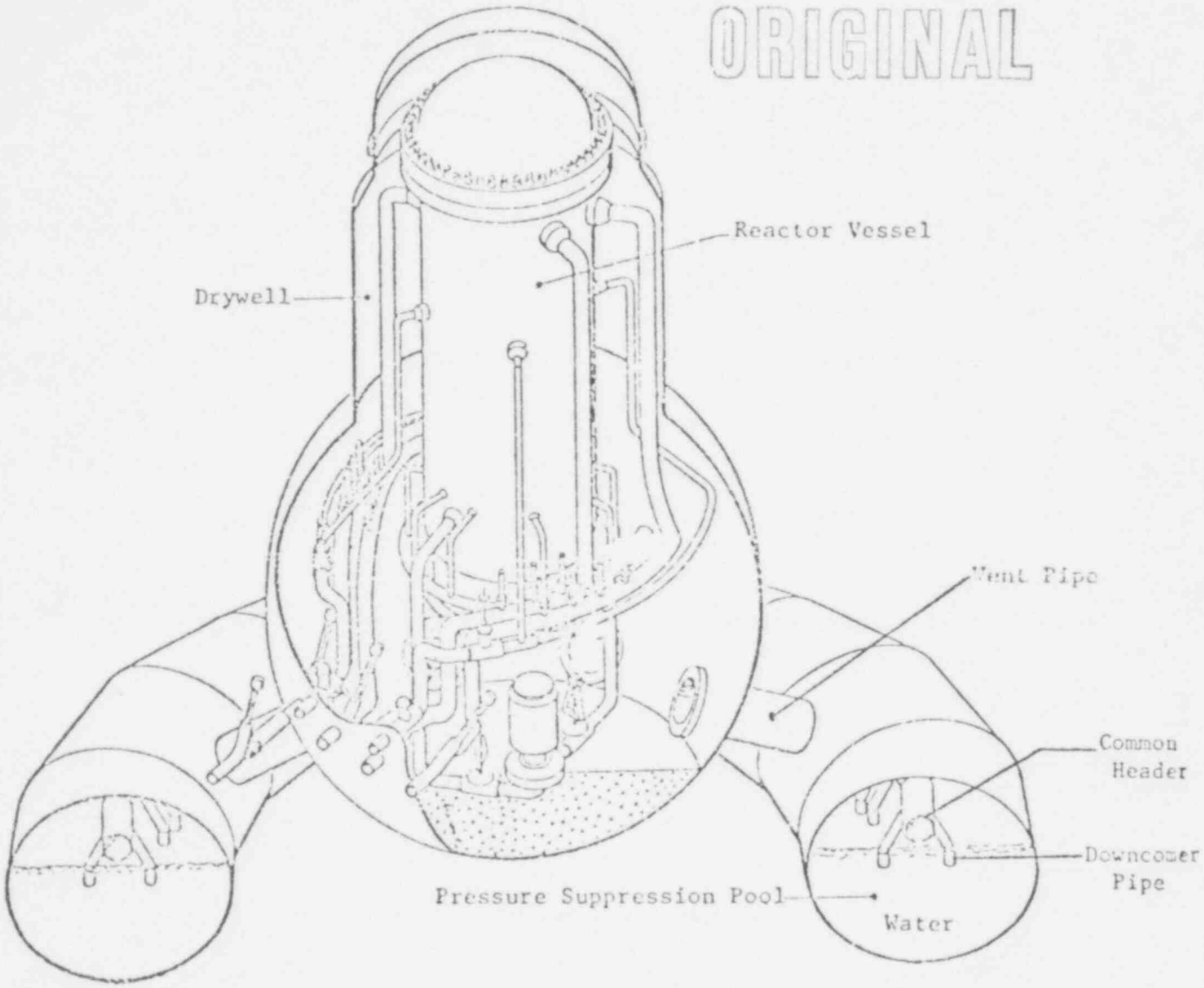

Figure 1.1. BWR Mark-I Primary Containment

The transient air and steam injection test program was initiated at UCLA on July 1, 1976. The basic purpose of the experimental program is to develop an understanding of the interacting thermal and hydraulic phenomena during the injection of steam-air mixtures in subcooled water. The specific objectives of the test programs are:

(a) To investigate the transient flow through a tube, and to determine whether the commonly-used vent-clearing model adequately describes the phenomena,

(b) To investigate the transient pool-surface motion,

(c) To investigate the dynamical forces during the entire transient,

(d) To investigate the transient steam flow in subcooled water,

(e) To investigate the effect of the presence of air in steam condensation,

(f) To establish appropriate scaling laws for the air and the steam transients, and

(g) To investigate the effects of experimental-error magnification on the actual system.

1.2 Organization of the Report

This report is divided into seven sections and seven appendices. Following the introduction, the work done on air and steam scaling is presented. A simple model for the vent-clearing process and for subsonic and sonic air discharge has been developed. In Section 3, the apparatus and the experimental procedure are described. Data for the rate and for the total time of vent clearing has been obtained for different submergence depths and upstream and test chamber pressures (Section 4.1). The

effects of the Taylor instability on vent clearing are examined in Section 4.2. Data for bubble-growth pattern, the hydrodynamical forces and the maximum swell height have been obtained, and the modes of the free surface motion have been studied from the motion pictures (Sections 4.3, 4.4, and 4.5). The effect of orificing on force measurement is examined in Section 4.6. Section 5 gives the error analysis for the experimental data, while the steam test apparatus is described in Section 6. Concluding remarks, based on the first years' work, are found in Section 7. Detailed instrumentation and photographic techniques are outlined in Appendices A, B, and C, and detailed information on vent clearing, bubble growth, bottom forces, and pool swelling is presented in Appendices D, E, F, and G.

2. SCALING LAWS

This section summarizes the various scaling algorithms used to model the pool dynamics in a BWR pressure suppression pool as a result of the influx of a large mass of air and steam during a design basis LOCA. The purpose of the scaling analysis is to identify all of the significant parameters and to provide a theoretical base relating the laboratory-scale experiments to the full-scale prototype. A completely simulated experiment should involve both geometrical and dynamical similarity.

Both UCLA [2-1] and General Electric [2-2] have independently applied the similitude method [2-3] to the equations that govern the slug motion and the bubble dynamics during the vent clearing and air discharge periods. The basic procedure in scaling involves the non-dimensionalization of all of the governing equations and boundary conditions of the physical problem in such a way that the magnitude of all variables and their derivates becomes of the order of unity. Dimensionless similarity parameters appear as coefficients in the formulation. A comparison of the numerical values of these coefficients may enable one to disregard the smaller coefficient. In order to maintain dynamical similarity, the remaining coefficients in a model test must be numerically equal to the prototype (full scale) system.

2.1 Air Scaling

2.1.1 Scaling in Vent Clearing

The governing equation for the one-dimensional water slug movement is the momentum equation

$$\frac{\partial u}{\partial t} + u \frac{\partial u}{\partial x} = - \frac{1}{\rho} \frac{\partial p}{\partial x} - g, \qquad (2.1)$$

where

u = the water velocity in the pipe,

p = pressure,

ρ = water density,

x = the coordinate along the vent pipe, and

t = time, and

g = the acceleration of gravity.

The boundary conditions for pressure are:

$p = p_D(t)$, the drywell pressure at the air-water interface, and (2.2)

$p = p_p(t)$, the pool pressure at the pipe exit. (2.3)

We introduce the following quantities as characteristic variables:

L_c = characteristic length,

ρ_c = characteristic density,

u_c = characteristic velocity,

p_c = characteristic pressure, and

t_c = characteristic time = L_c/u_c.

Using an asterisk to denote the normalized quantities, Equation (2.1) in dimensionless form becomes

$$\frac{\partial u^*}{\partial t^*} + u^* \frac{\partial u^*}{\partial x^*} = - \frac{p_c}{\rho_c u_c^2} \frac{1}{\rho^*} \frac{\partial p^*}{\partial x^*} - \frac{g L_c}{u_c^2}, \tag{2.4}$$

where

$u^* = u/u_c$,

$t^* = t/t_c$,

$x^* = x/L_c$,

$p^* = p/p_c$, and

$\rho^* = \rho/\rho_c$.

Two dimensionless groups appear in Equation (2.4); the Froude number,

gL_c/u_c^2, and the Euler number, $p_c/\rho_c u_c^2$. Similitude requires that

$$\left[\frac{gL_c}{u_c^2}\right]_p = \left[\frac{gL_c}{u_c^2}\right]_m \quad \text{and} \quad \left[\frac{p_c}{\rho_c u_c^2}\right]_p = \left[\frac{p_c}{\rho_c u_c^2}\right]_m \tag{2.5}$$

Subscripts p and m represent quantities for the prototype and the model, respectively. Similitude in the Froude number leads to the required scaling of the characteristic velocities:

$$u_{cp}/u_{cm} = \sqrt{L_{cp}/L_{cm}} \ . \tag{2.6}$$

It, in turn, determines the scaling of pressure and time

$$\frac{p_{cp}}{p_{cm}} = \frac{L_{cp}}{L_{cm}} \quad \text{and} \quad \frac{t_{cp}}{t_{cm}} = \left[\frac{L_{cp}}{L_{cm}}\right]^{1/2} \tag{2.7}$$

Numerical parameters for the 1/12 and the 1/5 scale model tests are summarized in Table 2.1. The Froude and the Euler numbers would be sufficient to model the vent-clearing process even with three-dimensional and virtual-mass effects (see Section 4.1). However, it was observed in the experiment that liquid was left behind on the wall in the form of a film as a result of the viscous effect and in the form of a water spike as a result of the Taylor instability (see Section 4.2). Based on this observation, the transient motion of the water slug in the vent during the vent-clearing transient cannot be treated as a rigid body. Both the Taylor instability and the viscous effect tend to reduce the effective mass of the accelerating liquid column, and hence, the actual vent-clearing time may be less than the predicted value. The virtual mass, on the other hand, tends to prolong the vent-clearing time.

The incorporation of the Taylor instability and the viscous effects

Table 2.1.

Parameters for Pool Swell in Pressure Suppression Pool.

PARAMETER	ACTUAL PLANT	1/12 SCALE	1/5 SCALE
Centerline Diameter	29.87 m	2.49 m	5.974 m
Cross Section Diameter	8.433 m	0.704 m	1.686 m
Water Volume	2,208.73 m^3	1.2782 m^3	17.67 m^3
Air Volume	3,058 m^3	1.7698 m^3	24.46 m^3
Downcomers (number)	98	98	98
Submerged Depth	1.22 m	0.1 m	0.244 m
Air Flow Area	40.275 m^2	0.2796 m^2	1.611 m^2
Pressure	115.11-287.43 kPa	9.58-23.99 kPa	23.02-57.49 kPa
Temperature	305.6-344.4 K	25-28.72 K	61.1-68.9 K
Dry Well Pressure	170.25-397.72 kPa	14.2-33.15 kPa	34.05-79.54 kPa
Dry Well Temperature	355.6-411.1 K	29.61-34.28 K	71.1-82.2 K

into the scaling laws would introduce two additional parameters:

$$\text{the Reynolds number} \qquad Re = \frac{\rho_c L_c u_c}{\mu_c} \tag{2.8}$$

and

$$\text{the Weber number} \qquad We = \frac{\rho_c L_c u_c^2}{\sigma_c}, \tag{2.9}$$

where μ = viscosity and σ = surface tension. In writing Equations (2.8) and (2.9), it is assumed that $\rho_g << \rho_c$. For small-scale tests, it is impractical to simulate all the non-dimensional parameters. Hence, the less-important parameters during vent clearing, namely the Reynolds and Weber numbers, have to be disregarded in the simulation process. However, neglect of these two numbers may affect the vent-clearing time, and care should be taken in the interpretation of the vent-clearing data in small-scale experimental tests.

2.1.2 Compressed Air Discharge

Once the vent is cleared of water, air starts to flow into the pool. The air bubble expands due to its initial high pressure and due to continuing air supply. The governing equations for the pool dynamics are:

(i) Continuity $$\vec{\nabla}\cdot\vec{u} = 0, \tag{2.10}$$

(ii) Momentum $$\left(\frac{\partial}{\partial t} + \vec{u}\cdot\vec{\nabla}\right)\vec{u} = -\frac{1}{\rho_w}\vec{\nabla}p + g, \tag{2.11}$$

with the boundary conditions:

(i) The normal component of the velocity at the wall is 0, and

(ii) The pressure at the free surface is equal to the external pressure.

The primary parameters for the pool dynamics are again the:

(i) Froude Number $\frac{u_c^2}{gL_c}$

and

(ii) Euler Number $\frac{p_c}{\rho_c u_c^2}$.

The governing equation for the wet well atmosphere is

$$p_w V_w^{\gamma} = \text{constant} .$$

Here,

p_w = wet well pressure

and

V_w = wet well volume.

The governing equations for the air expansion dynamics, found by considering the air region as a single node, are:

continuity

$$\frac{d(\rho_B V_B)}{dt} = \dot{M}A , \tag{2.12}$$

energy

$$\frac{1}{p_B}\frac{dp_B}{dt} = \gamma \dot{M} (p_D/\rho_D) \frac{A}{p_B V_B} - \frac{\gamma}{V_B}\frac{dV_B}{dt} ; \tag{2.13}$$

where

p_B = bubble pressure,

ρ_B = bubble density,

V_B = bubble volume,

A = minimum flow area,

p_D = drywell pressure,

ρ_D = drywell density, and

$\dot{M}$ = mass flux per unit area.

$$\dot{M} = \sqrt{\left(\frac{2}{\gamma+1}\right)^{\frac{\gamma+1}{\gamma-1}}} (p_D \rho_D)^{1/2} \quad \text{for} \quad p_B/p_D \leq 0.5283 \quad \text{(choked flow)}$$

(2.14)

$$\dot{M} = \rho_B \left[2 \left(\frac{\gamma}{\gamma-1}\right)\left(\frac{p_D}{\rho_D}\right)\left(1 - \frac{p_B}{p_D}\frac{\rho_D}{\rho_B}\right)\right]^{1/2} \quad \text{for } p_B/p_D > 0.5283$$

(non-choked flow) (2.15)

$$\gamma = C_p/C_V \ .$$

By defining

$$V_B^* = V_B/L_c^3$$

$$p_D^* = p_D/p_c$$

$$p_B^* = p_B/p_c$$

$$\rho_D^* = \rho_D/\rho_c$$

$$\rho_B^* = \rho_B/\rho_c$$

$$\dot{M}^* = \dot{M}/\dot{M}_c \qquad \dot{M}_c \equiv \rho_c u_c$$

$$A^* = A/A_c$$

$$t^* = t/t_c$$

Equations (2.12) and (2.13) become

$$\frac{d(\rho_B^* V_B^*)}{dt^*} = \left(\frac{u_c A_c t_c}{L_c^3}\right) \dot{M}^* A^* \tag{2.16}$$

$$\frac{1}{P_B^*}\frac{dP_B^*}{dt^*} = k\left(\frac{u_c A_c t_c}{L_c^3}\right) M^* \left(\frac{p_D^*}{\rho_D^*}\right)\left(\frac{A^*}{p_B^* V_B^*}\right) - \frac{\gamma}{V_B^*}\frac{dV_B^*}{dt^*} \tag{2.17}$$

Equations (2.14) and (2.15) become

$$\dot{M}^* = \sqrt{\left(\frac{2}{\gamma+1}\right)^{\frac{\gamma+1}{\gamma-1}}} \left[\frac{1}{u_c}\sqrt{\gamma\frac{p_c}{\rho_c}}\right](p_D^* \rho_D^*)^{1/2} \qquad (2.18)$$

$$\dot{M}^* = \left[\frac{1}{u_c}\sqrt{\gamma\frac{p_c}{\rho_c}}\right]\rho_B^* \left[2\left(\frac{1}{\gamma-1}\right)\left(\frac{p_D^*}{\rho_D^*}\right)\left(1 - \frac{p_B^*}{p_D^*}\frac{\rho_D^*}{\rho_B^*}\right)\right]^{1/2} . \qquad (2.19)$$

The non-dimensional coefficients are

$$, \quad \left(\frac{u_c A_c t_c}{L_c^3}\right), \quad \text{and} \quad \frac{1}{u_c}\sqrt{\gamma\frac{p_c}{\rho_c}} \quad .$$

If geometrical similarity is maintained (i.e., no orifice), then $A_c = L_c^2$ and

$$\frac{u_c A_c t_c}{L_c^3} = 1 .$$

If is also preserved, the parameter to be scaled becomes

$$\frac{u_c}{\sqrt{RT_c}} \quad \text{(the Mach number)} .$$

On the other hand, by substituting (2.14) or (2.15) into (2.12) and (2.13), the parameter to be scaled becomes

$$\left(\frac{A_c t_c}{L_c^3}\sqrt{p_c/\rho_c}\right) .$$

This term, in fact, is reduced to Moody's enthalpy flux term [2.2], i.e. to

$$\frac{\dot{M}_c A_c h_c}{\rho_c g^{3/2} L_c^{7/2}} ,$$

where h_c is the characteristic enthalpy, if it is combined with the Euler and Froude numbers. Again, if the geometrical similarity and k are preserved, both this term and the enthalpy flux term are reduced to the Mach number. However, if the restriction on A_c or the geometrical similarity is relaxed, one can choose A_c or the orifice size such that this coefficient is simulated.

2.1.3 Comparison With Other Studies

Three separate studies (LLL, MIT and UCLA) have been conducted for the problem of steam discharge into a suppression pool. Essentially all of them lead to the same set of parameters. There is no difference in opinion as to the identity of these parameters, the only question is the practicality of simulating some of them.

The LLL analysis is summarized in Table 2.2.

The MIT- Moody Scaling law, is as follows:

$$\frac{F}{\rho_c g_c L_c^3} = \phi\left[\frac{P_c}{\rho_c g_c L_c}, \frac{P_D}{P_c}, \gamma, \frac{h_c \dot{M}}{\rho_c g_c^{3/2} L_c^{7/2}}, \frac{t_c^2 g_c}{L_c}\right] \qquad \text{Moody}$$

$$\frac{F}{\rho_c g_c L_c^3} = \phi\left[\frac{P_c}{\rho_c g_c L_c}, \frac{P_D}{P_c}, \gamma, \left(\frac{RT_D}{g_c L_c}\right)^{1/2} C_{m_o}, \frac{t_c^2 g_c}{L_c}\right] \qquad \text{MIT}$$

where

F = force

h_c = enthalpy

T_D = temperature in the dry well

C_{m_o} = discharge coefficient .

For the MIT experiment, where the dry-well pressure, P_D, is essentially constant, the ratio p_D/p_c is not a function of time. In general, p_D/p_w varies as time increases; the exact simulation of p_D/p_w in a laboratory experiment is not straightforward.

The UCLA analysis yields scaling laws (see Table 2.3) for the vent-clearing period and the gas-discharge period. In essence, the only difference between these two time periods is the addition of the Mach

Model	Parameters	Verification	LLL Comments	Our Comments
A	$\left.\begin{matrix}\frac{F}{\rho_w g L^3} \\ \frac{S}{L}\end{matrix}\right\} = \phi\left[\frac{p_w}{\rho_e g L}, \frac{p_D}{\rho_w g L}, \frac{RT_D}{gL}, f, \gamma, \frac{t^2 g}{L}\right]$	No Verification	(1) Explicitly reveals the need for T_D, the dry well temperature. (2) No need to know the mass flux m.	(1) Impossible to scale to fw 1/5 scale. (2) f and not needed. (3) To(t), Po(t).
B	Same $= \phi\left[\frac{p_w}{\rho_w g L}, \frac{p_D}{\rho_w g L}, f, \gamma, \frac{t^2 g}{L}\right]$	Best for max. downward force and upward force. Poor time estimation.	Can be 'perfectly scaled' if To is dropped.	
C	Same $= \phi\left[\frac{p_w}{p_D}, \frac{p_D}{\rho_w RT_D}, f, \gamma, \frac{t^2 p_w}{\rho_w L^2}\right]$	Time is best scaled by this model in relation to B and D.	Can be 'perfectly scaled' if To is significant but, g is not. The 'zero-g' hypothesis	There is no water wave if g is dropped. Water fills the entire flask in a zero-g' environment.
D (Modified A)	Distortion produced by changing the temperature group RT_w/gL can be compensated by changing the flow resistance: $\left(\frac{fL}{D}\right)_m = \frac{L_p}{L_m}\left[1 + \left(\frac{fL}{D}\right)_p\right] - 1$	Good for max. upward force		

Table 2.2 Summary of LLL Scaling Analysis

number, which is based on the characteristic velocity u_c, and k of the gas-discharge period.

Table 2.3. UCLA Scaling Laws.

Vent Clearing	$\frac{F}{\rho_c u_c^2 L_c^2} = \phi\left[\frac{p_c}{\rho_c u_c^2}, \frac{g_c L_c}{u_c^2}, \frac{t_c u_c^2}{L_c}\right]$	LLL Model B reduces to UCLA expression if $gL/u_c^2 = 1$, without f and k.
Sonic Discharge and Subsonic Discharge	$\frac{F}{\rho_c u_c^2 L_c^2} = \phi\left[\frac{p}{\rho_c u_c^2}, \frac{gL}{u_c^2}, \frac{u_c^2}{\gamma RT_c} k, \frac{tu_c^2}{L_c}\right]$	LLL Model A reduces to UCLA expression if $gL/u_c^2 = 1$, without f and k.

For the LLL 1/5 scale experiment, namely $(L_c)_p/(L_c)_m = 5$, the scaling of all physical variables is feasible with the exception of the temperature requirement, that is

$$\frac{(kRT_c)_p}{(kRT_c)_m} = \frac{(L_c)_p}{(L_c)_m} = 5.$$

If $(T_c)_p$ is close to room temperature, the characteristic temperature of the model, $(T_c)_m$, would be unrealistically low, around 60° R. Mainly because of this requirement, the LLL Model A is modified to become Model D, in which the burden of simulating the temperature ratio is circumvented by the introduction of the orifice. By the same reasoning, simulation of the enthalpy-flux ratio in Moody's analysis is accomplished, in part, through the adjustment of the orifice flow coefficient (C_{mo}) used in the MIT scaling law. The impossibility of temperature scaling is circumvented by means of the orifice.

There is, however, major conceptual difficulty in accepting this

procedure, because the orifice does not exist in the downcomer of the prototype. Geometrical similarity is the first cardinal requirement in dynamical similitude, but is hindered by the introduction of the orifice, which substantially changes the geometry of the suppression pool.

Let us now address the question of orificing. The only reason for orificing the downcomer is to avoid temperature simulation. If orificing is done without altering the entire physical phenomenon or affecting the key results, room-temperature air could be used as the working medium in model testing. According to the simple solution obtained at UCLA for the vent-clearing problem, the maximum downward force could be correctly estimated with or without orificing, since the vent-clearing will not be affected by Mach number. However, the maximum upward force, as a result of pool swelling, is a direct consequence of air discharge. Orificing the downcomer would result in a rather long duration of "choking" at a specific mass flow rate. The exit pressure of the downcomer could conceivably vary, depending on the location of the orifice. The time history of the upward and downward loads, in our judgment, is not properly simulated by orificing the downcomer.

The recent MIT laboratory experiment, however, seems to support the practice of orificing. It is found that, for specific p_D/p_W and $p_w/\rho g L_c$ (3.0 and 4.2, respectively) ratios, the non-dimensional time, $t(g/L_c)^{\frac{1}{2}}$, for vent-clearing, and the minimum flow pressure and maximum ceiling pressures are practically independent of the enthalpy flow-rate. In fact, they are all independent of the linear scale of the apparatus (small system, D = 14 cm; medium system, D = 28 cm). Further discussions of the effects of orificing can be found in Section 4.6.

2.2 Steam Scaling

In the design of a scale model to study the steam transient phenomenon in subcooled water, it is necessary to preserve the important parameters of the prototype, to guarantee that all governing effects are included and that the negligible effects are excluded. Two periods should be distinguished in the steam transient of the LOCA. The first period would be characterised by a steam jet where momentum is an important parameter. The second period is the steam chugging period where steam flow rate and subcooling are important.

2.2.1 Steam Jet Condensation

For the transient steam jet in a subcooled liquid, the governing equations for the incompressible liquid medium are.

$$\nabla \cdot \vec{u}_\ell = 0, \tag{2.20}$$

$$\frac{D\vec{u}_\ell}{Dt} = -\frac{1}{\rho_\ell} \nabla P_\ell, \text{ and} \tag{2.21}$$

$$\frac{DT_\ell}{Dt} = \alpha_\ell \nabla^2 T_\ell, \tag{2.22}$$

where

$\vec{u}_\ell$ = the liquid velocity vector,

P_ℓ = the liquid pressure,

ρ_ℓ = the liquid density,

T_ℓ = the liquid temperature, and

α_ℓ = the liquid thermal diffusivity.

For the vapor region, the governing equations are:

$$\frac{\partial \rho_v}{\partial t} + \nabla \cdot \rho_v \vec{u}_v = 0, \tag{2.23}$$

$$\frac{D\vec{u}_v}{Dt} = -\frac{1}{\rho_v} \nabla P_v, \text{ and} \tag{2.24}$$

$$\frac{DT_v}{Dt} = \alpha_v \nabla^2 T_v + \frac{1}{\rho_v C_{pv}} \frac{DP_v}{Dt}, \tag{2.25}$$

where

$\vec{u}_v$ = the vapor velocity vector,

P_v = vapor pressure,

ρ_v = vapor density,

T_v = vapor temperature,

α_v = vapor thermal diffusivity, and

C_{pv} = vapor thermal capacity.

At the interface, $\vec{r}_i$, the conservation of mass, momentum, and energy requires that:

$$\rho_v(\vec{u}_v - \dot{\vec{r}}_i)\cdot\hat{n} = \rho_\ell(\vec{u}_\ell - \dot{\vec{r}}_i)\cdot\hat{n} = \dot{m}, \tag{2.26}$$

$$P_v - P_\ell = \sigma\left(\frac{1}{R_1} + \frac{1}{R_2}\right), \text{ and} \tag{2.27}$$

$$\gamma_\ell \frac{\partial T_\ell}{\partial n} - \gamma_v \frac{\partial T_v}{\partial n} = \dot{m} h_{fg}, \tag{2.28}$$

where

$\dot{\vec{r}}_i$ = the interfacial velocity,

$\hat{n}$ = the normal vector at the interface,

$\dot{m}$ = the condensation rate,

σ = surface tension,

R_1, R_2 = principal radii, and

h_{fg} = heat of evaporation.

In Equation (2.27), the liquid viscosity effect and the momentum transfer due to steam condensation are neglected, and the viscous dissipation and kinetic energy have not been included. If equilibrium is assumed at the interface, then

$$T_{v_i} = T_{\ell_i}, \tag{2.29}$$

and the pressure is approximated by the Clausius Clapeyron relation

$$P_{v_i} = P_{v_o} \exp\left[\frac{h_{fg}}{R_g T_{i_o}}\left(1 - \frac{T_{i_o}}{T_i}\right)\right], \tag{2.30}$$

where

T_{v_i} = the vapor temperature at the interface,

T_{ℓ_i} = the liquid temperature at the interface,

P_{v_i} = the vapor pressure at the interface,

P_{v_o} = the reference vapor pressure, and

T_{v_o} = the reference vapor temperature.

Besides the governing equation for the steam condensation, the liquid surface experiences tangential viscous shear from a parallel gas stream. The equation predicts instability for a flat liquid surface and a parallel gas flow when

$$u^2 = \frac{1}{\alpha_1 \alpha_2}\left[\frac{\sigma g(\alpha_1 - \alpha_2)}{\rho_\ell + \rho_v}\right]^{\frac{1}{2}}, \tag{2.31}$$

where

ρ_ℓ = liquid density,

ρ_v = vapor density,

$$\alpha_1 = \frac{\rho_\ell}{\rho_\ell + \rho_v}, \text{ and}$$

$$\alpha_2 = \frac{\rho_v}{\rho_\ell + \rho_v}.$$

If $\rho_\ell >> \rho_v$, $\alpha_1 = 1$, and $\alpha_2 = \rho_v/\rho_L$, then

$$u^2 = \frac{\rho_\ell}{\rho_v} \left(\frac{\sigma g}{\rho_\ell}\right)^{\frac{1}{2}} \tag{2.32}$$

If the velocity near the surface is related to the exit velocity, V_E, by

$$u = V_E \frac{d}{x}, \tag{2.33}$$

where

d = the diameter of the pipe, and

x = the distance from the jet,

then the similarity parameter for the stripping phenomenon is the Kelvin-Helmholtz instability number, defined as

$$I_{K\text{-}H} = \frac{V_E^2 d^2}{x^2\left[\frac{\rho_\ell}{\rho_v}\left(\frac{\sigma g}{\rho_\ell}\right)^{\frac{1}{2}}\right]} \tag{2.34}$$

If r_c = the characteristic length, then

U_c = the characteristic velocity,

t_c = the characteristic time = r_c/U_c,

P_c = the characteristic pressure,

ρ_c = the characteristic density,

T_c = the characteristic temperature,

α_c = the characteristic thermal diffusivity,

C_{pc} = the characteristic thermal capacity, and

h_c = the characteristic enthalpy = $C_{pc}T_c$.

Equations (2.10) through (2.18) can be expressed in non-dimensional form as:

$$\nabla \cdot \vec{u}_\ell^* = 0, \tag{2.35}$$

$$\frac{D\vec{u}_\ell^*}{Dt^*} = -Eu \frac{1}{\rho_\ell^*} \nabla P_\ell^*, \tag{2.36}$$

$$\frac{DT_\ell^*}{Dt^*} = Fo\ \alpha_\ell^* \nabla^2 T_\ell^*, \tag{2.37}$$

$$\frac{\partial \rho_v^*}{\partial t^*} + \nabla \cdot \rho_v^* \vec{u}_v^* = 0, \tag{2.38}$$

$$\frac{D\vec{u}_v^*}{Dt^*} = -Eu \frac{1}{\rho_c^*} \nabla P_v^*, \tag{2.39}$$

$$\frac{DT_v^*}{Dt^*} = Fo\ \alpha_v^* \nabla^2 T_v^* + \frac{Eu\ M^2}{(\gamma - 1)} \frac{1}{\rho_v^* C_{pv}^*} \frac{DP_v^*}{Dt^*}, \tag{2.40}$$

$$\rho_v^* (\vec{u}_v^* - \dot{\vec{r}}^*) \cdot \hat{n}^* = \rho_\ell^* (\vec{u}^* - \dot{\vec{r}}^*) \cdot \hat{n}^* = \dot{m}^*, \tag{2.41}$$

$$P_v^* - P_\ell^* = \frac{1}{Eu\ We} \left(\frac{1}{R_1^*} + \frac{1}{R_2^*} \right), \tag{2.42}$$

$$k_\ell^* \frac{\partial T_\ell^*}{\partial \eta^*} - k_v^* \frac{\partial T_v^*}{\partial \eta^*} = \frac{1}{Fo} \dot{m}^* h_{fg}^*, \tag{2.43}$$

$$T_{v_i}^* = T_{\ell_i}^*, \text{ and} \tag{2.44}$$

$$P_v^* = P_{v_o}^* \exp \left[\frac{\gamma}{\gamma - 1} \frac{h_{fg}^*}{T_{i_o}^*} \left(1 - \frac{T_{i_o}^*}{T_i^*} \right) \right]. \tag{2.45}$$

Hence the dimensionless groups are:

$$Fo = \text{the Fourier number} = \frac{\alpha_c t_c}{r_c^2}, \tag{2.46}$$

$$\gamma = \text{the specific heat ratio} = C_{pc}/C_{vc}, \tag{2.47}$$

$$M = \text{the Mach number} = (U_c^2/\gamma RT)^{\frac{1}{2}}, \tag{2.48}$$

$$We = \text{the Weber number} = (\rho_c U_c^2 r_c)/\sigma, \text{ and} \tag{2.49}$$

$$Eu = \text{the Euler number} = P_c/(\rho_c U_c^2). \tag{2.50}$$

Additional similitude parameters include:

$$\pi_1 = \frac{U_c^2}{(\frac{\sigma g}{\rho_c})^{\frac{1}{2}}}, \tag{2.51}$$

$$\pi_2 = \frac{h_c}{C_{pc} T_c}, \tag{2.52}$$

$$\pi_3 = \frac{u_c}{r_c/t_c}, \tag{2.53}$$

$$\pi_4 = \frac{P_v}{P_\ell}, \tag{2.54}$$

$$\pi_5 = \frac{\rho_v}{\rho_\ell}, \text{ and} \tag{2.55}$$

$$\pi_6 = \frac{T_v}{T_\ell}. \tag{2.56}$$

Actually, a combination of π_2 and π_5 would yield the Jacob number.

Since the vapor curve for water is non-linear, it is desirable to preserve the thermodynamical similarity. Hence,

$$(P_c)_m = (P_c)_p,$$

$$(T_c)_m = (T_c)_p, \text{ and}$$

$$(\rho_c)_m = (\rho_c)_p.$$

The subscript m refers to the model, and p refers to the prototype. With the choice of

$$(u_c)_m = (u_c)_p,$$

the Mach number, the specific heat ratio, the Euler number, π_1, π_2, π_3, π_4, π_5, and π_6 can be simulated, but the Fourier number and the Weber number cannot be simulated. Actually the Weber number is not very important in the steam condensation process; hence, it can be relaxed. The relaxation of the Fourier number may impose some doubt on the simulation of the conductive heat transfer process. However, if the Kelvin-Helmholtz instability phenomenon governs the heat transfer process, then the simulation of the parameter π_1 is more important than the simulation of the Fourier number.

2.2.2 Steam Chugging

During the steam chugging period, both the pool dynamic and the vapor acoustic effects are important. Considering a simple model as shown in Figure 2.1, the governing equations for the incompressible liquid medium are (see Equations (2.20) through (2.22)):

$$\nabla \cdot \vec{u}_\ell = 0, \tag{2.57}$$

$$\frac{D\vec{u}_\ell}{Dt} = -\frac{1}{\rho_\ell} \nabla P_\ell, \text{ and} \tag{2.58}$$

$$\frac{DT_\ell}{Dt} = \alpha_\ell \nabla^2 T_\ell. \tag{2.59}$$

Considering the vapor region as a single node, then the governing equations for the vapor bubble become:

Continuity: $$\frac{dP_B V_B}{dt} = \dot{m}_i A_i - \dot{m}_c A_c, \qquad P_B = \text{uniform}, \tag{2.60}$$

Energy: $$\frac{dU_B}{dt} = \dot{m}_i A_i h_i - \dot{m}_c A_c h_v - P_B \frac{dV_B}{dt},$$

where

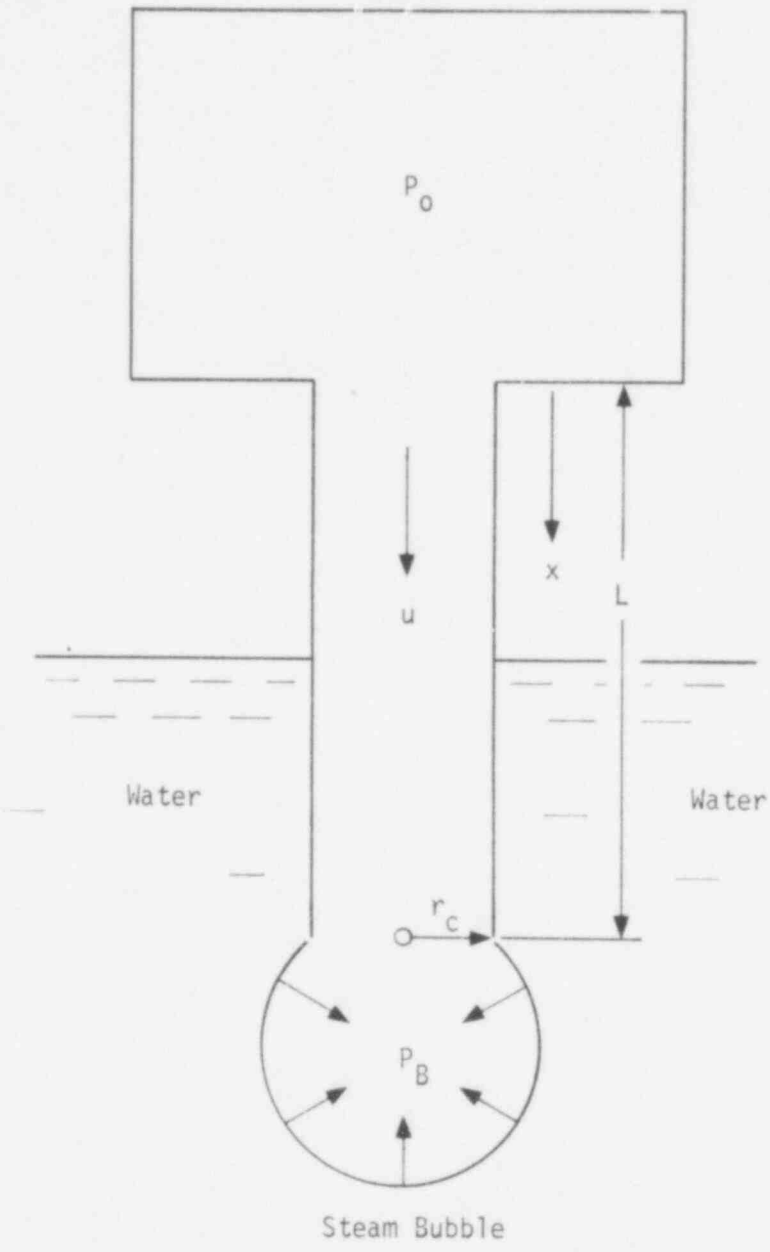

Figure 2.1. Simplified Model for Steam Chugging.

V_B = the bubble vapor volume,

A_i = the area of the inlet,

A_c = the condensation area,

m_i = the mass influx rate,

m_c = the condensation rate,

U_B = the vapor internal energy,

h_i = the inlet enthalpy,

h_v = the vapor enthalpy,

P_B = the bubble vapor pressure, and

ρ_B = the bubble vapor density.

Considering the vent flow in the simplified model as shown in Figure 2.1, the pressure transient in the pipe is given by:

Continuity: $$\frac{\partial \rho_v}{\partial t} + u_v \frac{\partial \rho_v}{\partial x} + \rho_v \frac{\partial u_v}{\partial x} = 0, \quad \text{and} \tag{2.63}$$

Momentum: $$\rho_v \frac{\partial u_v}{\partial t} + \rho_v u_v \frac{\partial u_v}{\partial x} + \frac{\partial P_v}{\partial x} = 0,$$

where

ρ_v = the vapor density,

u_v = the vapor velocity,

P_v = the vapor pressure,

t = time, and

x = the one-dimensional space co-ordinate.

The pressure at $x = 0$ is P_o, while at $x = L$ it is the steam bubble pressure, P_B.

The equations for the interface between the vapor and the liquid are given by Equations (2.26) through (2.28). During the bubble collapse process, depending on the acceleration of the interface, the Taylor-Rayleigh instability may dominate the heat transfer process.

In view of the conjugate nature of the problem, two characteristic lengths are suggested. If L is defined as the characteristic length for the vent pipe and r_c as the characteristic length for the vapor and the pool, then the length of the vent pipe should be scaled as

$$(L_c)_m = (L_c)_p. \tag{2.64}$$

in order to simulate the acoustic effect. The pipe radius should be scaled as

$$(r_c)_m = C(r_c)_p, \tag{2.65}$$

where C is the scale factor, for example 1/5 or 1/12.

By going through the process of non-dimensionalization, the non-dimensional groups for the bubble dynamics are:

$$\text{Fo} = \text{the Fourier number} = \frac{\alpha_c t_c}{r_c^2}, \tag{2.66}$$

$$\gamma = \text{the specific heat ratio} = C_{pc}/C_{vc}, \tag{2.67}$$

$$\text{M} = \text{the Mach number} = \left(\frac{U_c^2}{\gamma RT}\right)^{1/2}, \tag{2.68}$$

$$\text{We} = \text{the Weber number} = \frac{\rho_c U_c^2 r_c}{\sigma_c}, \text{ and} \tag{2.69}$$

$$\text{Eu} = \text{the Euler number} = \frac{p_c}{\rho_c U_c^2}. \tag{2.70}$$

The governing parameter for the Taylor-Rayleigh instability is the Bond number,

$$Bo = \frac{\rho_c a_c r_c^2}{\sigma_c},$$

where a_c is the characteristic acceleration. As mentioned in Section 2.1, in order to preserve thermodynamical similartiy,

$$(P_c)_m = (P_c)_p, \tag{2.72}$$

$$(T_c)_m = (T_c)_p, \text{ and} \tag{2.73}$$

$$(\rho_c)_m = (\rho_c)_p. \tag{2.74}$$

If the Euler number is important (collapse dominated by inertia), then the simulation should be

$$(u_c)_m = (u_c)_p. \tag{2.75}$$

On the other hand, if the collapse is governed by heat transfer, then the Fo and Bo numbers become important. However, it is difficult to satisfy both the Fourier number and the Bond number at the same time if the working fluid for both the prototype and the model is water. Even if we can relax the Bond number, it is uncertain at this stage whether the simulation can be completely achieved in practice, because

$$(u_c)_m = \frac{1}{C} (u_c)_p$$

for the simulation of the Fourier number.

REFERENCES FOR SECTION 2

2.1. Catton, I., C. K. Chan, V. K. Dhir, and C. Y. Liu, "A Research Proposal to Nuclear Regulatory Commission for Studies of Dynamic Loads in Pressure Suppression Containment," School of Engineering and Applied Science, University of California, Los Angeles, UCLA-ENG-P-3045-N-76.

2.2. Moody, F. J., "A Systematic Procedure for Scale-Modeling Problems in Unsteady Fluid Mechanics," unpublished paper.

2.3. Kline, S. L., Similitude and Approximate Theory, McGraw-Hill, 1965.

2.4. Sonin, A. A., "MIT Program on Modeling of Pool Swell Hydrodynamics," notes prepared for the Containment Code Review Group Meeting, Silver Spring, January 6, 1977.

2.5. McCauley, E. W., and J. H. Pitts, "Bench Scale Experiments to Test Air-Water Scaling Hypothesis for the Lawrence Livermore Laboratory; 1/5 Scale, BWR Mark-I Pressure Suppression Experiment Program," Lawrence Livermore Laboratory, September 1976.

3. EXPERIMENTAL APPARATUS AND PROCEDURE

The experimental apparatus was designed so that the vent clearing process and other associated phenomena could be studied from single vertical vents submerged in an axi-symmetric pool. The apparatus consists of a transparent cylindrical test chamber and a gas supply system, which is composed of a 51 mm nominal diameter pipe and a reservoir that can be filled with different gases.

3.1 Description of the Apparatus

A schematic diagram and a photograph of the experimental apparatus for the gas-water tests are shown in Figures 3.1 and 3.2. The test chamber is made of a plexiglas pipe, 45 cm in diameter and 120 cm in height. The pipe is held at the ends by two air-tight flanges made out of 2.5 cm thick aluminum plate. The bottom flange has two ports for connecting the test chamber to a fresh-water supply line and to a drain. Five holes, 6 mm in diameter, are tapped in each of the two planes of the bottom flange for the pressure transducers (see Figure 3.3). A 51 mm diameter tube holder is welded to the top flange, through which tubes of up to 46 mm diameter can be inserted into the test chamber. Ten holes, 19 mm in diameter, are also tapped in the top flange. These holes are generally open to the atmosphere, but can be closed when experiments are to be conducted at pressures other than atmospheric pressure.

The tube holder on the upper flange is connected to the 51 mm diameter air supply line via a Thermo Systems Model 1051-1 Anemometer. The maximum response frequency of the anemometer in air is 10 kHz, and the anemometer is capable of measuring a maximum velocity of 300 m/s. A Statham pressure transducer is placed downstream of the flow meter to

Figure 3.1. Schematic Diagram of the Apparatus.

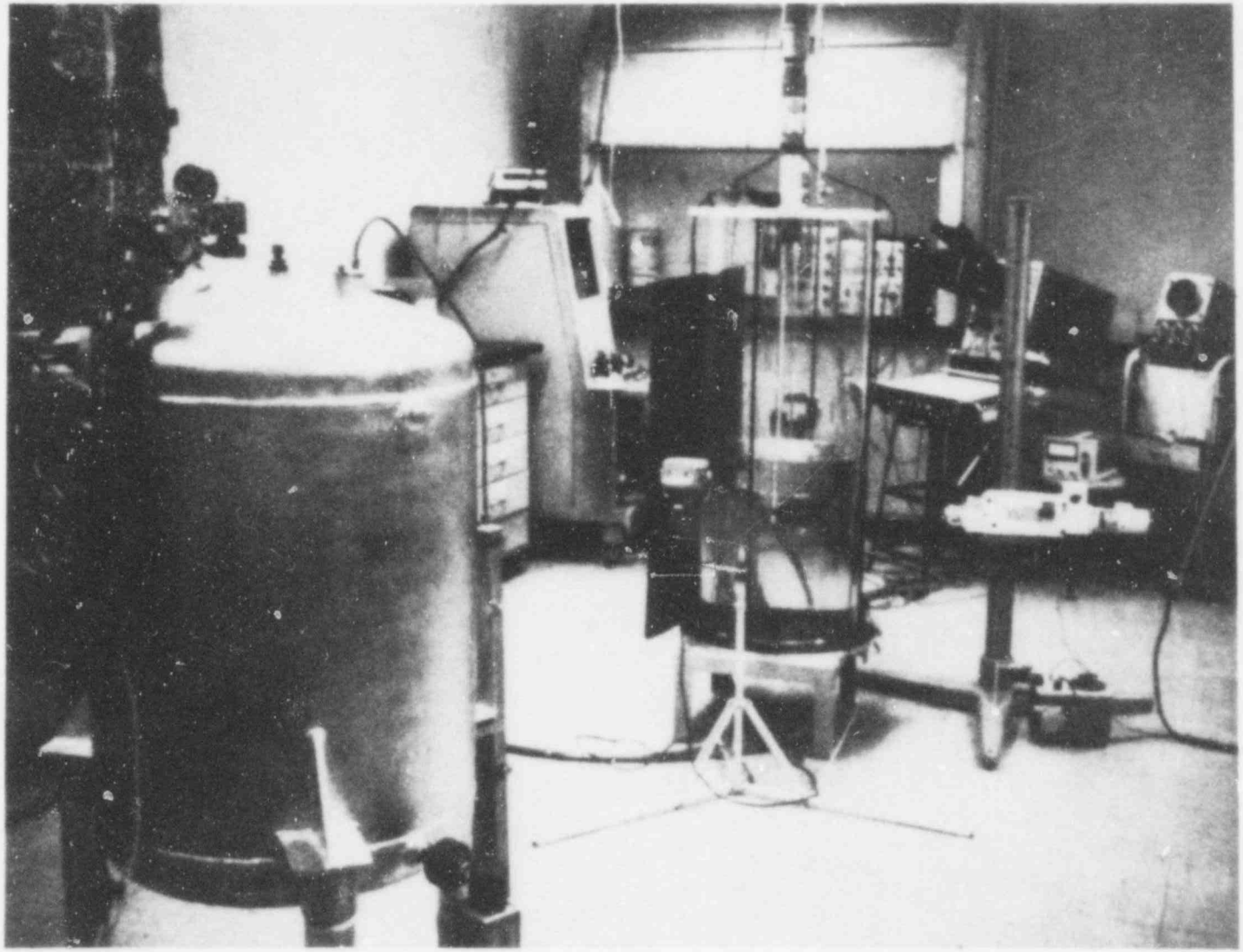

Figure 3.2 Photograph of the Apparatus

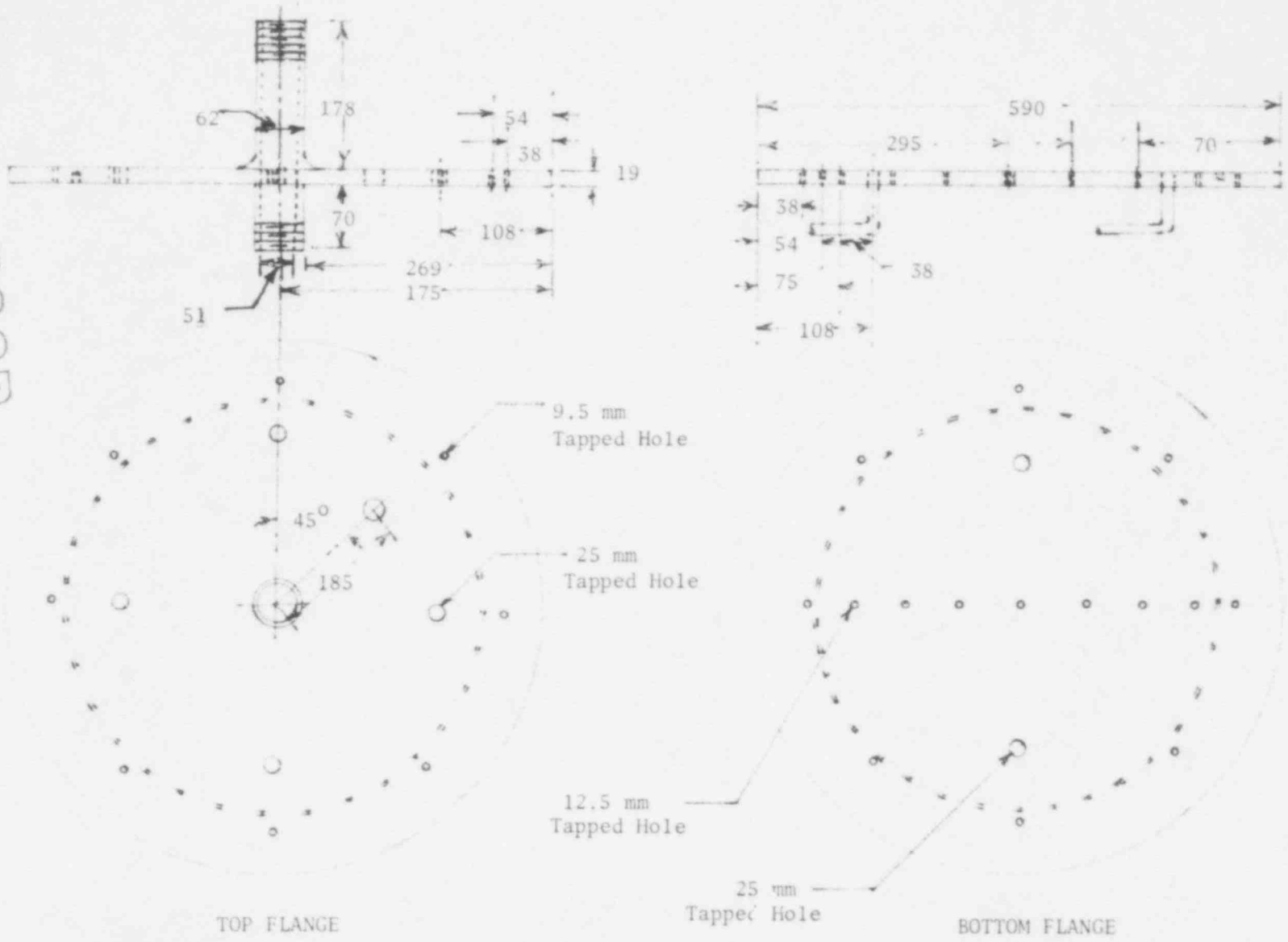

All Dimensions in mm

Figure 3.3. Scaled Drawing of the Top and Bottom Flanges of the Test Chamber.

measure the line static pressure. The analog output of the pressure transducer is supplied to a Tektronix 564 storage oscilloscope. The time response of this oscilloscope is 0.5 microsecond.

The air reservoir is a cylindrical steel tank, 0.3 m^3 in volume. The safe working pressure for the reservoir is 200 kPa, and is controlled by the actuation of a safety relief valve attached to the vessel. The pressure inside the vessel is monitored by a Bourden-type pressure guage and by a Celesco strain-guage type pressure transducer. The pressure transducer signal is recorded on a Hewlett-Packard Mosley X-Y recorder. The reservoir can be pressurized by the opening of a solenoid valve, connected to the utility air-supply system of the laboratory. A 37 mm diameter quick-acting solenoid valve connects the reservoir to the test chamber through the 51 mm nominal diameter pipe line. The solenoid valve opens completely 32 to 64 ms after it is actuated. The orifice is placed in the pipe line between the upstream pressure transducer and the test chamber.

In addition to the movie technique, a laser system was set up as an alternative means of measuring the vent clearing time, as shown in Figure 3.4. The beam from a 15 mW He-Ne laser is directed through the test chamber and the glass tube at a level just below the air-water interface. The beam is redirected downwards by a glass prism to a silver mirror, which reflects the beam back through the test chamber at a level that just clears the vent tube. The intensity of the laser beam is detected by a silicon photo-multiplier. The signal from the photo-multiplier is recorded by a Tektronix 564 storage oscilloscope.

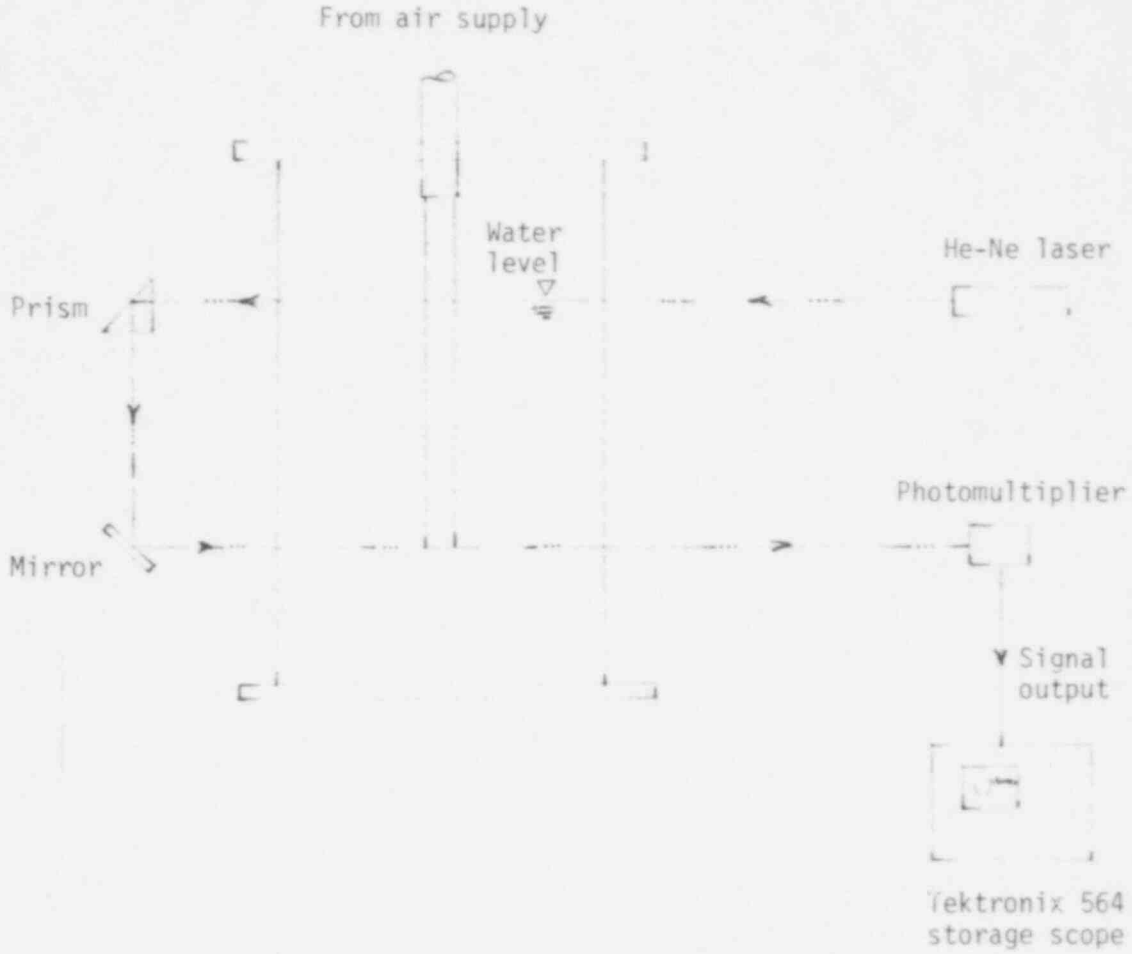

Figure 3.4 Laser System for Vent-Clearing Time Measurement

3.2 Experimental Procedure

Before starting the experiment, the flowmeter, pressure transducers, recorders, and movie camera were synchronized, and their operability checked. A plexiglas tube of the desired size, with a centimeter scale pasted on it, was inserted through the tube holder on the upper flange and was held rigidly. The tube length was adjusted to place the exit plane of the tube about 24 or 50 cm from the bottom of the test chamber. The test chamber was then filled with fresh water to give a pre-selected submergence depth for the tube. Then, the air reservoir was pressurized. The Photosonics movie camera and all other systems, and the quick-acting solenoid valve, were activated. The vent-clearing process and bubble growth were captured on fast movie film at a maximum speed of about 680 frames per second, while the exposure time varied from 500 to 563 micro-seconds. After the reservoir was emptied, the pool was allowed to reach its undisturbed position and the experiment was repeated with a different maximum reservoir pressure. In this study, data for vent clearing and bubble growth were taken for tubes of 21, 34, and 47 mm diameters, when the maximum reservoir pressure was varied between 115.1 kPa to 177.2 kPa, and the submergence depth was varied from 10 cm to 60 cm. The ambient test chamber pressure was varied from 60.7 kPa to 101.4 kPa.

A similar procedure was followed when the vent-clearing time was determined by the laser technique. The oscilloscope was triggered automatically after the valve started to open. The laser beam was interrupted by the interface; first, when it passed through the upper beam, and then when it passed through the lower beam (Figure 3.4). The beam thus produced two distinct signals on the oscilloscope. The vent-clearing time was then the time difference between the two signals.

3.3 Data Reduction

Photographic information was used to determine the displacement of the interface, the total time of vent clearing, the bubble growth rate, the pool free surface swell height, and the mode of free-surface oscillations.

The 16 mm movies were projected on a screen and a preliminary survey was made to determine the portions of interest. Starting from a frame in which the interface had just moved, the location of the interface was measured from the tube exit plane. The number of frames during which the interface moved a certain distance was then counted. The exact frame speed during this period was determined from the neon timing-light marks on the film. A similar procedure was used to determine the bubble growth rate and the pool free surface swell height.

The movies have been coded according to the date and experimental conditions. The movies are stored in the Nuclear Energy Laboratory of the Chemical, Nuclear, and Thermal Engineering Department of the School of Engineering and Applied Science at the University of California, Los Angeles. The movies and the raw data are available on request.

4. EXPERIMENTAL AND ANALYTICAL RESULTS

Ninety-two tests involving four different pipe sizes (D_i = 46, 34, 22, and 9 mm); four different test chamber pressures (P_i = 101.4, 87.8, 74.3, and 60.7 kPa); five different submergence depths (L = 60, 45, 30, 20, 10 cm); various distances between the pipe exit and the bottom plate (B = 3 to 49.5 cm); various dry well pressure (P_o = 177.2 to 115.1 kPa); and three gases (air, argon, and helium) were performed. The test conditions are summarized in Table 4.1. In some cases, movie pictures were taken and the pressure force was recorded. The objective of each run is listed in the 'comment' section of Table 4.1. The major objectives involve studying of the vent clearing phenomenon, bottom pressure forces, bubble growth dynamics, and pool swelling. The data of these test runs are summarized in Appendices D, E, F, and G, while the results are discussed in the following sections.

TEST MATRI. ABLE

L = Submergence Depth
B = Distance of the Tube Exit from the Bottom of the Chamber
P_o = Upstream Reservoir Pressure
P_i = Ambient Test Chamber Pressure
D_i = Vent Tube Diameter

Run	Date	Medium (Gas)	D_i (mm)	Test Chamber	L (cm)	B (cm)	P_o (kPa)	P_i (kPa)	COMMENT
1	8-5-76	Air	46	Open	0.2	8.6	Steady State	101.4	To observe the relation of air flow rate and swell height.
2	8-5-76	Air	46	Open	10	8.6	"	101.4	"
3	8-5-76	Air	46	Open	18	8.6	"	101.4	"
4	8-9-76	Air	34	Open	7	11.5	184.1	101.4	"
5	8-10-76	Air	34	Open	30	11.5	184.1	101.4	"
6	8-10-76	Air	34	Open	30	11.5	184.1	101.4	"
7	8-10-76	Air	34	Open	60	5.6	Steady State	101.4	"
8	8-11-76	Air	22	Open	60	5.6	"	101.4	"
9	8-11-76	Air	22	Open	30	10	"	101.4	"
10	8-11-76	Air	22	Open	3	3	"	101.4	"
11	8-12-76	Air	9	Open	7	11	"	101.4	"
12	8-12-76	Air	9	Open	30	11	"	101.4	"
13	8-12-76	Air	9	Open	60	6	"	101.4	"
14	8-27-76	Air	46	Open	60	6	"	101.4	Vent Clearing Time Measurement.
15	9-2-76	Air	46	Open	30	6	"	101.4	"

Run	Date	Medium (Gas)	D_i (mm)	Test Chamber	L (cm)	B (cm)	P_o (kPa)	P_i (kPa)	COMMENT
16	9-3-76	Air	46	Open	30	6	115.1 135.8 149.6 156.5	101.4	Vent Clearing Time Measurement.
17	9-3-76	Air	46	Open	60	6	"	101.4	"
18	9-10-76	Air	46	Open	30	14.6	115.1 122.0 135.8	101.4	"
19	9-22-76	Air	46	Open	30	10	122.0 128.9 135.8 149.6	101.4	"
20	9-23-76	Air	46	Open	20	10	115.1 122.0 128.9 135.8 142.7	101.4	"
21	9-23-76	Air	46	Open	10	10	115.1 122.0 128.9 135.8	101.4	"
22	9-28-76	Air	46	Open	45	10	Steady State	101.4	To observe the relation of air flow rate and swell height.
23	9-28-76	Air	46	Open	30	10	"	101.4	"
24	9-28-76	Air	46	Open	15	10	"	101.4	"
25	9-28-76	Air	34	Open	15	10	"	101.4	"
26	9-28-76	Air	34	Open	30	10	"	101.4	"
27	9-28-76	Air	34	Open	45	10	"	101.4	"

Run	Date	Medium (Gas)	D_i (MM)	Test Chamber	L (cm)	B (cm)	P_o (kPa)	P_i (kPa)	COMMENT
28	9-30-76	Air	34	Open	10	10	115.1 128.9 142.7	101.4	Vent Clearing Time Measurement.
29	10-1-76	Air	34	Open	30	10	"	101.4	"
30	10-1-76	Air	34	Open	60	10	"	101.4	"
31	10-2-76	Air	22	Open	10	12.3	Steady State	101.4	To observe the relation of air flow rate and swell height.
32	10-2-76	Air	22	Open	30	12.3	"	101.4	"
33	10-2-76	Air	22	Open	60	12.3	"	101.4	"
34	10-2-76	Air	22	Open	60	12.3	115.1 128.9 142.7	101.4	Vent Clearing Time Measurement.
35	10-2-76	Air	22	Open	30	12.3	"	101.4	"
36	10-2-76	Air	22	Open	10	12.3	"	101.4	"
37	11-5-76	Air	15.9	Open	10	13.7	"	101.4	To observe the relation of air flow rate and swell height.
38	11-5-76	Air	15.9	Open	30	13.7	"	101.4	"
39	11-5-76	Air	15.9	Open	60	13.7	"	101.4	"
40	11-5-76	Air	6.4	Open	10	36.2	"	101.4	"
41	11-5-76	Air	6.4	Open	30	36.2	"	101.4	"
42	11-5-76	Air	6.4	Open	60	36.2	"	101.4	"
43	11-8-76	Air	15.9	Open	10	14	"	101.4	"
44	11-19-76	Air	15.9	Open	60	26.7	"	101.4	"

Run	Date	Medium (Gas)	D_i (mm)	Test Chamber	L (cm)	B (cm)	P_o (kPa)	P_i (kPa)	COMMENT
45	11-19-76	Air	15.9	Open	30	26.7	"	101.4	To observe the relation of air flow rate and swell height.
46	11-19-76	Air	15.9	Open	10	26.7	"	101.4	"
47	11-19-76	Air	15.9	Open	10	26.7	"	101.4	To observe the transient swelling and vent clearing.
48	11-19-76	Air	15.9	Open	30	26.7	"	101.4	"
49	11-19-76	Air	15.9	Open	45	26.7	"	101.4	"
50	11-19-76	Air	15.9	Open	10	26.7	"	101.4	To observe the transient swelling and vent clearing with close-up lens.
51	11-27-76	Air	46	Open	30	26.7	115.1 122.0 128.9 135.8	101.4	Interface movement observation.
52	11-27-76	Air	46	Open	30	26.7	"	101.4	Bubble formation observation.
53	11-27-76	Air	46	Open	30	26.7	"	101.4	Transient swelling height observation.
54	12-15-76	Air	46	Open	30	26.7	115.1 128.9	101.4	Interface movement observation.
55	12-16-76	Air	46	Open	30	26.7	115.1 122.0 128.9	101.4	Interface movement observation.
56	12-16-76	Air	46	Open	30	26.7	122.0 128.9	101.4	To take the movie of whole chamber.
57	3-3-77	Air	46	Oper.	10	24.1	122.0 135.8	101.4	Pressure forces measurements.
58	3-31-77	Air	46	Open	30	24.1	122.0 135.8	101.4	To take the movie of whole chamber and measure the pressure forces.

Run	Date	Medium (Gas)	D_i (mm)	Test Chamber	L (cm)	B (cm)	P_o (kPa)	P_i (kPa)	COMMENT
59	3-31-77	Air	46	Open	10	24.1	149.6 163.4 177.2	101.4	To take the movie of whole chamber and measure the pressure forces
60	3-31-77	Air	46	Open	30	24.1	122.0 135.8 149.6	101.4	"
61	4-5-77	Air	46	Open	10	24.1	191.0	101.4	"
62	4-5-77	Air	46	Open	20	24.1	122.0 135.8 149.6	101.4	To measure the pressure forces.
63	4-6-77	Air	46	Open	20	24.1	163.4 177.2	101.4	"
64	4-6-77	Air	46	Open	30	24.1	163.4 177.2 191.0	101.4	"
65	4-7-77	Air	46	Open	10	24.1	122.0 135.8 149.6 163.4 177.2	101.4	"
66	4-8-77	Air	46	Open	20	49.5	"	101.4	"
67	4-21-77	Air	46	Open	10	26.7	122.0 135.8 149.6 163.4 177.2 191.0	101.4	To measure the pressure forces with the upstream pressure transducer above the orifice position. No orifice.
68	4-21-77	Air	46	Open	10	26.7	"	101.4	To measure the pressure forces with 25.4 mm I.D. orifice.
69	4-22-77	Air	46	Open	10	26.7	"	101.4	To measure the pressure forces with the upstream pressure transducer below the orifice posiiton. No orifice.

Run	Date	Medium (Gas)	D_i (mm)	Test Chamber	L (cm)	B (cm)	P_o (kPa)	P_i (kPa)	COMMENT
70	5-5-77	Air	46	Closed	10	26.7	177.2	60.7 74.3 87.8 101.4	To measure the pressure forces with 25.4 mm I.D. orifice.
71	5-6-77	Air	46	Closed	10	26.7	177.2	"	To measure the pressure forces without orifice.
72	5-9-77	Ar	46	Closed	10	26.7	177.2	"	"
73	5-9-77	Ar	46	Closed	10	26.7	177.2	"	To measure the pressure forces with 25.4 mm I.D. orifice.
74	5-13-77	He	46	Closed	10	26.7	177.2	"	"
75	5-13-77	He	46	Closed	10	26.7	177.2	"	To measure the pressure forces without orifice.
76	6-21-77	Air	46	Closed	10	26.7	177.2	87.8 101.4	To take the movie of whole chamber and measure the pressure forces and flow rate without orifice.
77	6-21-77	Air	46	Closed	10	26.7	177.2	60.7 74.3	"
78	6-21-77	Air	46	Closed	10	26.7	177.2	87.8 101.4	To take the movie of whole chamber and measure the pressure forces and flow rate with 25.4 mm I.D. orifice.
79	6-21-77	Air	46	Closed	10	26.7	177.2	60.7 74.3	"
80	6-24-77	Air	46	Closed	10	26.7	177.2	87.8 101.4	To take the movie of whole chamber and measure the pressure forces and flow rate with 15.6 mm I.D. orifice.
81	6-24-77	Air	46	Closed	10	26.7	177.2	60.7 74.3	"
82	6-25-77	He	46	Closed	10	26.7	177.2	60.7 74.3 87.8 101.4	"

Run	Date	Medium (Gas)	D_i (mm)	Test Chamber	L (cm)	B (cm)	P_o (kPa)	P_i (kPa)	COMMENT
83	6-27-77	He	46	Closed	10	26.7	177.2	60.7 74.3 87.8 101.4	To take the movie of whole chamber and measure the pressure forces and flow rate without orifice.
84	6-27-77	He	46	Closed	10	26.7	177.2	87.8 101.4	To take the movie of whole chamber and measure the pressure forces and flow rate with 25.4 mm I.D. orifice.
85	6-27-77	He	46	Closed	10	26.7	177.2	60.7 74.3	"
86	6-28-77	Ar	46	Closed	10	26.7	177.2	60.7 74.3 87.8 101.4	To take the movie of whole chamber and measure the pressure forces and flow rate with 15.6 mm I.D. orifice.
87	6-28-77	Ar	46	Closed	10	26.7	177.2	"	To take the movie of whole chamber and measure the pressure forces and flow rate without orifice.
88	6-29-77	Ar	46	Closed	10	26.7	177.2	"	To take the movie of whole chamber and measure the pressure forces and flow rate with 25.4 mm I.D. orifice.
89	7-20-77	Air	46	Closed	2.54	26.7	177.2	74.3 101.4	To measure the pressure forces and flow rate without orifice.
90	7-20-77	Air	46	Closed	30	26.7	177.2	87.8 101.4	"
91	7-20-77	Air	46	Closed	45	26.7	177.2	101.4	"
92	7-20-77	Air	46	Closed	60	26.7	177.2	101.4	"

Table 4.1

4.1 Slug Motion with Virtual Mass Effects

The water slug in the vent during the vent-clearing transient is usually assumed to behave as a rigid body [4.1]. The forces assumed to act are: The drywell pressure (P_o), the friction force due to the walls of the vent, the weight of the water slug, $\rho_L - \rho_x$, the back pressure exerted by the liquid, ρL, and the wet well gas pressure on the pool free surface, P_i. The apparent mass effects resulting from fluid motion are studied in the present analysis. From the force balance on the water mass (Figure 4.1.1), the momentum equation is:

$$\frac{d(mu)}{dt} + \rho_w u^2 A = [(P_o - P_i) - \rho_w x]A - \frac{f_m(L - x)u^2 A}{2d}\rho_w, \quad (4.1)$$

where

x = the interfacial location (Figure 4.1.4), related to the slug velocity, u, by

$$\frac{dx}{dt} = u, \quad (4.2)$$

and

P_o = the dry well pressure,

L = the submergence depth,

ρ_w = the water density,

A = the area of the pipe,

d = the pipe diameter,

t = time,

f_m = the Fanno friction factor,

m = the total mass, and

P_i = the wet well pressure.

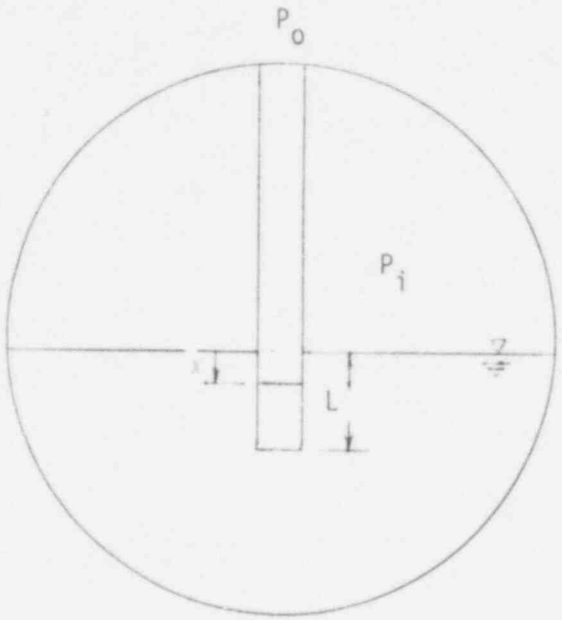

Figure 4.1.1 Physical Model for Vent Clearing

m is composed of two parts, the real mass during the transient, i.e., $\rho(L - x)A$, and the apparent mass, m_{ao}, which is assumed to be a linear function of x, i.e.,

$$m_{ao} = \beta \rho_w A x. \tag{4.3}$$

β is a constant and, as will be shown, is usually of the order of unity. For an ellipsoid of evolution, the apparent mass is given by

$$m_{ao} = \frac{\alpha_o}{2 - \alpha_o} \frac{4}{3} \pi (abc) \rho_w, \tag{4.4}$$

where

a, b, c = the major and minor radii, and

α_o = a function of the eccentricity, e, defined by a and b as

$$\alpha_o = \frac{2(1 - e^2)}{e^3} \left(\frac{1}{2} \log \frac{1 + e}{1 - e} - e \right). \tag{4.5}$$

For spheres of radius a,

$$m_{ao} = \frac{2}{3} \pi \rho_w a^3. \tag{4.6}$$

For a disk of radius a,

$$m_{ao} = \frac{8}{3} \rho_w a^3. \tag{4.7}$$

Based on the results of these geometries, the value of β was taken to be unity. During the actual vent clearing, β may be a function of time. The calculation of an exact value for β requires a complete solution of the transient fluid motion inside the vent and the pool. At this stage, the effect of β on vent clearing will be studied by solving Equations (4.1) and (4.2) with the specified dry well pressure, P_D. Figure 4.1.2 shows the effect of β on the interface location for various ΔP's. The interface moves much faster for smaller β. The solid lines are computed for ΔP = 34.5 kPa. The interfacial motion, x/L, can be

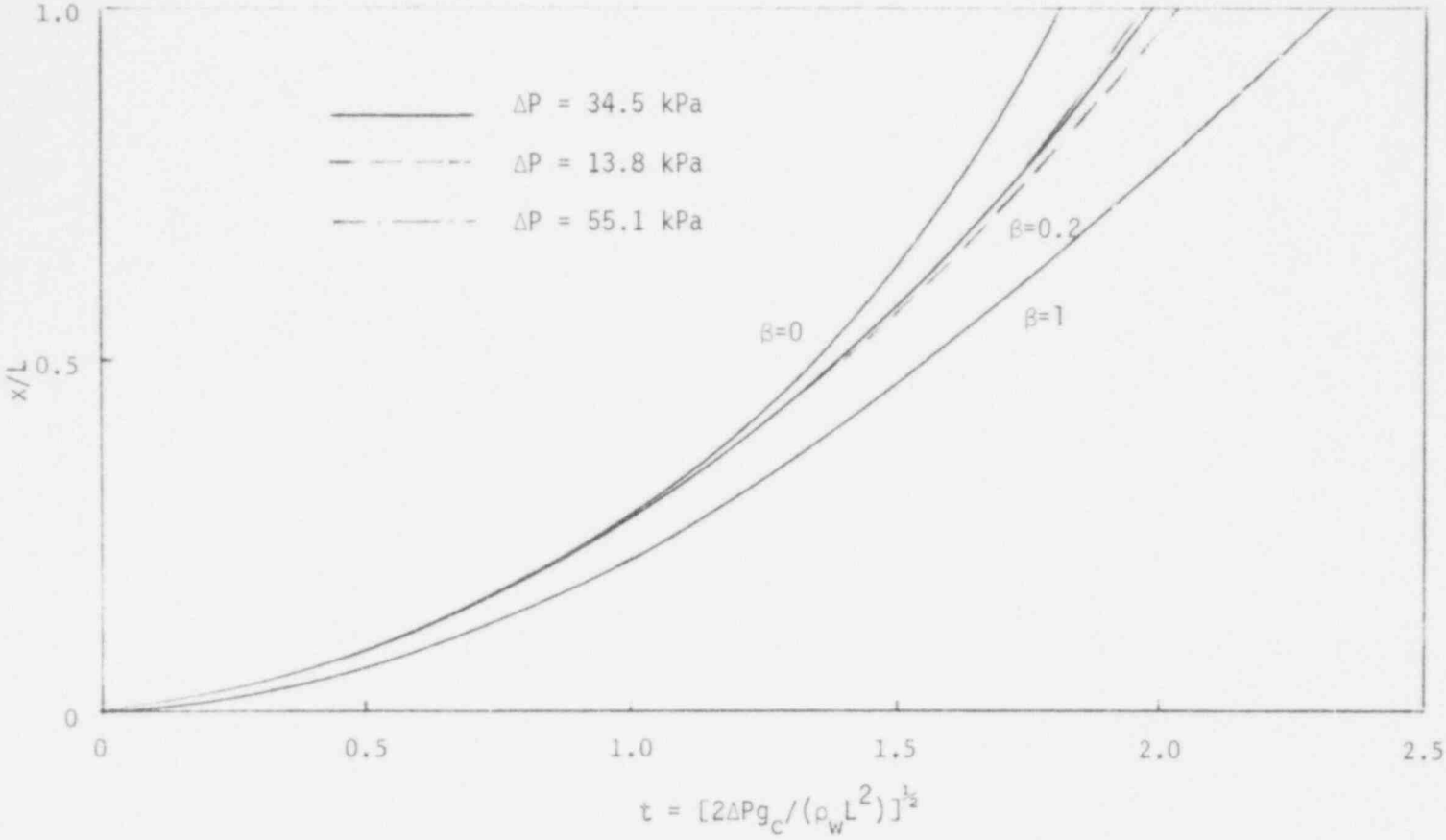

Figure 4.1.2. Effects of β on Interface Motion

approximately correlated by the single non-dimensional parameter $t[2\Delta Pg_c/(\rho_w L^2)]^{\frac{1}{2}}$, as demonstrated by comparing the results for 34.5 kPa, 13.8 kPa, and 55.1 kPa, shown in Figure 4.1.2. In other words, the vent-clearing time decreases with the square root of ΔP, and increases linearly with L. The actual dependence of the vent-clearing time on pressure and submergence depth is more complicated. Figure 4.1.3 shows the variation of the non-dimensional vent-clearing times, $t[2\Delta Pg_c/(\rho_w L^2)]^{\frac{1}{2}}$, as functions of the pressure difference. For large ΔP, the gravitational term in Equation (4.1) is less important, and the term $t[2\Delta Pg_c/(\rho_w L^2)]^{\frac{1}{2}}$ remains nearly constant. Similarly, for small submergence depths with fairly large ΔP, the vent-clearing time is again proportional to $L/(\Delta P)^{\frac{1}{2}}$, as shown in Figure 4.1.4.

The effects of β on the actual vent-clearing time in a BWR system are demonstrated by using the transient drywell pressure given in the FSAR of the Vermont Yankee nuclear power plant [4.2]. The vent diameter is 61 cm and the submergence depth is 152 cm. As β increases, the velocity of the water slug decreases (Figure 4.1.5).

β is found to have more influence on the velocity when the vent starts to clear. Figure 4.1.6 shows the non-dimensional exit velocity, defined as the ratio of the exit velocity to the velocity at $\beta = 0$. As β increases, the velocity is found to decrease. It reaches an asymptotic value of 0.25 at $\beta > 0.5$.

Hence, the virtual mass can have two opposite effects on vent clearing. A high β means a longer vent-clearing time, and hence, allowing the pressure in the vent to attain a higher value when bubble growth starts. On the other hand, the virtual mass tends to decrease the exit velocity. The combined effects of the virtual mass on the dynamical forces require further investigation.

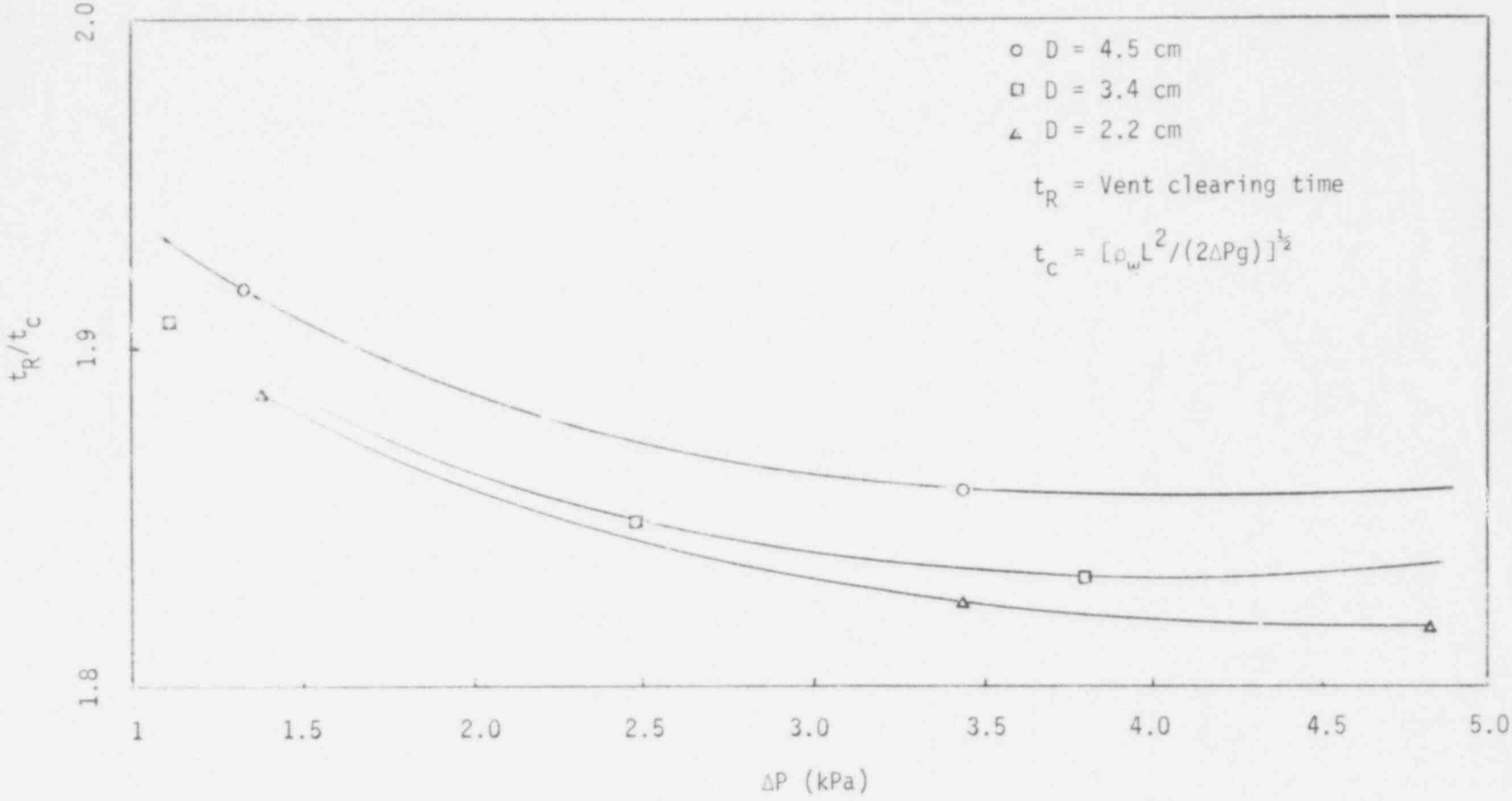

Figure 4.1.3. Effect of ΔP on Non-Dimensional Vent Clearing Time.

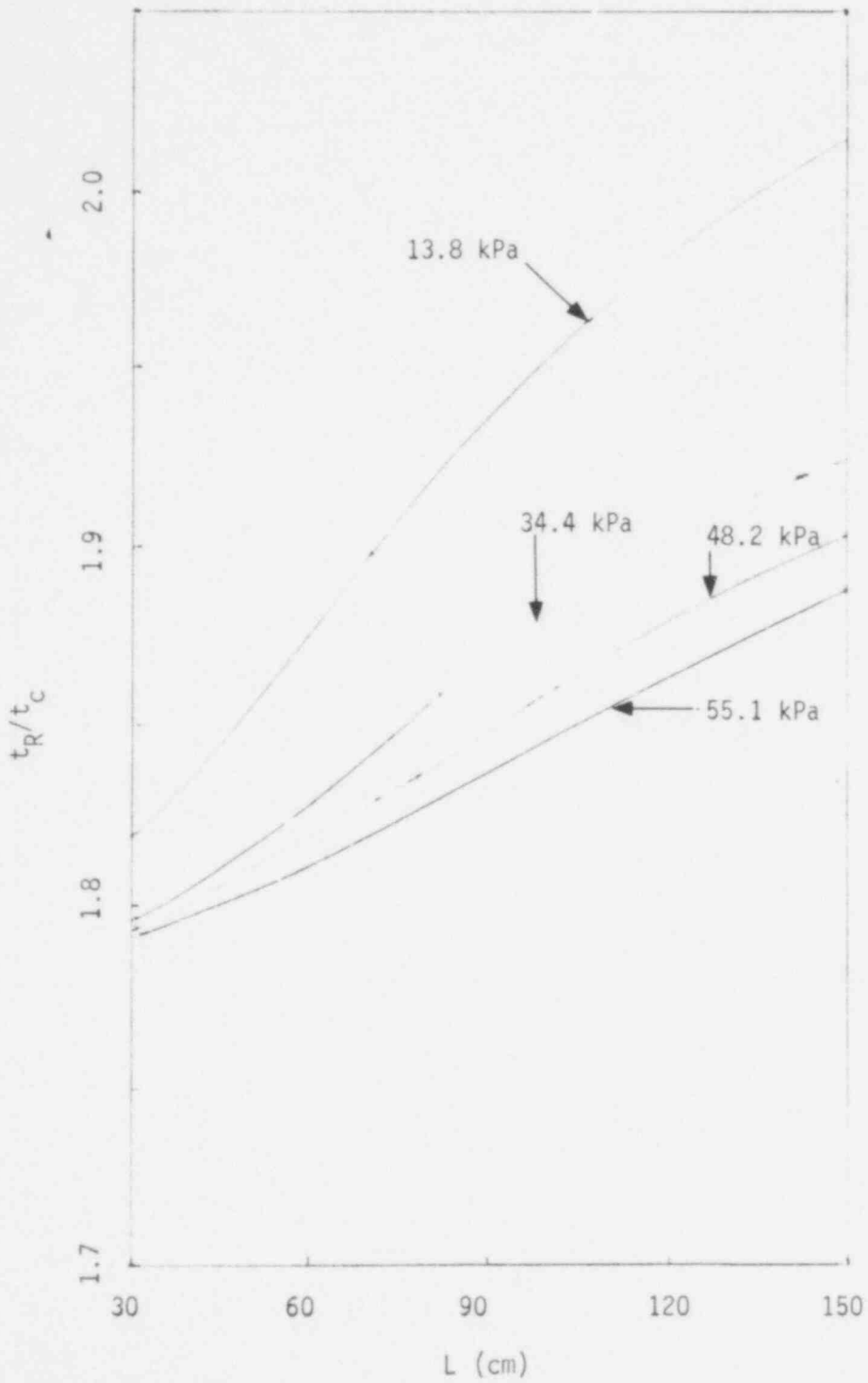

Figure 4.1.4. Effect of Submergence Depth on Non-Dimensional Vent Clearing Time.

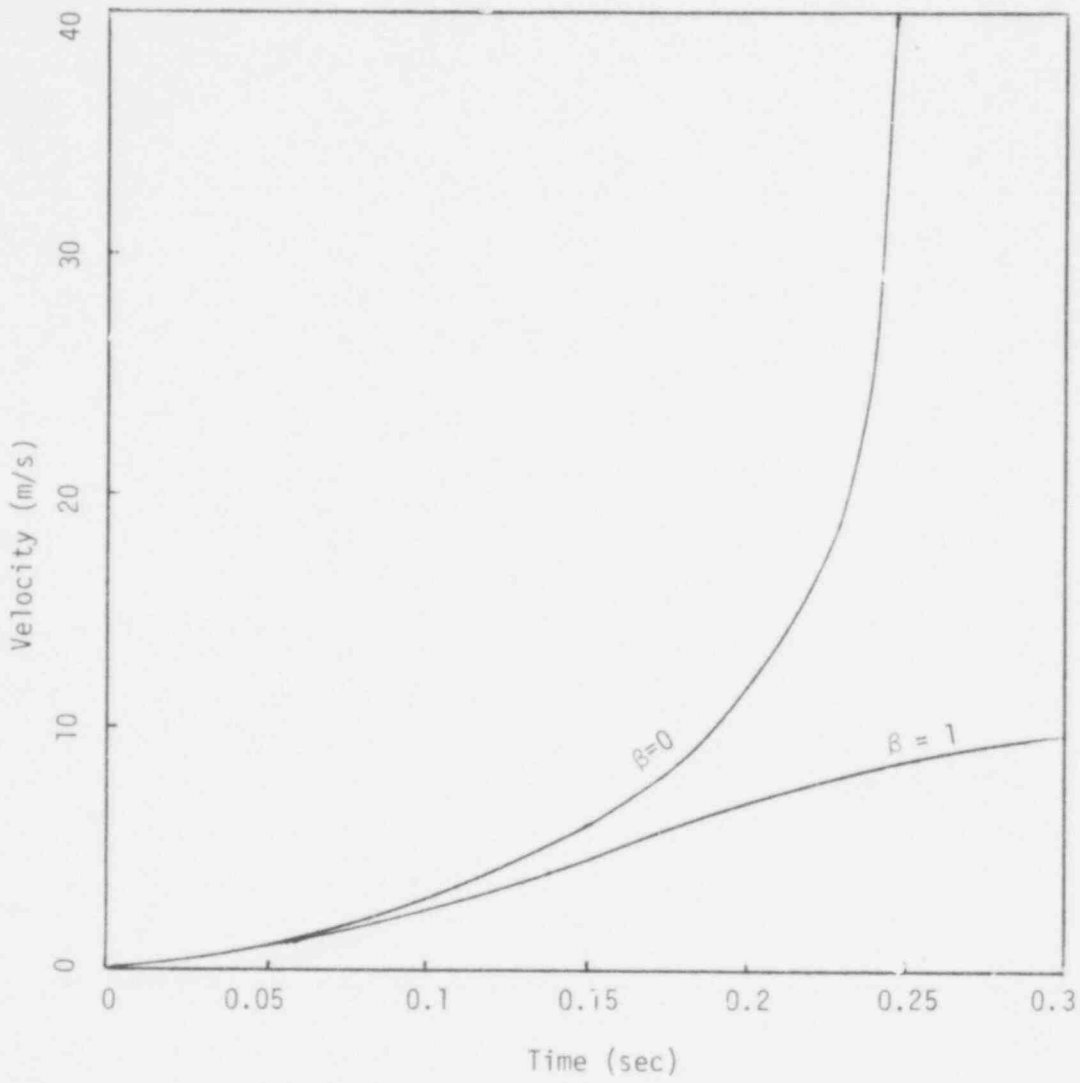

Figure 4.1.5 The Effect of β on Slug Velocity

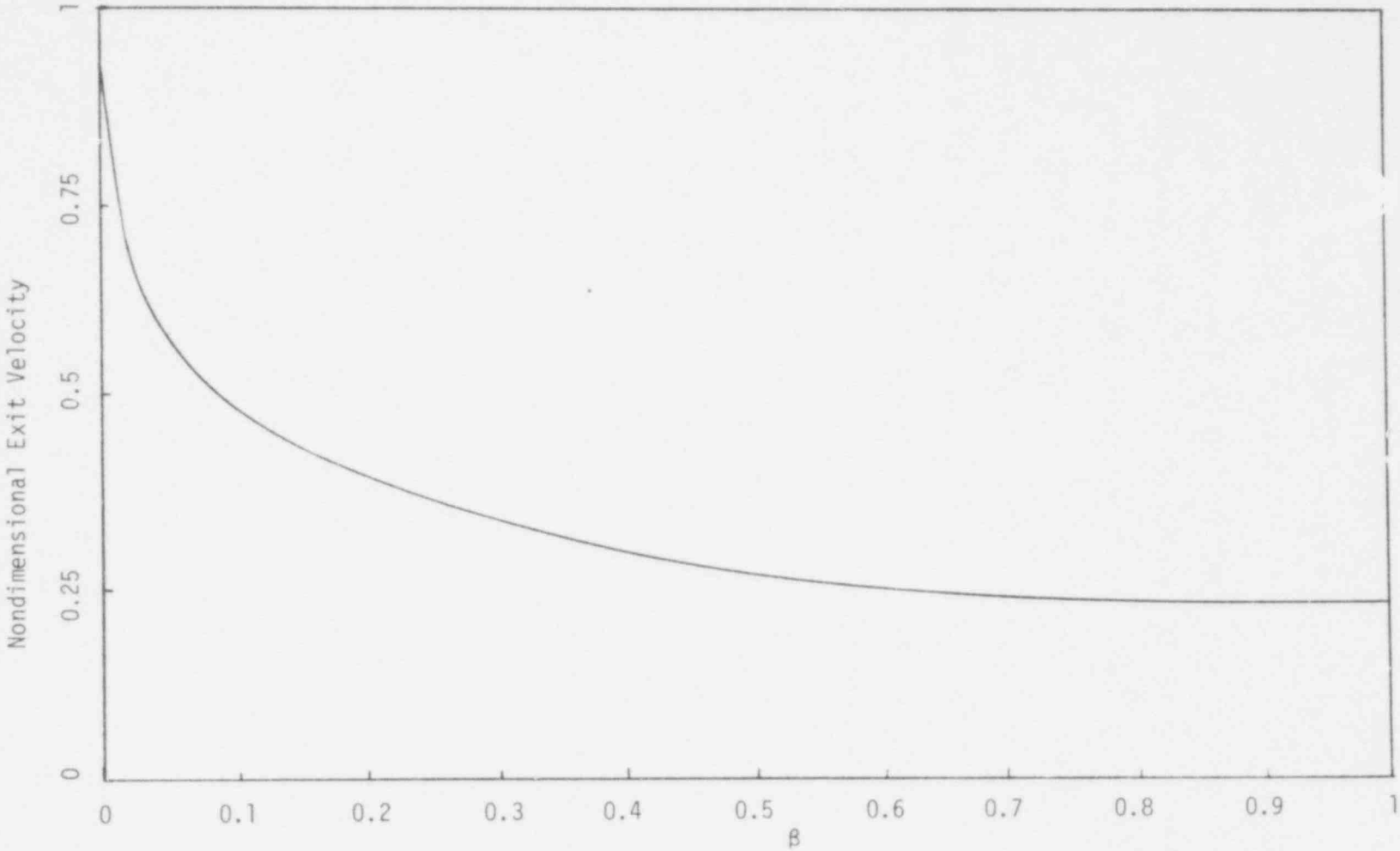

Figure 4.1.6 The Effect of β on Exit Velocity

4.2 Role of the Taylor Instability during Vent Clearing

During the vent clearing process, the liquid/gas interface is pushed out of the vent with an acceleration. The direction of the resulting reactive force is opposite to the gravitational force. The liquid/gas interface will remain stable as long as the magnitude of the reactive force is less than the gravitational force, because the direction of the net force remains from the lighter to the heavier fluid. However, when the acceleration force exceeds the gravitational force, the interface would become unstable. Perturbations at the liquid/gas interface would start to grow when the net acceleration from liquid to gas is such that the wavelength of the neutral wave is less than the diameter of the vent.

For incompressible, inviscid fluids of infinite depth, linear stability theory gives the minimum unstable wavelength as

$$\lambda_c = 2\pi\sqrt{\sigma/[a(\rho_w - \rho_a)]}, \tag{4.2.1}$$

the "fastest-growing" wavelength as

$$\lambda_d = 2\pi\sqrt{3\sigma/[a(\rho_w - \rho_a)]}, \tag{4.2.2}$$

and the growth rate of the "fastest-growing" wavelength as

$$w = 0.62 \left[\frac{(\rho_w - \rho_a)^2 a^3}{\sigma(\rho_w + \rho_a)}\right]^{1/4}. \tag{4.3.3}$$

Visual observations during the vent-clearing phase of the experiments (46 mm tube) showed that the moving liquid interface indeed became unstable, and a standing spike of liquid was observed on the interface (see Figure 4.2.1). The spike grew with time, but invariably broke up prior to complete clearing of the vent. Figures 4.2.2, 4.2.3, and 4.2.4 show the position, velocity, and acceleration of the moving interface (P_1), as well as the

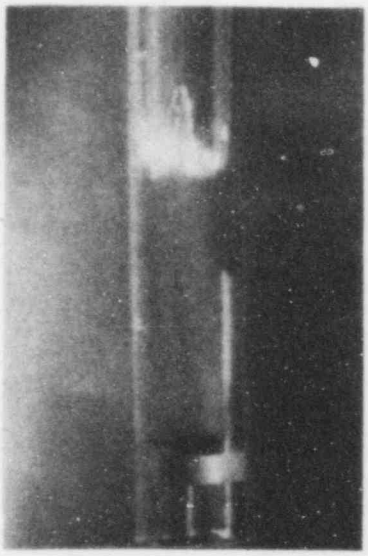

1.

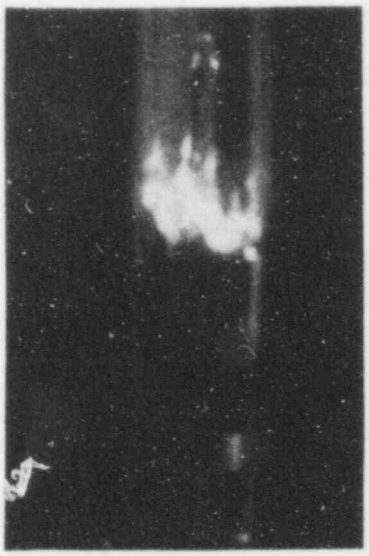

2.

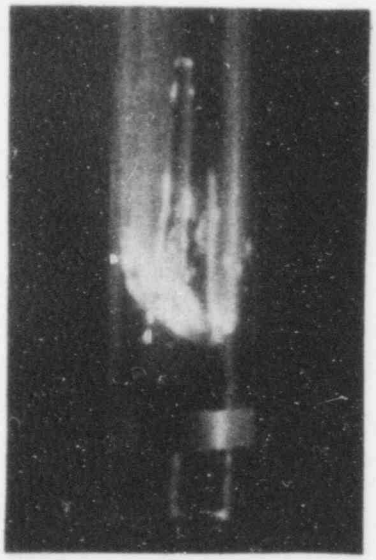

3.

4.

Figure 4.2.1 The Formation of Water Spike in Vent Clearing
Vent Diameter = 4.6 cm
Upstream Air Pressure = 122.0 κ Pa
Submergence Depth = 30 cm
Exposure Time = 0.001 sec

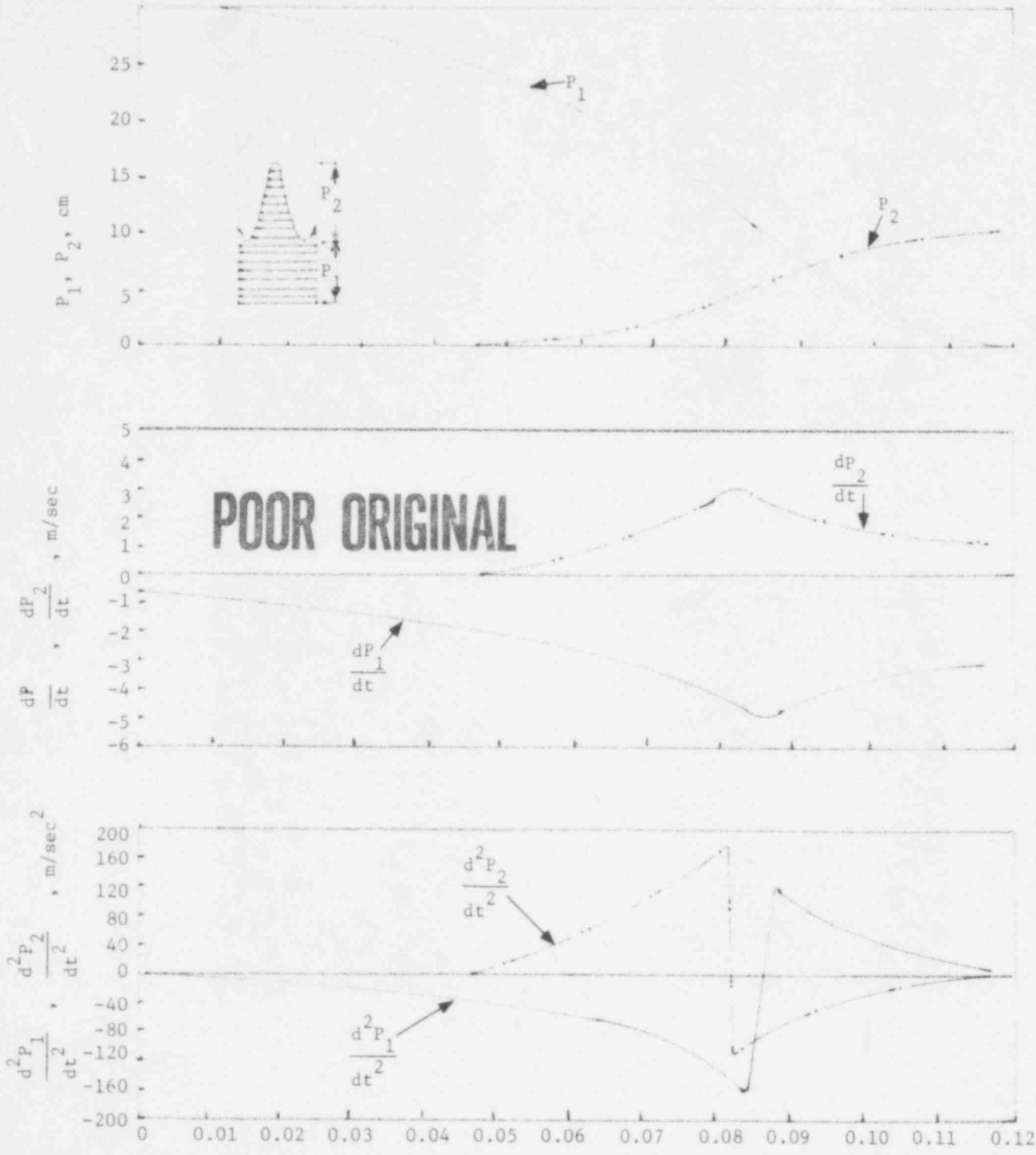

Figure 4.2.2 Position, Velocity and Acceleration of the Air-Water Interfaces During Vent Clearing (46 mm ID Tube) with Upstream Pressure of 115.1 kPa.

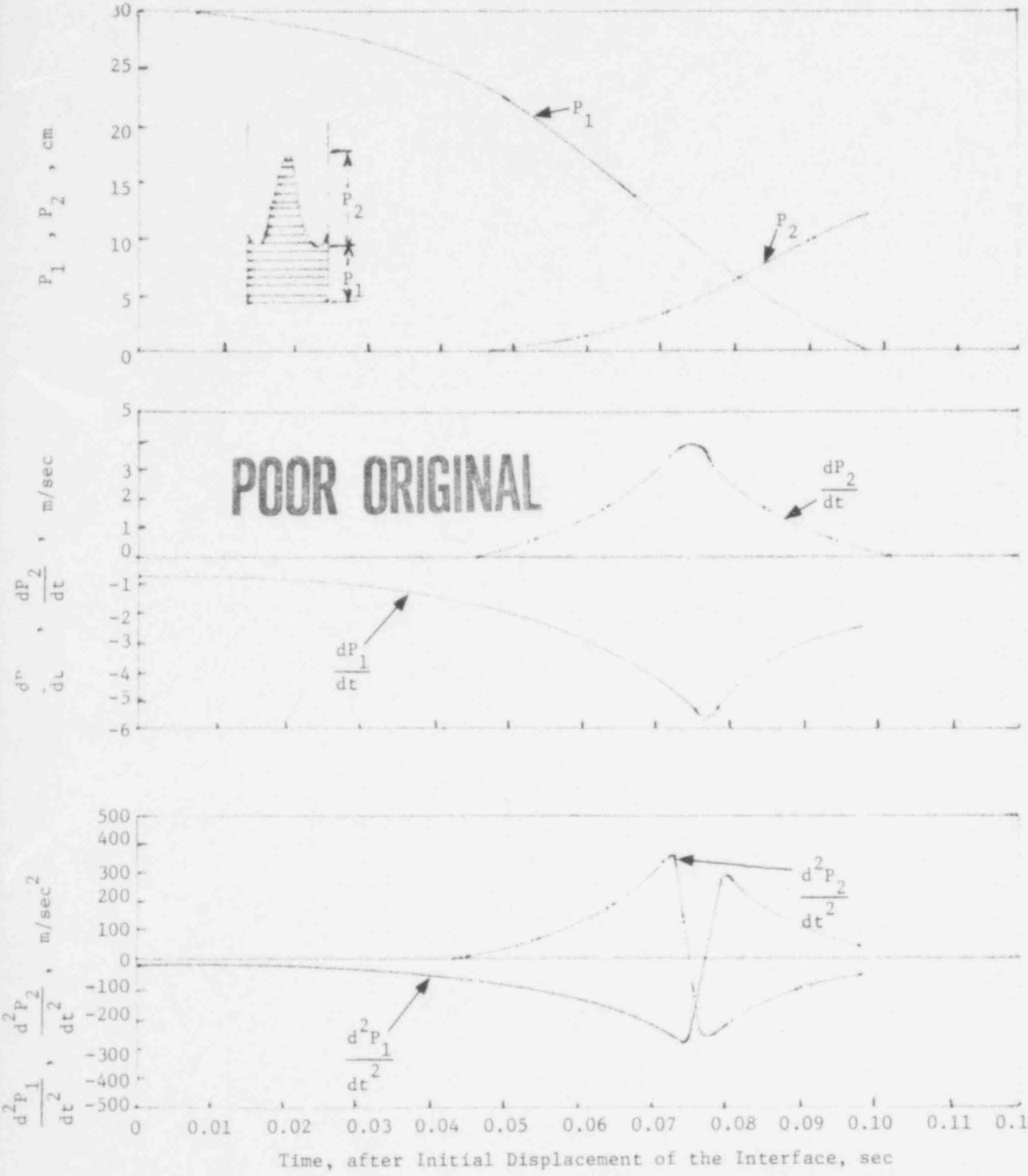

Figure 4.2.3 Position, Velocity and Acceleration of the Air-Water Interfaces During Vent Clearing (46 mm ID Tube) with Upstream Pressure of 122.0 kPa.

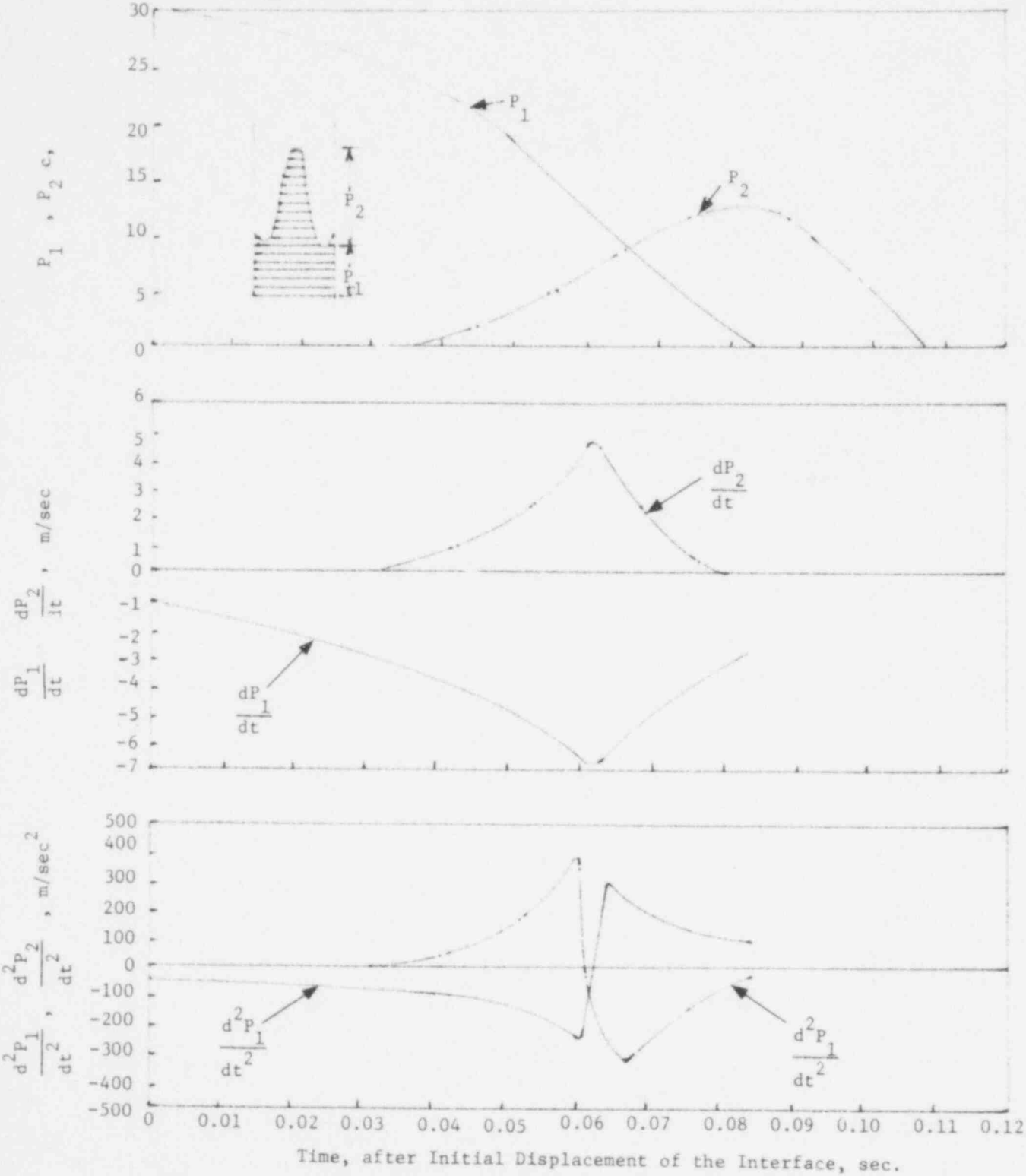

Figure 4.2.4 Position, Velocity and Acceleration of the Air-Water Interfaces During Vent Clearing (46 mm ID Tube) with Upstream Pressure of 128.9 kPa.

liquid spike (P_2) standing above the interface. The data shown in Figures 4.2.2 through 4.2.4 are for upstream pressures of 115, 122, and 129 kPa, when the submergence depth of the 46 mm diameter vent tube was fixed to be 30 cm. The data for the interface heights were reduced from movies taken at 780 frames per second. These heights were then used to calculate the interface velocities and accelerations. The maximum inaccuracy is expected to occur in calculating the acceleration, but the maximum uncertainty should be less than ±25%.

It is observed from Figures 4.2.2 through 4.2.4 that the liquid spike grows monotonically with time, but the growth rate decreases as the liquid spike attains a finite height. The velocity and acceleration of the liquid/gas interface (P_1) increase rapidly during the early stages of vent clearing, but slow down considerably during the later periods. The slowdown is probably caused by the additional drag induced by the sticking of the liquid to the tube wall and by the drag at the surface of the liquid spike. The theoretical models of the vent-clearing phenomena do not account for these effects. For the same reasons, these models predict a continuous increase in interface velocity and acceleration.

Figures 4.2.1 through 4.2.4 show that the liquid spike grows to about 12 cm before it breaks up. Thus, the linear theory discussed earlier is bound to be inadequate. However, it can provide a starting point for further investigation of the phenomena. Knowing the acceleration of the liquid/air interface, the growth rate of the liquid spike can be written as:

$$P_2 = P_{2o}\, e^{w(t)t}, \qquad (4.2.4)$$

where

$$w(t) = C_1\left[\frac{g^3(\rho_w - \rho_a)^2\left(\frac{1}{g}\left|\frac{d^2P_1}{dt^2}\right| - 1\right)^3}{\sigma(\rho_w + \rho_a)}\right]^{\frac{1}{4}} \qquad (4.2.5)$$

In Equation (4.2.4), P_{2o} is the initial height of the interface and is generally unknown. In the present case, an appropriate choice for P_{2o} could be

$$P_{2o} = \sqrt{\sigma/[(\rho_w - \rho_a)g]}. \qquad (4.2.6)$$

This gives a value of P_{2o} = 0.25 cm for earth normal gravity and for a water/air interface at room temperature. This value of P_{2o} is also about the height of the interface discerned from the movies. The constant in Equation (4.2.5) is expected to be less than 0.6, because in the early stages of vent clearing, the growth rate corresponding to shorter and slower waves may be more favorable. The dimensionless liquid spike height (P_2/P_{2o}) corresponding to upstream pressures of 115, 122, and 129 kPa is plotted in Figures 4.2.5 through 4.2.7 as a function of time. It is seen that during the early stages of interface growth, when d^2P_1/dt^2 changes slowly with time, the linear theory can be used to predict the spike height. The constant, C_1, is found from the three observations to be 0.6 ±0.2. The linear theory becomes more and more inaccurate as the liquid spike grows to a finite height.

4.2.1 Application to Vent Clearing in a BWR Suppression Pool

The acceleration of the water/air interface during vent clearing in a BWR suppression pool (Mark I and Mark II) is plotted in Figure 4.2.8. Although the maximum acceleration of the liquid is much less than that observed in laboratory experiments, its magnitude for β = 1 (Mark I) is about five times greater than earth normal gravity. The instabilities at

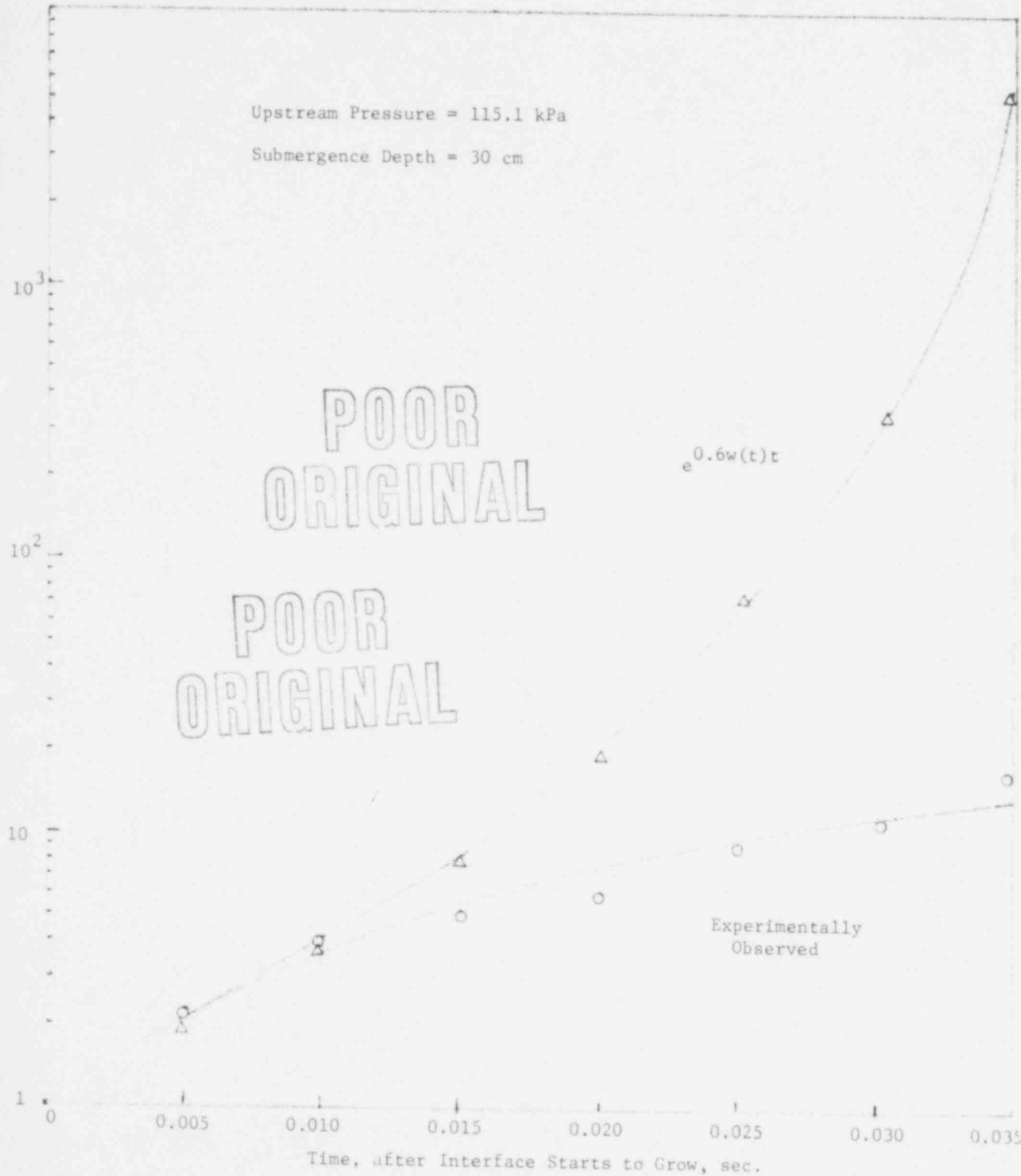

Figure 4.2.5 Growth Rate of the Interface in 46 mm Diameter Tube with Upstream Pressure of 115.1 kPa.

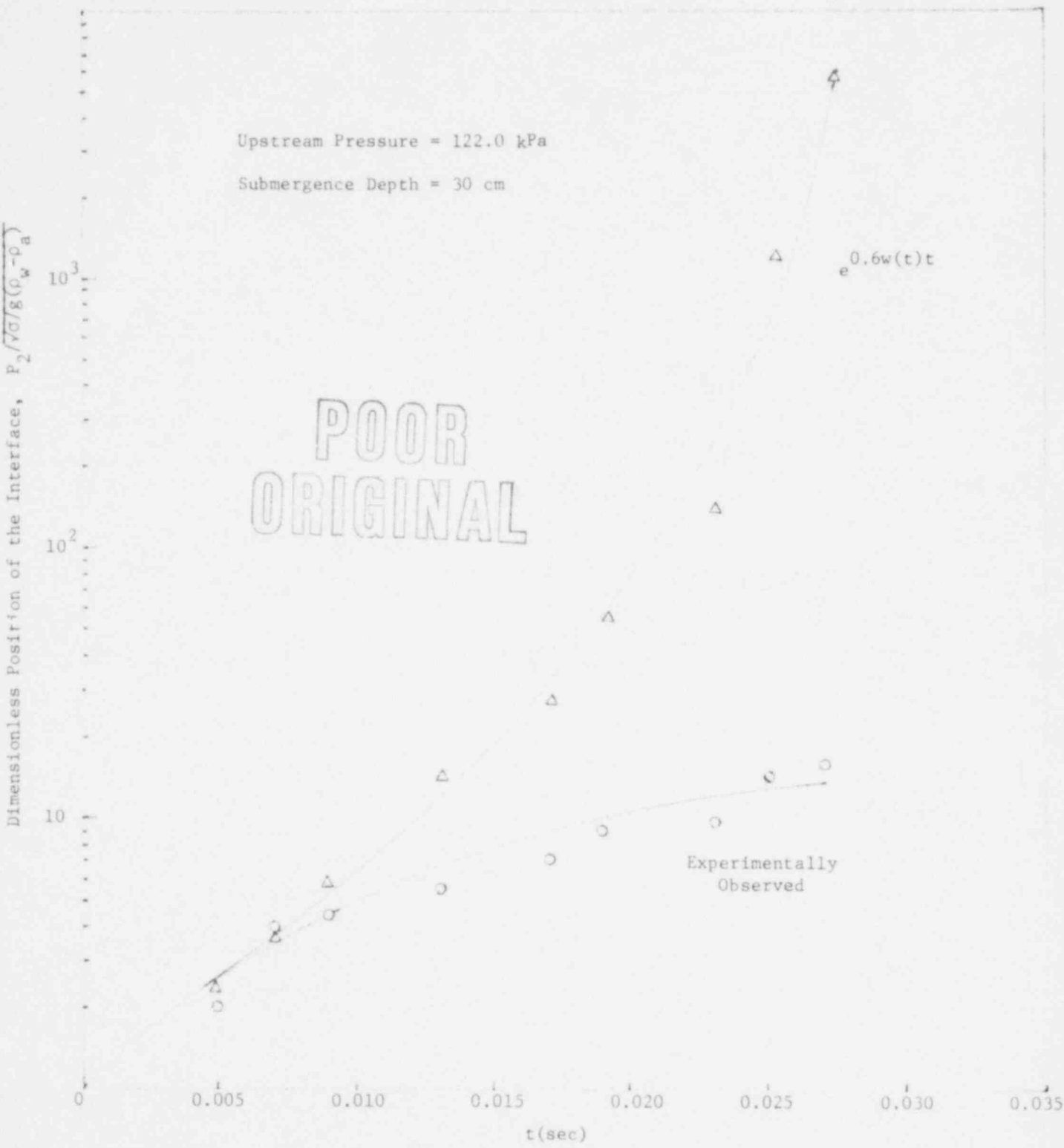

Time, after Interface Starts to Grow, sec

Figure 4.2.6 Growth Rate of the Interface in 46 mm Diameter Tube with Upstream Pressure of 122 kPa.

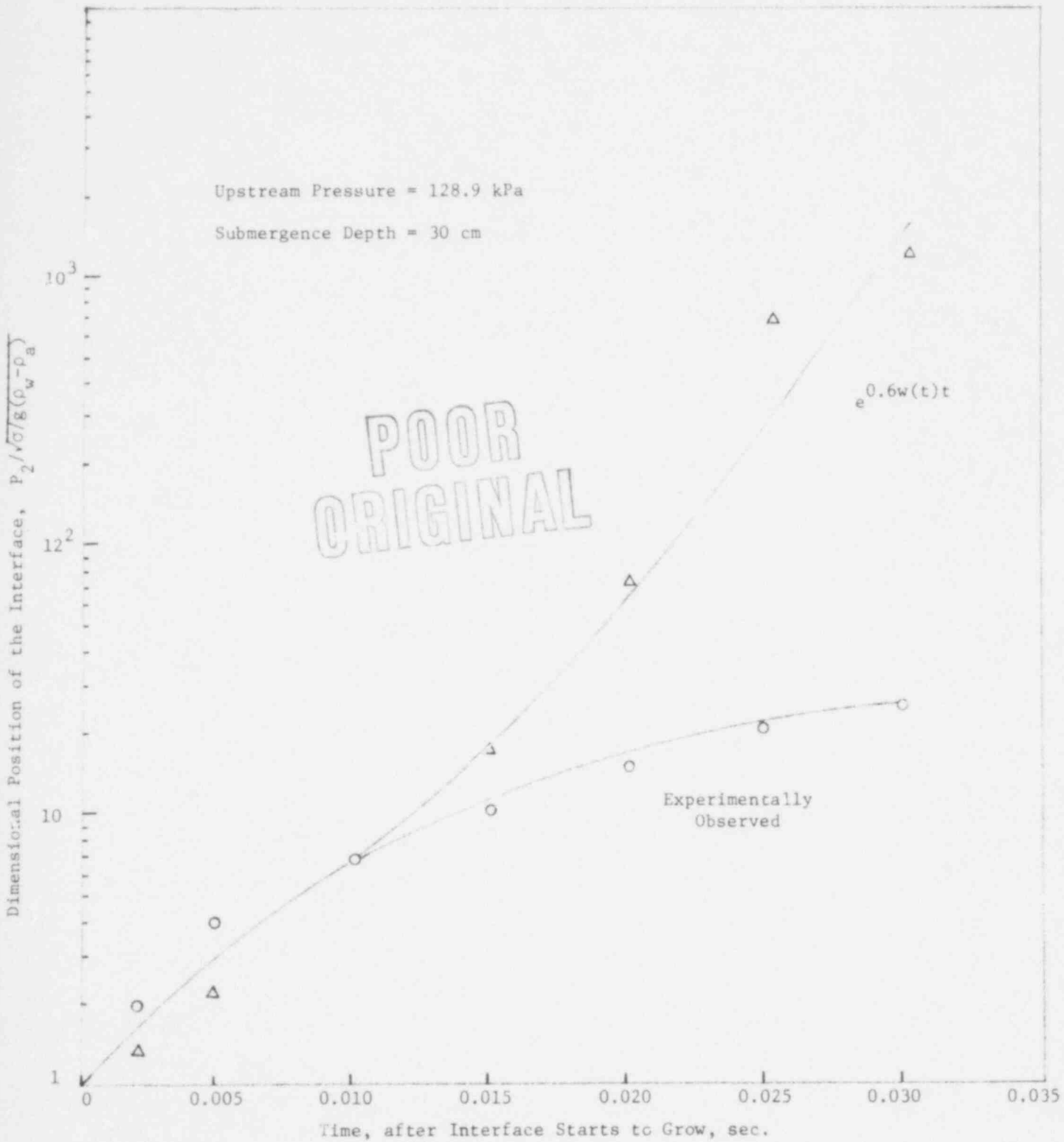

Figure 4.2.7 Growth Rate of the Interface in 46 mm Diameter Tube with Upstream Pressure of 128.9 kPa.

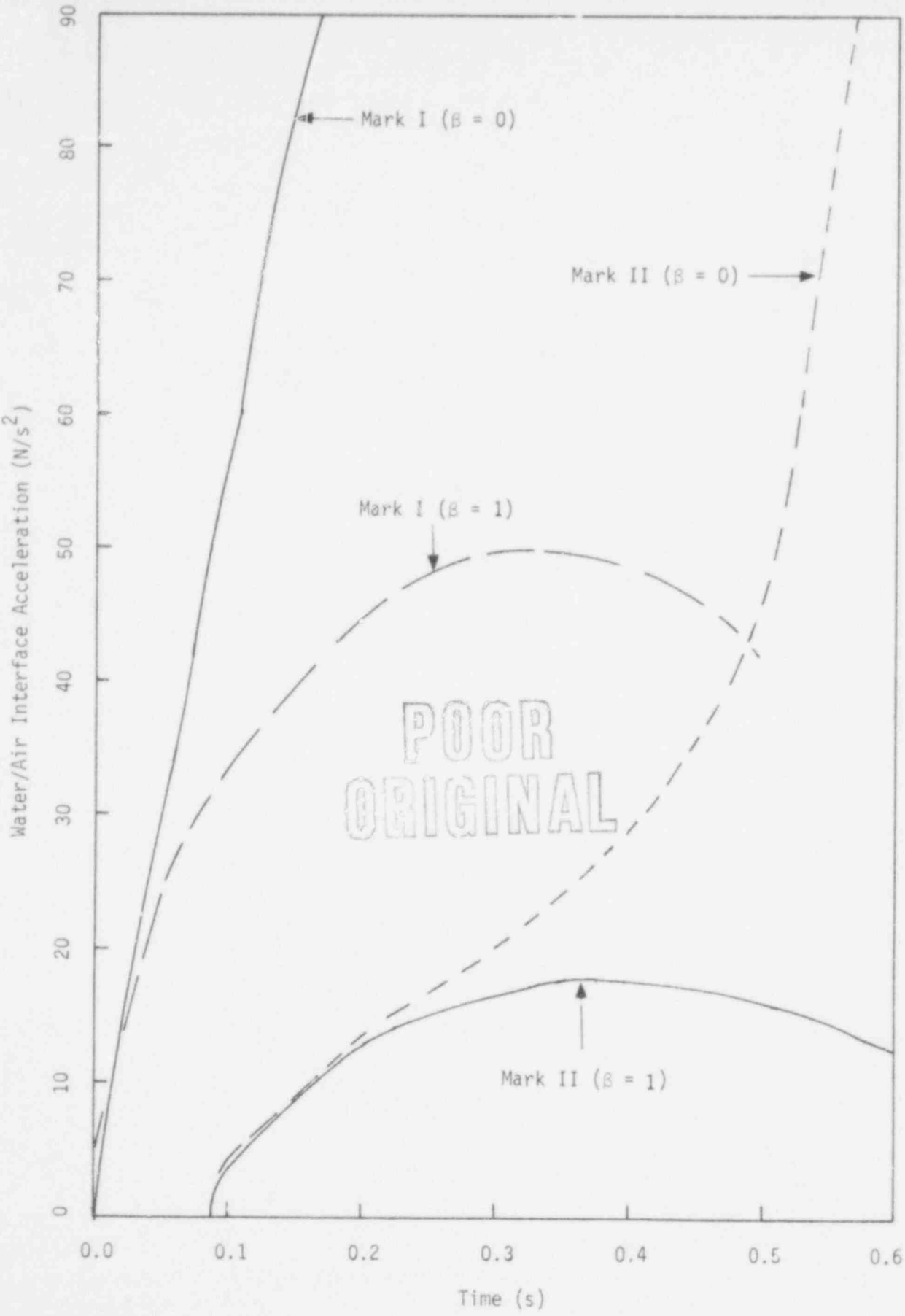

Figure 4.2.8. Predicted Acceleration of the Interface during Vent Clearing in a BWR Pressure Suppression Pool.

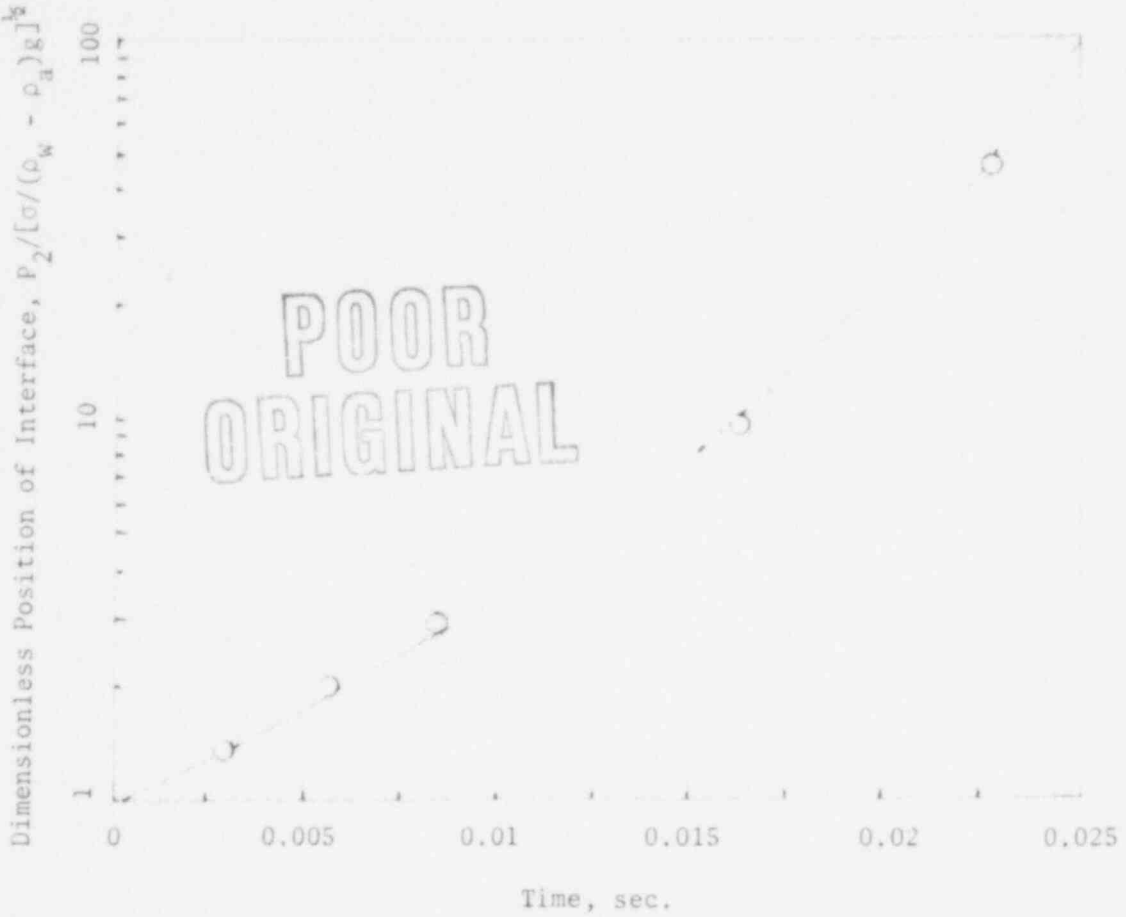

Figure 4.2 ° Predicted Growth Rate of Interface During Vent Clearing in a BWR Suppression Pool (Mark 1), $\beta = 1$.

the interface will start to grow when its acceleration is such that the shortest unstable wavelength can be accomodated in the vent. For a 0.6 meter diameter vent, the acceleration of the interface needs to be only 9.85 m/s^2 for the interface to start to grow. However, as the acceleration exceeds this value, the wavelength of the unstable waves will become shorter, and a number of liquid spikes may start to grow on the moving surface. The growth rate of a liquid spike, as predicted by linear theory, is shown in Figure 4.2.9.

4.3 Bubble Formation and Growth

High-speed movies of the bubble growth at the vent exit were made for different upstream pressures and submergence depths. The figures in Appendix E show sketches of the growth pattern of a bubble at the exit plane of the 46 mm tube for three difference gases, three orifices, and four test chamber pressures. The submergence depth for all cases was 10 cm, and the distance between the pipe exit and the test chamber bottom was 24 cm. In this section, only cases associated with air and without an orifice will be discussed.

Figures 4.3.1 and 4.3.2 show the photo-pictures of the bubble formation at the exit plane of a 46 mm tube for upstream pressures of 135.8 and 177.2 kPa, while the submergence depth was 10 cm and the initial test chamber pressure was 101.4 kPa. Figure 4.3.3 shows the sketch of the growth pattern of a bubble for an upstream pressure of 135.8 kPa while the submergence depth was changed to 30 cm. In this case, the tank was open to the atmosphere and hence the back pressure was always constant. Figure 4.3.4 shows the sketch of the growth pattern of a bubble in a closed tank for an upstream pressure of 177.2 kPa.

For low pressures, the bubble expansion is much slower, as shown in Figure 4.3.5. The bubble is observed to grow spherically only for a very short period of time, and soon the bubble is cut into two regions by the fluid circulation (see Figure 4.3.3). For high pressure, the bubble is observed to take the form of a pancake before it changes to an ellipsoid and then to a strawberry shape (Figure 4.3.4). The bubble shape is controlled by the solid boundary condition. The initial bubble growth is driven by the internal pressure expansion, augmented later by the mass influx. During the later stages of growth, the bubble shape is controlled

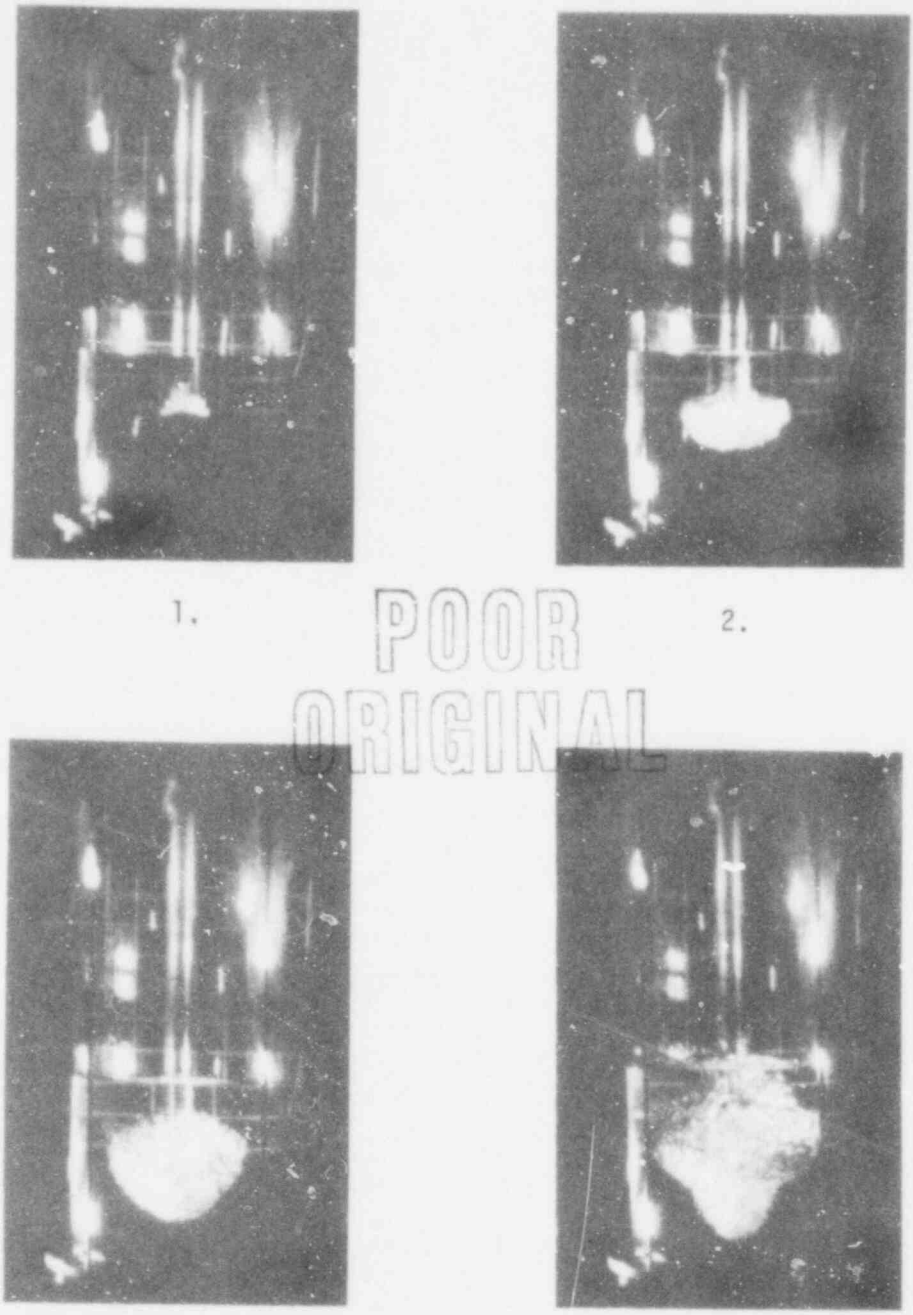

1. 2.

3. 4.

Figure 4.3.1 Bubble Formation History for P_o = 135.8 κ Pa
Vent Diameter = 4.6 cm
Upstream Air Pressure = 177.2 κ Pa
Ambient Test Chamber Pressure = 101.4 κ Pa
Submergence Depth = 10 cm
Distance of Tube Exit from the Bottom of the Chamber = 26.7 cm

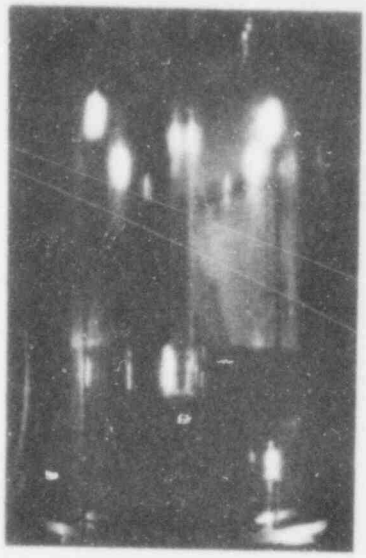

1.

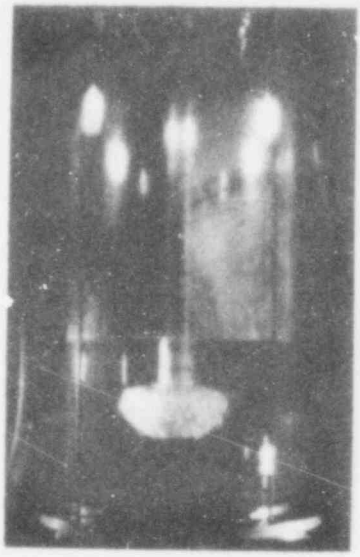

2.

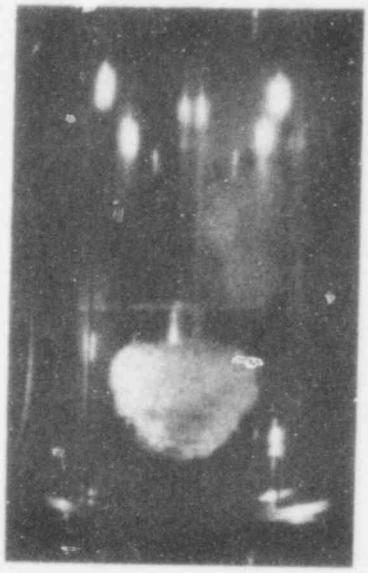

3.

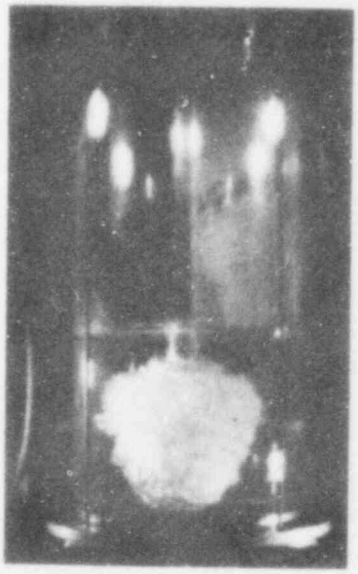

4.

Figure 4.3.2 Bubble Formation History for P_i = 177.2 κ Pa

Vent Diameter = 4.6 cm
Upstream Air Pressure = 177.2 κ Pa
Ambient Test Chamber Pressure = 101.4 κ Pa
Submergence Depth = 10 cm
Distance of Tube Exit from the Bottom of the Chamber = 26.7 cm

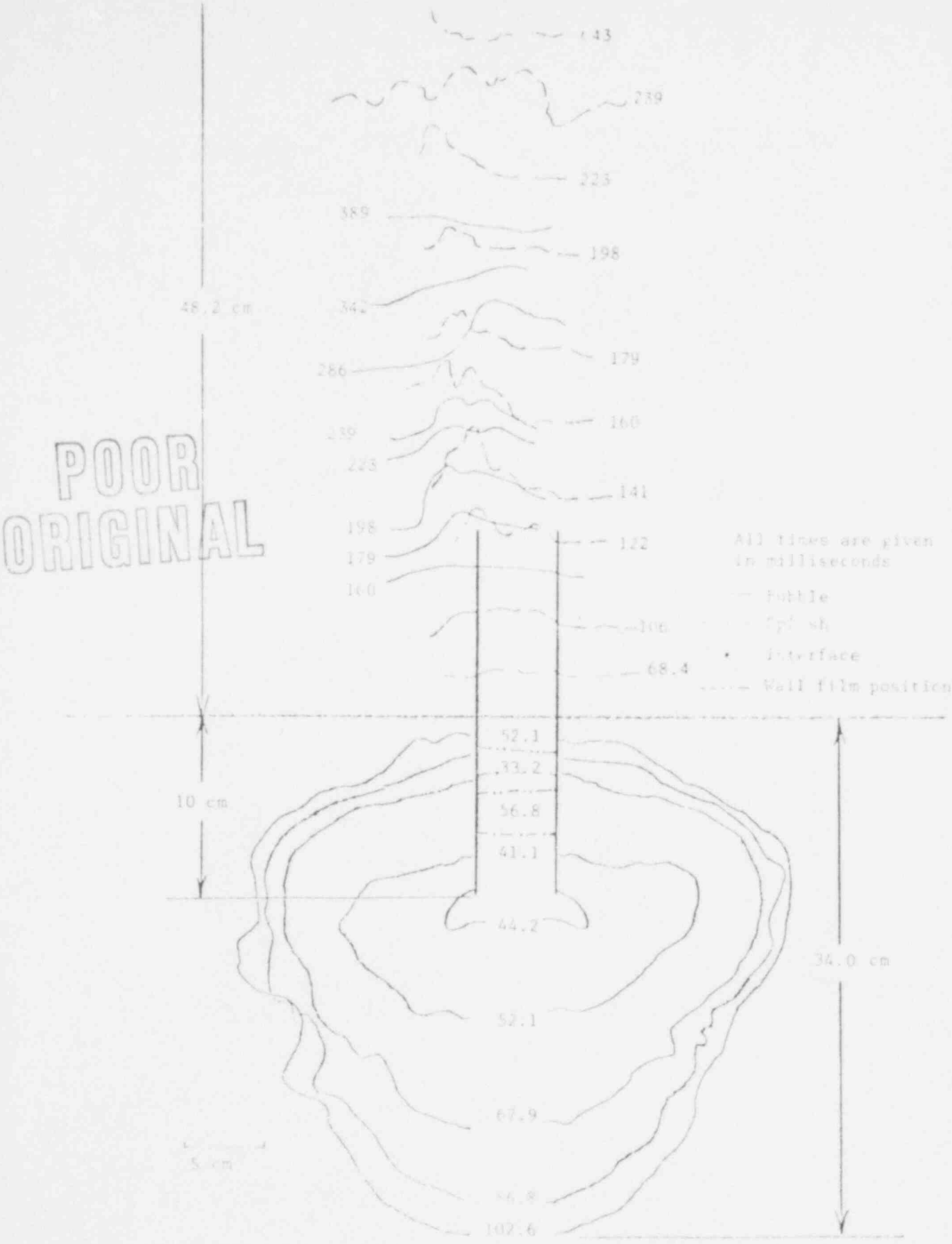

Figure 4.3.3. Bubble Growth and Free Surface Swelling Response Histories for Air without Orifice, Ambient Test Chamber Pressure 10L4 kPa.

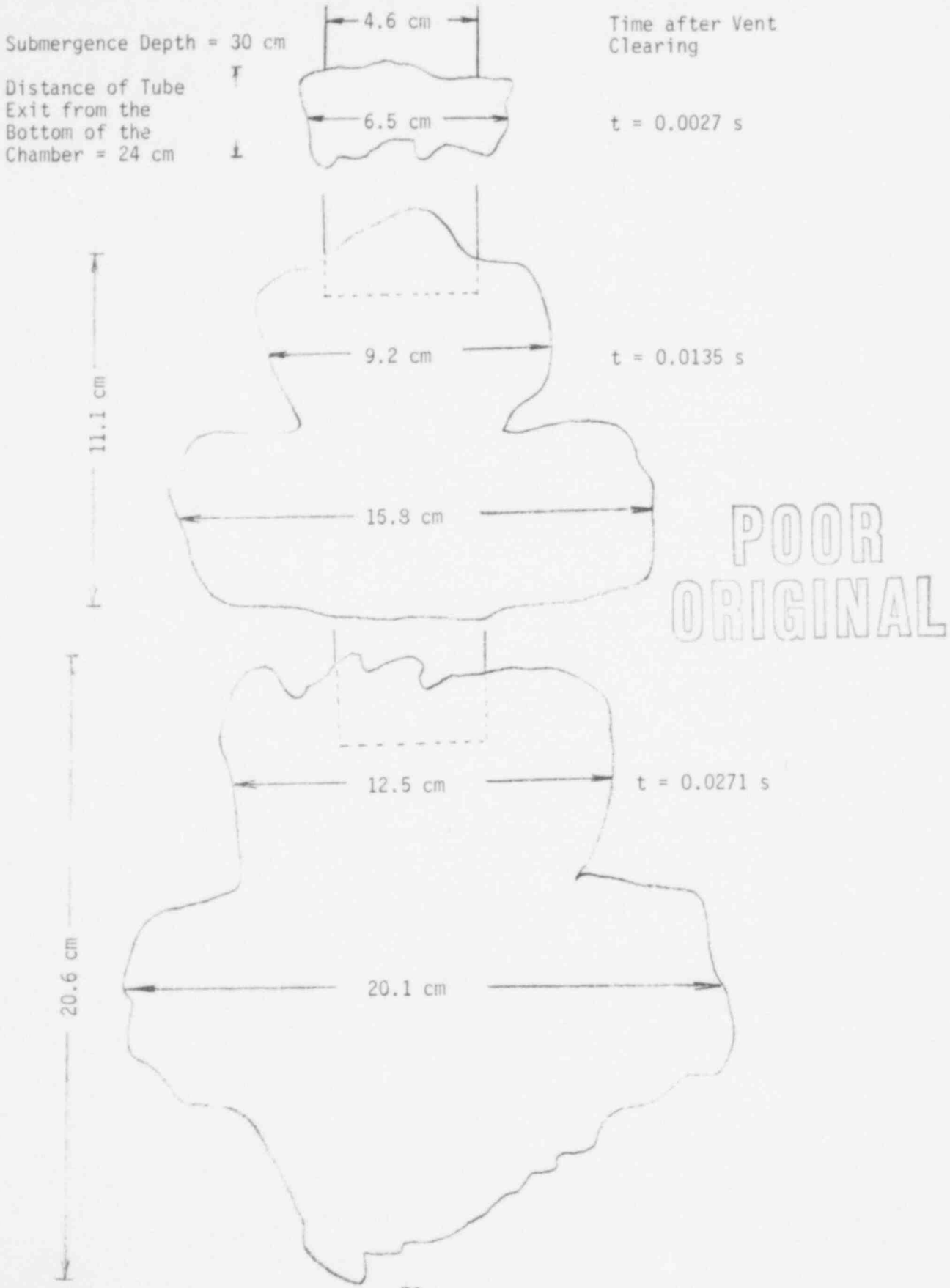

Figure 4.3.4. History of Bubble Growth at the Exit of a 4.6 cm ID Tube with Upstream Pressure of 135.8 kPa.

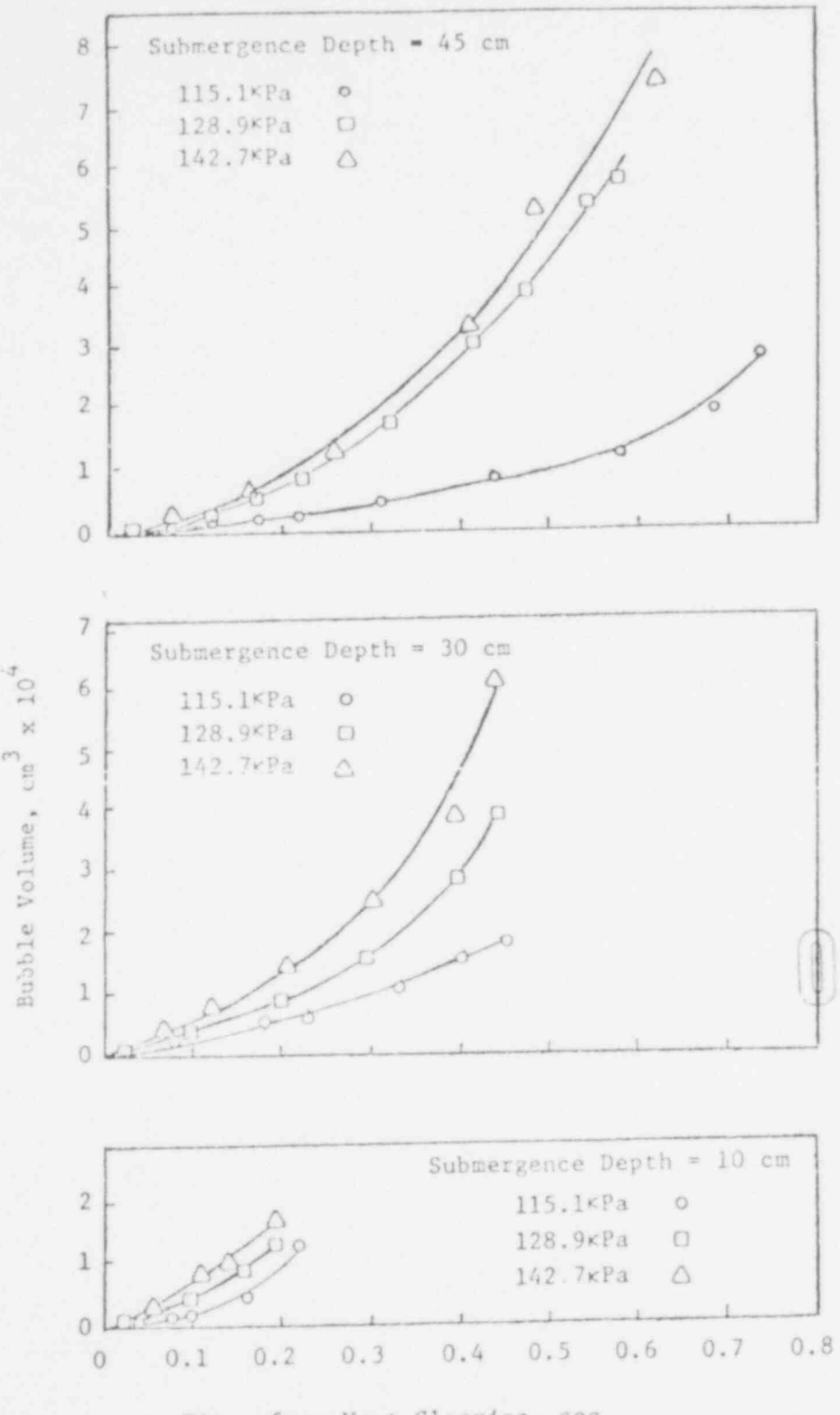

Figure 4.3.5. Dependence on Time of the Volume of the Air Bubble at the Exit of the 16 mm ID Tube.

by a balance between gravity and inertial forces. The inertial forces tend to elongate the bubble, while the buoyancy forces tend to flatten it. As a result, the bubble acquires a strawberry shape. The flow pattern in the surrounding liquid also has an influence on the shape of the bubble.

Greater submergence depth is seen to enhance the buoyancy effect and tends to flatten the bubble. The time taken by the bubble to attain a finite size prior to leaving the vent is also seen to depend on the submergence depth. It can be observed from the movies that the bubble surface is not smooth. There are waves that propagate in both the longitudinal and the circumferential directions. Although these waves have minor effects on the force measurement, they would play a more important role in the steam transient case.

4.4 Pressure and Flow Rate Histories during Vent Clearing

Appendix F shows the time-dependent total pressures at the center and side of the bottom of the test chamber, the free space above the pool surface, the static pressure, and the flow rate upstream of the water slug but downstream of the solenoid valve. In these figures, the times after activation of the quick-acting solenoid valve at which the pressurization of the region ahead of the slug begins, complete vent clearing takes place, the bubble hits the bottom surface, and the bubble breaks through the free surface are marked by Arabic numerals 1, 2, 3, and 4, respectively. As seen from these figures, the interface movement takes place while the pressurization of the gas space above it continues. The flow rate shows an oscillatory behavior during the vent clearing process. The oscillations in the flow are caused by the acoustic waves traveling back and forth between the slug interface and the reservoir, in the pipe connecting the reservoir with the space above the water slug. Interestingly, the period of these oscillations is found to be about 5 ms, which is roughly the time required for an acoustic wave to travel up and down the distance of about 0.8 m from the slug interface to the valve exit. After vent clearing, the flow rate increases rapidly to a maximum value before decreasing again due to the reduction of pressure in the reservoir.

Just after vent clearing, an impulsive force reaching its peak value within 3 to 4 ms is felt at the center of the bottom of the test chamber. As this impulse dies down, a second impulse is felt, which gives rise to another peak in the downward force on the bottom. The time interval between these two peaks is 7 to 8 ms. Finally, the force at the bottom tends to reach an asymptotic value in an oscillatory fashion, probably due to superimposition of structural vibrations. The side

pressure transducer, which is located about 20 cm from the center, shows a similar behavior, though the magnitude of the pressure is generally less than at the center. The free surface above the pool shows a steady pressurization after vent clearing. The pressure increase is caused by the upward displacment of the pool surface, and later by the breakthrough of the bubble. Similar behavior is repeated as the ambient test chamber pressure is reduced below atmospheric pressure. Choking of the flow is seen to occur when the test chamber pressure is 87.8 kPa or less. The maximum flow velocity shown by the anemometer is only about 60 m/s, because choking occurs at a constriction near the solenoid valve. The area of this restriction is about 4 times less than the vent pipe. The increase in the reservoir-test chamber pressure ratio tends to increase the maximum downward force. The correlation of this force with system parameters will be presented in the next quarterly report.

4.5 Pool Swelling and Splashing Prior to and During Bubble Breakthrough

The approximate shapes and relative locations of the crest of the pool free surface during the periods of bubble growth and bubble breakthrough are shown in Appendix E. In the figures contained in Appendix E, the free surface swelling during the bubble growth period and the splashing thereafter is shown by dotted lines, whereas the pool surface behavior during bubble breakthrough is shown by solid lines. The displacement of the free surface during periods of bubble growth and breakthrough are plotted as a function of time in Appendix G.

Visual observations showed that during the early period of bubble growth, the free surface rises uniformly, but soon acquires the shape of a half standing wave with a peak in the middle. The crest of the free surface eventually breaks up in the form of a splash. Initially, a large mass of liquid is moved upwards. The movement of the free surface is rather slow, but as the surface acquires the shape of a half standing wave, less and less liquid is moved upward. The result is a rapid increase in the free surface displacement, before it slows down again. The later behavior of the free surface is similar to that of a growing disturbance, and is probably the reason for the observed inflection in the displacement versus time graphs shown in Appendix G. The maximum uplift is expected to occur during the early periods of free surface upswelling.

The increase in pressure of the free space above the pool surface as a result of the pool swelling is plotted in Appendix F (containing data on flow rate and pressure histories). The rate of pressurization of the free space is greatest in the early stages of upswelling, and is indicative of the occurence of maximum uplift during this period of time.

After bubble breakthrough, the wet well pressure asymptotically reaches its maximum value. The experimental observations of wet well pressure in 1/5 scale tests conducted at the Lawrence Livermore Laboratory [4.3] also show similar behavior. However, in the MIT experiments [4.4], a sharp peak or oscillations are observed in the wet well pressure before it attains an asymptotic value. It is possible that the sharp pulse-type increase in pressure in the MIT experiments may have been due to some of the water slug hitting the ceiling of the wet well. A major difference between the UCLA and MIT test conditions is that in the MIT experiments, the wet well volume has been properly scaled, while in the UCLA experiments, it is not properly scaled. The wet well volume in the UCLA experments is very large. Further experiments with reduced free space volume are being pursued.

4.6 Effect of Orificing in Air Transient Test

This section presents the experimental results of an investigation of the effects of inserting an orifice in small-scale air transient test apparatuses for the simulation of the proper enthalpy flux. The objective of the present scaling test is to study the effect of orificing on (i) vent clearing, (ii) bottom downward force, and (iii) uplift force, during a BWR pressure suppression pool simulation. The basic motive for orificing is the practical limitation of simulating the Mach number (or temperature effect) in reduced-scale test apparatus. The previous section on scaling analysis shows that both geometrical and dynamical similarity between the prototype and the reduced scale test can be achieved, if the Euler number, the Froude number, the isentropic gas constant (γ), and the Mach number are preserved. If the same fluids are used in the test as in the prototype, then it is extremely difficult to simulate the Mach number, because

$$\frac{(\gamma RT)_{prototype}}{(\gamma RT)_{test}} = \frac{L_{prototype}}{L_{test}}, \tag{4.6.1}$$

where

R = the gas constant,

L = length, and

T = temperature.

In order to circumvent this difficulty, one can go back to the governing equation of the bubble growth equations, and lump the term (γRT) with the vent area to form the π_4' group [4.4]:

$$\pi_4' = 2^{\frac{1}{2}} \frac{\gamma}{\gamma - 1} \frac{P_i}{\rho g D} \frac{P_o}{P_i} \left(\frac{P_o - P_i}{P_o} \right)^{\frac{1}{2}} \left(\frac{RT_o}{gD} \right)^{\frac{1}{2}} C_m. \tag{4.6.2}$$

732 217

For the same γ, $P_i/\rho gD$, and P_o/P_i, π_4' [4.4] is equivalent to:

$$\pi_4 \equiv \left(\frac{RT_o}{gD}\right)^{\frac{1}{2}} C_m \qquad \text{(Sonin's reduction [4.5])} \qquad (4.6.3)$$

Physically, C_m is the area reduction factor $A_{orifice}/A_{line}$, coupled with the effect of the discharge coefficient.

Several questions were raised with regard to the use of the orifice to release the burden on the temperature scaling:

(i) Since inserting an orifice changes the geometrical similarity, what would be the effect on the entire air transient; in particular, how would it affect the magnitude and the time history of the pressure measurement?

(ii) Since π_4 does not simulate the sonic speed, how important is the wave propagation phenomenon to the result?

In order to clarify some of these points, nine sets of scaling tests were performed at UCLA. It should be noted that similar tests have been performed at MIT [4.5]. The UCLA test conditions are summarized in Table 4.6.1.

The test apparatus is basically the same as reported in Chapter 3. However, some small changes in the test set-up have been made for the orificing tests. To investigate the role played by an orifice placed in the line, a 25.4 mm diameter or 15.6 mm diameter orifice plate, built according to ASME specifications, was installed in the pipeline connecting the reservoir with the test chamber. The location of the orifice is also marked on Figure 3.1. The ratios of the area of the orifice to the area of the downcomer are 0.29 and 0.11. The orifice plate has not yet been calibrated for the discharge coefficient, but in the reported experimental results, the discharge coefficient for the orifice has been assumed to be

Table 4.6.1. System Parameters for Scaling Tests.

Test Series	π_4
(i) Air without orifice	666
(ii) Argon without orifice	403
(iii) Helium without orifice	1,276
(iv) Air with 25.4 mm diameter orifice	267
(v) Argon with 25.4 mm diameter orifice	162
(vi) Helium with 25.4 mm diameter orifice	511
(vii) Air with 15.6 mm diameter orifice	101
(viii) Argon with 15.6 mm diameter orifice	61
(ix) Helium with 15.6 mm diameter orifice	194

Pressure Ratios Run for Each Test Series, P_i/P_o (P_i = Dry well pressure, or test chamber pressure in Matrix Table; P_o = Wet well pressure, or upstream reservoir pressure)	
(i) 1.74	(non-choked)
(ii) 2.02	(marginal)
(iii) 2.39	(choked)
(iv) 2.92	(choked)

Critical Pressure Ratio	
Argon and Helium	2.05
Air	1.89

Data Obtained (see Figure 3.1 for the position of these pressure measurements)

(i) Pressure in the air supply line

(ii) Pressure at the center of the bottom plate

(iii) Pressure at the side of the bottom plate

(iv) Pressure in the wet well atmosphere

0.62. The submergence depth in all the reported data was fixed to be 10 cm, while the distance of the exit of the downcomer pipe from the bottom of the test chamber was 24 cm.

After the pressure transducers and the quick-acting solenoid valve were synchronized, the reservoir was pressurized to the desired pressure. At the same time, a vacuum pump was used to bring the pressure in the test chamber down to the desired value. The solenoid valve was then activated and all the pressure signals recorded on an oscilloscope. Thereafter, the data for the maximum and minimum pressures at the bottom of the chamber, the upstream pressure, the pressure in the free space above the pool, and various times of interest were reduced from the pictures of the oscilloscope output.

Nine series of tests were performed, each series corresponding to a particular gas (air, argon, or helium) without orifice, with 25.4 mm diameter orifice, and with 15.6 mm diameter orifice. In each series, pressure ratios of four different values were performed. In these nine test series, the critical parameters are the isentropic gas constant (γ), the sonic speed, and $\pi_4 \equiv \gamma/(\gamma - 1)C_m(RT/gD)^{\frac{1}{2}}$, listed in Table 4.6.2. If γ is an important parameter, it is more meaningful to compare argon with helium. However, if the acoustic effect is a more important parameter, one should compare the argon test with the air test, since the sonic speeds are closer together. Sample pressure data for our scaling test are shown in Figure 4.6.1. The terminology is explained in Figure 4.6.2. Figure 4.6.3 shows the first bottom peak pressure, Figure 4.6.4 shows the second bottom peak pressure, Figure 4.6.5 shows the maximum difference between the top and bottom pressures, and Figures 4.6.6 and 4.6.7 show the time difference between the two peaks and between the

Table 4.6.2. Critical Parameters.

Test Series	γ	Sonic Speed (ft/s, T = 530 °R)	π_4
Air without Orifice	1.40	1,128	666
Argon without Orifice	1.67	1,050	403
Helium without Orifice	1.67	3,318	1,276
Air with 25.4 mm Diameter Orifice	1.40	1,128	267
Argon with 25.4 mm Diameter Orifice	1.67	1,050	162
Helium with 25.4 mm Diameter Orifice	1.67	3,318	511
Air with 15.6 mm Diameter Orifice	1.40	1,128	61
Argon with 15.6 mm Diameter Orifice	1.67	1,050	101
Helium with 15.6 mm Diameter Orifice	1.67	3,318	194

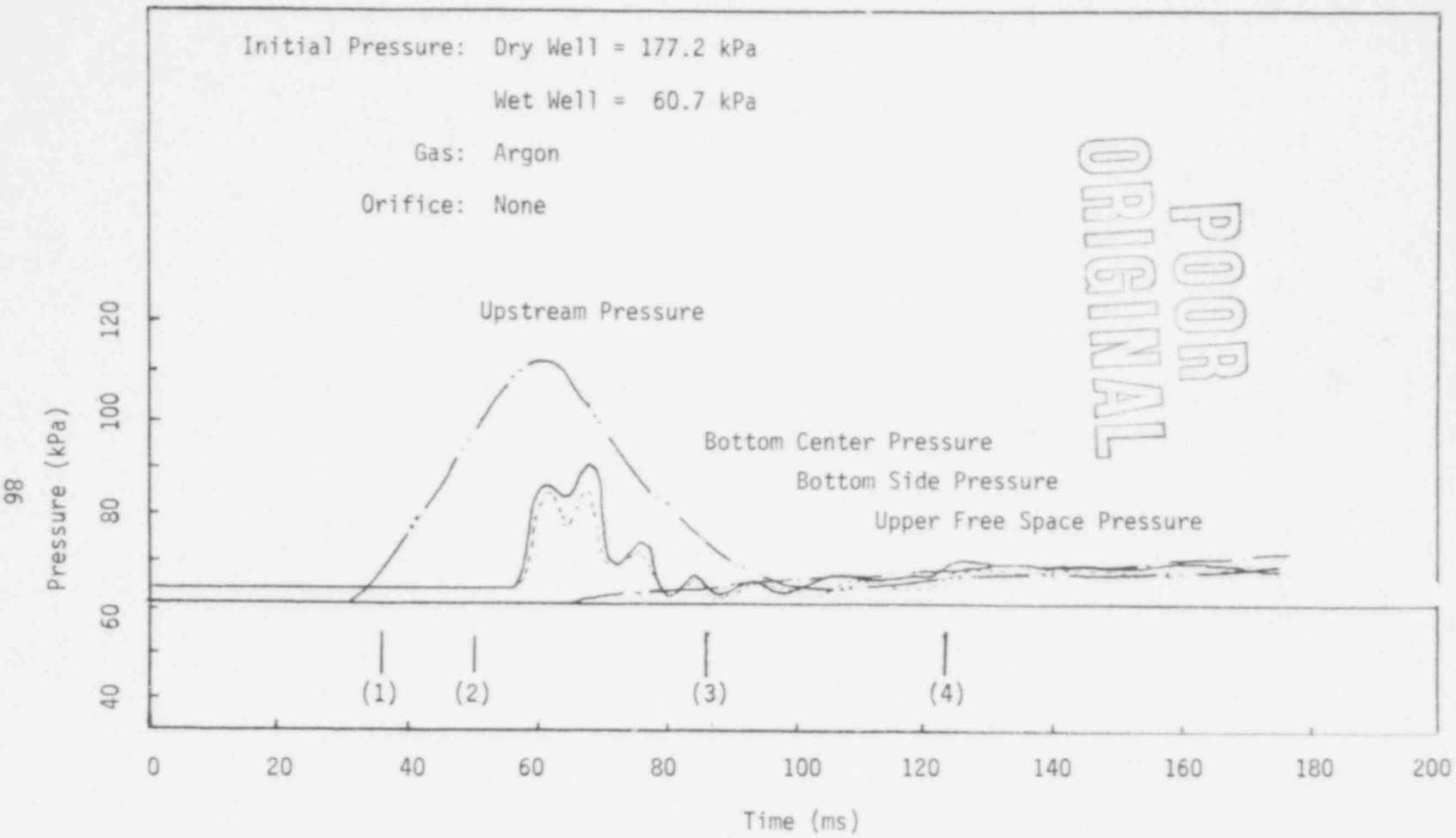

Figure 4.6.1. Sample Pressure Data of the Air Scaling Tests at UCLA.

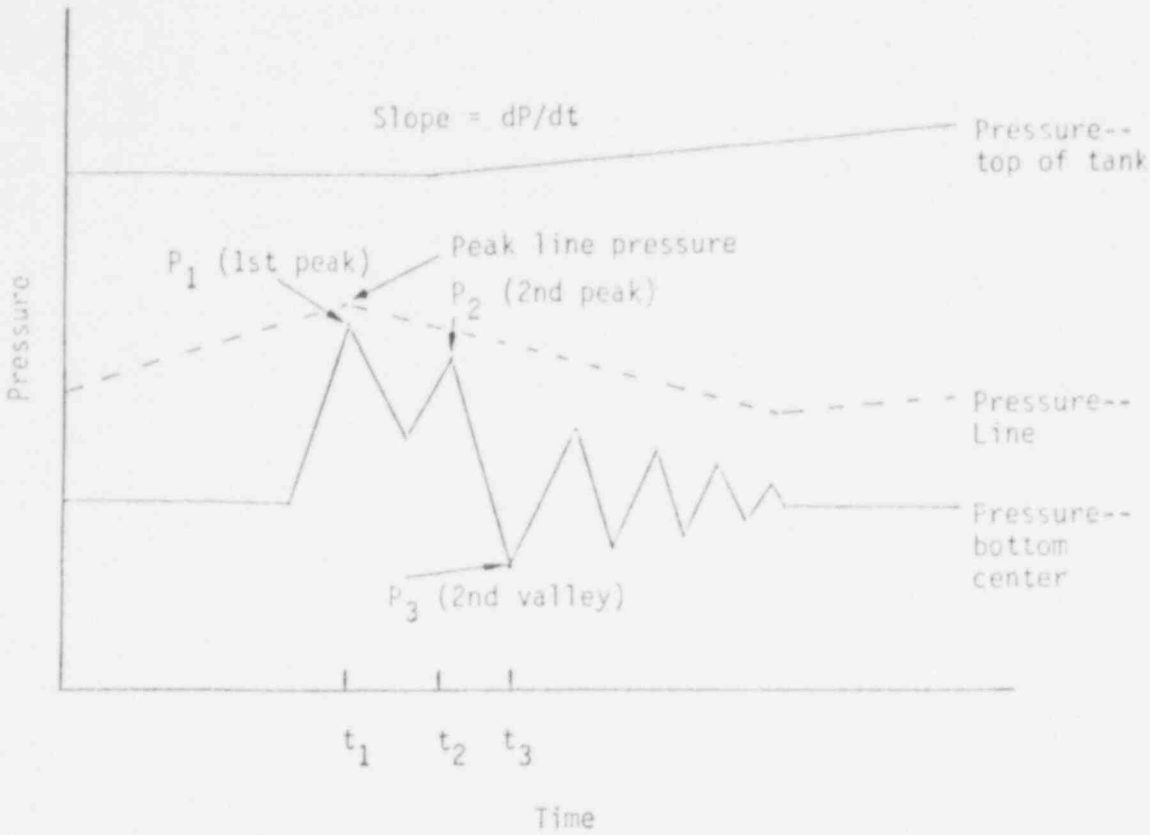

Figure 4.6.2. Typical Pressure Response and Terminology.

Table 4.6.3. The Numbers Correspond to Those Denoted in the Following Figures.

Number	Test Series	π_4
(1)	Argon with 15.6 mm Diameter Orifice	61
(2)	Air with 15.6 mm Diameter Orifice	101
(3)	Argon with 25.4 mm Diameter Orifice	162
(4)	Helium with 15.6 mm Diameter Orifice	194
(5)	Air with 25.4 mm Diameter Orifice	267
(6)	Argon without Orifice	403
(7)	Helium with 25.4 mm Diameter Orifice	511
(8)	Air without Orifice	666
(9)	Helium without Orifice	1,276

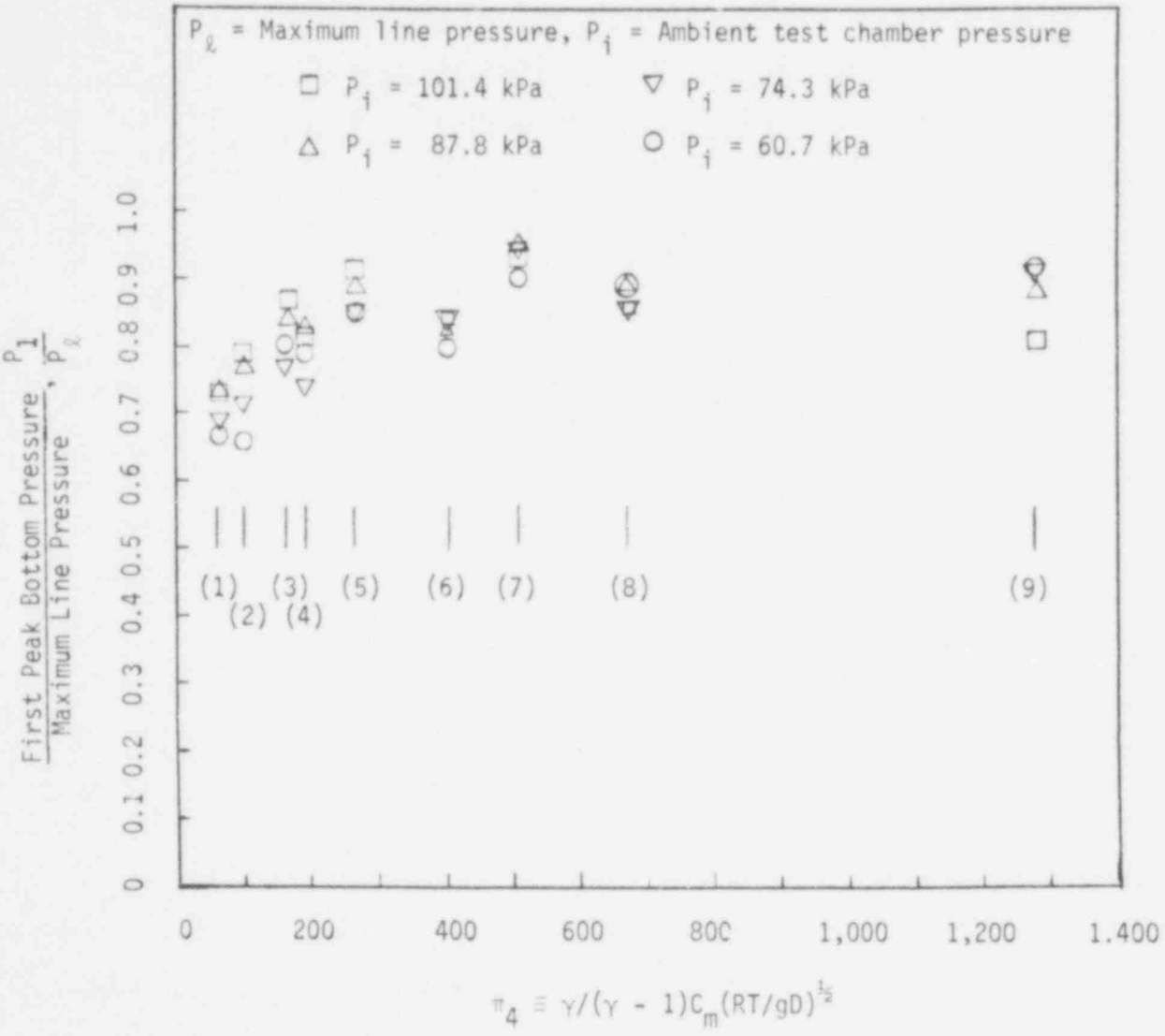

Figure 4.6.3. The First Peak Bottom Pressure vs. π_4

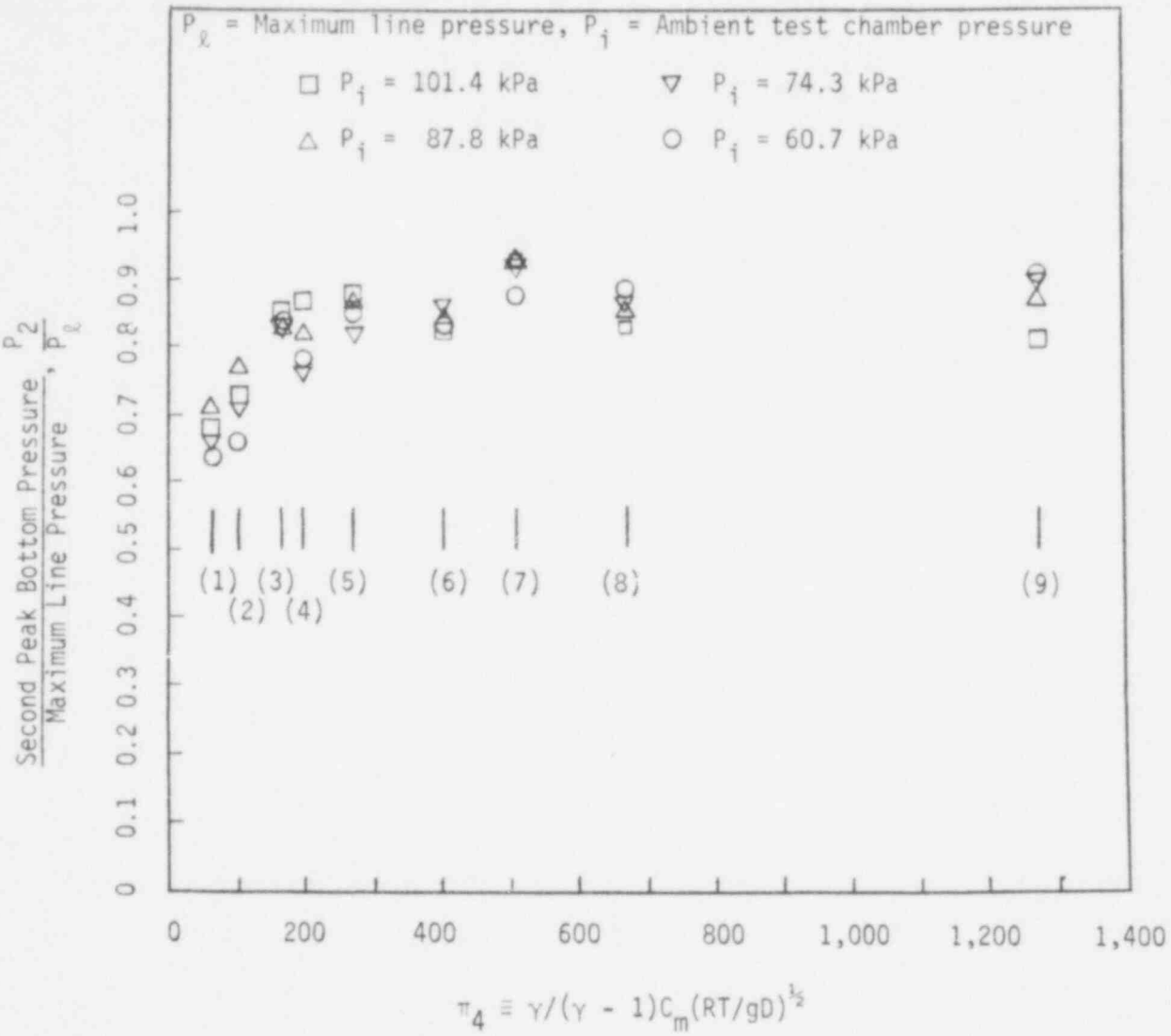

Figure 4.6.4. The Second Peak Bottom Pressure vs. π_4.

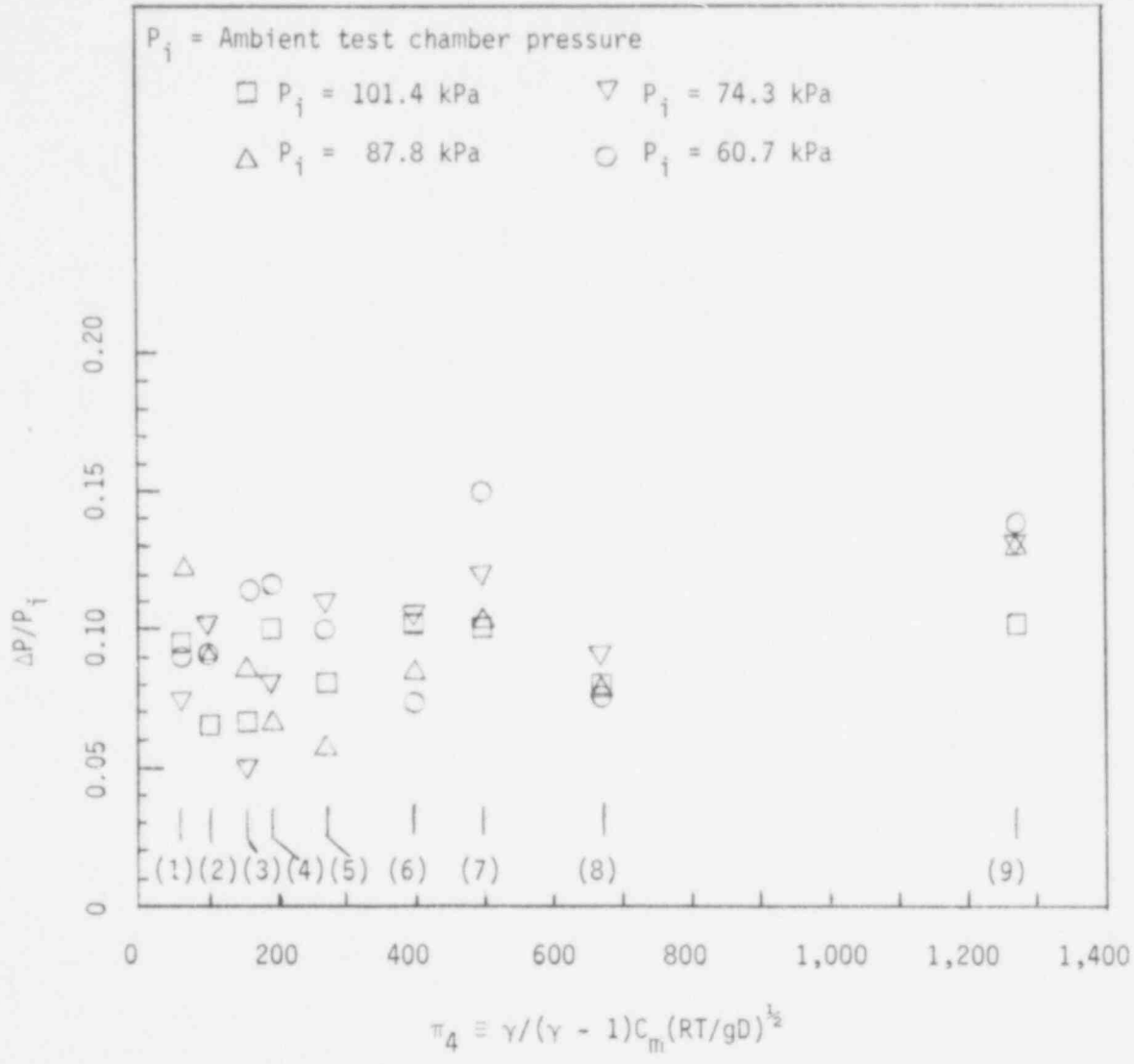

Figure 4.6.5. The Maximum Pressure Difference, ΔP, between Top Presure and Bottom Pressure vs. π_4.

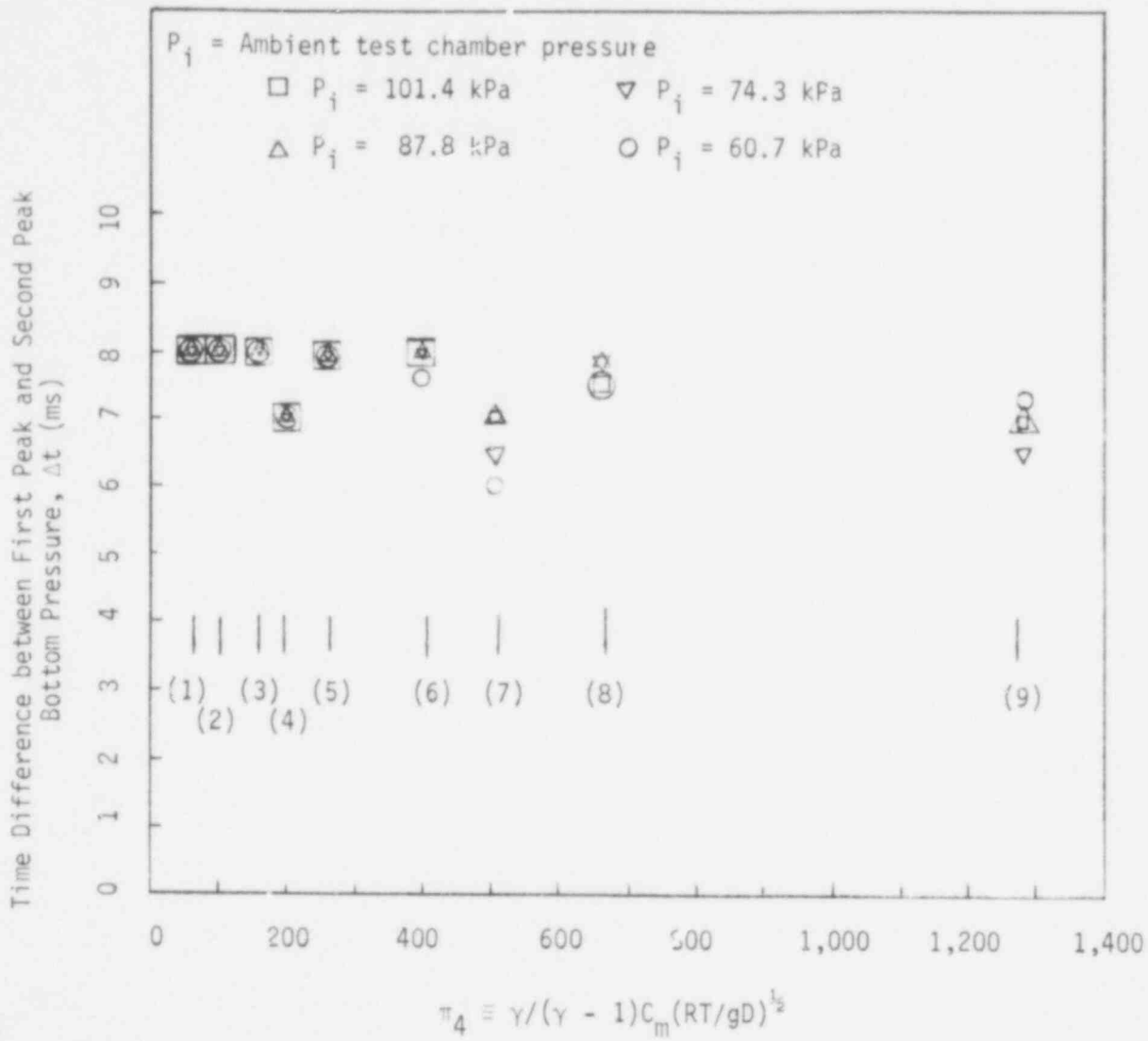

Figure 4.6.6. Time Difference between First Peak and Second Peak Bottom Pressure vs. π_4.

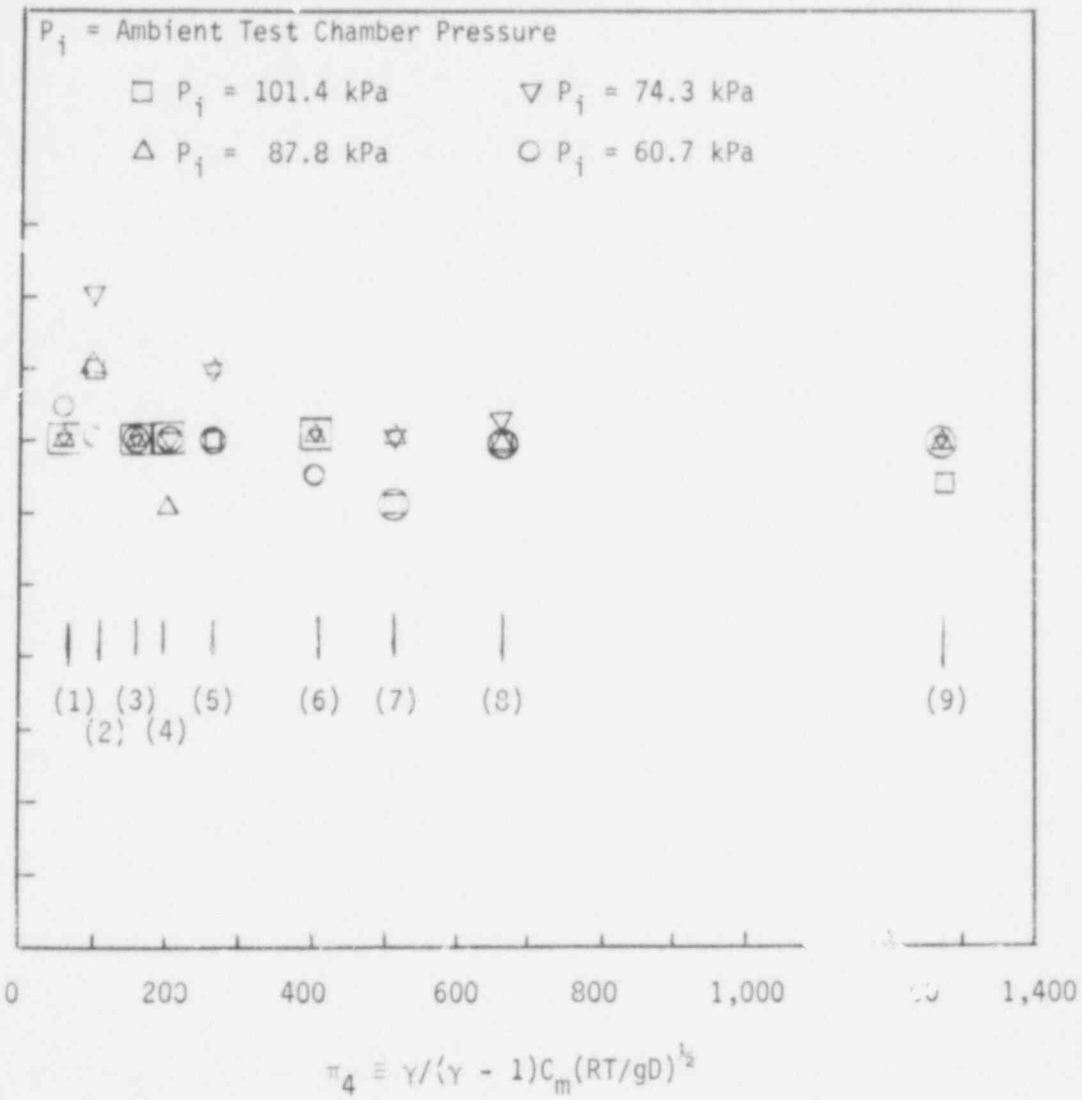

Figure 4.6.7. Time Difference between First Peak Bottom Pressure and Second Valley Bottom Pressure vs. π_4.

first peak and the second valley (this is the time for the maximum pressure difference to occur), respectively. The rate of chamber pressurization at the onset of pool surface movement is shown in Figure 4.6.8.

It is clear from Figures 4.6.3 and 4.6.4 that π_4 is not a parameter for the downward force. It is observed that helium, which usually has the highest peak force, is followed by air, and then argon. Before the experiment, we thought that since the first peak is due to the motion of the tail end of the water slug, it should be independent of the gas and also of the parameter π_4. However, in reality, there is the wave phenomenon, which has been neglected in the vent clearing model. As the valve opens in the test, there is a rarefaction wave that propagates from the valve back to the gas chamber. The reflection of this wave causes the pressurization of the gas volume of the water slug, and pushes the slug downward. In the case of helium, the sonic speed is much faster, and hence the pipeline can be pressurized much faster. Thus, the slug is cleared at a much higher velocity and yields the higher peak value. Because of this wave propagation characteristic, an orifice would retard the propagation of the wave, and hence prolong the vent clearing period. The effect may be minor in comparison with the time for the propagation of the rarefaction wave. Hence, orificing does not show much of an effect on the first peak bottom pressure. This may not be the case for a different orifice area ratio.

The second pressure peak shows a random effect (Figure 4.6.4). It is thought that it must be caused by a combination of different vent clearing phenomena and bubble expansion. In that case, it is not expected to correlate well with π_4 alone. More work will be performed in

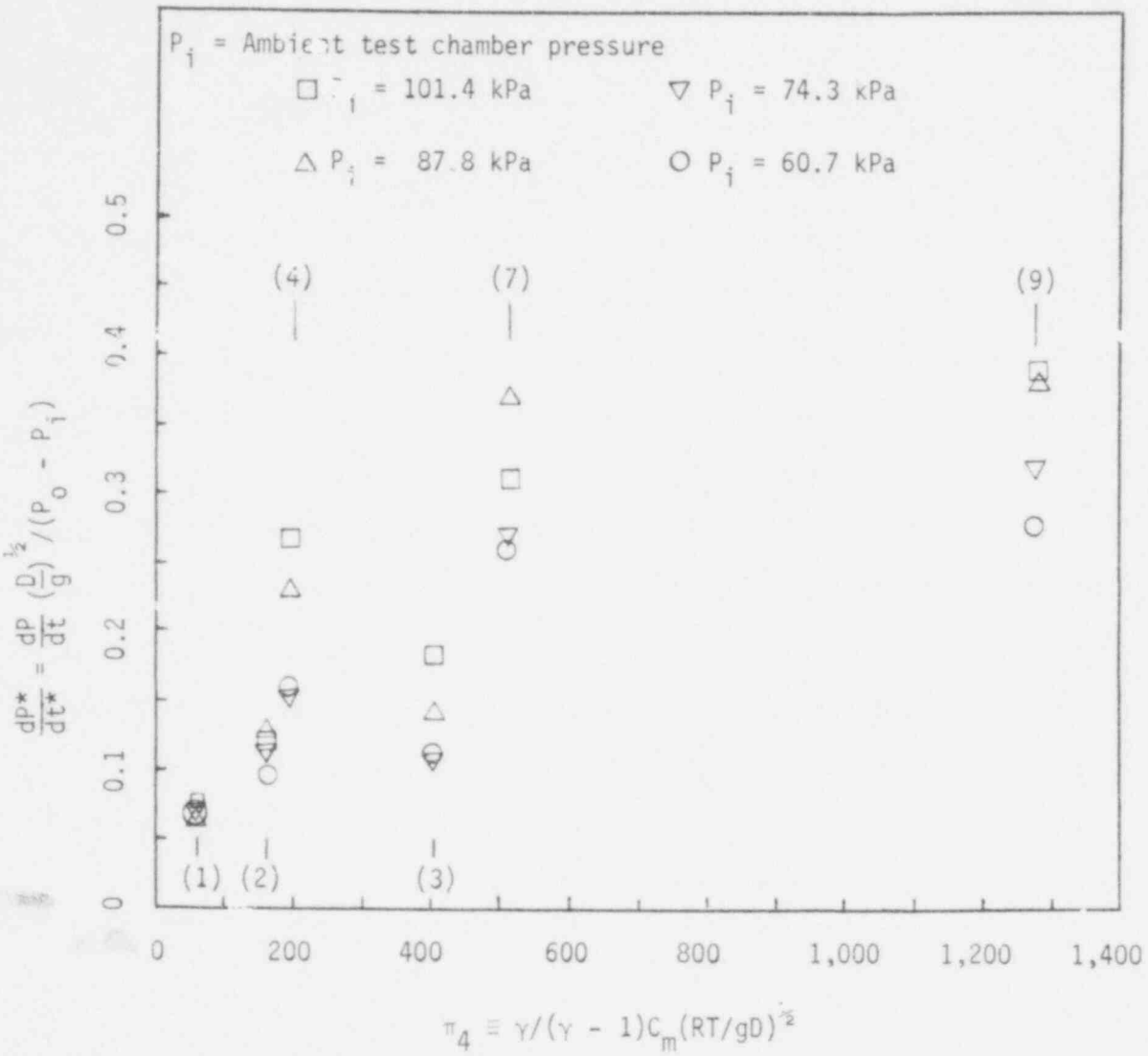

Figure 4.6.8. The Rate of Chamber Pressurization at the Onset of Pool Surface Movement vs. π_4.

this area for a better understanding of the second peak.

The upward lift on the torus will depend on the amount and rate at which the liquid in the pool is accelerated into the free space above the pool surface. In our experimental set-up, it is difficult to directly determine the magnitude of the uplift, although the data for the acceleration of the fluid can be deduced from the movies. In the results communicated in this report, the rate of pressurization of the free space just after a liquid slug hits the bottom of the pool has been taken as an indication of the uplift. Thus, the data for ΔP and dP/dt nondimensionalized with $(P_o - P_i)/(g/D)^{\frac{1}{2}}$ is plotted in Figure 4.6.8 as a function of the enthalpy flux parameter π_4. Helium and argon are chosen as the test gases. Both of the gases have $\gamma = 1.67$ and pressures in the reservoir and the test chamber are varied to have both choked and non-choked flow. The data with and without orifice show considerable scatter, and it seems that two different curves can be drawn for helium and argon.

Although dP/dt seems to decrease as π_4 is decreased, the relative reduction for the two gases is not the same. Thus, on the surface it may look as though the enthalpy flux model holds good, yet it seems that there is another parameter which has not been taken into account in the scaling analysis. It is possible that the distance of the relief valve from the reservoir and the velocity of sound in the gas may also play a role in determining the rate of pressurization of the pipeline prior to vent clearing.

The time differences between the first and second peaks, and also between the first peak and the second valley, do not seem to depend on the parameter π_4. Further investigation of these effects is being pursued.

We may summarize our conclusions as follows.

With respect to the location of the orifice in relation to the downcomer, orificing seems not to affect the downward peak forces. Over a wide range of variation in π_4, the first and second peak bottom pressures seem unchanged (Figures 4.6.3 and 4.6.4). In fact, P_1/P_ℓ and P_2/P_ℓ are practically independent of π_4. Moreover, all time correlations, such as the time difference between the first and second peak bottom pressures (Figure 4.6.6), as well as the non-dimensional vent clearing time (see Sonin's result [4.5]), are all independent of π_4. Whenever the data correlate, we find that the non-dimensional quantities all have a weak dependence on π_4. This observation is generally valid for experiments performed at UCLA, MIT, and LLL, where the positions of the orifice are relatively far away from the downcomer exit. In other words, the orifice serves to provide additional flow resistance and metering; it does not affect, however, the downward pressures and timing. Vent clearing is a phenomenon governed by the dynamics of the fluids and the geometry of the configuration; it is only slightly affected by orificing, unless the position of the orifice is so close to the downcomer exit that the basic fluid dynamics are altered by its presence. The subsequent gas discharge is definitely affected and is briefly discussed in Section 4.7.

The peak downward pressure is best normalized by the maximum line pressure, while the downward pressure is calibrated to be zero before the vent clearing starts. Symbolically, the non-dimensional parameter

$$\frac{P_{\text{downward}} - P_{\text{wet-well}}}{P_{\text{maximum line}}}$$

seems to correlate better than other dimensionless groups.

In evaluating our data, the line resistance between the dry well and the wet well is found to be small in comparison with the frictional

loss due to the orifice. Under the following assumed conditions (assumed to be the "worst" possible), we may conclude that the line resistance is negligible. The assumed operating conditions are:

(1) Flow in the pipe is turbulent, with a Reynolds number (based on the diameter of the pipe) larger than 10^5.

(2) The interior wall of the pipe is so rough that it can be classified as sand-grained.

(3) The reduction in area due to the orifice is between 11 and 29%.

(4) The total pipe length is 15 feet.

We find that the ratio of the pressure loss, namely

$$(\Delta P)_{\text{orifice}}/(\Delta P)_{\text{line resistance}},$$

ranges from 5.0 to 35. This estimation is probably low by a factor of 3 due to the extreme assumption of a sand-grained pipe wall. The line resistance is hence negligible in relation to the orifice loss. The conclusion is independent of the nature of the gas as well as the mass flow rate.

4.7 Role of Acoustics during Vent Clearing

The pressure and flow histories plotted in Appendix F show that during vent clearing, the pressure in the pipe volume between the water slug and the quick-acting solenoid valve is continuously increasing, while the pressure in the upstream reservoir during this period is constant. The rate of pressurization of the pipe volume between the water slug and the quick-acting solenoid valve after the opening of the valve depends on:

(i) The time rate of opening of the valve,

(ii) The velocity of sound in the gas, and

(iii) The density of the gas.

The time rate of opening of the valve will govern the volume flux of the gas leaving the valve. The opening characteristics of the valve depend on the temperature, pressure drop, valve size, and electrical circuitry. For most of the experiments reported in this work, the effect of these variables, except the pressure drop, should be the same for all the gases studied.

The velocity of sound in the gas would govern the pressure conditions both upstream and downstream of the solenoid valve, and in turn control the transient flow rate of gas into the pipe volume between the water slug and the solenoid valve. The higher the sonic velocity, the faster the upstream and downstream pressure conditions should be established. An indication of the travel of waves of compression and rarefaction in the pipe can be obtained by noting the oscillations in the centerline velocity of the pipe between the water slug and the quick-acting solenoid valve. As is seen from the figures contained in Appendix F, the oscillations are very pronounced for air and argon but are

smeared out in the case of helium. The speed of sound in helium is about 3 times that in either air or argon.

The density of the gas should affect the rate of pressurization such that the higher the density of the gas, the faster becomes the rate of pressurization. Argon (ρ = 1.63 kg/m^3) is the heaviest gas, followed by air (ρ = 1.19 kg/m^3) and helium (ρ = 0.164 kg/m^3). Under the combined effect of the above variables, it is observed that the rate of pressurization is fastest for helium, which in turn results in the highest downward force on the bottom of the test chamber.

It should be pointed out that the oscillations in the pipe centerline velocity are observed ahead of the water slug and occur mostly prior to complete vent clearing. These oscillations are not carried over to the bubble. However, the presence of an orifice in the line may influence the flow oscillations prior to vent clearing, and inhibit the flow just after vent clearing. The presence of an orifice tends to attenuate the flow oscillations ahead of the orifice and also increases the number of wave reflections. This results in a choppiness in the flow rate profile as compared to the well-marked oscillations in the absence of the orifice. The rate of pressurization of the pipe volume ahead of the orifice is also faster because of the reduced volume of the pipe. For the case of helium, however, no distinct fluctuations or oscillations in the flow are observed.

The presence of the orifice, although it has little effect on the rate of vent clearing, the total time to clear the vent, or the magnitude of the downward forces, does seem to inhibit the expansion of the bubble after vent clearing. Figure 4.7.1 compares the static line pressures upstream and downstream of the orifice. It is noted that soon after vent

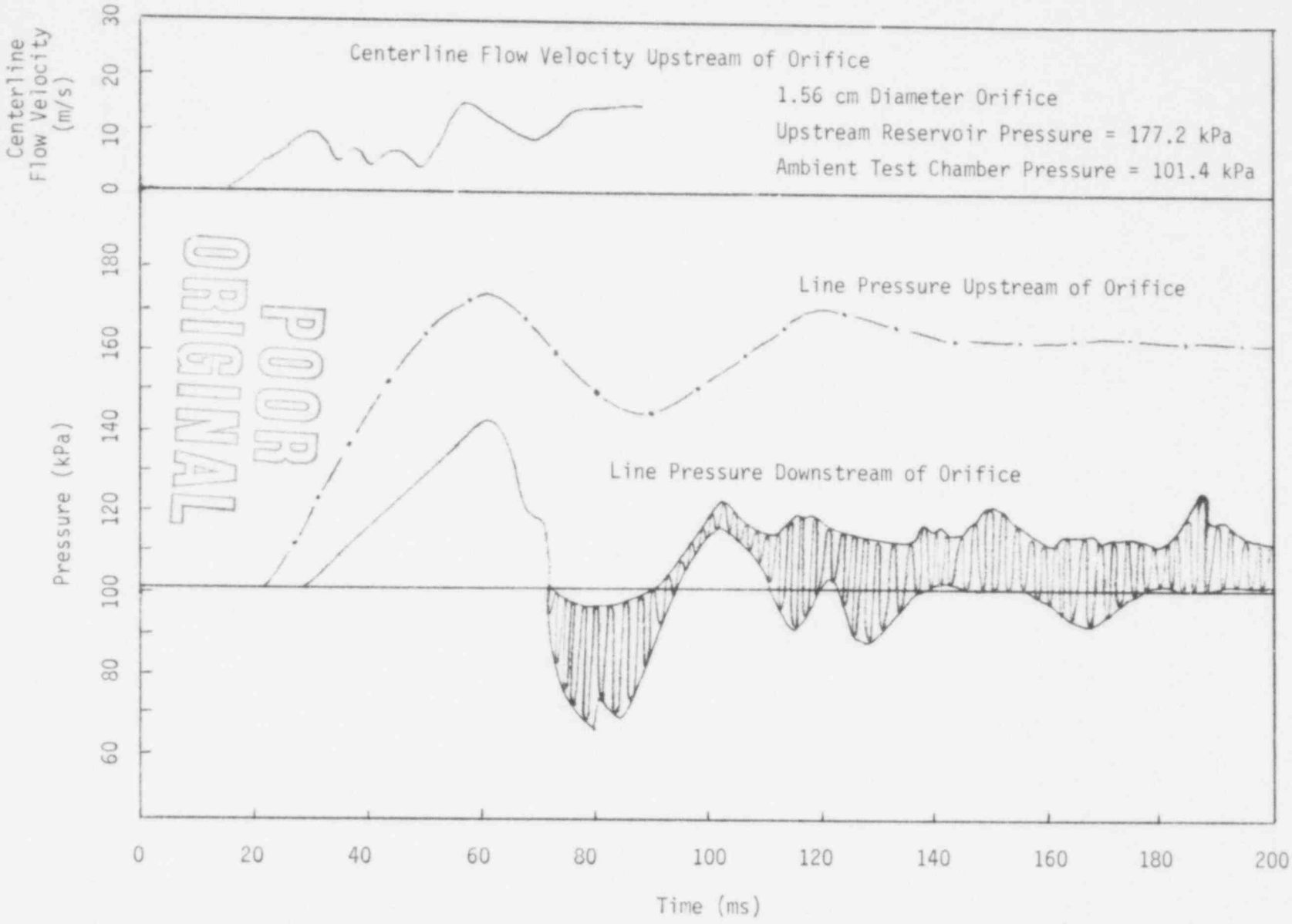

Figure 4.7.1. Comparison of Line Static Pressures Upstream and Downstream of the Orifice.

clearing, the pressure in the pipeline between the orifice and the vent exit becomes negative. The reason for this could be that the influx of gas through the orifice cannot keep up with the suction created by the inertia of the expanding bubble. This in turn may lead to an oscillatory behavior in the bubble. These oscillations in the bubble could not be discerned from the movies. However, the static pressure downstream of the orifice shows a markedly oscillatory behavior.

REFERENCES FOR SECTION 4

4.1. Carmichael, C. F., and S. A. Marko, "CONTEMPT-PS-- A Digital Computer Code for Predicting the Pressure-Temperature History within a Pressure Suppression Containment Vessel in Response to a Loss-of-Coolant Accident," Idaho Nuclear Company, IDO-17252, April 1969.

4.2. "Final Safety Analysis Report," Vermont Yankee Nuclear Power Plant.

4.3. Pitts, J. H., and E. W. McCauley, "A 1/5 Scale Experiment of a Mark I Boiling-Water Reactor Pressure-Suppression System under Hypothetical LOCA Conditions," paper presented at the International Conference on Thermal Reactor Safety, Sun Valley, Idaho, July 31-August 4, 1977.

4.4. Moody, F. J., "A Systematic Procedure for Scale-Modeling Problems in Unsteady Fluid Mechanics," unpublished paper.

4.5. Sonin, A. A., "MIT Program on Modeling of Pool Swell Hydrodynamics," notes prepared for the Containment Code Review Group Meeting, Silver Spring, January 1977.

5. ERROR ANALYSIS

Data for the upstream pressure, the pressure at the bottom of the test chamber, the rate of pressurization of the free space above the pool, and the gas flow rate through the vent pipe were obtained. The displacement of the gas-liquid interface during vent clearing, the total vent clearing time, the bubble growth rate after vent clearing, and the free surface response were obtained from the movies. In the following paragraphs, uncertainty in the measurement of each of these quantities is discussed.

Pressures

Statham Model TPI 145 pressure transducers with holders, as shown in Figure 1 of Appendix B, were used to measure transient pressures. A calibration for the output of the pressure transducer in mV as a function of input voltage and applied pressure was made under static conditions. A check on the transient response was also made, and the response time of the pressure transducers was found to be about 2 milliseconds. Details of the calibration for amplitude and response are given in Appendix B. In the experiments, the output of the pressure transducers was recorded on an oscilloscope and was photographed for data reduction and permanent record. Recording of up to four signals simultaneously resulted in limitations on the sensitivity of the oscilloscope. Thus, the maximum percentage error resulted when the magnitude of the output signal was the smallest. The output signal in terms of pressure can be written as

ΔP = (Pressure transducer output, mV) × (Conversion constant, C_1),

or

$$\frac{d(\Delta P)}{\Delta P} = \frac{d(mV)}{mV} + \frac{dC_1}{C_1}.$$

In practice, the maximum probable error in pressure is [1]:

$$\frac{d(\Delta P)}{\Delta P} = \left\{\left[\frac{d(mV)}{mV}\right]^2 + \left(\frac{dC_1}{C_1}\right)^2\right\}^{\frac{1}{2}}.$$

The error d(mV)/mV arises mainly from inaccuracies in reading from the photographs and shifts in the baseline. The error in the conversion constant results from the input voltage being different than that used for calibration, and uncertainty in obtaining C_1 from the data used in calibration. For the smallest signal, the combined error due to shift in baseline and reading inaccuracy is expected to be less than ±10%, while error in C_1 should be less than ±1%. Thus, the maximum error in pressure is:

$$\frac{d(\Delta P)}{\Delta P} = [(10)^2 + (1)^2]^{\frac{1}{2}} \approx 10\%.$$

Flow Rate

As discussed earlier, two different methods were used to measure the flow rates in the vent line. When the maximum flow velocities were less than 50 m/s, a TSI flow gun was used. However, for higher flow velocities, a hot wire anemometer was used. Separate calibrations of these two instruments were performed, the details of which are given in Appendices C.1 and C.2. The maximum error in the measurement of the flow velocity by the TSI Model 4100 flow gun is expected to be less than ±2%. The Model 1211 probe of the anemometer was calibrated for air up to the velocity of sound in air, and deviations in the flow velocity from the calibration curve are expected to be less than ±1%. The probe was not calibrated for use with helium or argon, but calibration curves for these

gases were deduced from the calibration curve for air, as described in Appendix C.1. Although no counterchecking of this extension of the air calibration to argon or helium gases was made, uncertainty in the flow rate of these gases is expected to be less than ±5%. The flow velocities as indicated by the TSI Model 4100 flow gun and the anemometer under the same conditions were also compared. It was observed that generally the flow velocity given by the anemometer was 15-20% higher than that given by the flow gun. This is expected, since the flow gun gives the average velocity through the pipe cross-section, while the anemometer probe reads only the maximum velocity. For a turbulent velocity profile in the pipe, it is expected that the maximum velocity should be about 20% higher than the average velocity. Thus, the flow gun and anemometer readings are consistent with each other. The maximum error in the pipe-line center velocity of air, as measured by the hot-wire anemometer, should not be more than ±3%. However, this uncertainty for helium and argon could be as high as ±7%.

Displacement of Gas-Liquid Interfaces

The displacement of the various interfaces (gas-liquid interfaces in the vent and the pool free surface) from their original positions were measured from the projection of the movies on a screen. The scaling factors for the conversion of the projected lengths to the original lengths were obtained by noting the projected distances between various bench marks. The main errors in measurement arose because of the fuzziness of the projected interfaces. The maximum error in the shortest distance measured (~1 cm) is expected to be less than ±10%. However, as the measured distances become larger, this error should be considerably smaller.

Vent Clearing Times

The time at which the relief was actuated was determined from the movies by noting the initiation of a streak of light which was synchronized with the activation of the quick-acting solenoid valve. There was a 15-20 millisecond delay between the activation and the opening of the valve. The exact time at which the valve opened could not be determined from the movies, but was determined from the oscillographs by noting the time at which the pressure or flow rate in the vent pipe started to increase. As a certain pressure is required to build up ahead of the water slug before the interface started to move, and as the movement of the interface was very slow in the beginning, it was difficult to ascertain the exact time at which the interface started to move. Thus, while plotting the interface displacement, zero time has been assumed to be the time at which the pressure ahead of the water slug started to increase.

To avoid errors in obtaining the time elapsed between each frame of the movie during the accelerating and decelerating phases of the camera, the number of frames between light marks of known frequency on the film was counted. This resulted in a rather precise determination of the time equivalence of one frame in any segment of the movie. The maximum error in determining the total vent clearing time is expected to be less than ±2 frames or ±3.4 milliseconds.

REFERENCES FOR SECTION 5

1. Kline, S. J., and F. A. McClintock, "The Description of Uncertainties in Single Sample Experiments," Mechanical Engineering 75, 1953.

6. DESCRIPTION OF THE STEAM INJECTION EXPERIMENT

This section presents the final design of the steam injection system, currently under construction. The system is designed to allow vertical or horizontal steam injection into a pool of water for various submergence depths. The major components of the system include a boiler, a superheater, a surge tank and a test section, simulating the suppression pool. The schematic of the system is shown on Figure 6.1.

6.1 System Description

1. Boiler -- The maximum steam-generation rate of the boiler is 7.56 gm/sec, operating at 790.0 kPa with a heat load of 17.0 kW.

2. Superheater -- The maximum heat output of the superheater is 1.5 kW, which can generate a superheat up to 106 ^{o}C for the maximum steam-flow rate.

3. Surge Tank -- It is designed for up to 1185 kPa internal pressures. The superheated steam is used to pressurize the surge tank for steam injection. Figure 6.2 shows the details of the surge tank design. The side openings are for the insertion of instrumentation.

4. Test Section -- It is designed to withstand internal pressures up to 790 kPa. The details of the design are shown on Figure 6.3. The basic design consists of two hexagonal sections stacked on top of each other. Each flat face of the hexagon has a window opening. These openings are designed with a glass or stainless steel plate cover. The glass-plate cover allows visual observation and movie lighting control, while the steel-plate covers allow for insertion of various measuring devices.

5. Instrumentation -- The instrumentation upstream from the vent pipe is isolated by the check valve (V7) and the solenoid valve (V2). The function

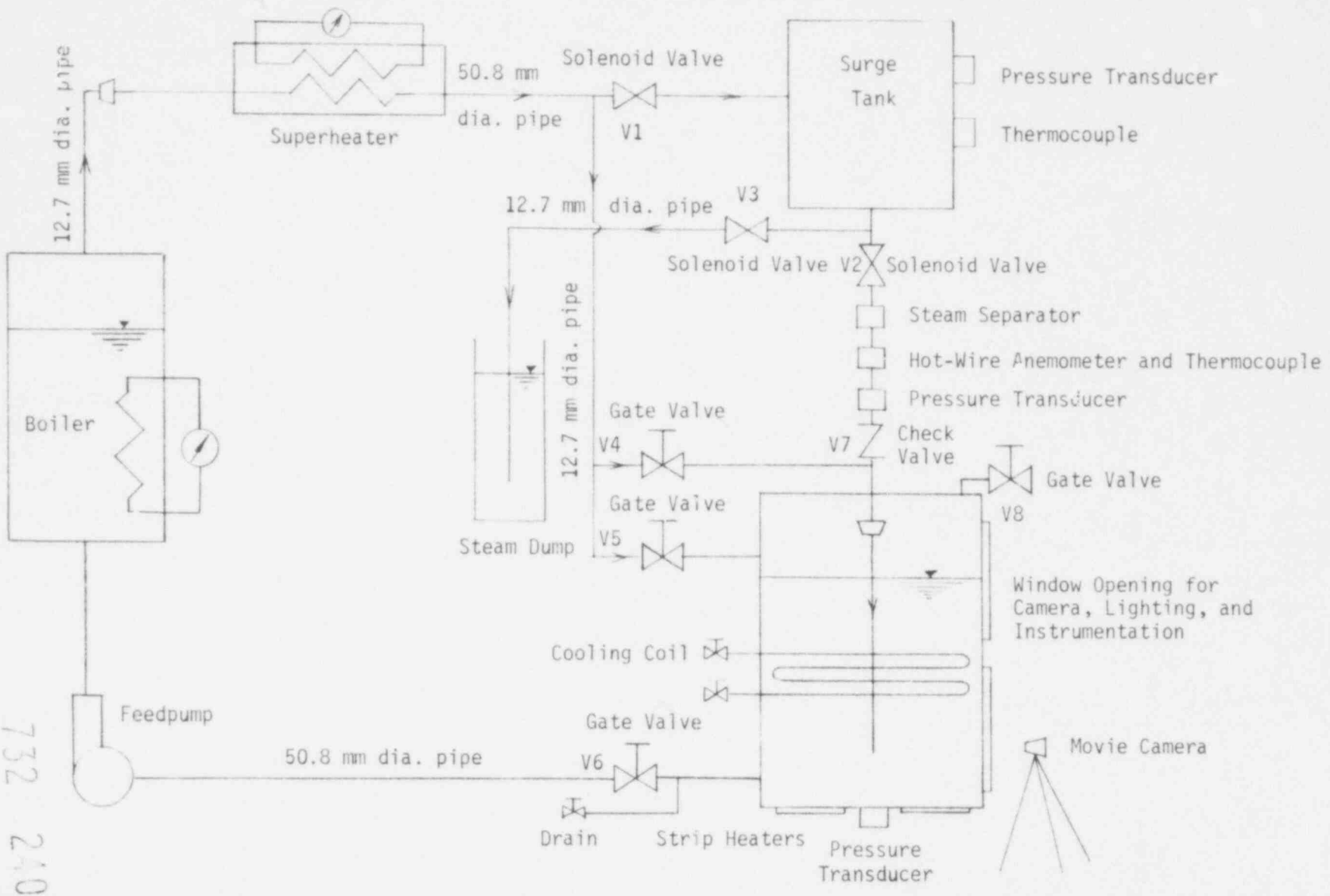

Figure 6.1 Steam Injection System.

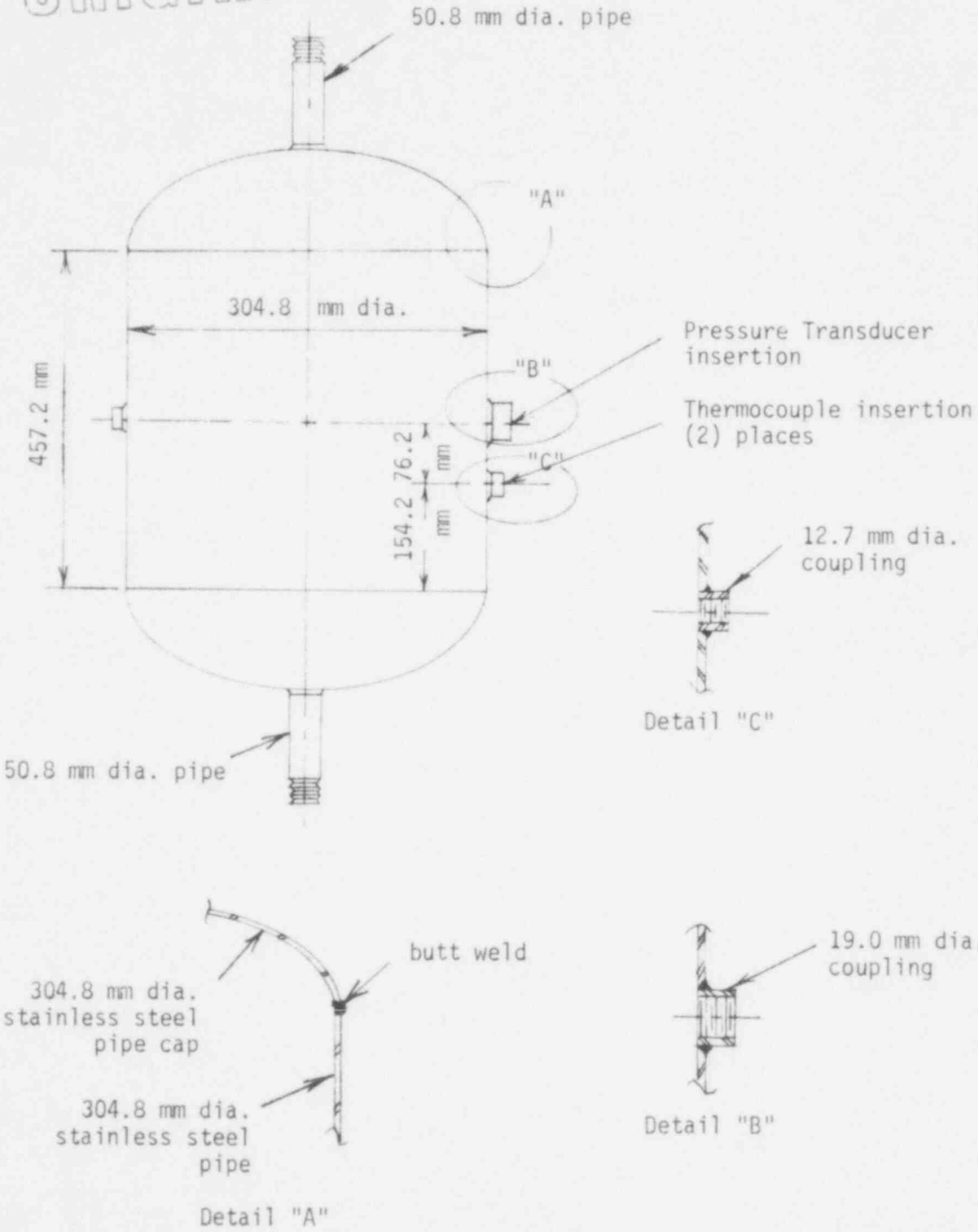

Figure 6.2 Surge Tank.

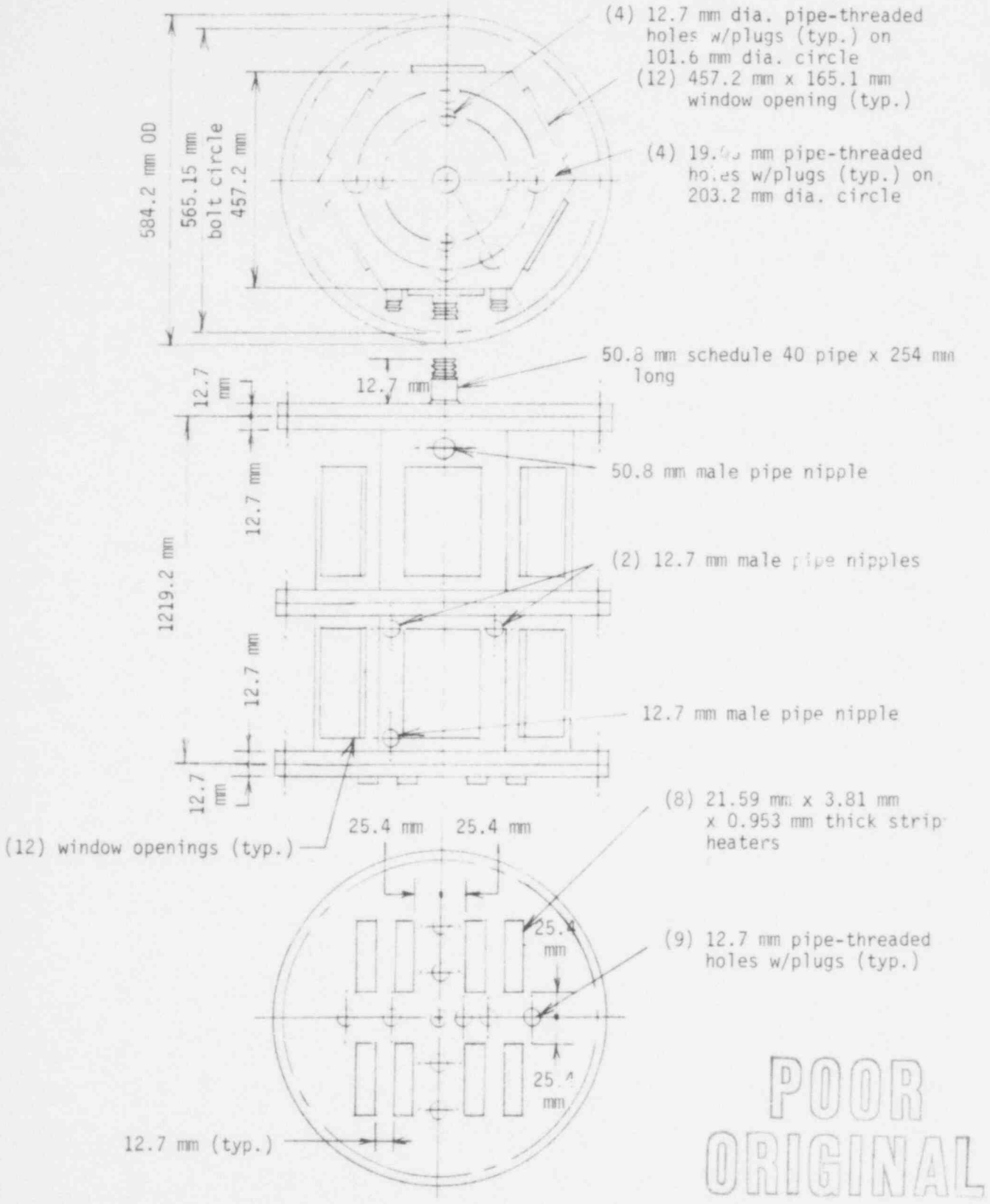

Figure 6.3 Test Section.

of the check valve is to prevent water upflow, which may destroy the hot-wire anemometer. The solenoid valve serves dual purpose: for instrumentation isolation, and as a steam-injection trigger. The heaters at the bottom and the cooling coil provide pool temperature control. Instrumentation necessary for measurements in the test section can be inserted from the top, bottom, or through the side windows.

6. Feed-pump -- It is a high-pressure, low-capacity pump that provides a discharge pressure greater than 790 kPa and a low flow of 7.56 gm/sec.

6.2 System Operation and the Degas Process

The initial phase of system operation is called the Degas process. It can be divided into two stages. The first step is to eliminate the air present in the system, e.g., in the piping, surge tank, etc. The second step is to eliminate the dissolved air in the distilled water of the system.

Step I: The air initially in the system is to be driven out by the steam generated in the boiler. This is achieved by turning on the boiler, closing valve V2, and opening valves V1 and V3. The air-steam mixture is discharged into the steam dump while the boiler is warming up. Subsequently, valves V4 and V5 are opened so that the air initially in these pipes is driven into the test section and then to the atmosphere through valve V8. Subsequently, the air initially in the vent pipe is driven into the pool by turning on valve V2 and turning off valves V3, V4, and V5.

Step II: By the actuation of V6, which allows water flow into the boiler, the initially dissolved air in the water is boiled off. This small portion of air is then mixed with the steam and is discharged into the pool. The steam will condense while the air will float to the pool surface, and is then mixed with the steam coming through valve V5, and discharged through

732 245

valve V8. While the discharge steam and the bottom heaters are heating the pool, the air initially dissolved in the pool water is also driven out. Again, this process is continued long enough to ensure that all dissolved air is driven out of the system.

At the end of the Degas process, valve V2 is closed so that no more steam gets injected into the pool. Then, after the surge tank is pressurized to the desired pressure, valve V1 is closed and the boiler is adjusted to a lower power level to maintain a small steam-generation rate. The pool is allowed to set while the bottom heaters are turned off and cold water is run through the cooling coil to reduce the pool temperature to the desired subcooling. Steam generated from the boiler is continuously fed into the test section over the pool surface to keep the test section's pressure above atmospheric pressure, to prevent back-flow of air into the test section. Then, valve V2 is triggered to inject the pressurized steam from the surge tank into the pool.

6.3 Instrumentation

1. Temperature Measurement -- A fast-response thermocouple was made by using 25.4 μm diameter chromel-alumel wire. The response time of this thermocouple is on the order of 4-5 milliseconds. The measurement was made by immersing the hot junction of the thermocouple from air into ice water and from air into hot water. The response time was 4 ms when the hot junction was immersed into ice water, and was about 5 ms when it was immersed into hot water. The thermocouple responses were recorded on an oscilloscope. Typical results, reduced from photographs of the oscilloscope, are shown on Figures 6.4 and 6.5. The response time, t_R, is defined as the time period required to change the thermocouple's initial temperature to

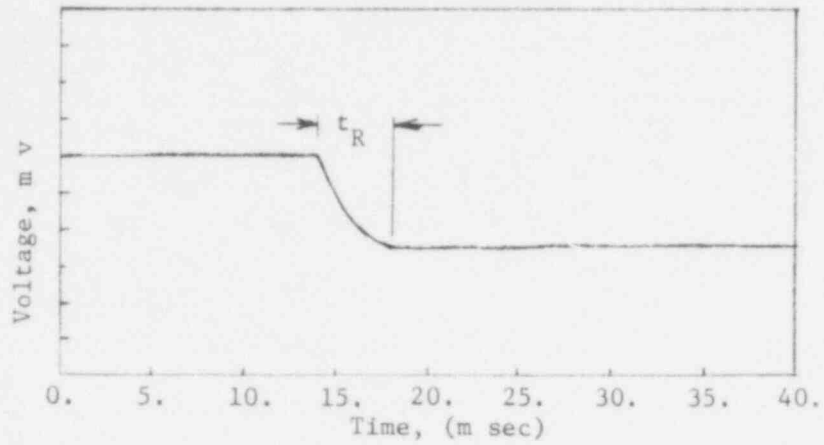

Figure 6.4 Hot Junction of Thermocouple Dipped into Ice Water.

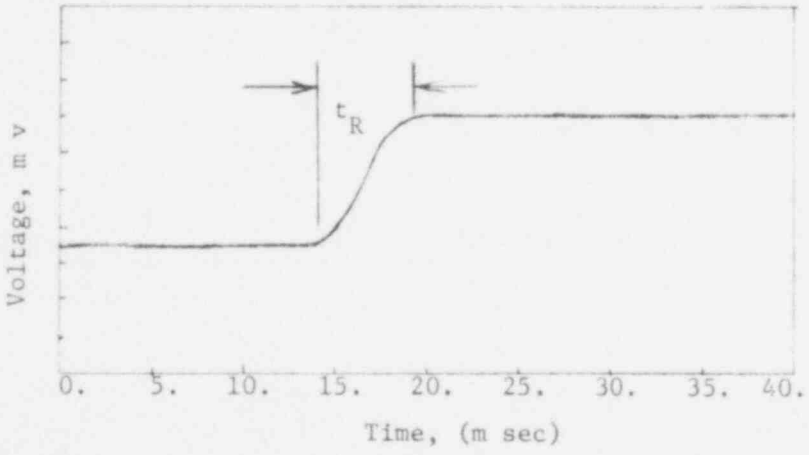

Figure 6.5 Hot Junction of Therm couple Dipped into Hot Water.

final temperature.

2. Pressure Measurement -- Regular, unbonded, strain-guage pressure transducers were used for the pressure measurements because of their fast response and low sensitivity to temperature effects. However, some problems were encountered with the time-dependent temperature field. Firstly, diaphragm movements due to thermal expansion lead to a zero shift. Secondly, a transient temperature field leads to a thermal gradient on the pressure transducer. This causes a zero shift as well as time lags in the temperature compensation circuit. An experiment was designed to obtain the correct calibration of the pressure transducers operating in a time-varying temperature field. Contact has been made with the Idaho National Engineering Laboratory.

7. CONCLUSIONS

The similitude method has been applied to establish the appropriate scaling laws for vent clearing, bubble growth, bubble motion, and pool surface swelling for both air injection and pure steam condensation.

For the phenomenon of the discharge of a water slug into a pool of water, the similitude parameters are the Froude number, the Euler number, the Reynolds number, and the Weber number. In small model tests, it is impractical to simulate all of these parameters. The Weber number, which characterises the Taylor instability phenomenon at the air/water interface, and the Reynolds number, which characterises the wall viscous effects, have to be disregarded in the small scale test. Similitude in the Froude and the Euler numbers leads to a linear scaling relation for pressure and a square-root scaling relation for velocity and time.

The similitude parameters during bubble growth after vent clearing include the Froude and Euler numbers as well as the Mach number, and the specific gas constant if geometrical similarity is to be maintained. The simulation of the Mach number leads to a linear scaling of the temperature, which is difficult to achieve. One practical method of circumventing the temperature scaling difficulty is to use an orifice to simulate the enthalpy flux.

Two periods were distinguished in the scaling of the steam transient. The first period is characterised by a steam jet where momentum is important. It is advisable to maintain thermodynamical similarity, which leads to similitude in the Jacob number, the Kelvin-Helmholtz instability number, the Mach number, and the Euler number, but not in the Fourier number of the Weber number. During the later steam chugging period, two characteristic lengths have been suggested. In

addition to the thermodynamical similarity, the pipe lengths in the model and the prototype should be the same in order to simulate the acoustic effect, although the pipe radius could be scaled down. If the steam/water interfacial movement is governed by inertia, the simulation of the steam chugging may be possible. If the interfacial movement is governed by heat transfer, steam scaling appears to be more difficult. More fundamental understanding of steam chugging will be achieved in our second year program.

From the transient air/water tests, it was observed that the moving liquid interface became unstable during vent clearing, due to Taylor instability, and a standing spike of liquid grew with time on the interface. This water spike invariably broke up prior to complete clearing of the vent. The appearance of the spike depends on the acceleration, which in turn is governed by the driving pressure and the submergence depth. Using linear instability theory, it was found that similar water spikes would be experienced in the BWR containment during the vent clearing process. The consequence of the Taylor instability is to reduce the effective mass that can be accelerated during vent clearing, and thus lead to an earlier vent clearing time. On the other hand, the simple slug model shows that the virtual mass can prolong the vent clearing time, therefore allowing the pressure in the vent to attain a higher value as the vent is clearing. The pressure build-up in the vent during vent clearing is the dominant factor for the downward force. The coupling between the virtual mass and the Taylor instability complicates the interpretation of vent clearing data.

It was found that the first impulse force peak occurred just after vent clearing. As this impulse dies down, a second impulse is felt which

gives rise to another peak in the downward force on the pool bottom. The downward force characteristics depend to a large extend on the vent pipe pressure and the initial bubble growth. Depending on the driving pressure, the initial bubble expansion can vary from a spherical shape to a pancake shape. The growth of the bubble is controlled by the solid boundary, gravity, and the inertial forces, and also by the flow pattern in the surrounding liquid. It was also observed from the movie that the bubble surface is characterised by wave propagation. During the early period of bubble growth, the free surface rises uniformly, but soon acquires the shape of a half standing wave with a peak in the middle. The gas space space above the free surface was monotonically compressed by the water swelling, and no bubble oscillation was observed.

Tests with different gases (air, helium, and argon) showed that the velocity of sound and the density of the gas governed the pressure conditions both upstream and downstream of the solenoid valve, and in turn controlled the transient flow rate of gas into the pipe volume between the water slug and the solenoid valve. The presence of the orifice has little effect on the rate of vent clearing, the total time to clear the vent, or the magnitude of the downward force when the positions of the orifice are relatively far away from the downcomer exit. However, the presence of the orifice seems to inhibit the expansion of the bubble after vent clearing.

A simple error analysis showed that the maximum error in the pressure measurement is 10%, in the flow rate measurement is less than 3%, in the distance measurement from the movie is 10%, and in the vent clearing time measurement is less than 3.4 ms.

The steam transient test apparatus design was completed, and

testing will begin during the next quarter.

APPENDIX A -- PHOTO-TECHNIQUE

Extensive effort was spent on photo technique for an acceptable movie recording of the interfacial motion. The governor and gearing system on the Photosonics 1B-AC high-speed movie camera was modified to give a constant rate of 680 frames per second (fps) at full speed. A method has also been developed for remotely starting the camera.

A 135 mm telephoto lens has been fitted to the Photosonic camera to allow focusing on a much smaller field of view of approximately 10 cm. Formerly, a 13 mm wide-angle lens was used that limited the field of view to approximately 30 cm. The use of the telephoto lens also increased the depth of field for better resolution of the three-dimensional bubble surfaces.

An improved through-the-lens viewing system was adapted to allow more precise focusing. The improved focus resulted better resolution at 1/3,400 second exposure time. Because this Photosonic camera has an adjustable rotating shutter as well as a rotating prism, exposures of up to 1/27,200 second are possible; however, the lighting intensity becomes critical at these short exposures.

Four thousand watts tungsten filament lighting is used for 1/3,400 second exposures. The lighting is remotely controlled and turned on for only brief periods of time to prevent melting of the plexi-glass cylinder. Expertise has been developed in the use of a light meter with an extrapolated exposure-time scale that permits exact camera aperture settings in this high-intensity lighting situation.

Kodak Tri-X reversal film with an ASA rating of 160 has been used effectively with exposures of 1/3,400 second. However, 4-X reversal films with an ASA of 320 were found to give a brighter, if somewhat grainier, image.

The bubble contour drawings were made by projecting the film onto a sheet of paper and tracing the projection. A 16 mm L-W International projector with frame-by-frame operational capabilities was used to provide maximum flexibility in contour selection.

Editing and processing experience has been gained. A 16 mm Bell and Howell movie camera with 18 fps speed was used for titling, to enable to produce quality films. Composite printing of a white grid over footage of the growing bubble was performed by a film-processing laboratory in West Hollywood and parallax correction data has been compiled.

A system was developed for putting timing flashes on the film. Intense high frequency flashes were needed at these high filming speeds. The flashes were synchronized to start when the upstream air system valve became activated.

The film broke frequently at these high speeds, but the precise adjustment of the film take-up clutch has minimized this problem. Excessive camera and lens vibration has also been encountered, but was minimized by clamps and supports.

We are presently also using a Kodak 3,000 fps camera. A General Electric camera capable of 5,000 fps has been obtained but was not tested yet. With these cameras, 4-X negative film up to 1,000 ASA will be used to compensate for the decreased exposure time.

APPENDIX B -- PRESSURE TRANSDUCER CALIBRATION

Various pressure transducers were tested to determine their time responses to dynamical pressure; the first one was a Celesco LC-10 hydrophone. In accordance with the specifications, a free field response of 2.78 μV/μb was obtained for the frequency range 0 to 300 kHz. The capacitance across the leads was 7,146 pf and the resistance was 100 kΩ. The hydrophone was mounted at the end of a 12.7 cm tube, extended from a solenoid valve, as shown in Figure B-1(a). The output data of the hydrophone is shown in Table B-1. A typical hydrophone output response is shown in Figure B-1(b). The response time is about 4 msec. As shown in Table B-1, the voltage measured in the test was different from the calibration by a factor of two, which was probably due to the slow transient time.

The procedure was repeated with a Celesco KP15 variable-reluctance pressure transducer in conjunction with a model CD-25 transducer indicator in place of the hydrophone. According to the supplier, the time response of the transducer is less than 1 msec, however, the test results showed rise times of 120 to 140 msec for a quick release of upstream pressure (122.0 kPa to 142.7 kPa). A typical oscillogram is shown in Figure B-1(c). Obviously, the time response characteristic of the Celesco does not match with the supplier's specification.

The Statham differential pressure transducer model PM 131TC is an unbonded, fully active strain-gage type transducer. The response time, which is 1/5 of the natural frequency, is estimated to be 0.6 msec, based on information from the supplier. The output of this transducer is nominally 4 mV/V, corresponding to a full-scale output of 20 mV for 15 psid. A 5 V excitation is required for the transducer.

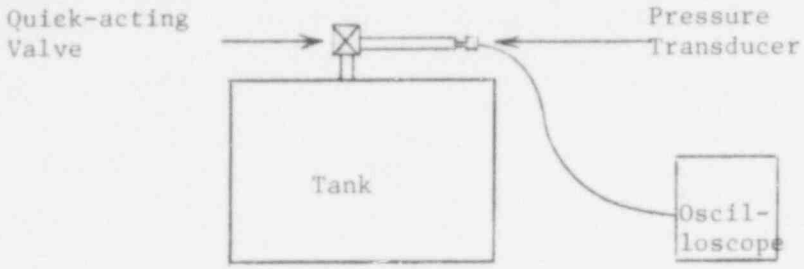

Figure B.1 (a) Experimental Setup for the Testing of Various Pressure Transducers

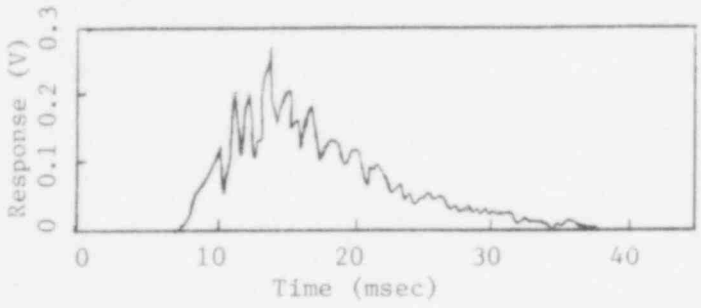

Figure B.1 (b) Typical Analog Response of a Celesco LC-10 Hydrophone. The Tank Pressure Was 122 kPa.

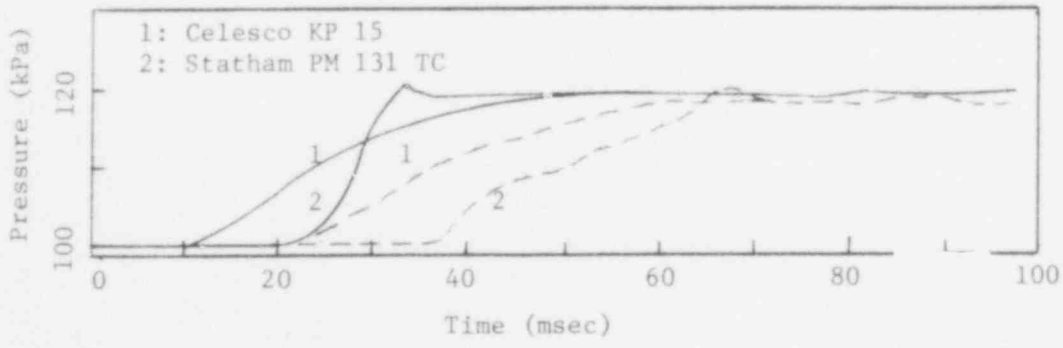

Figure B.1 (c) Time Responses of the Pressure Transducers to a Release of 122 kPa Upstream Pressure through a Solenoid Valve. The solid and broken lines indicate the outputs when the transducers were located 12.7 cm and 381 cm, respectively, from the valve.

Tank Pressure	Voltage Measured (V)	Voltage Calculated (V)
115.1	0.15	0.378
122.0	0.30	0.567
128.9	0.34	0.756
135.8	0.34	0.945
142.7	0.42	1.13
149.6	0.45	1.32

Table B.1.

Calibration Test Data of Hydrophone LC-10

The Statham transducer was tested by measuring the pressure of a rapidly opening valve. The results are shown in Figure B-1(c). The rise times are summarized in Table B-2. The Statham transducer seems to have a far quicker response than the Celesco unit, however, it has the drawback of a small output voltage (20 mV full scale). Pre-amplification of the signal would be required for the use of this transducer, with a mini-computer to be purchased at the same time. An Endevco 4621A DC amplifier was recently used in conjunction with the Statham transducer. while it was possible to magnify the transducer output a hundredfold, a time delay of about 200% was also noted. As an advantage, the Statham can be flush-mounted on the bottom plate of our test chamber. This helps to eliminate the spring-mass damping effect, found in most cavity-type arrangements (the water mass in the cavity is significantly large compared to the mass of the transducer's sensing element).

TRANSDUCER	PRESSURE (kPa)	RISE TIME (msec)
Statham	122.0	8.0
	135.8	7.5
	149.6	6.5
Celesco	122.0	130
	135.8	120
	149.6	130

Table B.2

Statham and Celesco Transducer Responses.

APPENDIX C. THE CALIBRATION OF THE THERMO-SYSTEMS INC. 1050 SERIES HOT WIRE ANEMOMETER

The transducer used with the 1050 Series Anemometer is a small resistance element, which is heated and controlled at an elevated temperature and placed in the flow stream. The sensor used in the present experiments is a Platinum-Iridium Alloy (P15) hot wire sensor. The specifications of this hot wire sensor are as follows:

Diameter of sensing area (D) = 12.7 μ

Length of sensing area (L) = 2.5 mm

Distance between supports = 3.5 mm

Sensor operating resistance (R_p) = 3.9Ω

Temperature coefficient of resistance (α) = 0.0009346/°C

Maximum recommended operating temperature in air = 750 °C

Upper frequency response in air at 100 m/sec = 10 KHs

The heat-transfer rate from the wire is

$$q = E^2 \frac{R_p}{(R_3+R_p)^2} \left[A + B(\rho v)^{\frac{1}{n}} \right] (t_s - t_e), \qquad (1)$$

where

E = bridge voltage

R_3 = 40 Ω resistor in series with the sensor

A,B = Constants. Their value depends on the fluid and the type of sensor used. The variables include thermal conductivity, viscosity, and Prandtl number

ρ = density of the fluid

v = velocity

n = exponent, is approximately 2

t_s = sensor operating temperature

t_e = fluid temperature.

It was found from the calibration curve for air, that it fits the following empirical equation, if the flow rate is in the range of 0 to 200 m/sec

$$N_u = \frac{hD}{\gamma} = 0.193\ Re^{0.618}\ Pr^{1/3} \qquad (2)$$

Thus, the value of n in Equation (1) is approximately equal to $1/0.618 = 1.62$.

Since the initial output voltage, $E_o = 3.83$ V without flow, Equation (1) can be written as

$$q = E_o^2 \frac{R_p}{(R_3+R_p)^2} + (E^2 - E_o^2) \frac{R_p}{(R_3+R_p)^2}$$

$$= E_o^2 \frac{R_p}{(R_3+R_p)^2} + h(\pi DL)(t_s - t_e) \quad , \qquad (3)$$

where h = heat-transfer coefficient.

The value of h can be corrected for two different gases by the heat transfer coefficient

$$\frac{E_1^2 - E_o^2}{E_2^2 - E_o^2} = \frac{h_1}{h_2} = \frac{Nu_1\ \gamma_1}{Nu_2\ \gamma_2} \qquad (4)$$

Here subscript (1) refers to air and (2) to the other gas. By substituting Equations (2) and (4) into Equation (3), calibration curves can be obtained for Argon and Helium. Calibration curves are shown in Figure C.1.

The TSI Model 1050 Series Hot-Wire Anemometer was calibrated by using the TSI Model 4100 air flow meter. The difference between the maximum measured flow velocities indicated by the anemometer and by the air flow meter was 10-15%.

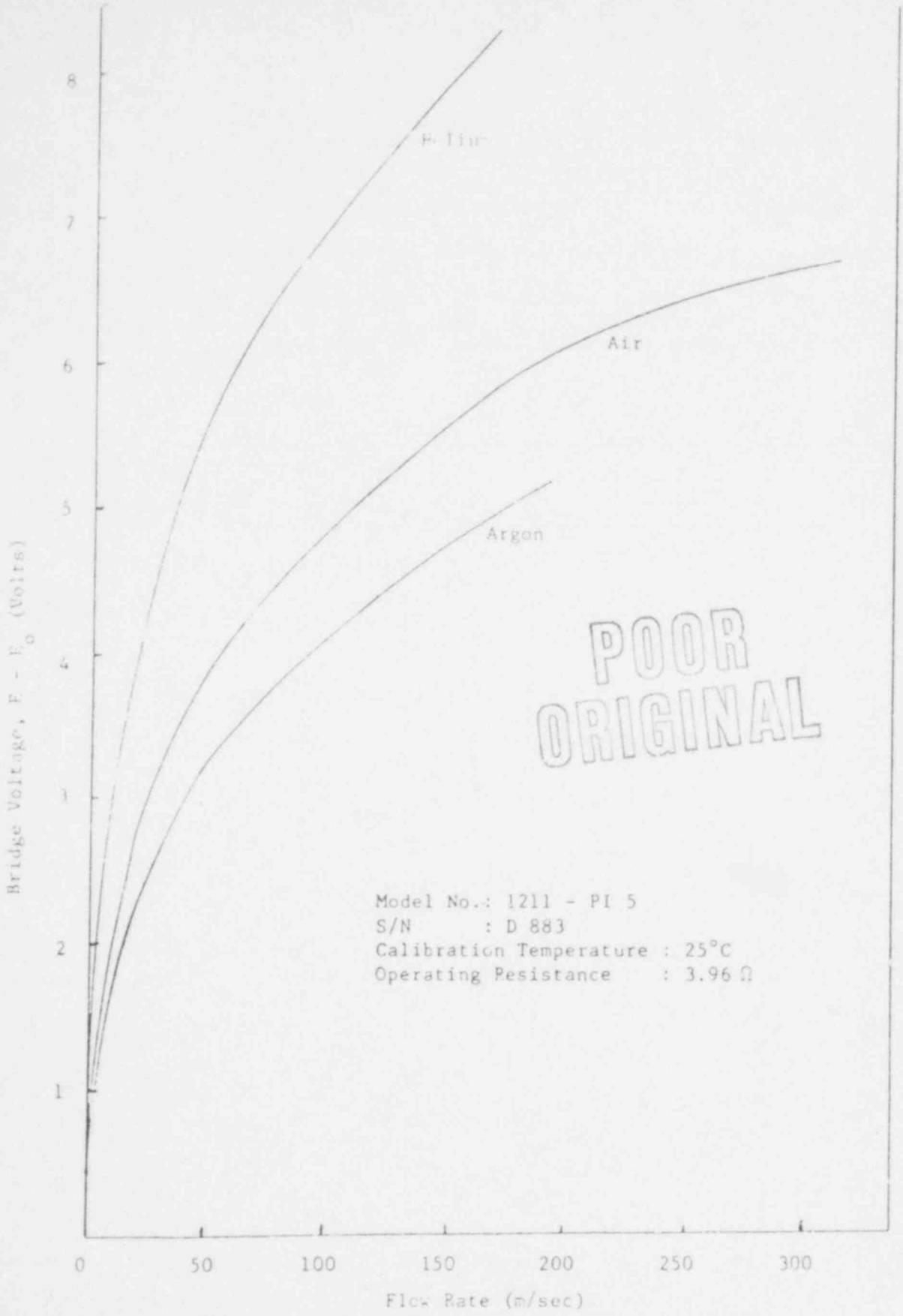

Figure C.1. Calibration Curves of Bridge Voltage vs. Flow Rate for Air, Argon, and Helium

Appendix D. Interface Motion During Vent Clearing

In this Appendix, data of the interface motion during vent clearing are presented. The nine figures represent cases with different gases and three different orifices. Each figure shows four different test chamber pressures. The submergence depth for all these cases was 10 cm.

Orifice	Pi \ Gas	Air	He	Ar
No Orifice	101.4 kPa 87.8 kPa 74.3 kPa 60.7 kPa	D-1	D-4	D-7
2.54 cm Diameter Orifice	101.4 kPa 87.8 kPa 74.3 kPa 60.7 kPa	D-2	D-5	D-8
1.56 cm Diameter	101.4 kPa 87.8 kPa 74.3 kPa 60.7 kPa	D-3	D-6	D-9

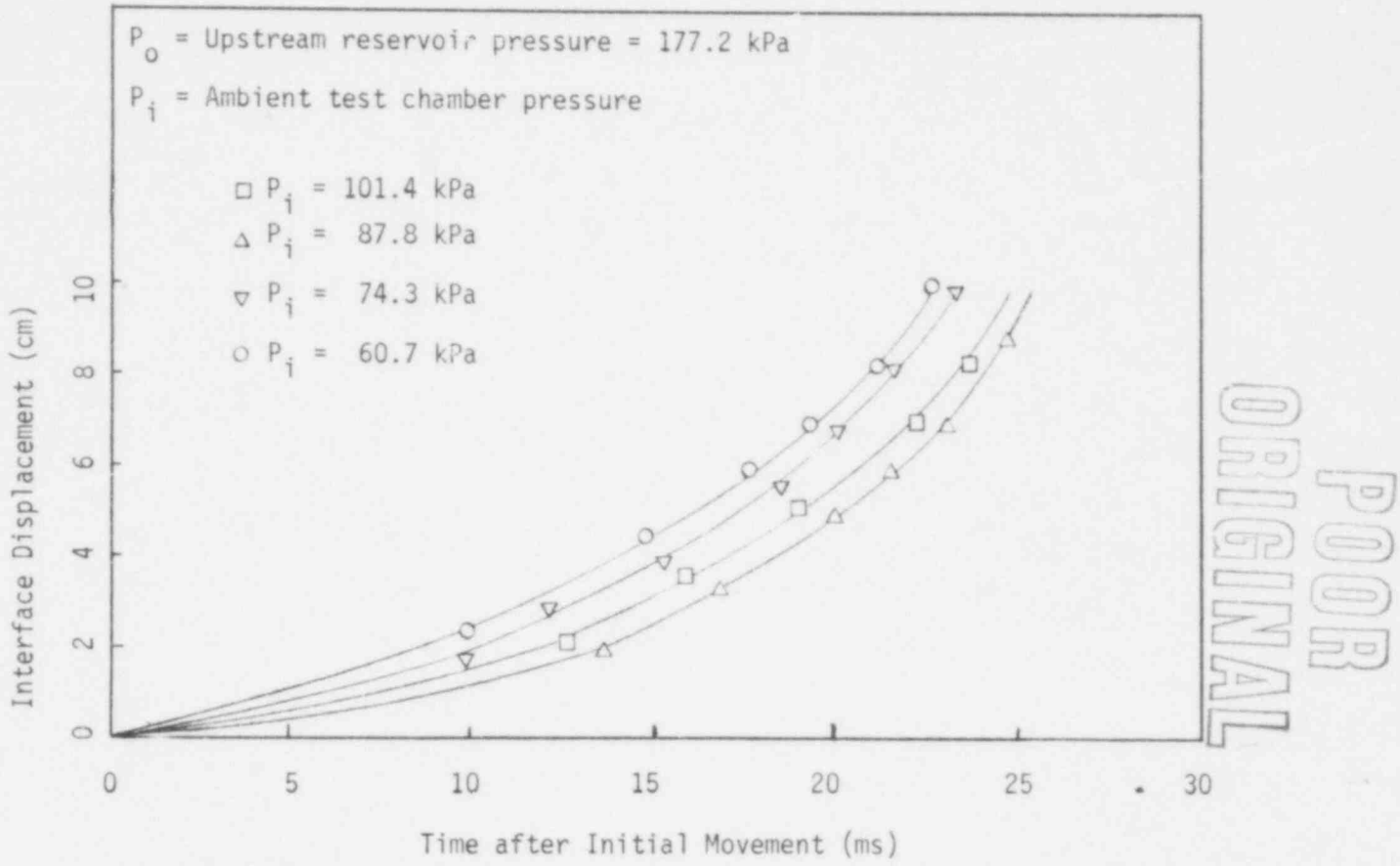

Figure D.1. Interface Motion during Vent Clearing for Air without Orifice.

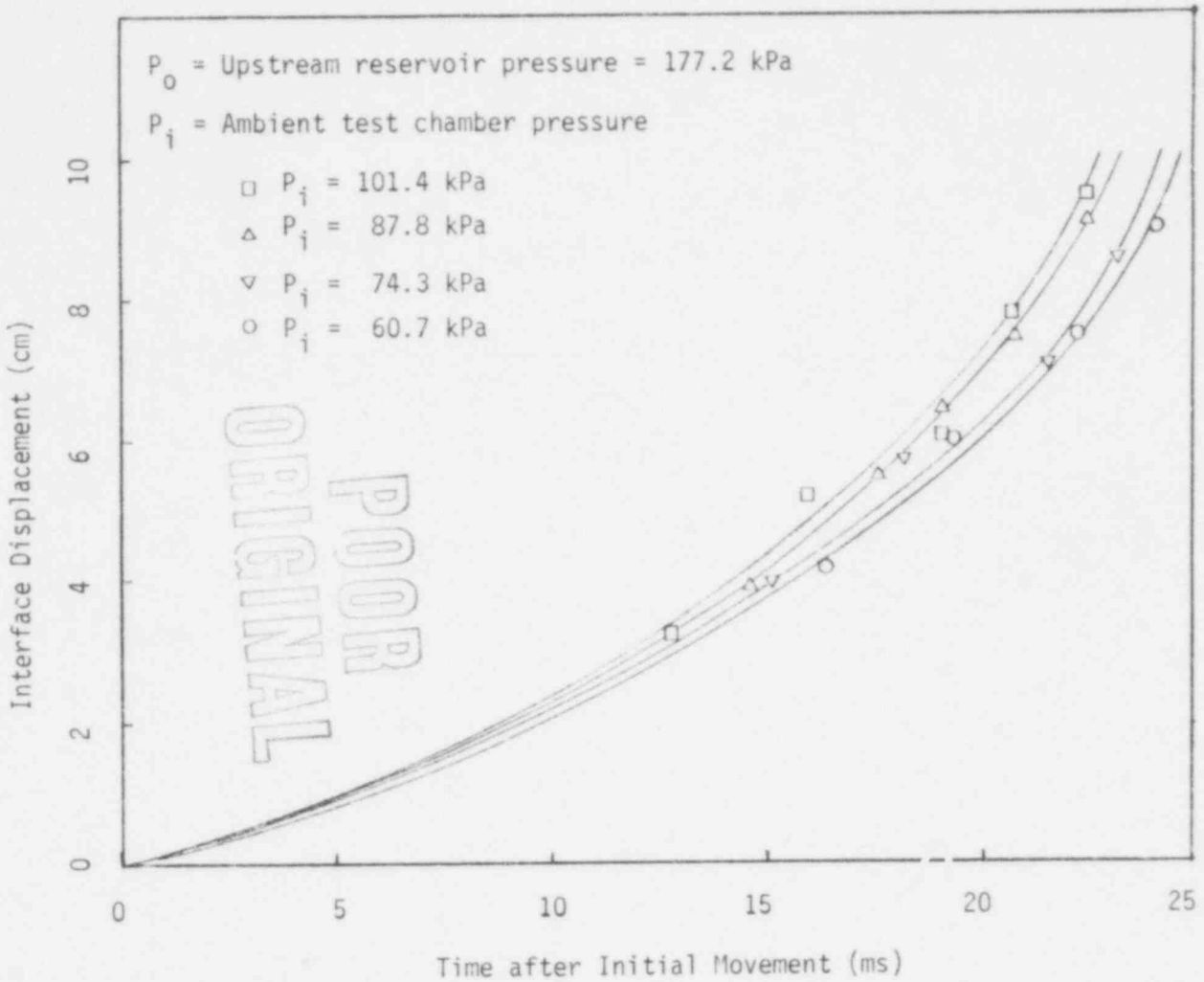

Figure D.2. Interface Motion during Vent Clearing for Air with 2.54 cm Diameter Orifice.

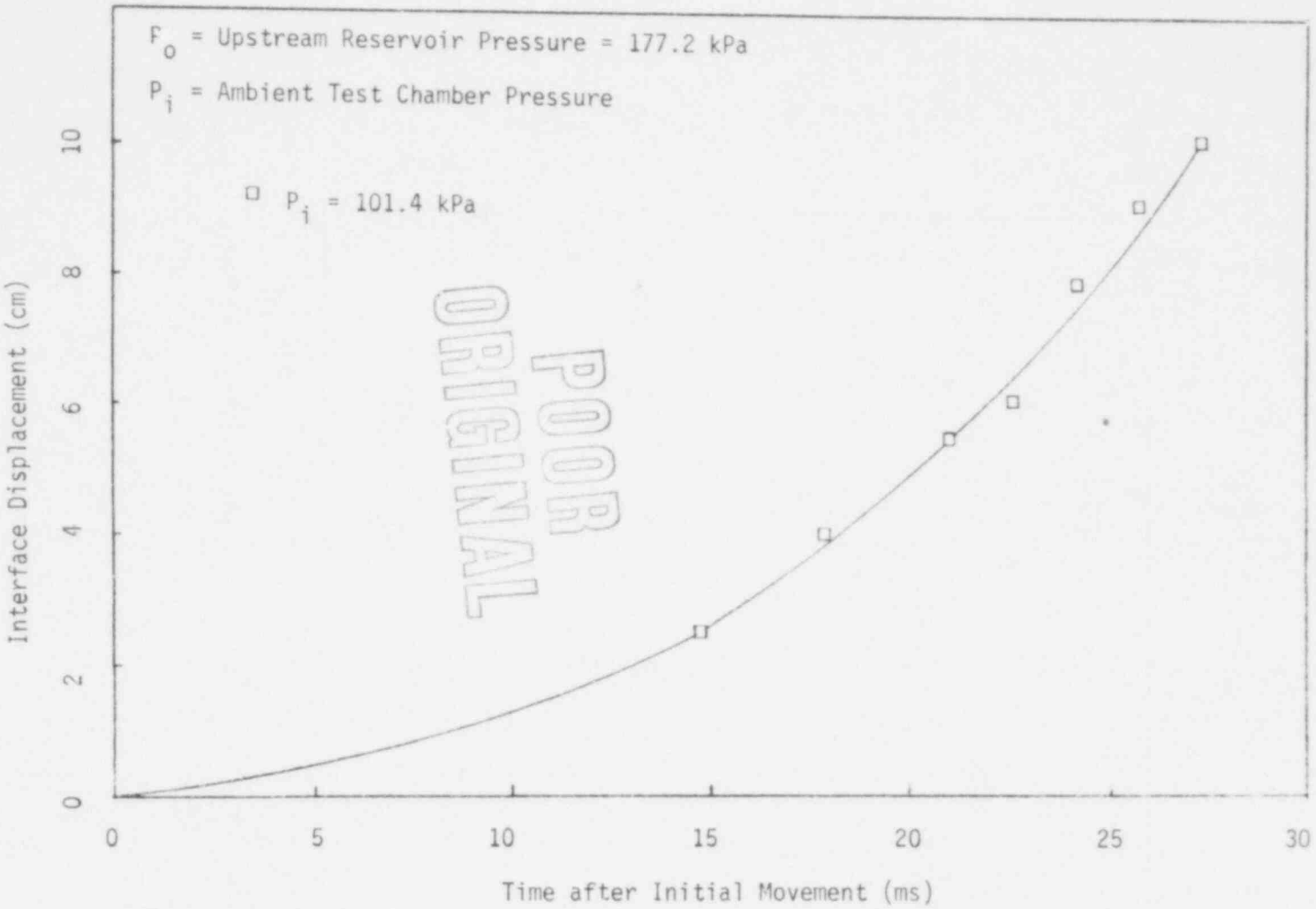

Figure D.3. Interface Motion during Vent Clearing for Air with 1.56 cm Diameter Orifice.

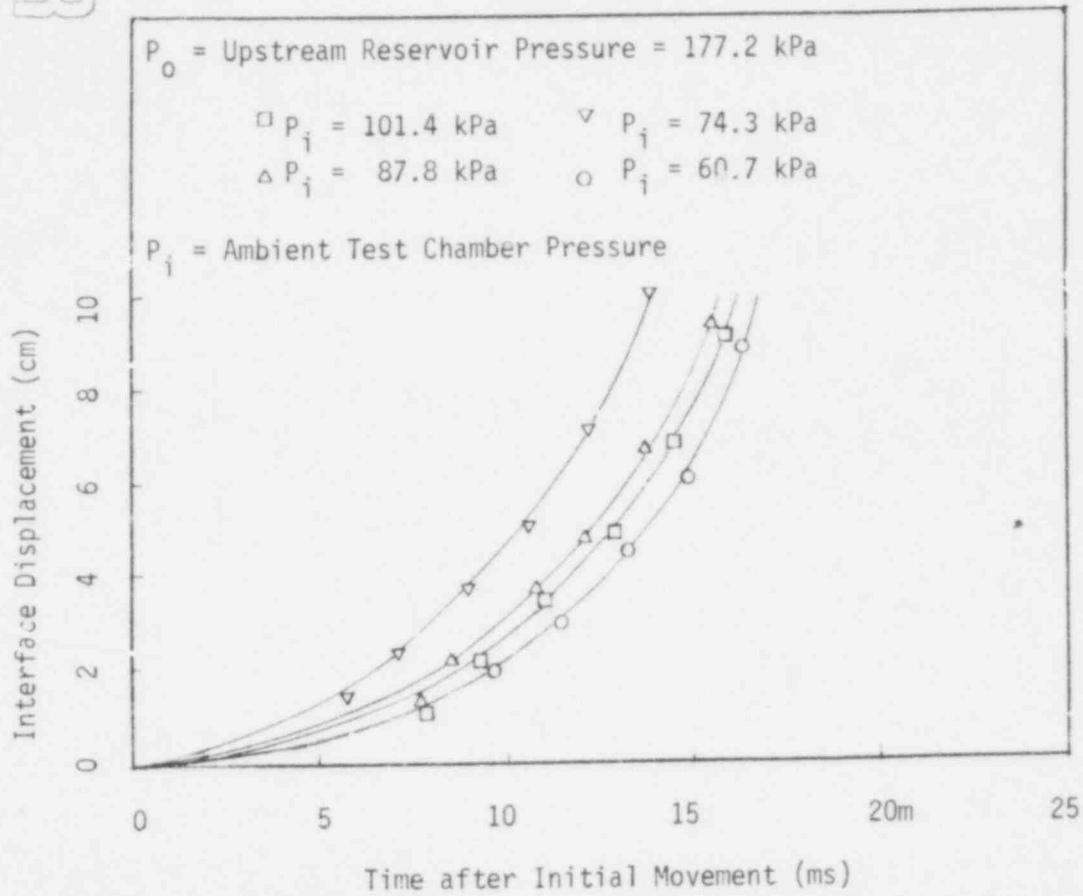

Figure D.4. Interface Motion during Vent Clearing for Helium without Orifice.

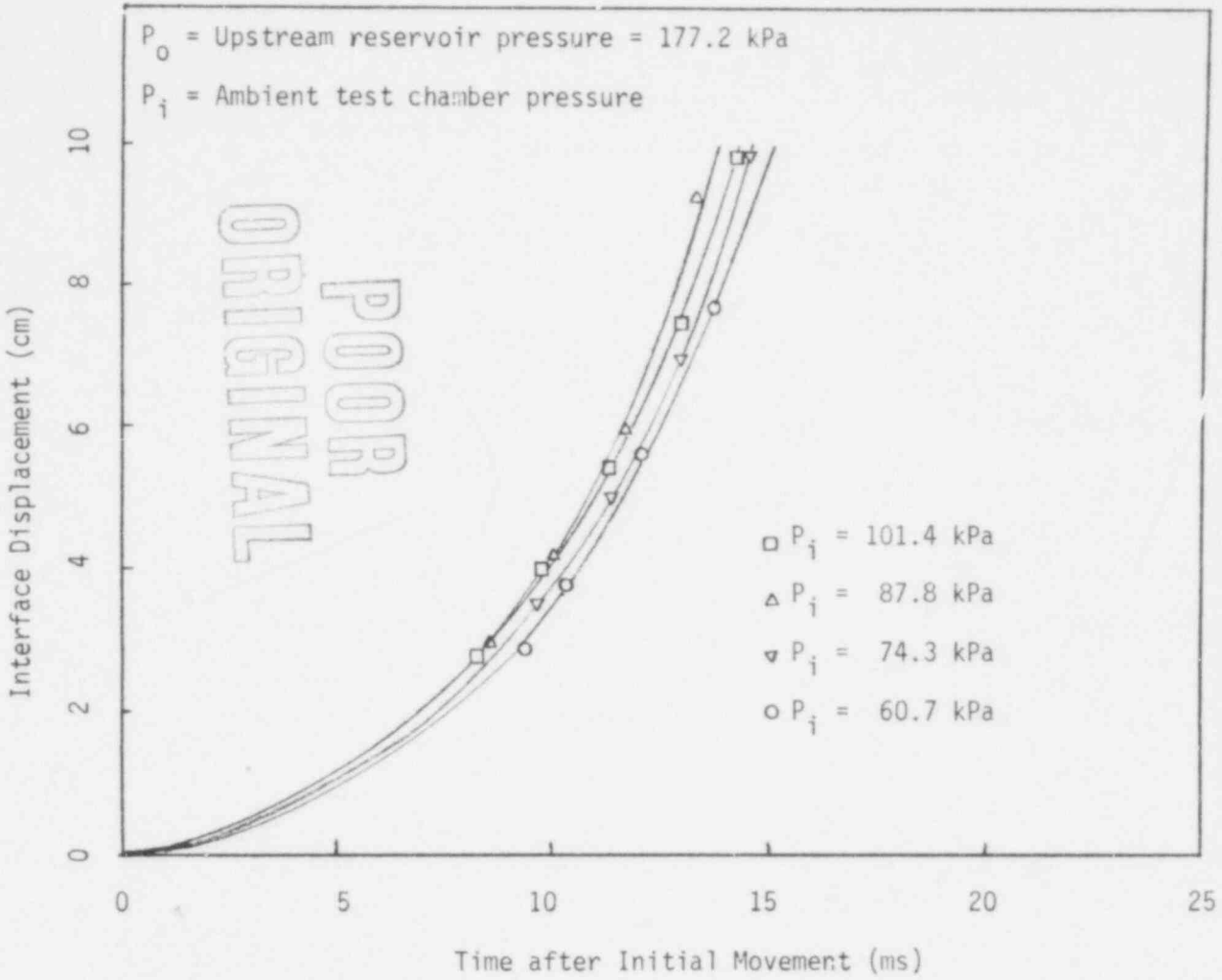

Figure D.5. Interface Motion during Vent Clearing for Helium with 2.54 cm Diameter Orifice.

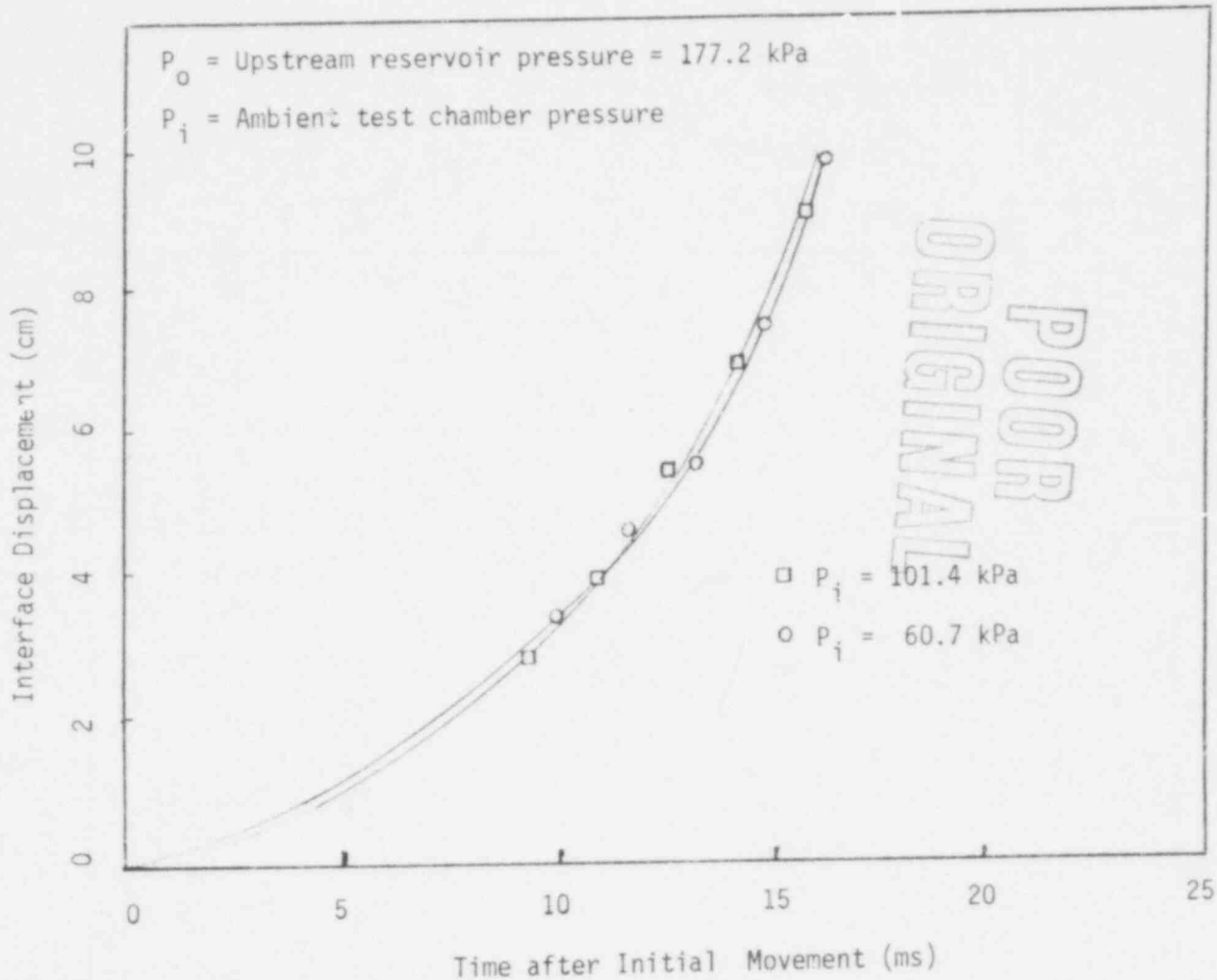

Figure D.6. Interface Motion during Vent Clearing for Helium with 1.56 cm Diameter Orifice.

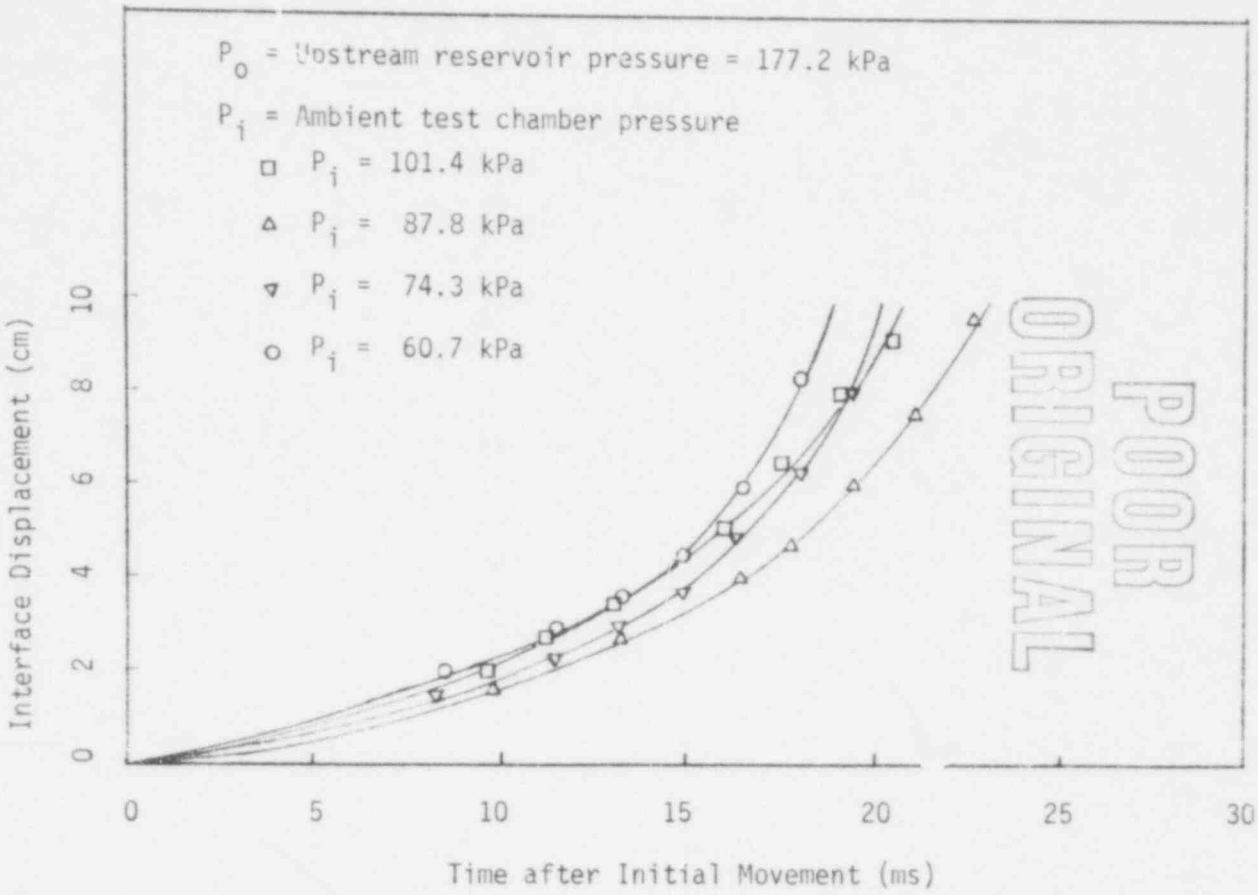

Figure 2.7. Interface Motion during Vent Clearing for Argon without Orifice.

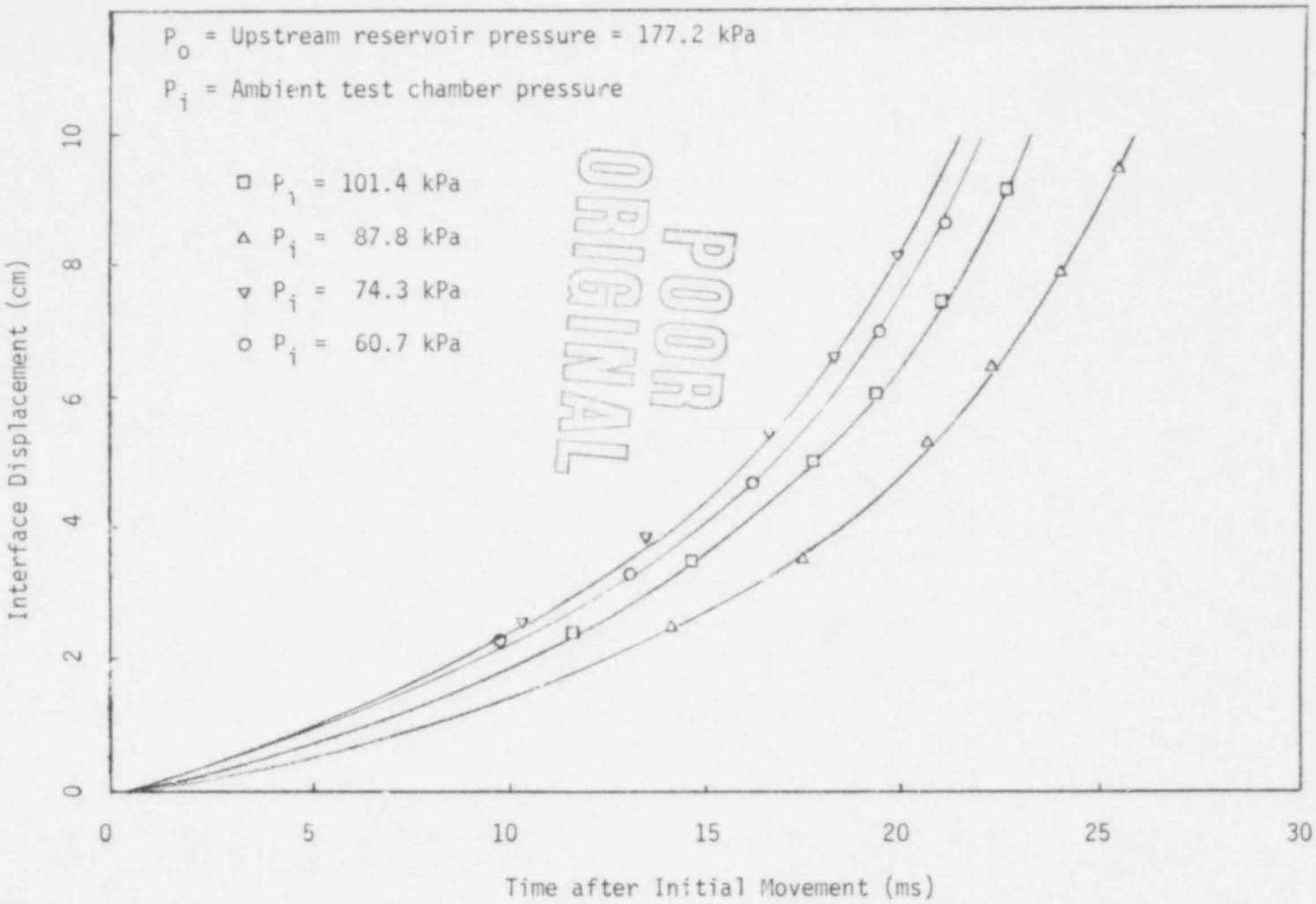

Figure D.8. Interface Motion during Vent Clearing for Argon with 2.54 cm Diameter Orifice.

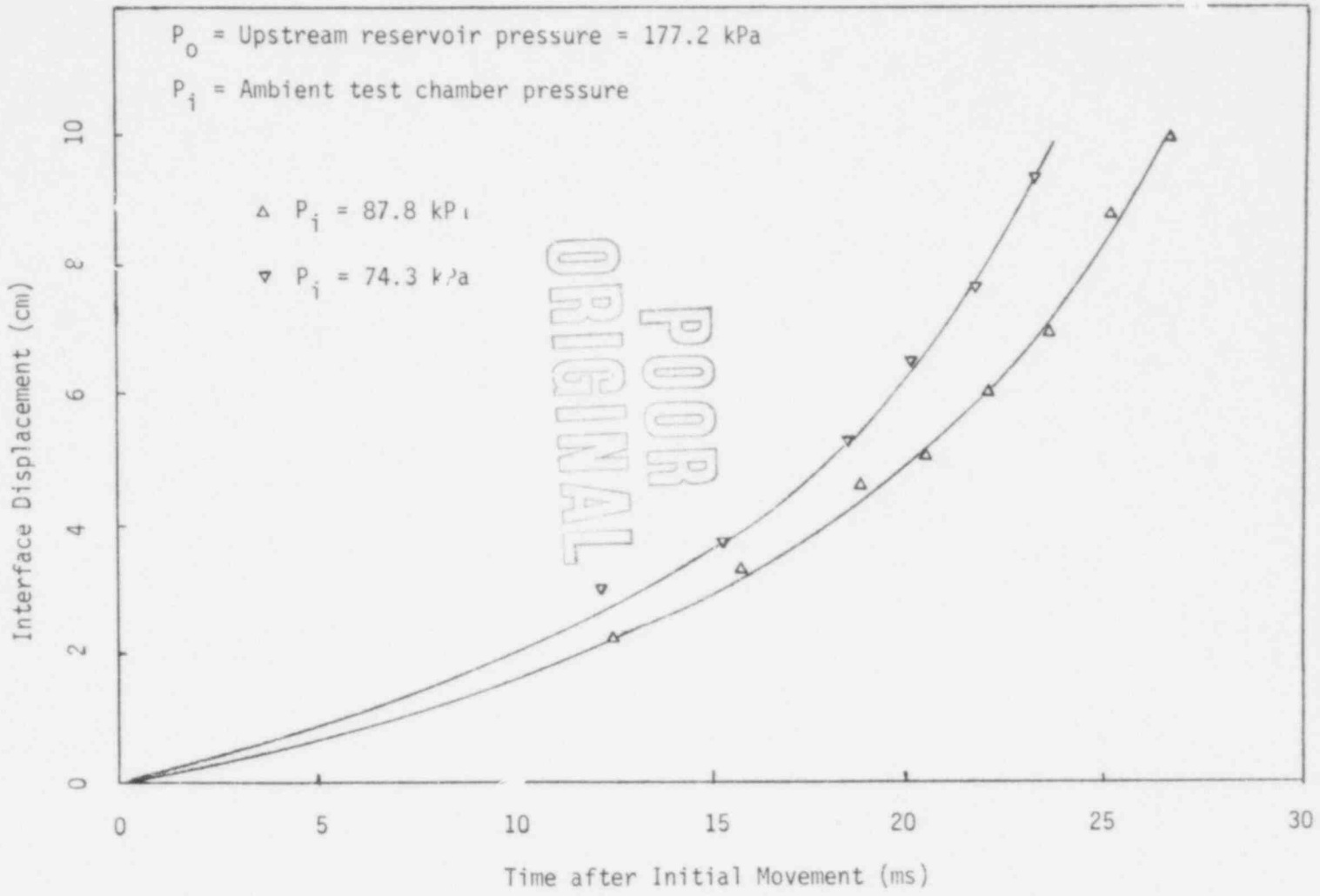

Figure D.9. Interface Motion during Vent Clearing for Argon with 1.56 cm Diameter Orifice.

Appendix E. Bubble Growth and Free Surface Swell Histories

In this Appendix, data on bubble growth and pool swelling are presented. The measurements were taken for three gases, three orifices, and four test chamber pressures. The submergence depth for all cases was 10 cm and the distance between the pipe exit and the test chamber bottom was 24 cm.

On Figures E.1 through E.33, the solid line represents the bubble contours and the free surface; the dotted line shows the splashing level. The numbers on the lines are the times in milliseconds after triggering.

The thirty-three cases of the experimental data are listed in the following table.

Pi = Ambient Test Chamber Pressure

Orifice	Gas / Pi	Air	He	Ar
NO ORIFICE	101.4 kPa	E-1	E-13	E-24
	87.8 kPa	E-2	E-14	E-25
	74.3 kPa	E-3	E-15	E-26
	60.7 kPa	E-4	E-16	E-27
2.54 cm Diameter Orifice	101.4 kPa	E-5	E-17	E-28
	87.8 kPa	E-6	E-18	E-29
	74.3 kPa	E-7	E-19	E-30
	60.7 kPa	E-8	E-20	E-31
1.56 cm Diameter Orifice	101.4 kPa	E-9	E-21	
	87.8 kPa	E-10		E-32
	74.3 kPa	E-11	E-22	E-33
	60.7 kPa	E-12	E-23	

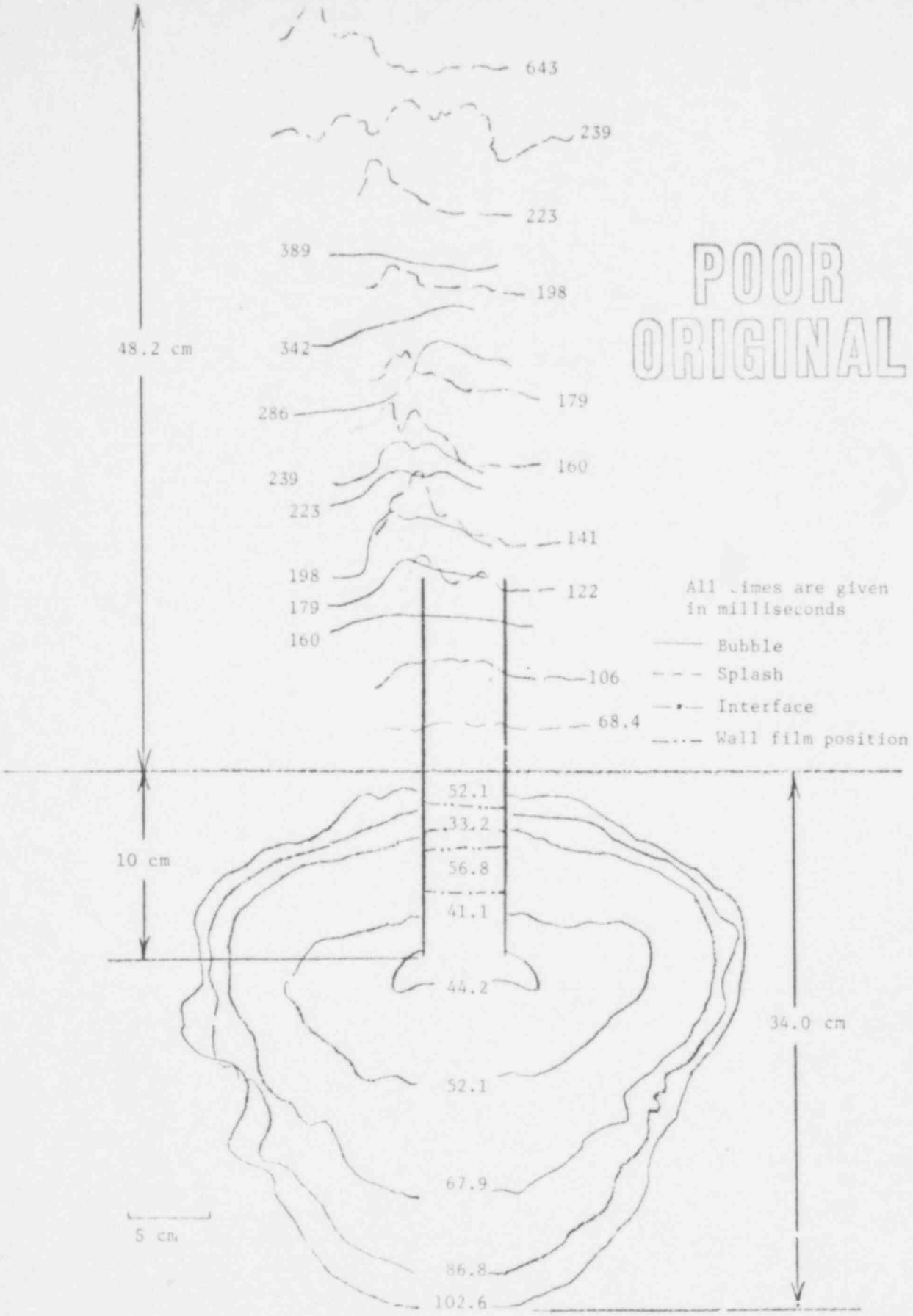

Fig. E.1 Bubble Growth and Free Surface Swelling Response Histories for Air without Orifice. Ambient Test Chamber Pressure 101.4 kPa.

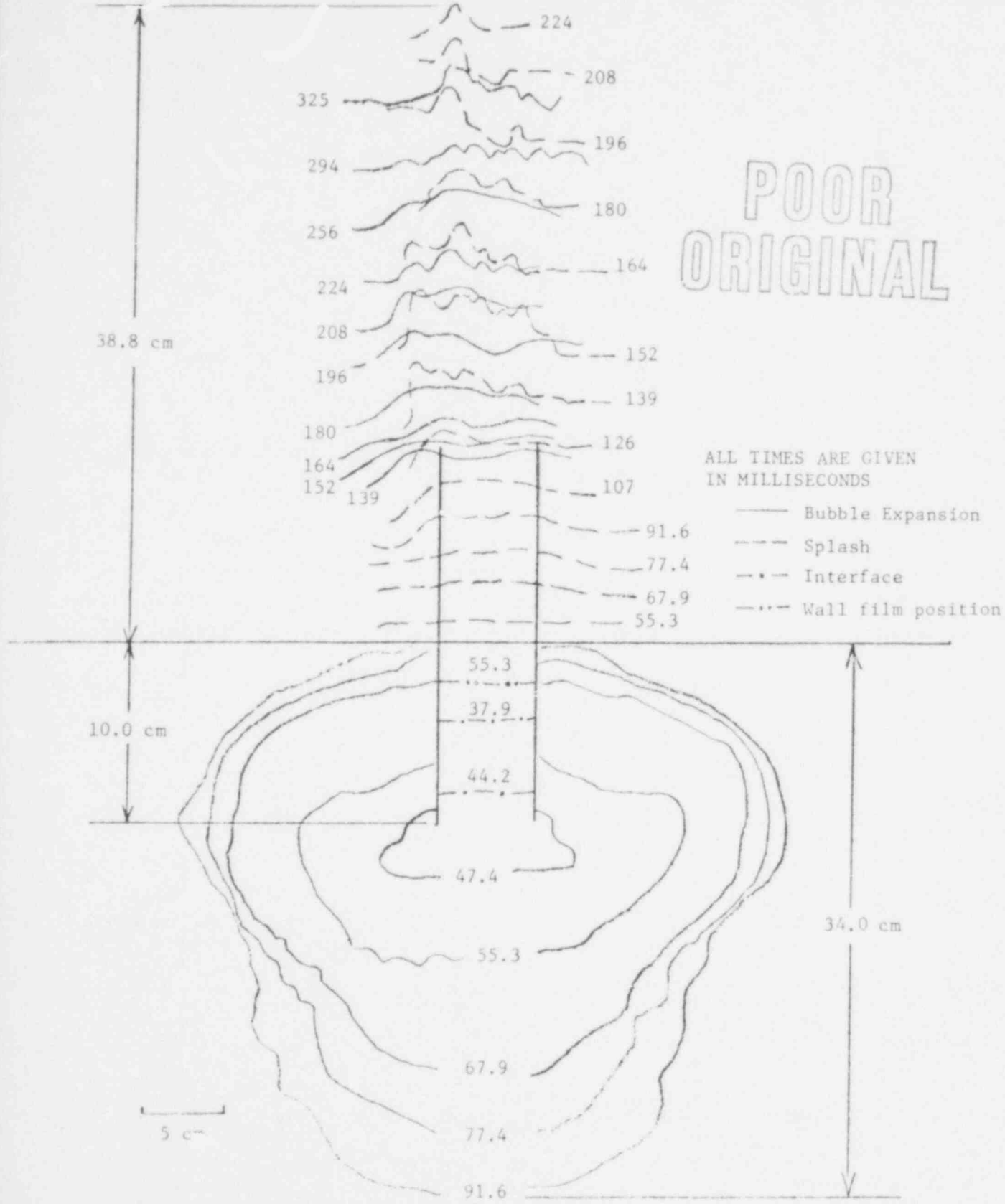

Figure E.2 Bubble Growth and Free Surface Swelling Response Histories for Air without Orifice. Ambient Test Chamber Pressure 87.8 K Pa.

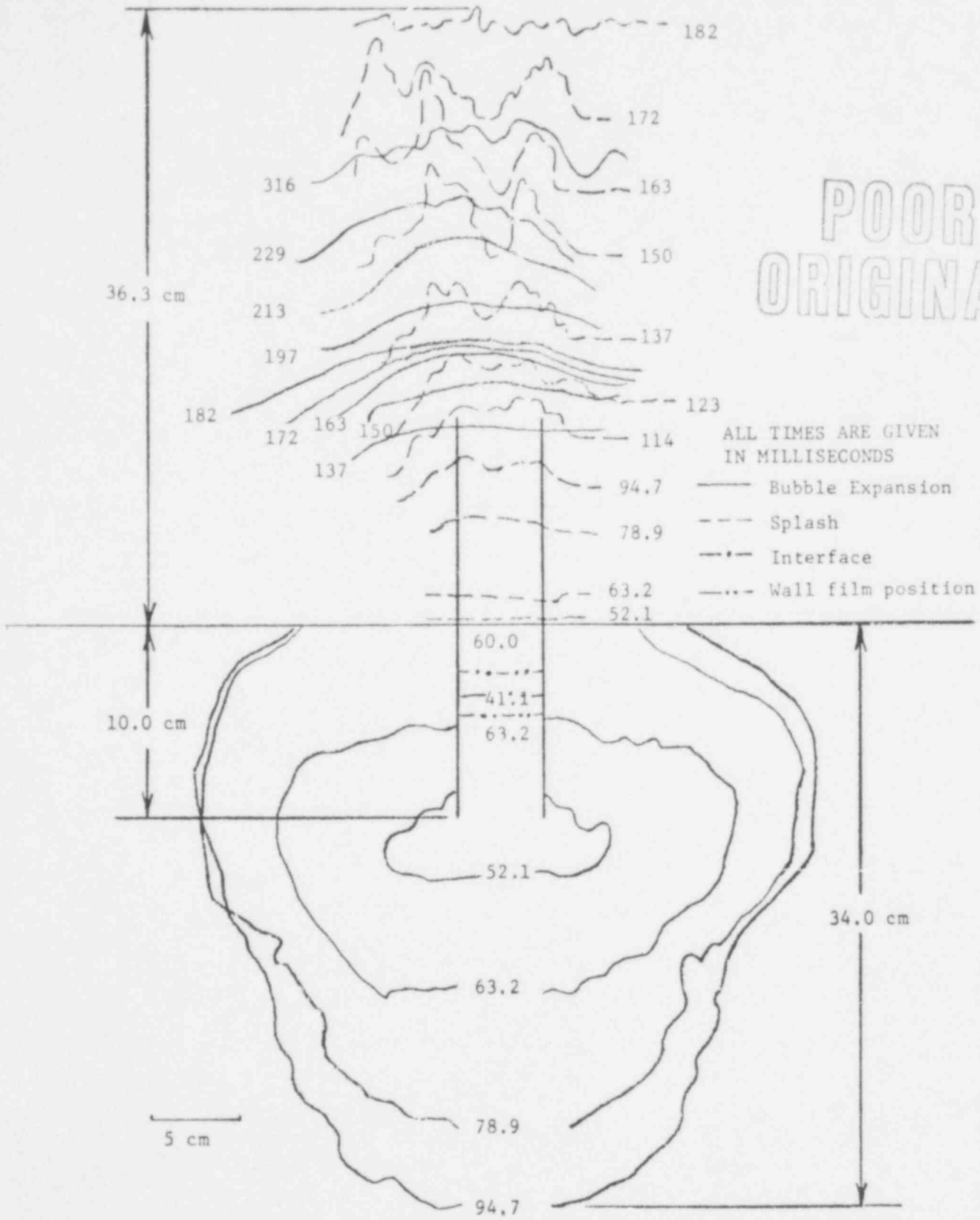

Figure E.3 Bubble Growth and Free Surface Swelling Response Histories for Air without Orifice. Ambient Test Chamber Pressure 74.3 K Pa.

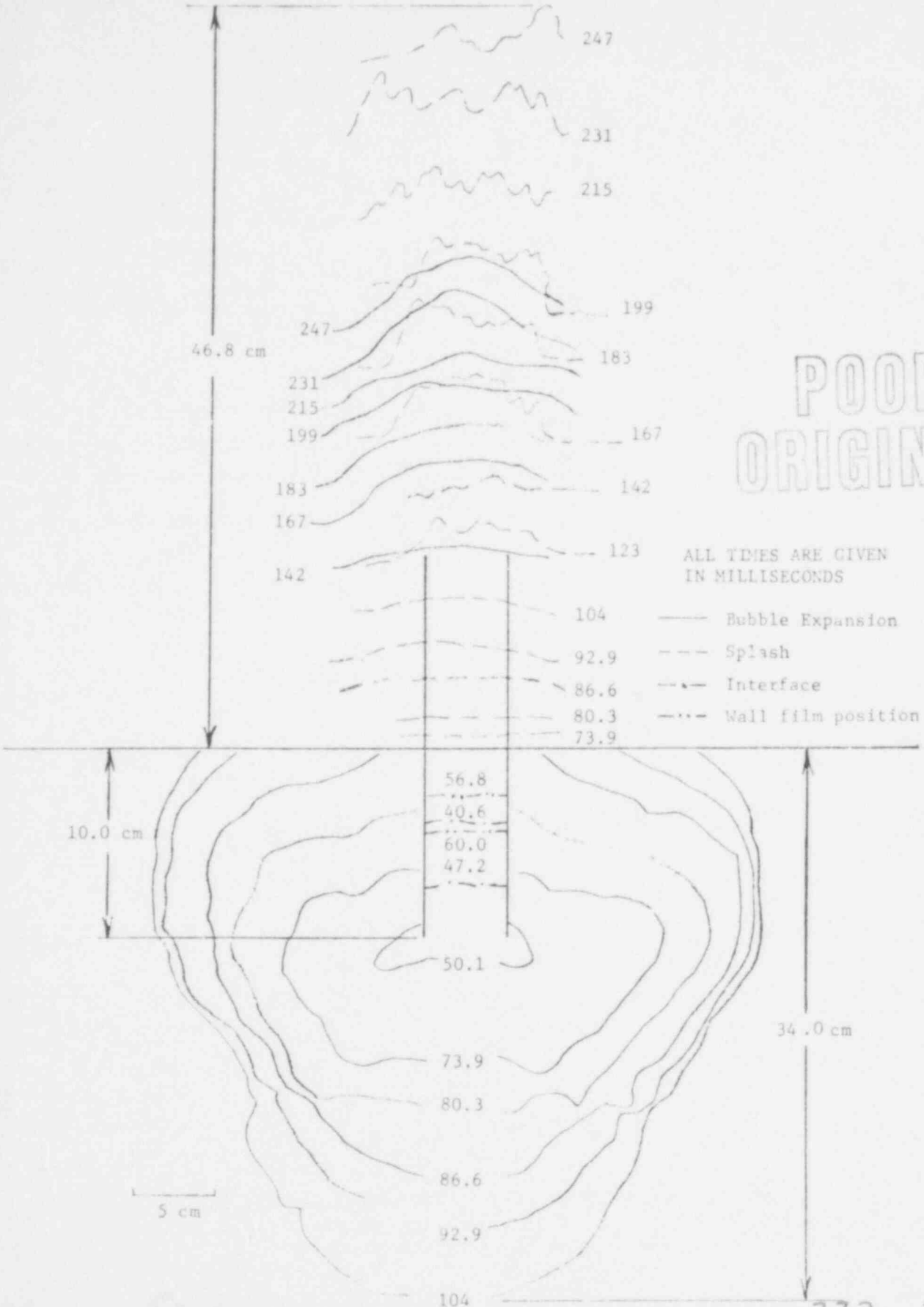

Fig.E.4 Bubble Growth and Free Surface Swelling Response Histories for Air without Orifice. Ambient Test Chamber Pressure 60.7 kPa.

732 276

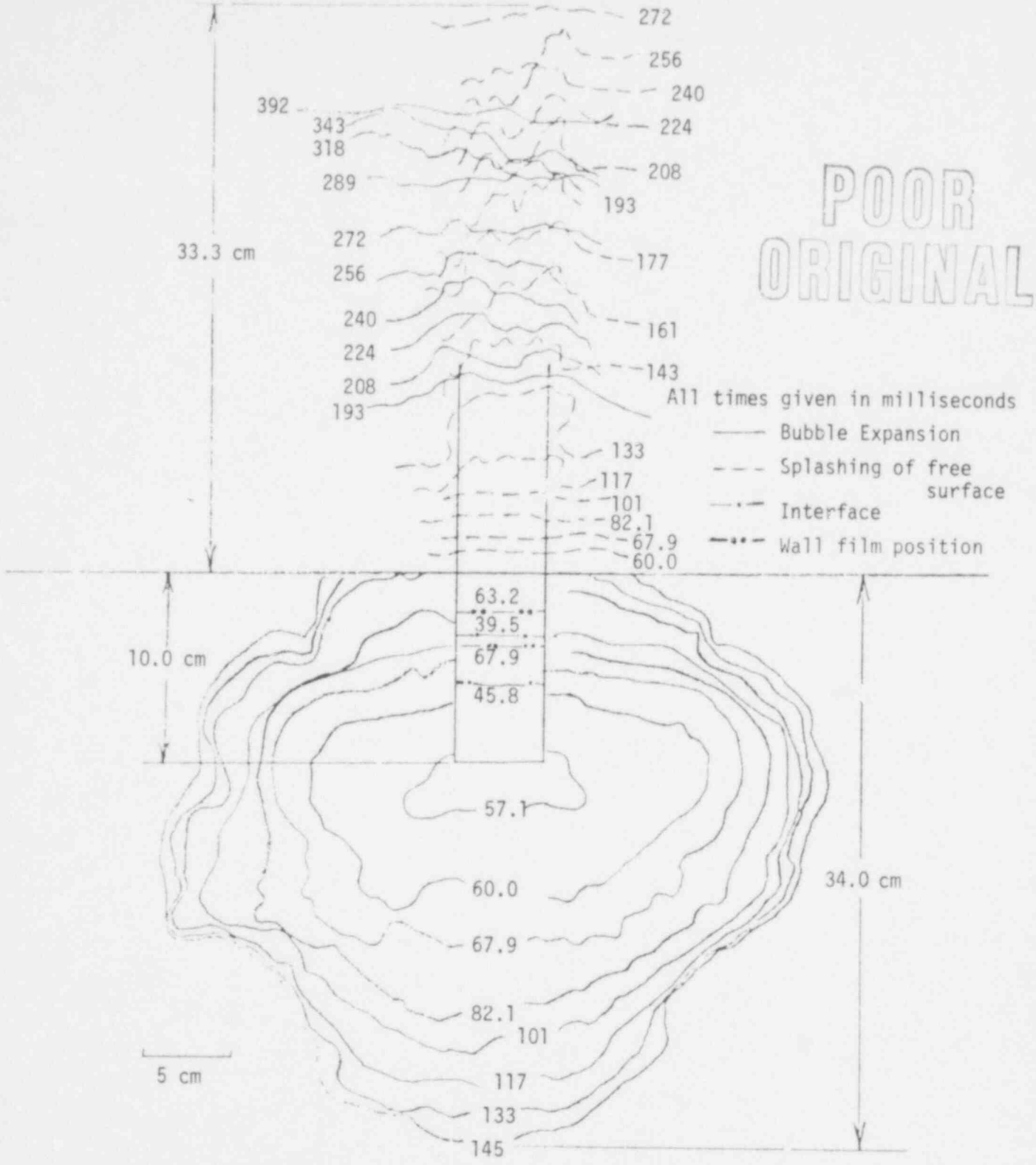

Fig. E.5 Bubble Growth and Free Surface Swelling Response Histories for Air with 2.54 cm Diameter Orifice, Upstream Reservoir Pressure = 177.2 kPa, Ambient Test Chamber Pressure = 101.4 kPa.

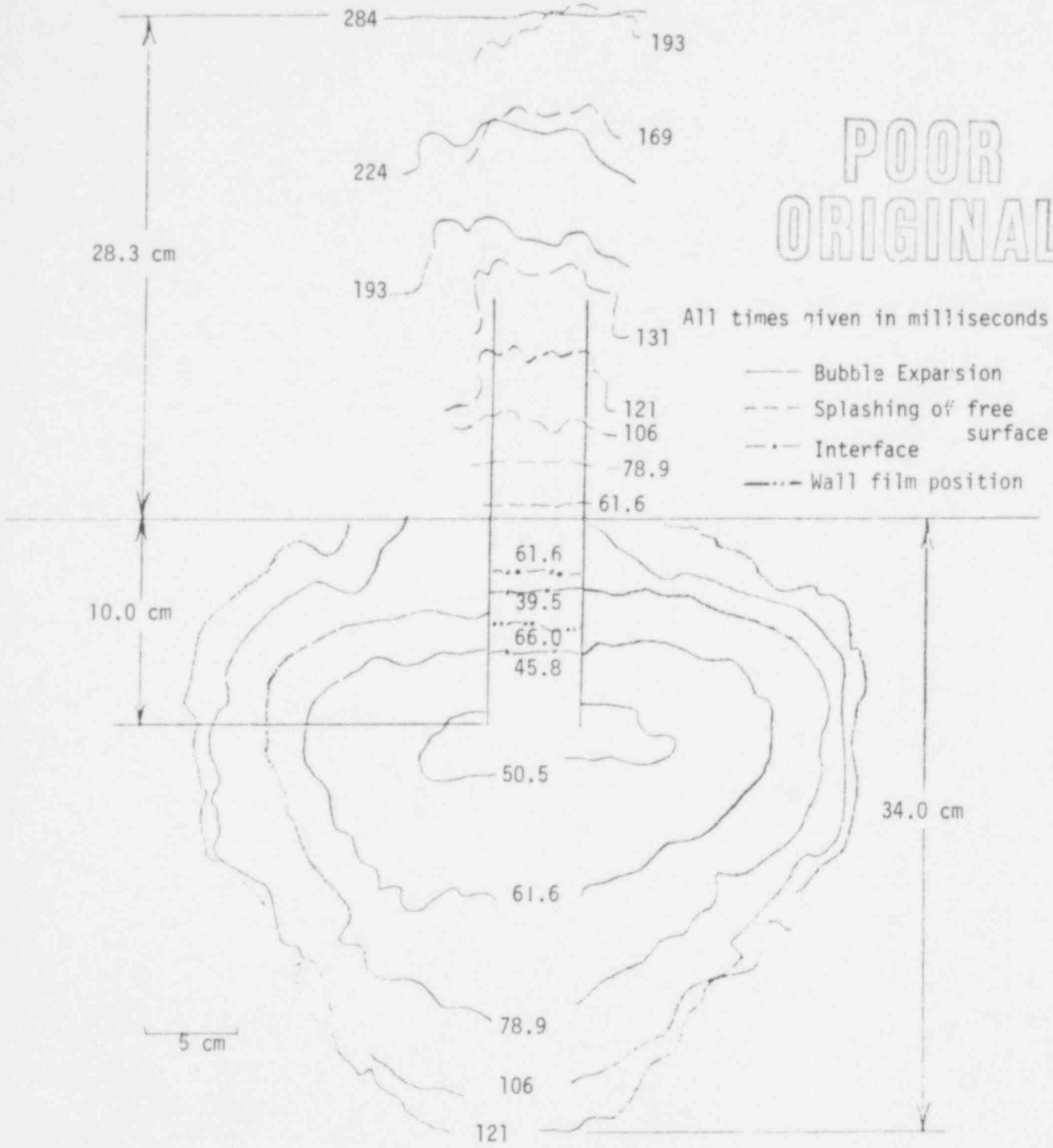

Fig. E.6 Bubble Growth and Free Surface Swelling Response Histories for Air with 2.54 cm Diameter Orifice, Upstream Reservoir Pressure = 177.2 kPa, Ambient Test Chamber Pressure = 87.8 kPa.

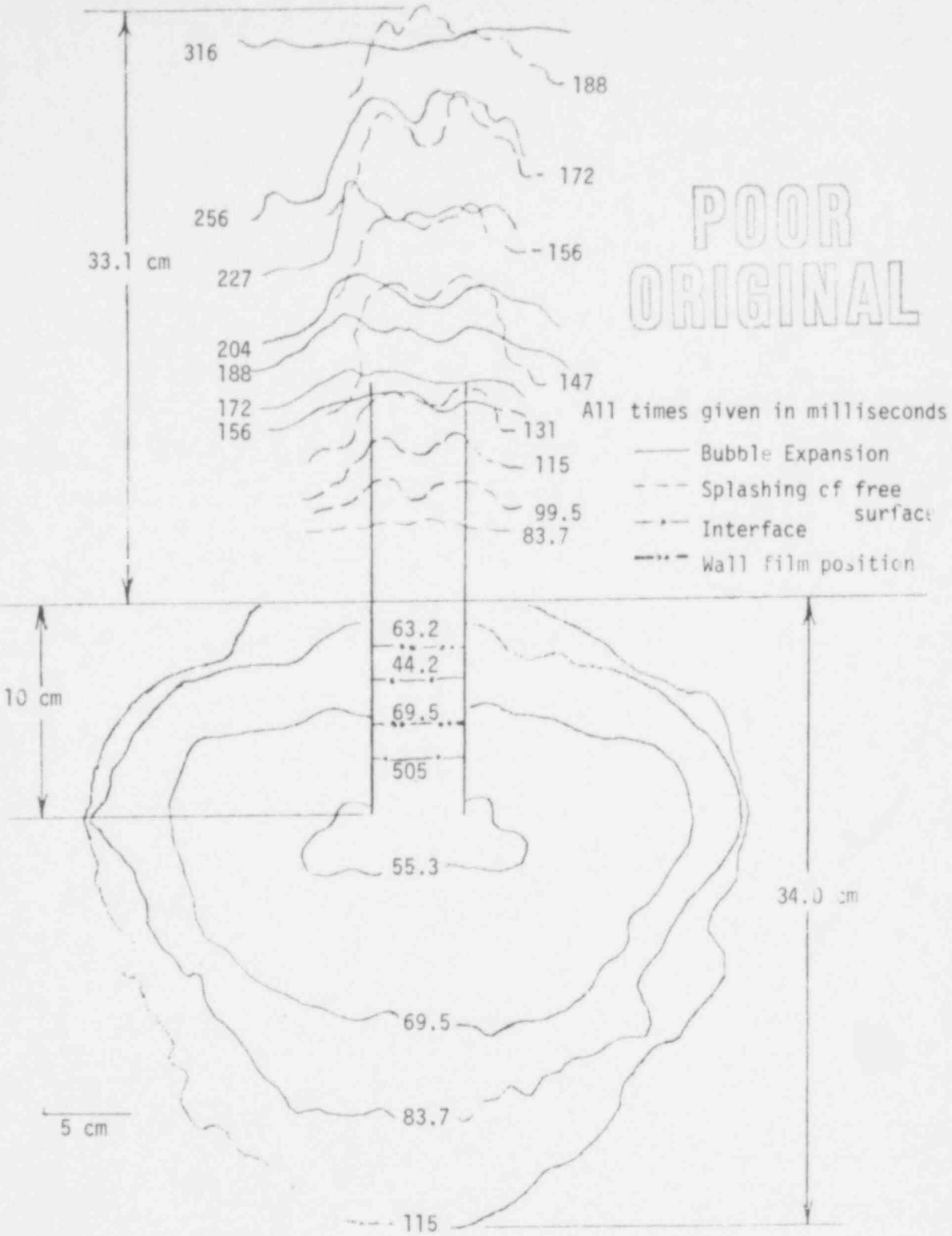

Fig. E.7 Bubble Growth and Free Surface Swelling Response Histories for Air with 2.54 cm Diameter Orifice, Upstream Reservoir Pressure = 177.2 kPa, Ambient Test Chamber Pressure 74.3 kPa.

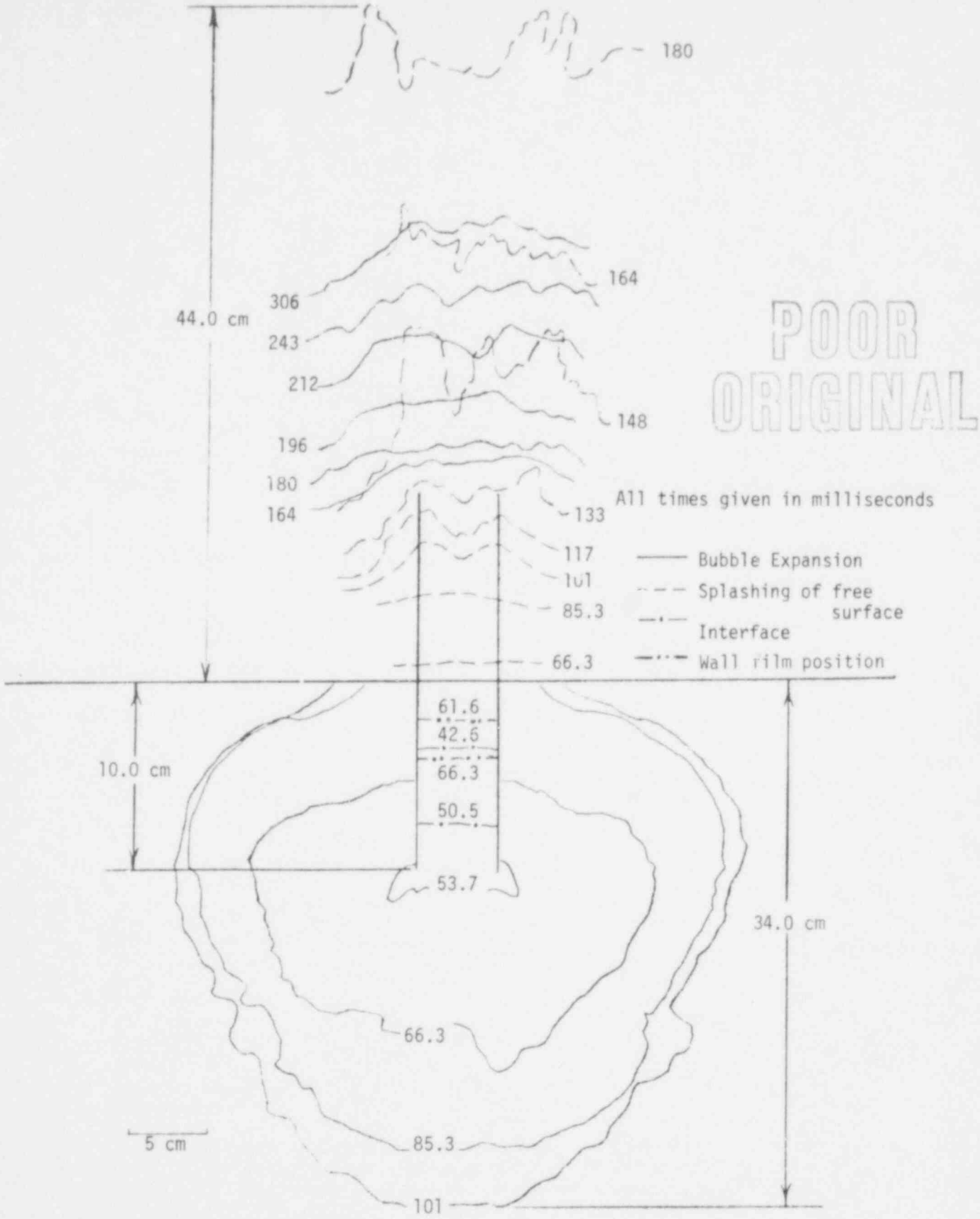

Fig. E.8 Bubble Growth and Free Surface Swelling Response Histories for Air with 2.54 cm Diameter Orifice, Upstream Reservoir Pressures = 177.2 kPa, Ambient Test Chamber Pressure = 60.7 kPa.

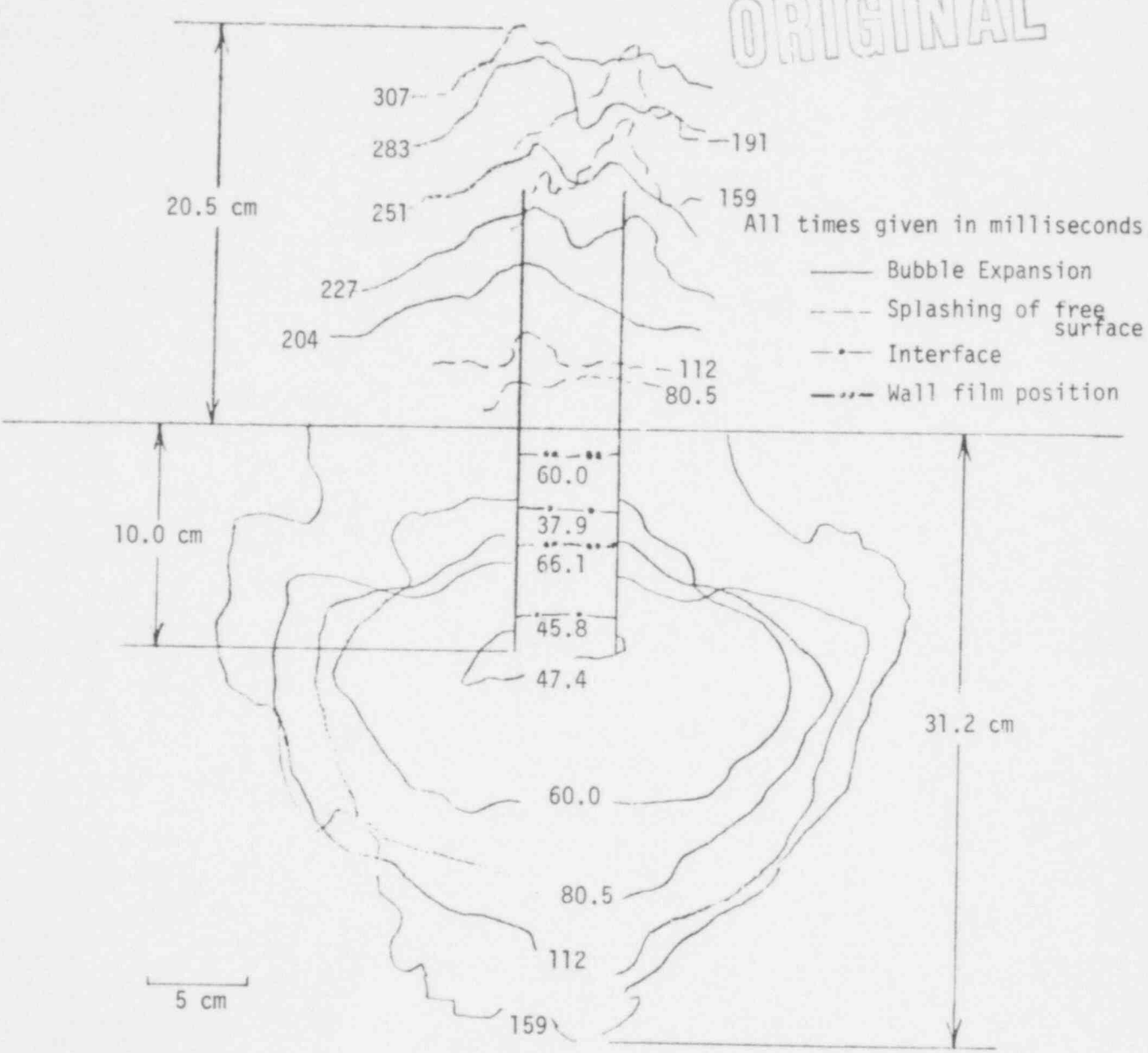

Fig. E.9 Bubble Growth and Free Surface Swelling Response Histories for Air with 1.56 cm Diameter Orifice, Upstream Reservoir Pressure = 177.2 kPa, Ambient Test Chamber Pressure = 101.4 kPa.

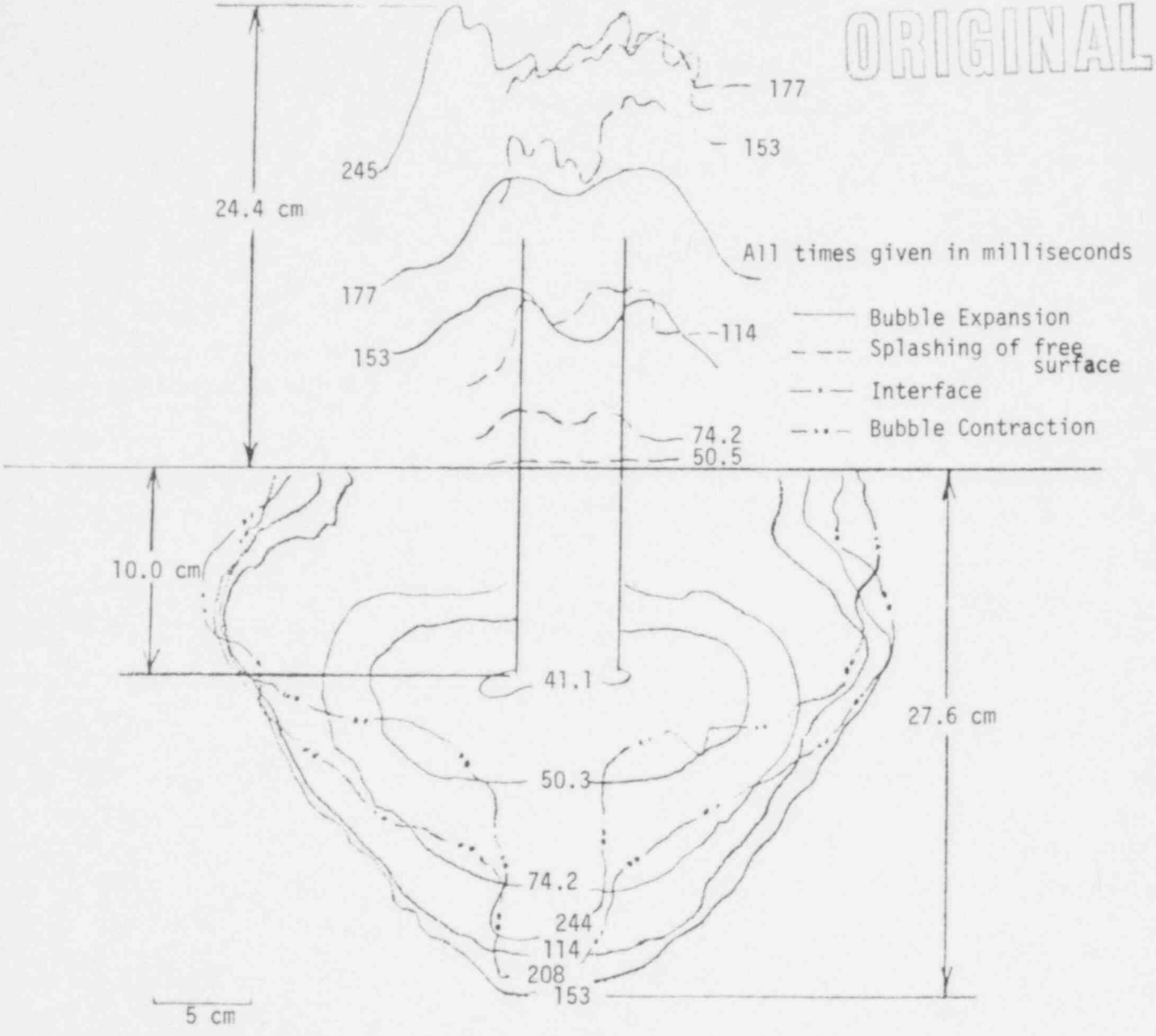

Fig. E.10 Bubble Growth and Free Surface Swelling Response Histories for Air with 1.56 cm Diameter Orifice, Upstream Reservoir Pressure = 177.2 kPa, Ambient Test Chamber Pressure = 87.8 kPa.

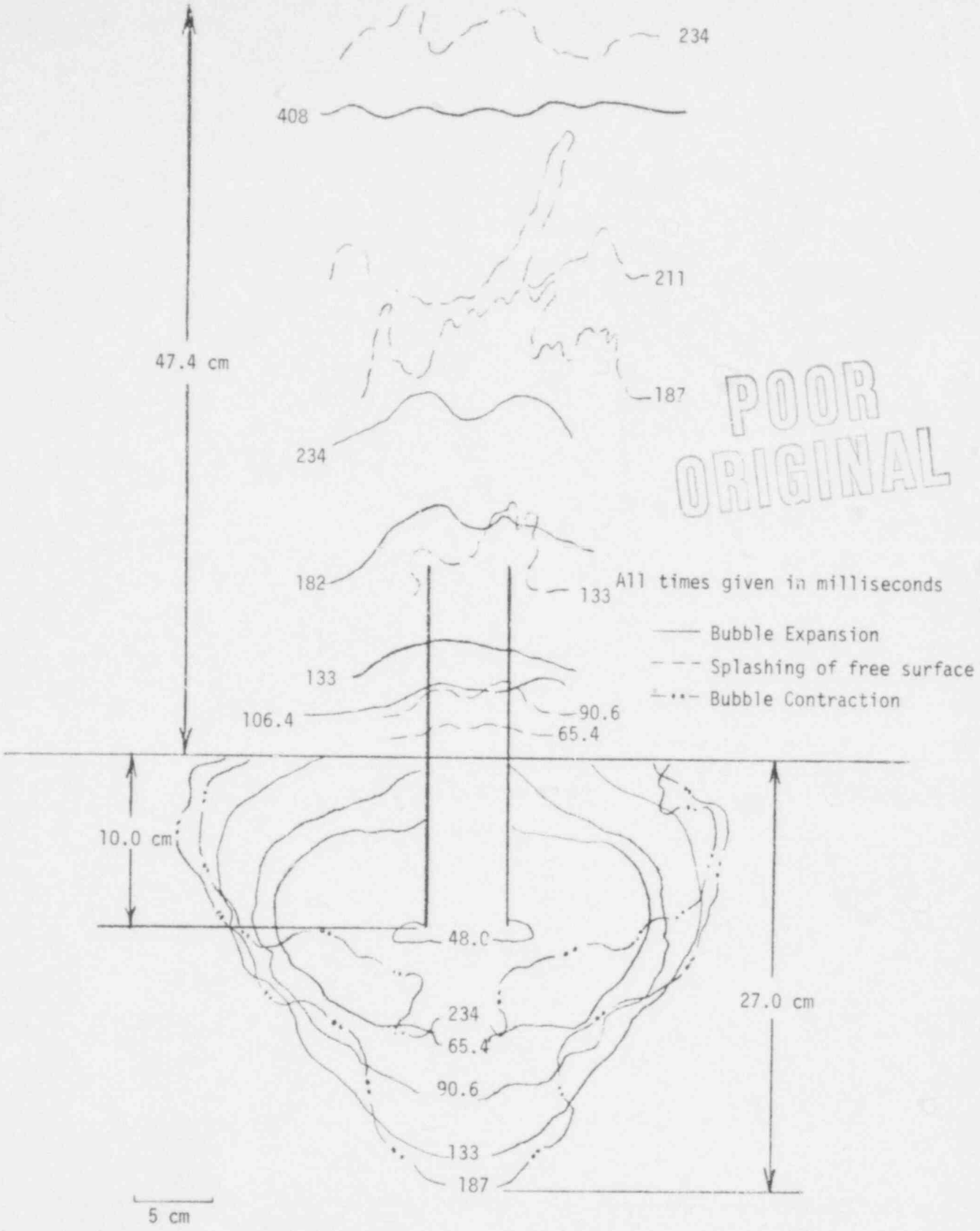

Fig. E.11. Bubble Growth and Free Surface Swelling Response Histories for Air with 1.56 cm Diameter Orifice, Upstream Reservoir Pressure = 177.2 kPa, Ambient Test Chamber Pressure = 74.3 kPa.

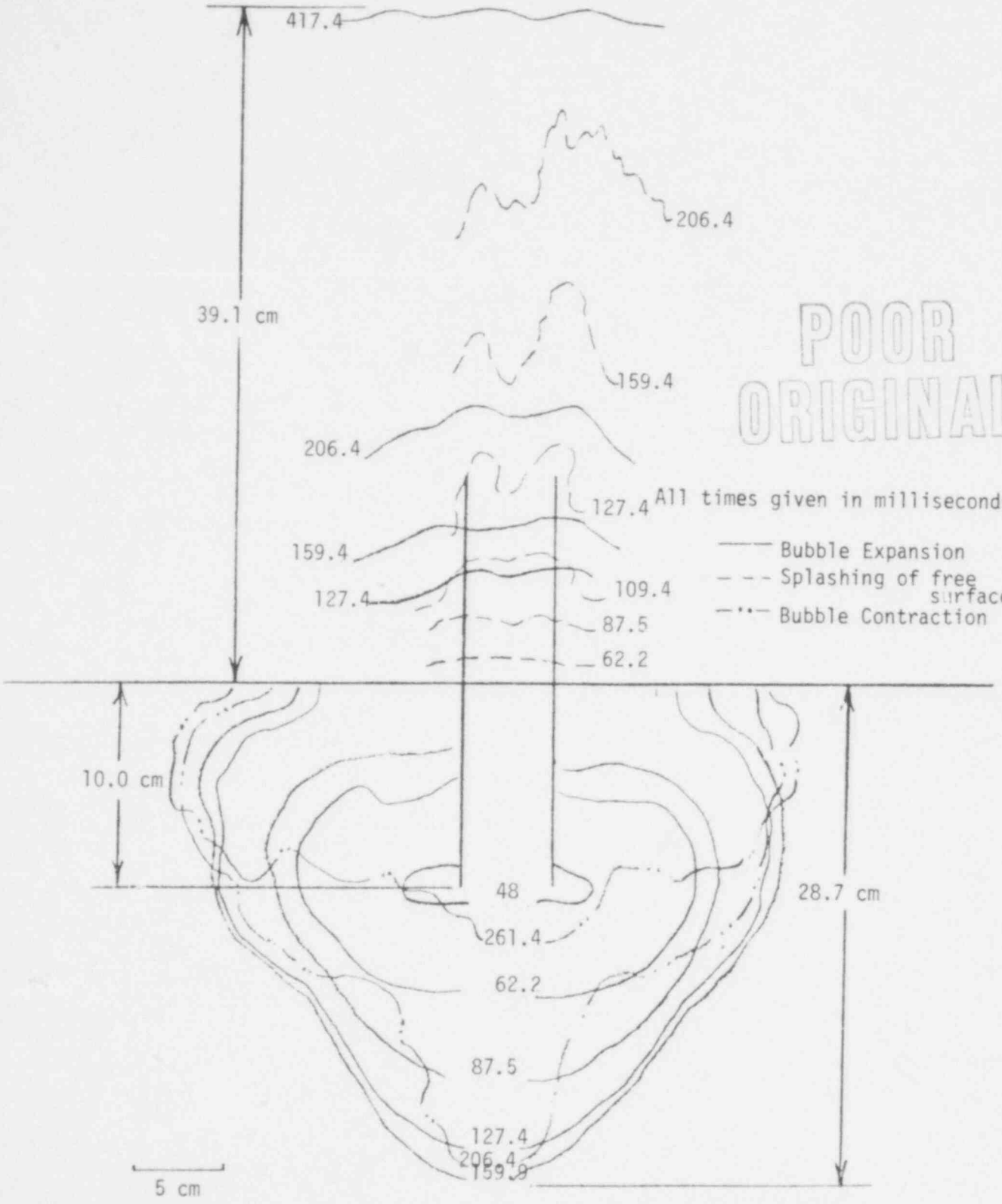

Fig. E.12 Bubble Growth and Free Surface Swelling Response Histories for Air with 1.56 cm Diameter Orifice, Upstream Pressure = 177.2 kPa, Ambient Test Chamber Pressure = 60.7 kPa.

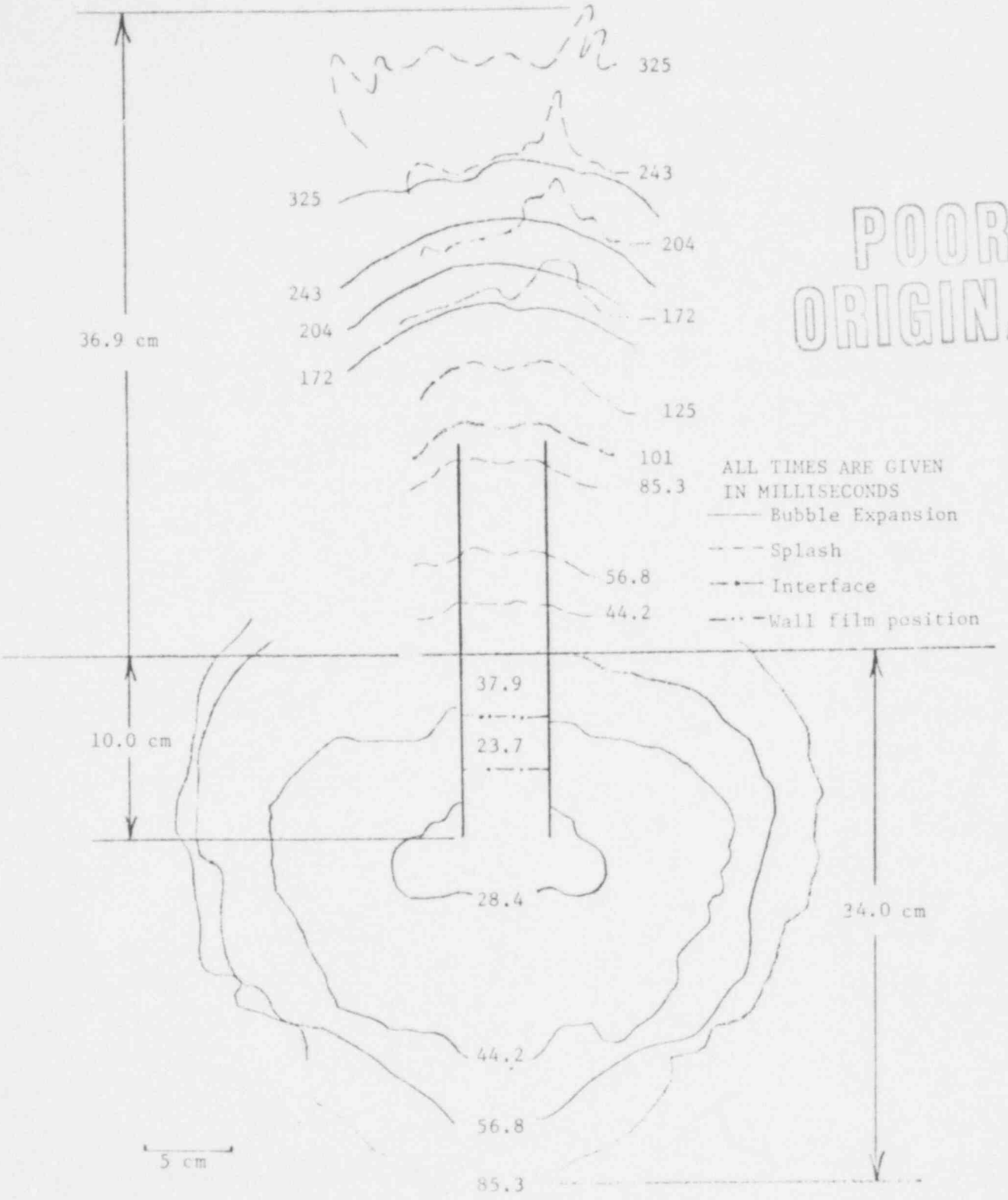

Figure E.13 Bubble Growth and Free Surface Swelling Response Histories for Helium without Orifice. Ambient Test Chamber Pressure 101.4 K Pa.

285

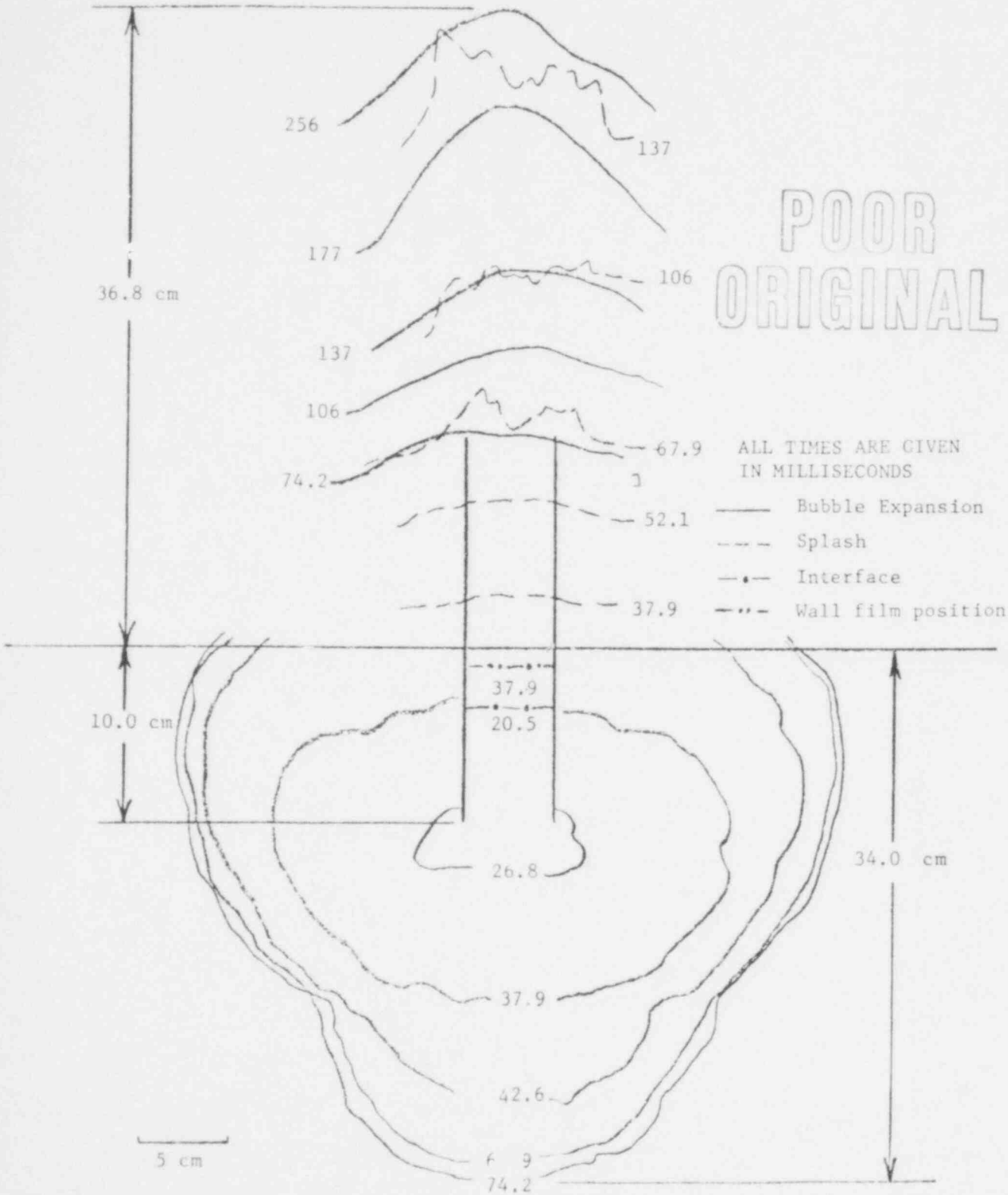

Figure E.14 Bubble Growth and Free Surface Swelling Response Histories for Helium without Orifice. Ambient Test Chamber Pressure 87.8 K Pa.

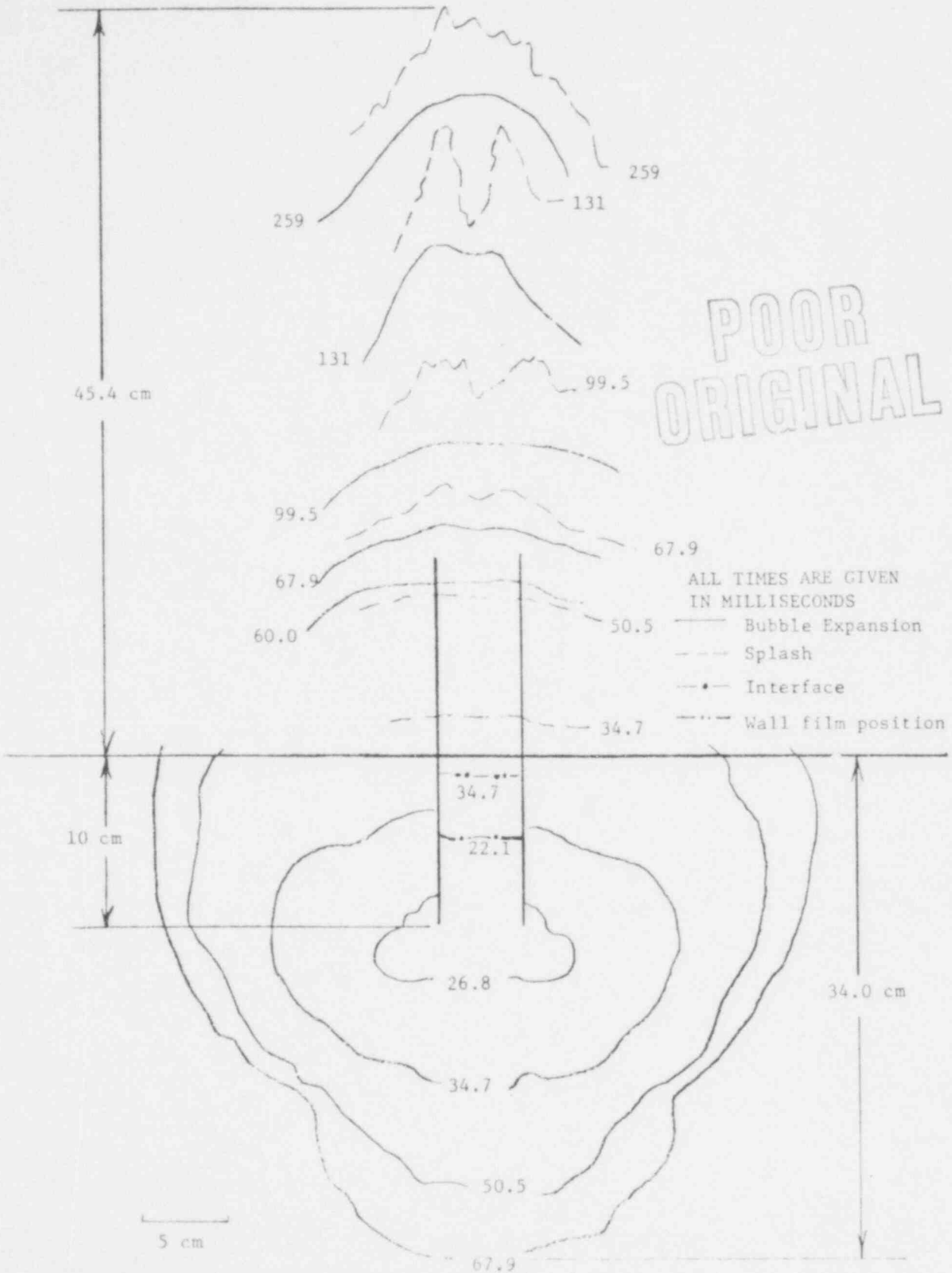

Figure E.15 Bubble Growth and Free Surface Swelling Response Histories for Helium without Orifice. Ambient Test Chamber Pressure 74.3 K Pa.

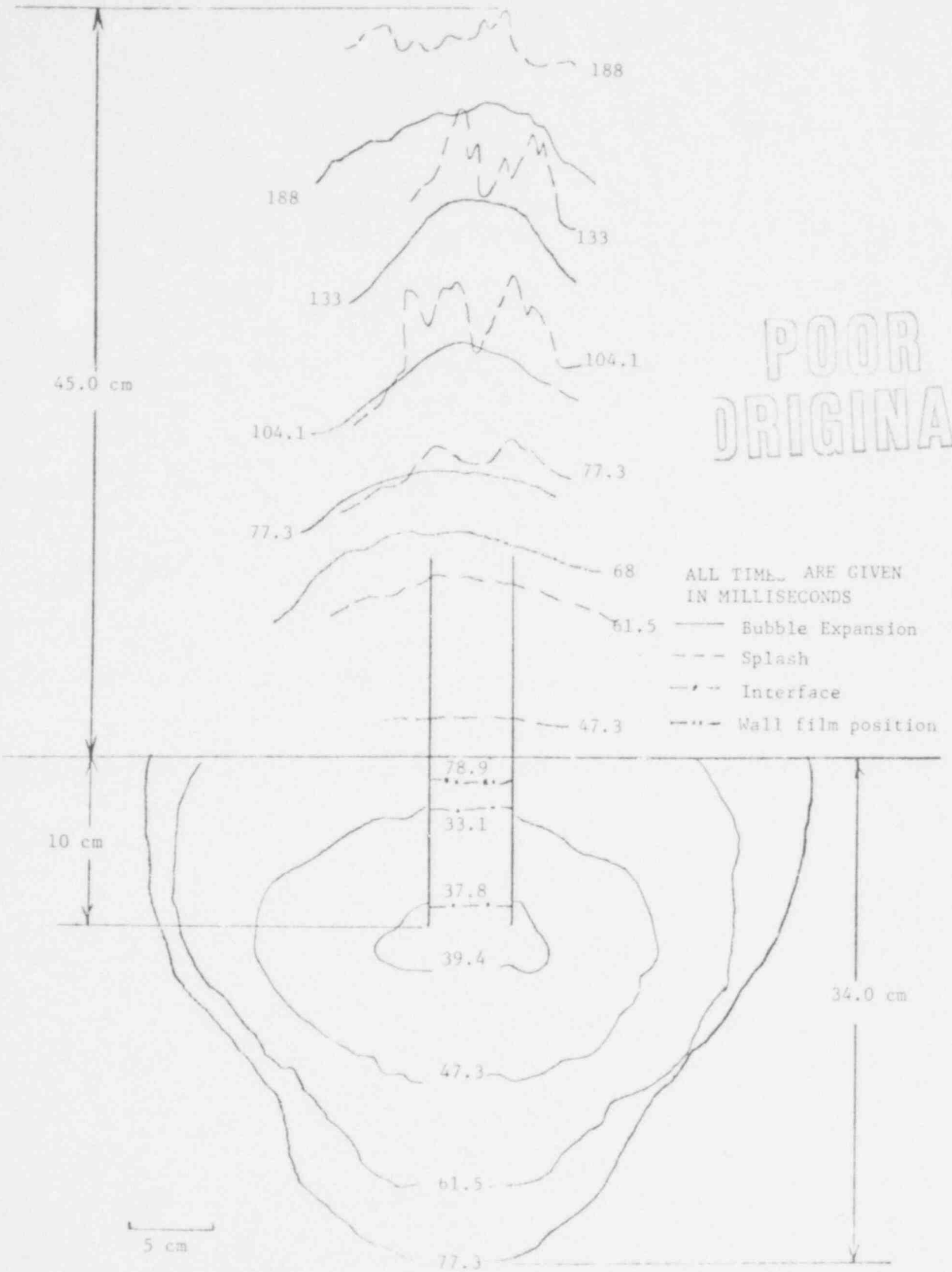

Figure E.16 Bubble Growth and Free Surface Swelling Response Histories for Helium without Orifice. Ambient Test Chamber Pressure 60.7 K Pa.

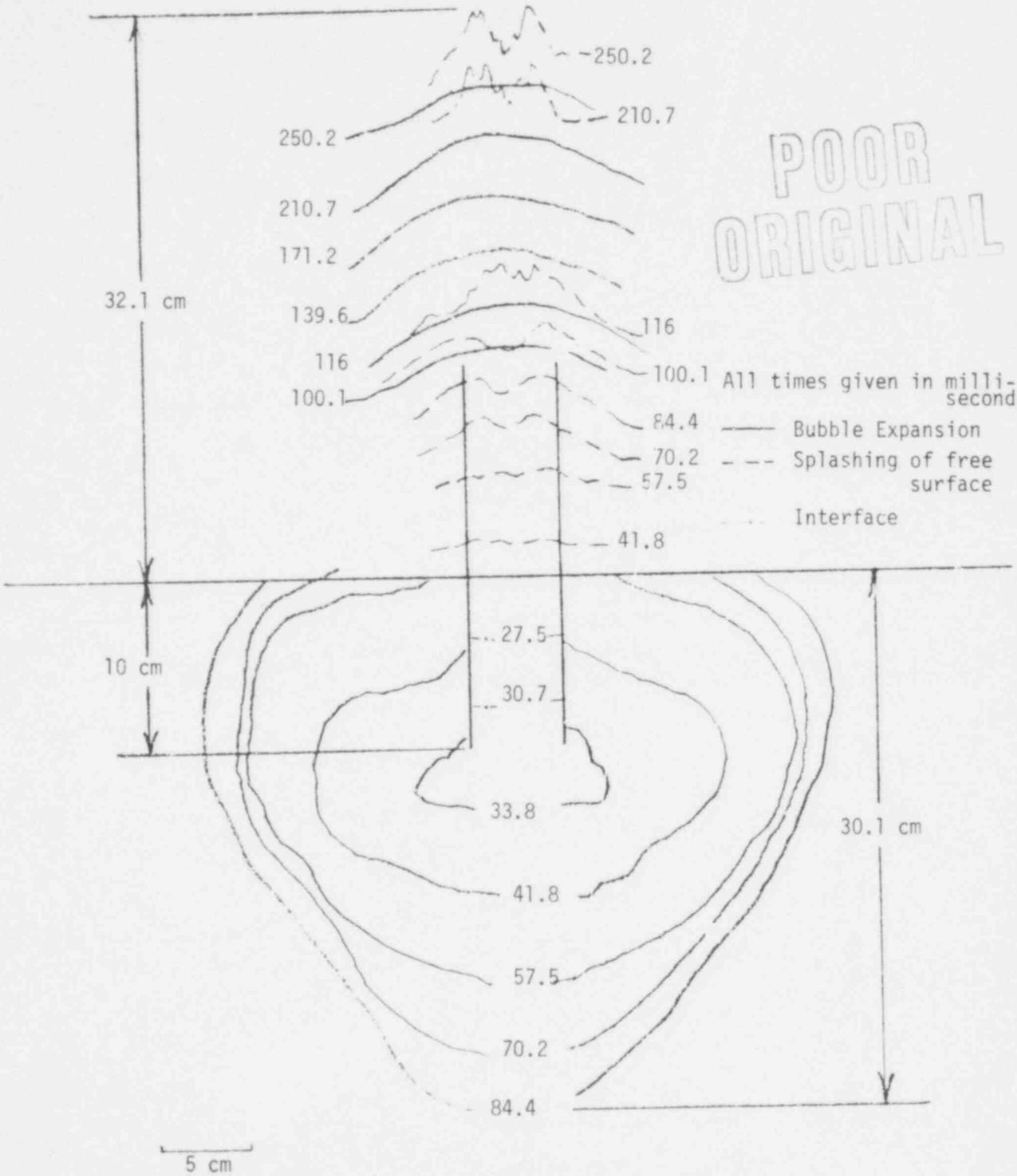

Figure E.17 Bubble Growth and Free Surface Swelling Response Histories for Helium with 2.54 cm Diameter Orifice, Upstream Reservoir Pressure = 177.2 kPa, Ambient Test Chamber Pressure = 101.4 kPa.

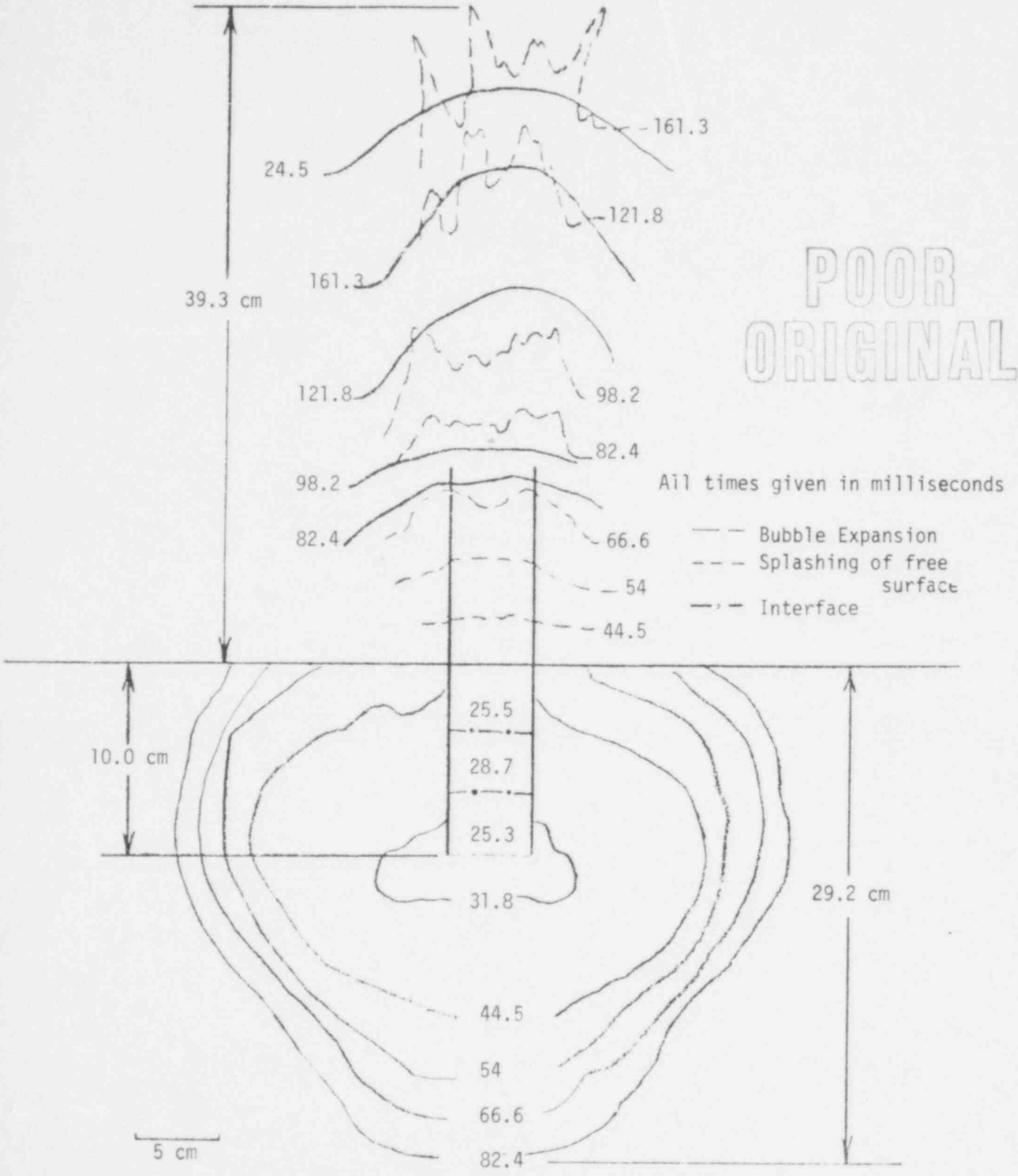

ure E. 18 Bubble Growth and Free Surface Swelling Response Histories for Helium with 2.54 cm Diameter Orifice, Upstream Reservoir Pressure = 177.2 kPa, Ambient Test Chamber Pressure = 87.8 kPa.

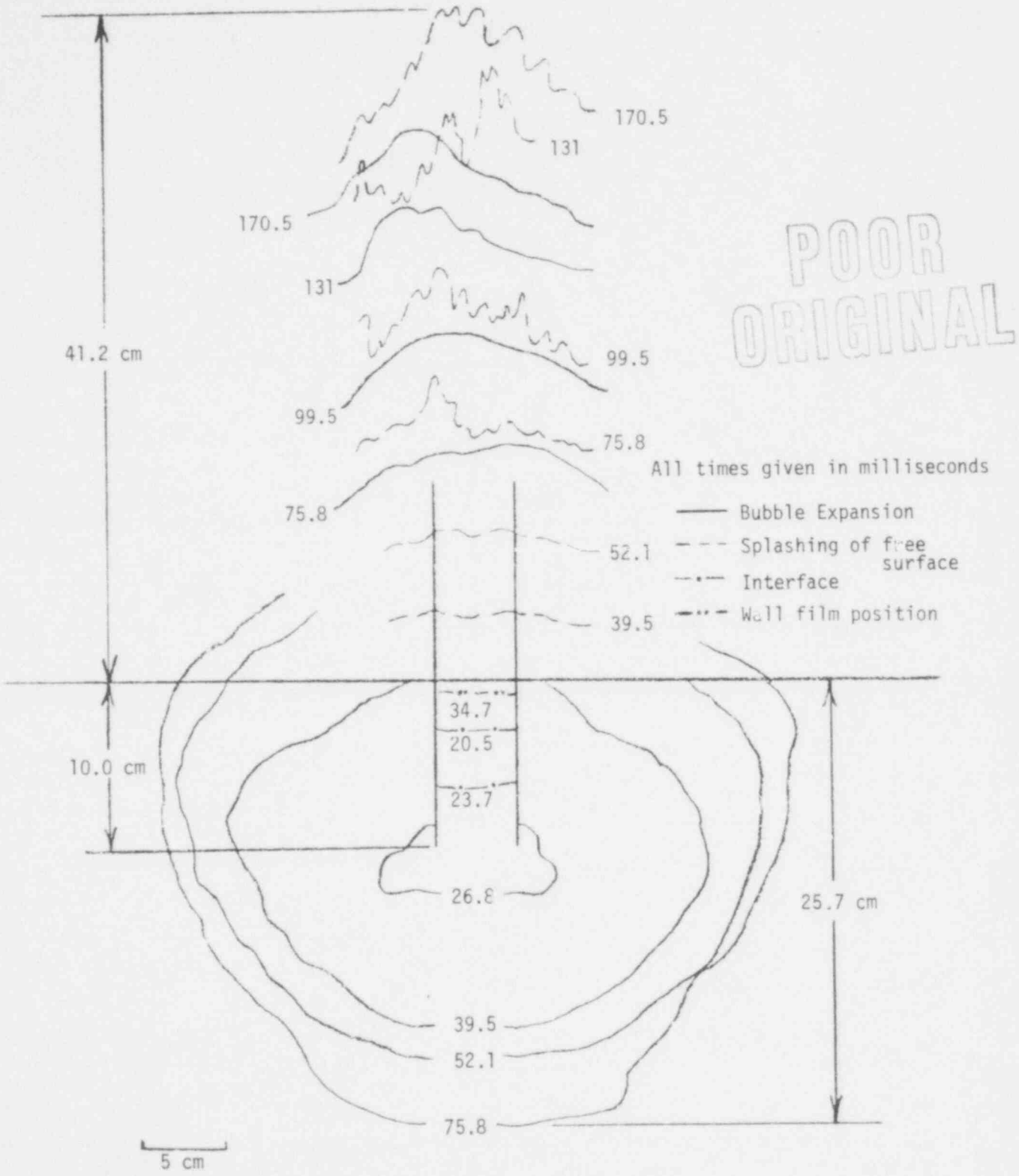

Figure E.19 Bubble Growth and Free Surface Swelling Response Histories for Helium with 2.54 cm Diameter Orifice, Upstream Reservoir Pressure = 177.2 kPa, Ambient Test Chamber Pressure = 74.3 kPa.

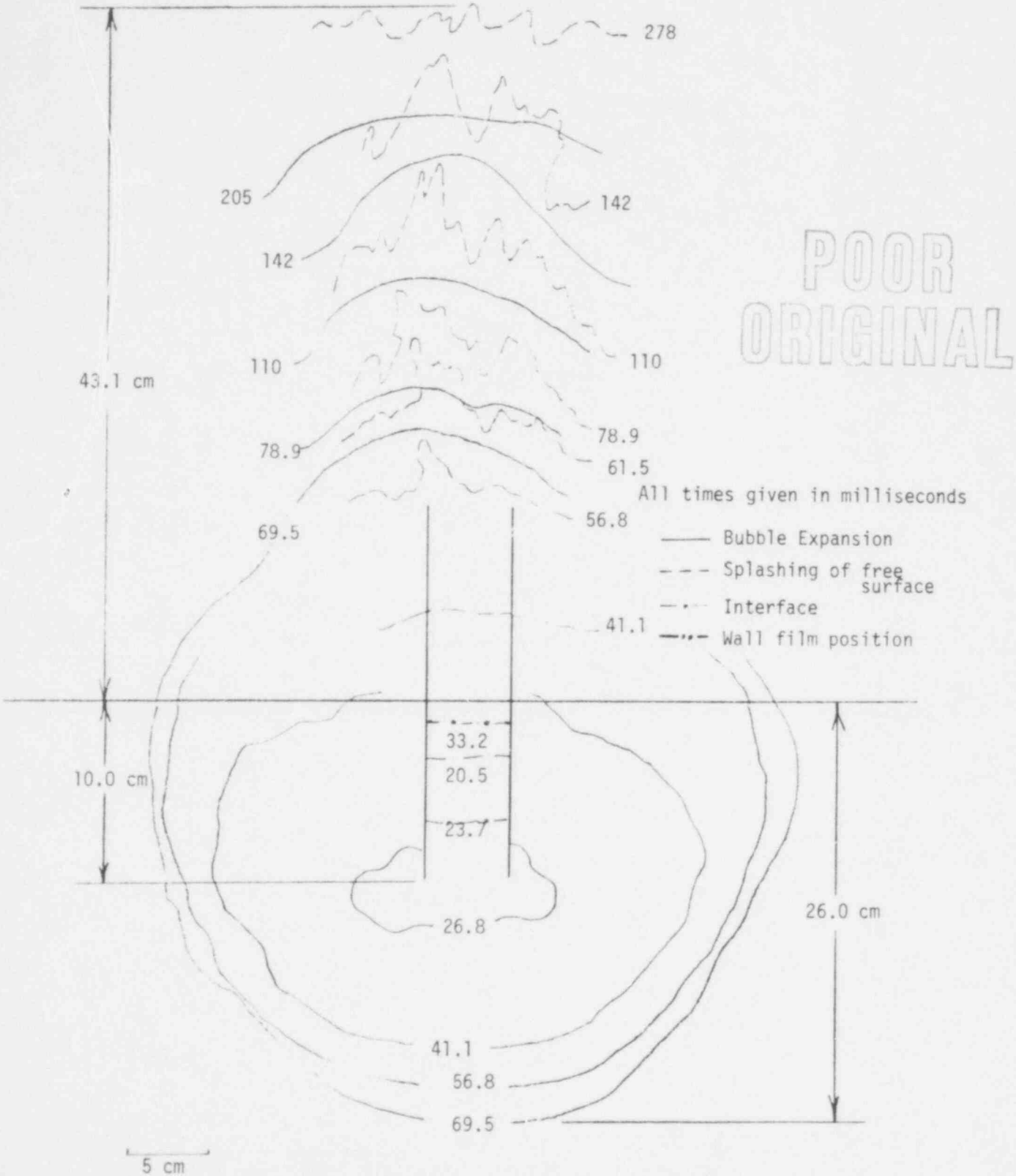

Fig. E.20 Bubble Growth and Free Surface Swelling Response Histories for Helium with 2.54 cm Diameter Orifice, Upstream Reservoir Pressure = 177.2 kPa, Ambient Test Chamber Pressure = 60.7 kPa.

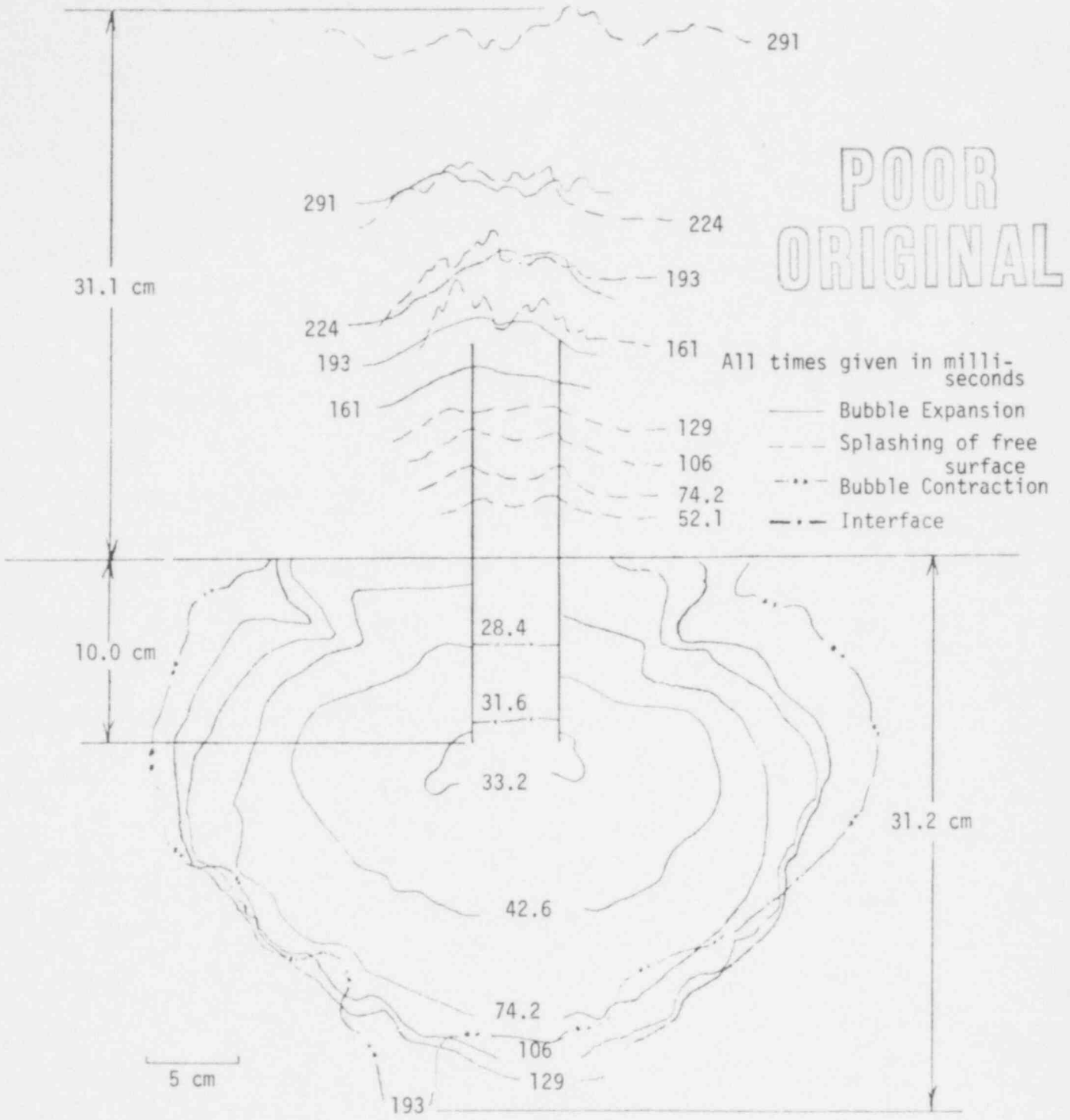

Fig. E.21 Bubble Growth and Free Surface Swelling Response Histories for Helium with 1.56 cm Diameter Orifice, Upstream Reservoir Pressure = 177.2 kPa, Ambient Test Chamber Pressure = 101.4 kPa.

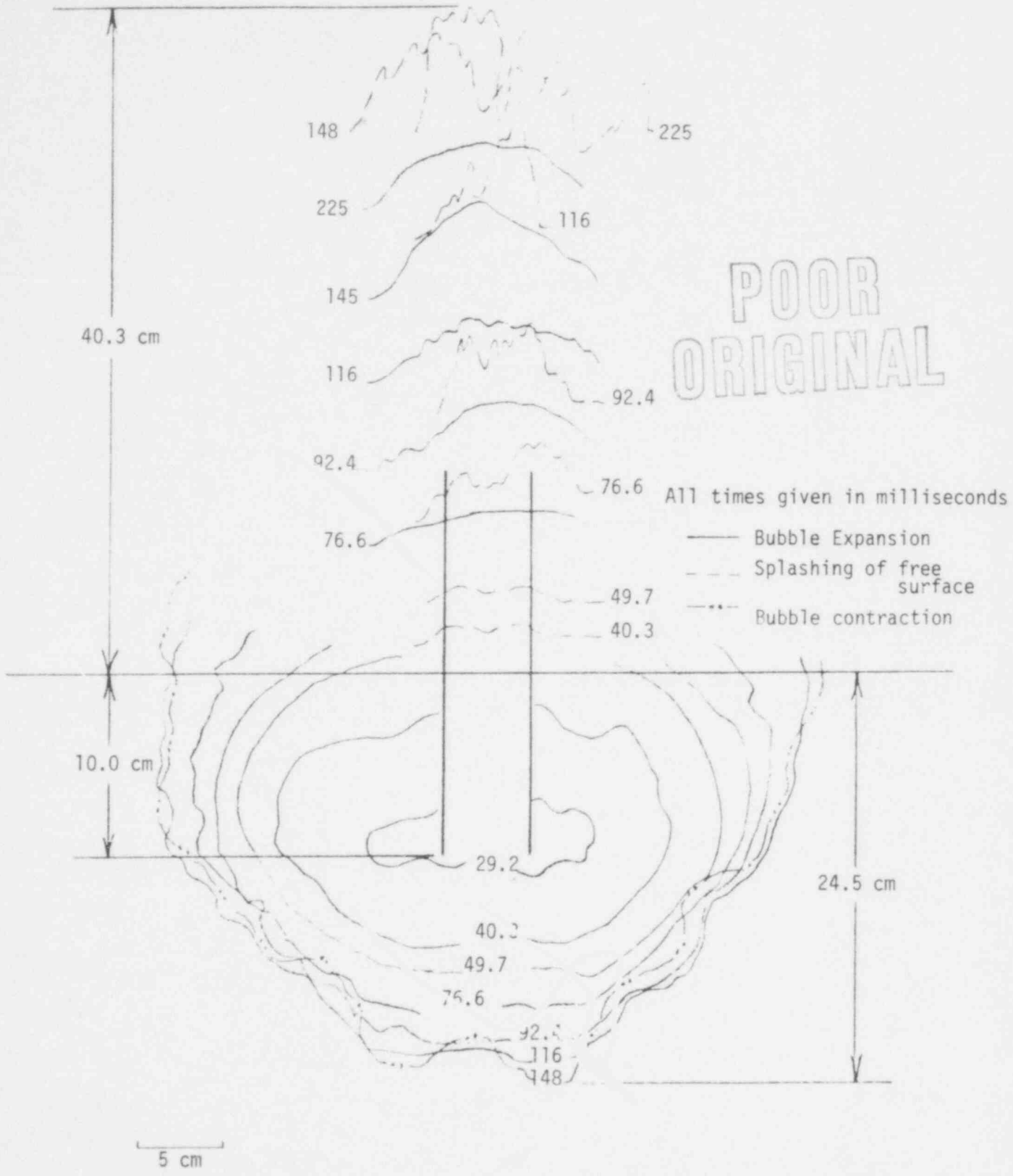

Fig. E.22 Bubble Growth and Free Surface Swelling Response Histories for Helium with 1.56 cm Diameter Orifice, Upstream Reservoir Pressure = 177.2 kPa, Ambient Test Chamber Pressure = 74.3 kPa.

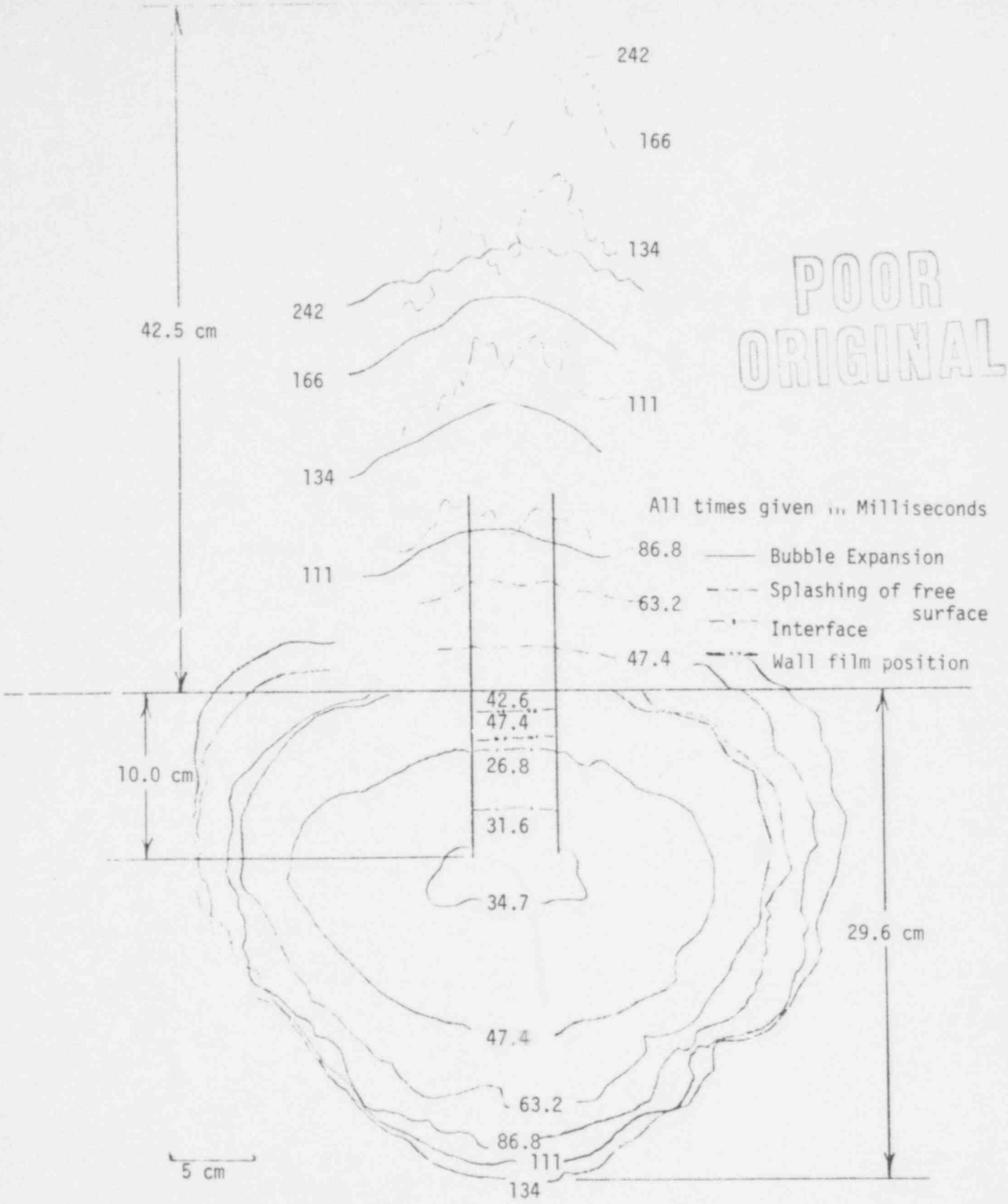

Fig. E.23. Bubble Growth and Free Surface Swelling Response Histories for Helium with 1.56 cm Diameter Orifice, Upstream Reserboir Pressure = 177.2 kPa, Ambient Test Chamber Pressure = 60.7 kPa.

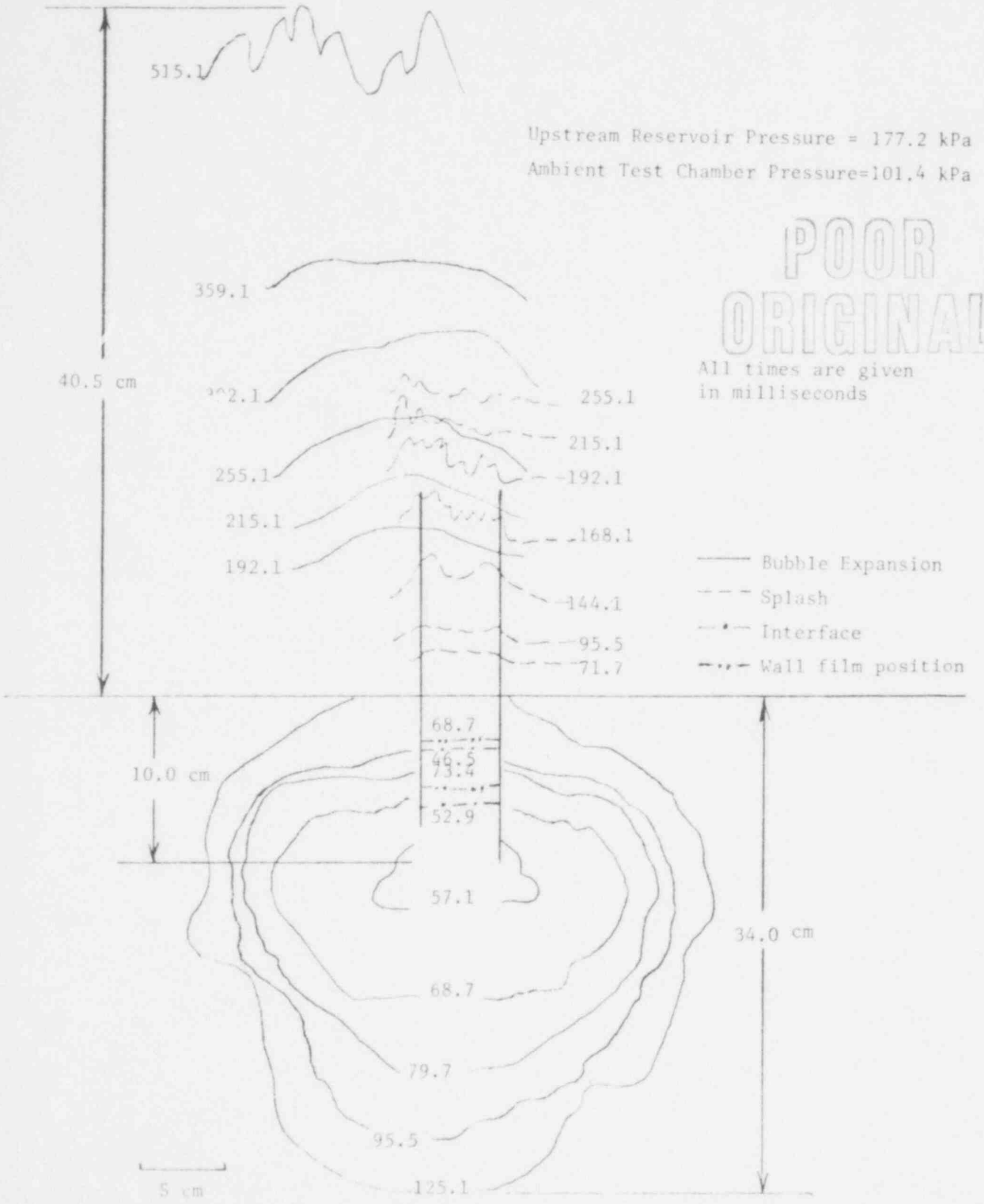

Figure E.24. Bubble Growth and Free Surface Response Histories Without Orifice and Using Argon Gas. Ambient Test Chamber Pressure 101.4 kPa.

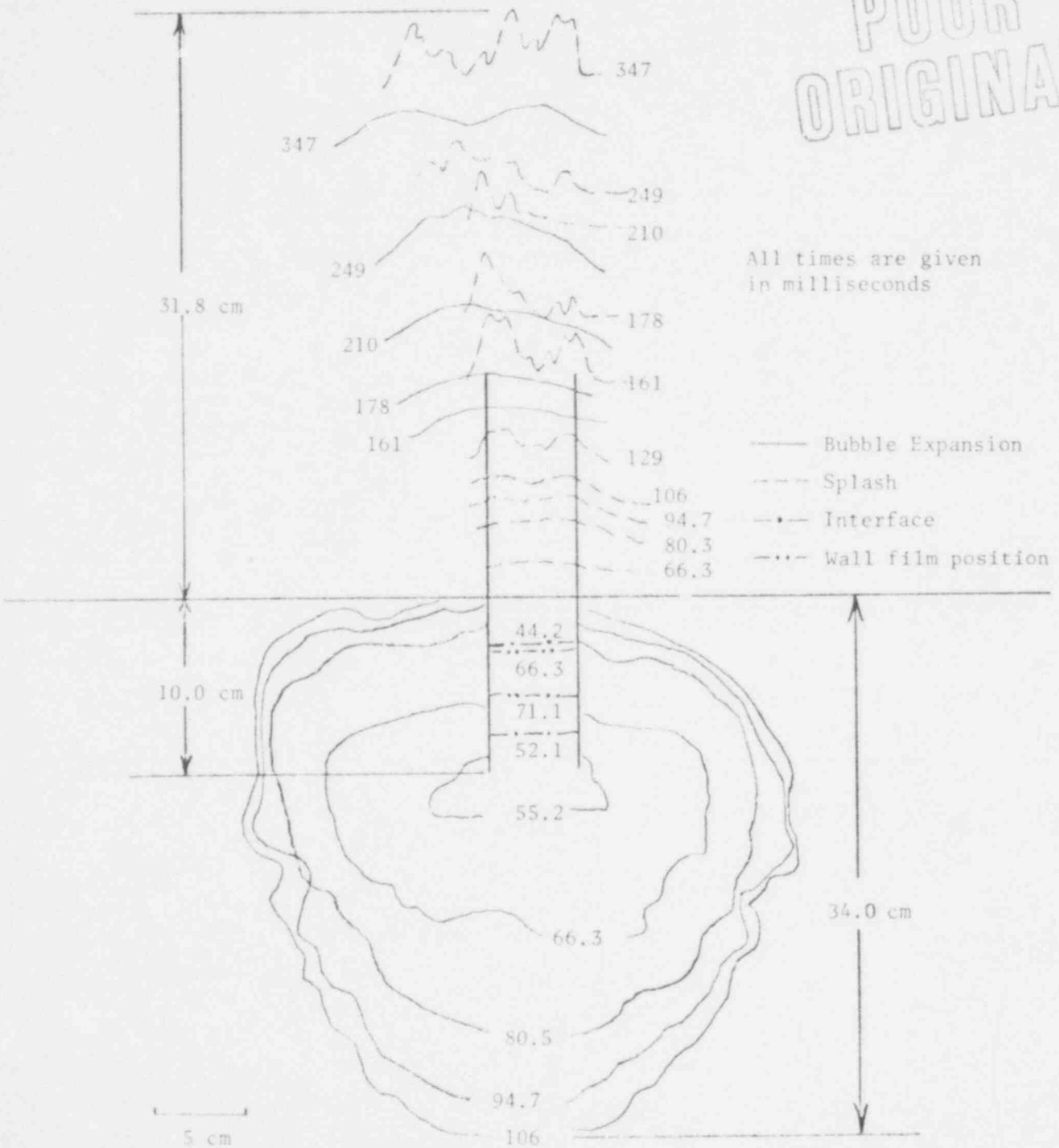

Fig. F.25 Bubble Growth and Free Surface Swelling Response Histories for Argon without Orifice. Ambient Test Chamber Pressure 87.8 kPa.

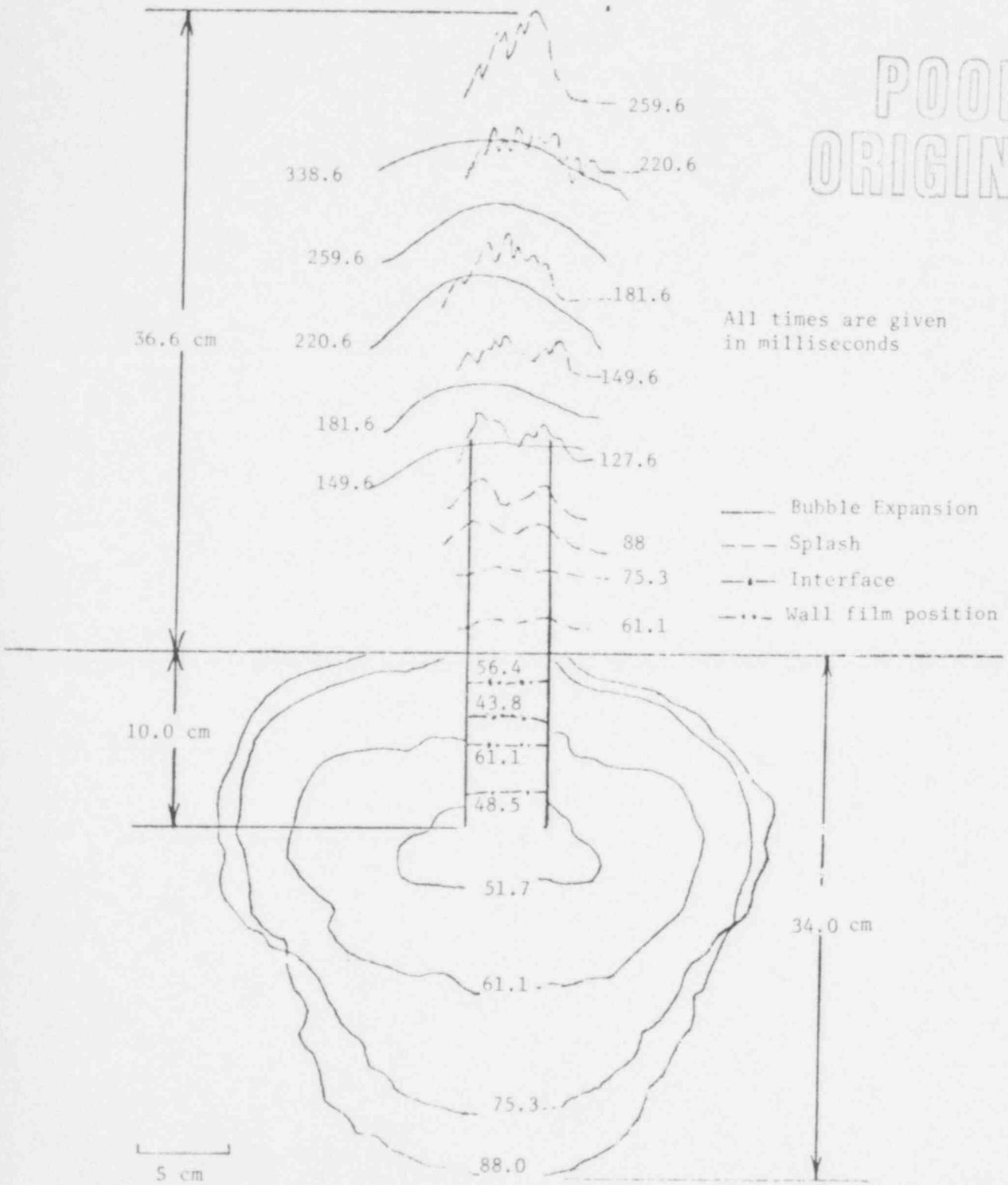

Figure E.26 Bubble Growth and Free Surface Swelling Response Histories for Argon without Orifice. Ambient Test Chamber Pressure 74.3 kPa.

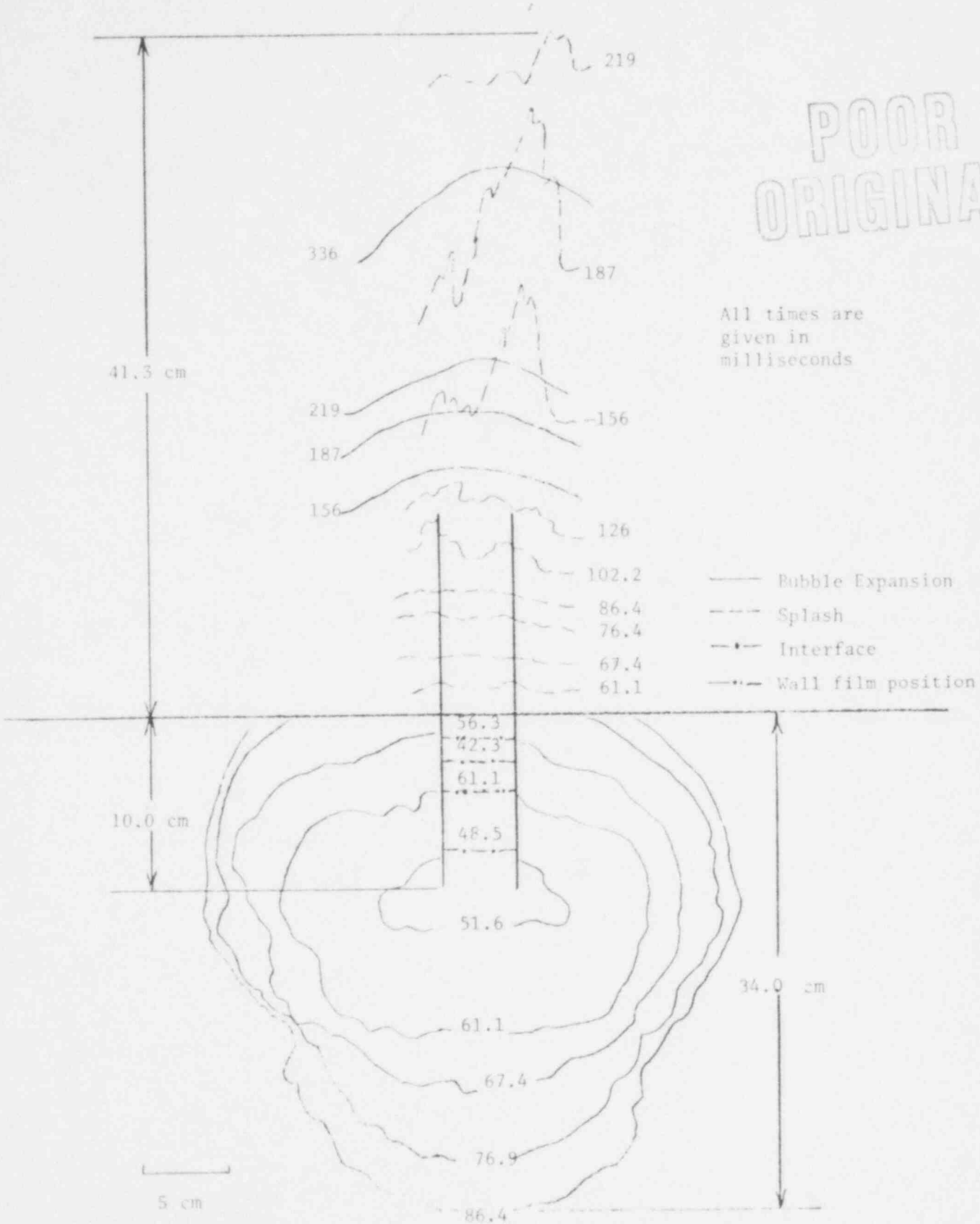

Figure E.27 Bubble Growth and Free Surface Swelling Response Histories for Argon without Orifice. Ambient Test Chamber Pressure 60.7 kPa.

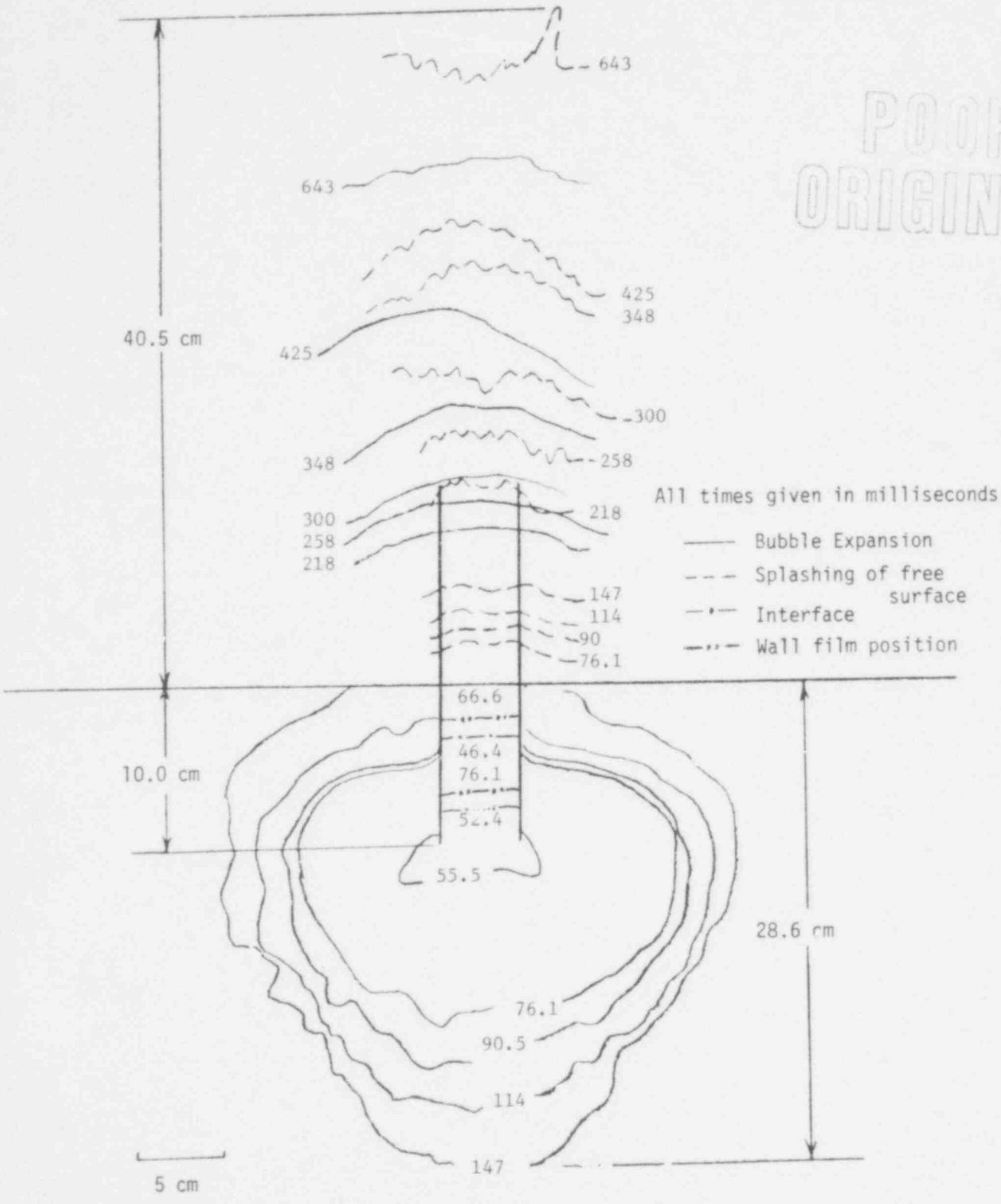

Fig. E.28 Bubble Growth and Free Surface Swelling Response Histories for Argon with 2.54 cm Diameter Orifice, Upstream Reservoir Pressure = 177.2 kPa, Ambient Test Chamber Pressure = 101.4 kPa.

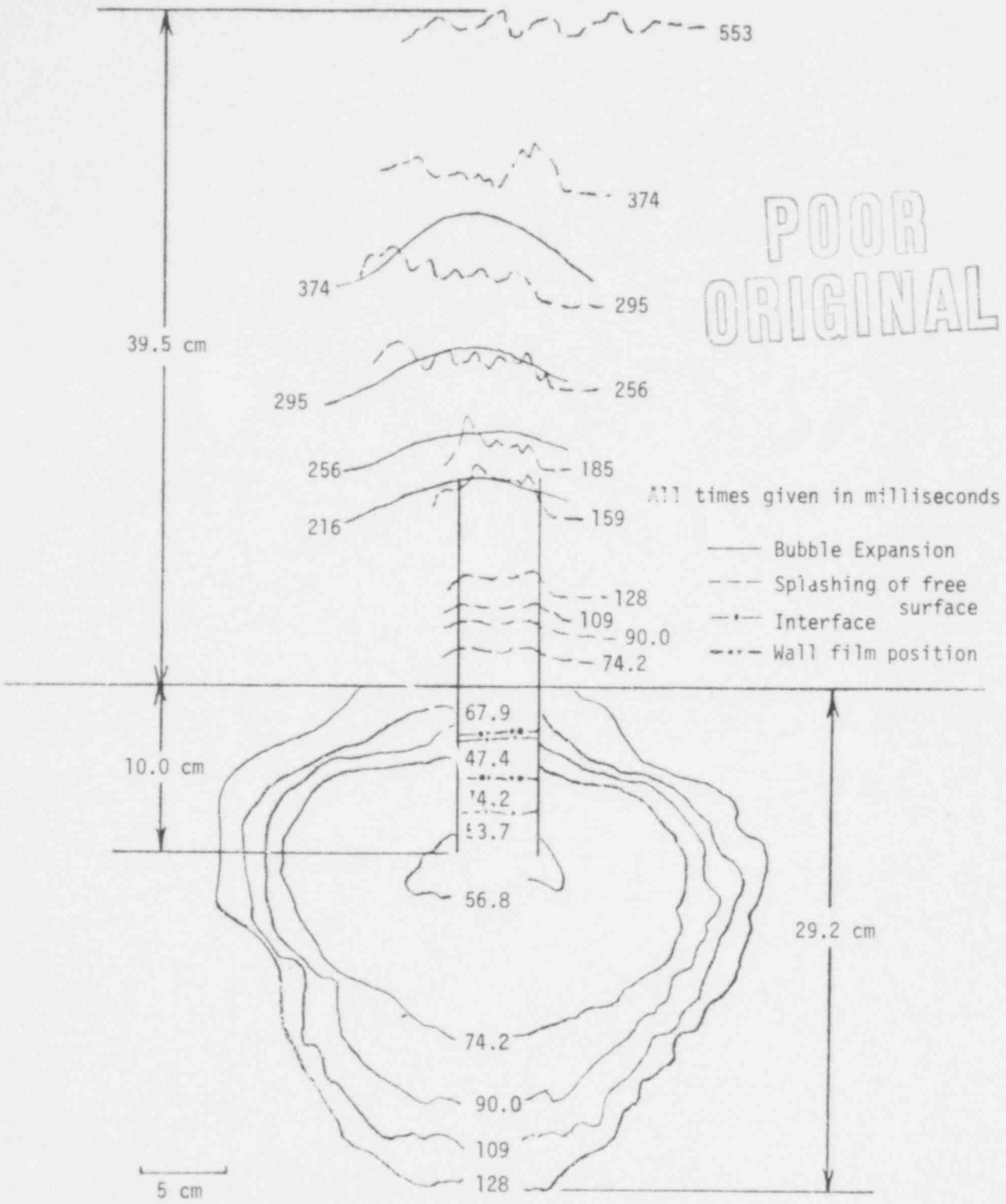

Fig. E.29 Bubble Growth and Free Surface Swelling Response Histories for Argon with 2.54 cm Diameter Orifice, Upstream Reservoir Pressure = 177.2 kPa, Ambient Test Chamber Pressure = 87.8 kPa.

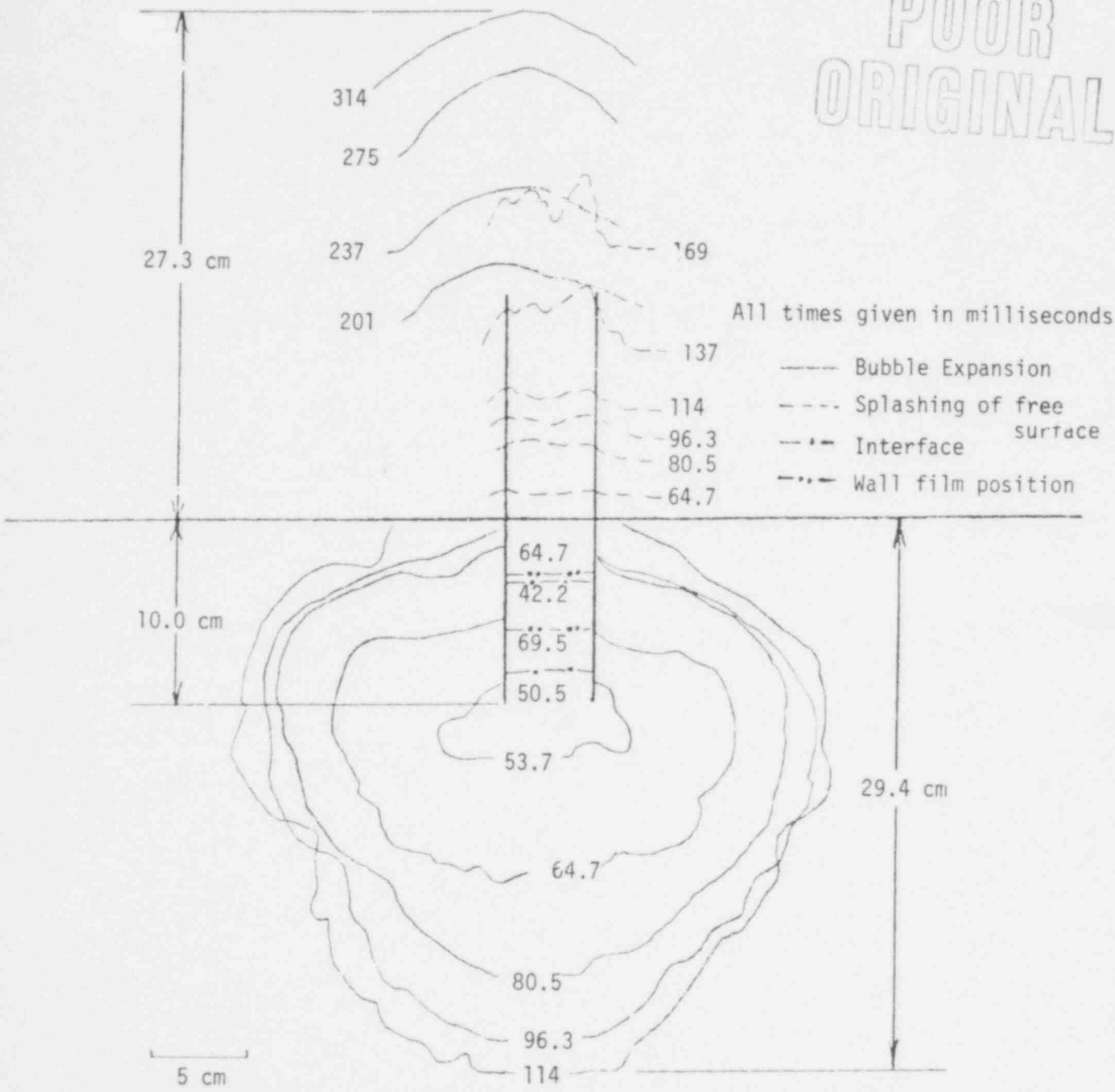

Fig. E.30 Bubble Growth and Free Surface Swelling Response Histories for Argon with 2.54 cm Diameter Orifice, Upstream Reservoir Pressure = 177.2 kPa, Ambient Test Chamber Pressure = 74.3 kPa.

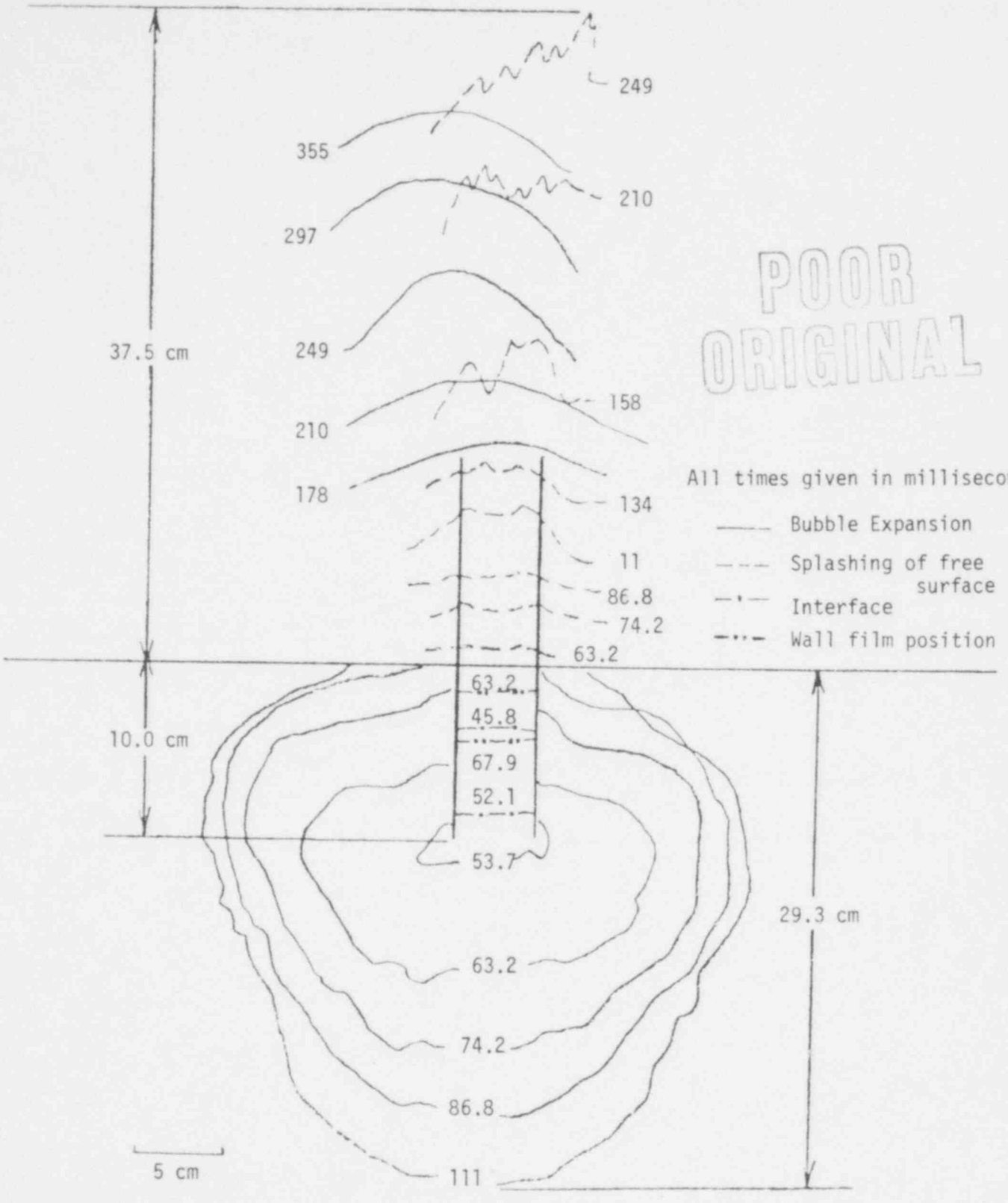

Fig. E.31 Bubble Growth and Free Surface Swelling Response Histories for Argon with 2.54 cm Diameter Orifice, Upstream Reservoir Pressure = 177.2 kPa, Ambient Test Chamber Pressure = 60.7 kPa.

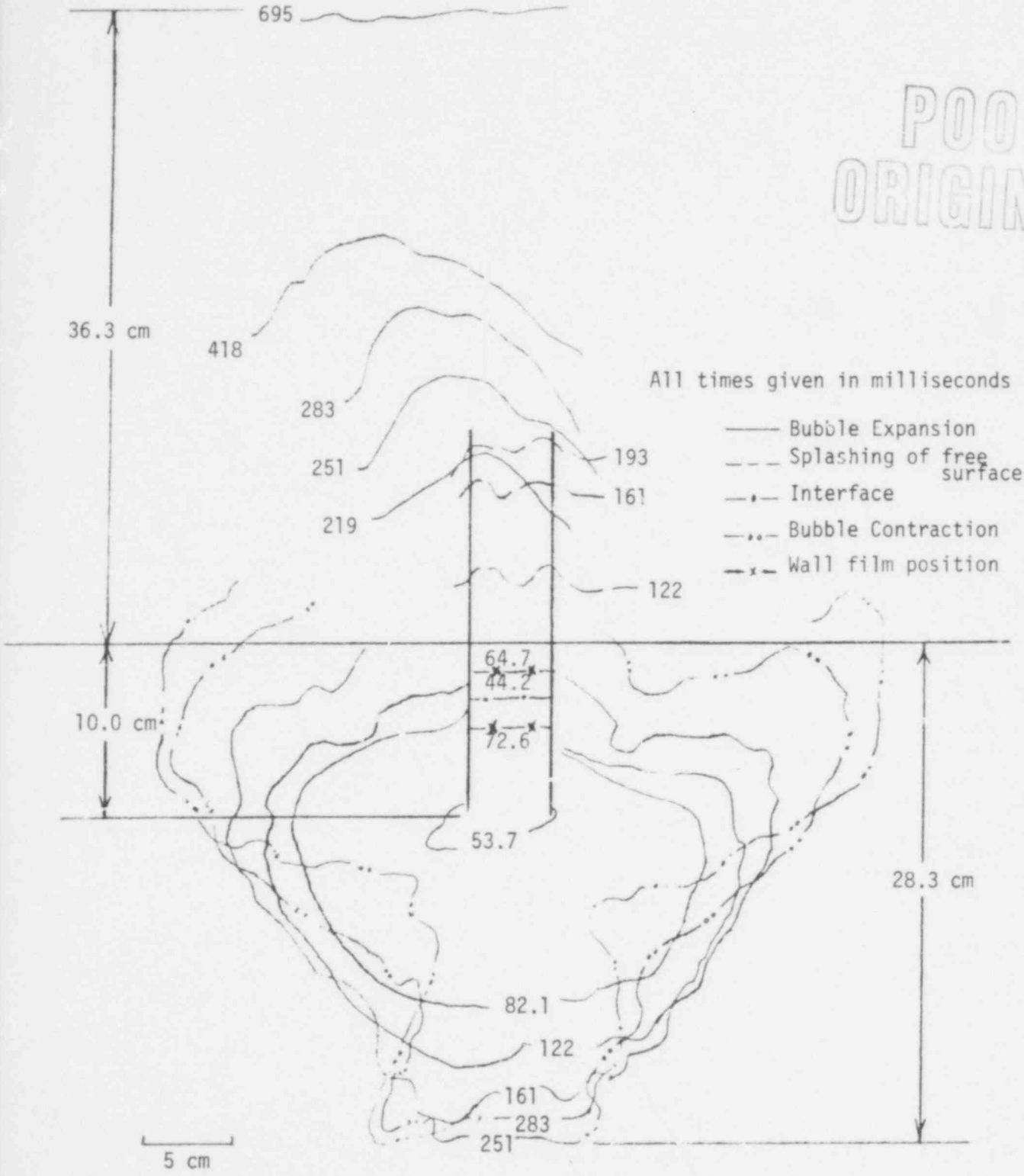

ig. E.32 Bubble Growth and Free Surface Swelling Response Histories for Argon with 1.56 cm Diameter Orifice, Upstream Reservoir Pressure = 177.2 kPa, Ambient Test Chamber Pressure = 97.8 kPa.

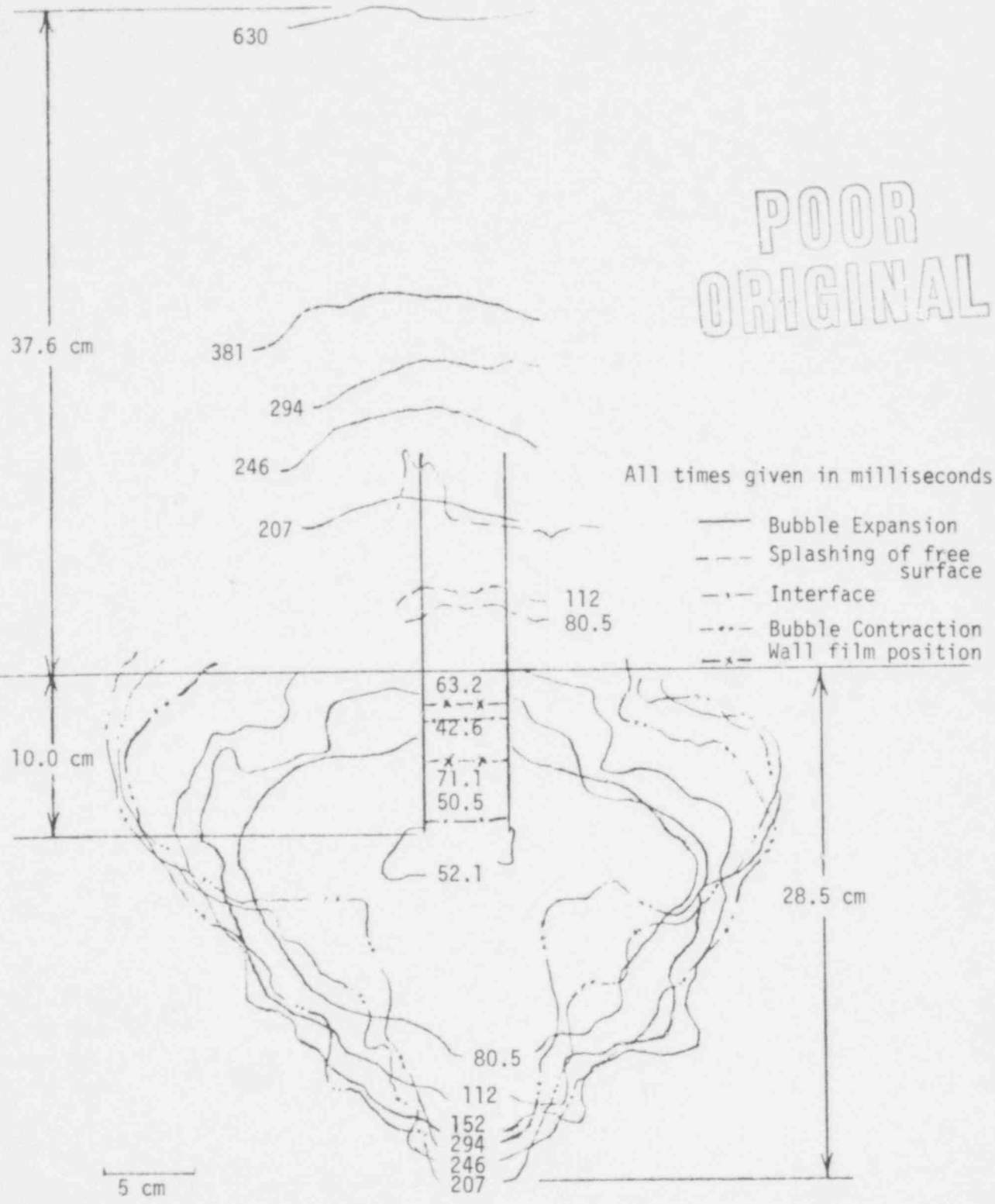

Fig. E.33 Bubble Growth and Free Surface Swelling Response Histories for Argon with 1.56 cm Diameter Orifice, Upstream Reservoir Pressure = 177.2 kPa, Ambient Test Chamber Pressure = 74.3 kPa.

Appendix F. Flow Rate and Pressure Histories

In this Appendix, experimental data on flow rate and pressure (including upstream, bottom side, bottom center and upper free space pressure) histories are listed. They are divided into three groups for three different gases, i.e., Air, Helium and Argon. In addition, two different sizes of orifices were used, with diameters of 1.56 cm and 2.54 cm. For every experiment, the upstream reservoir pressure was fixed to 177.2 kPa; however, the test chamber pressures varied. Their values were: 101.4 kPa, 87.8 kPa, 74.3 kPa and 60.7 kPa.

The thirty-six cases of the experimental data are listed in the following table.

Orifice Size	Gas Pi	Air	Helium	Argon
	101.4 kPa	Figure F.1	Figure F.13	Figure F.25
NO	87.8 kPa	" F.2	" F.14	" F.26
Orifice	74.3 kPa	" F.3	" F.15	" F.27
	60.7 kPa	" F.4	" F.16	" F.28
	101.4 kPa	" F.5	" F.17	" F.29
2.54 cm	87.8 kPa	F.6	" F.18	" F.30
Dia.	74.3 kPa	" F.7	" F.19	" F.31
Orifice	60.7 kPa	" F.8	" F.20	" F.32
	101.4 kPa	" F.9	" F.21	" F.33
1.56 cm	87.8 kPa	" F.10	" F.22	" F.34
Dia.	74.3 kPa	" F.11	" F.23	" F.35
Orifice	60.7 kPa	" F.12	" F.24	" F.36

*Pi = test chamber pressure.

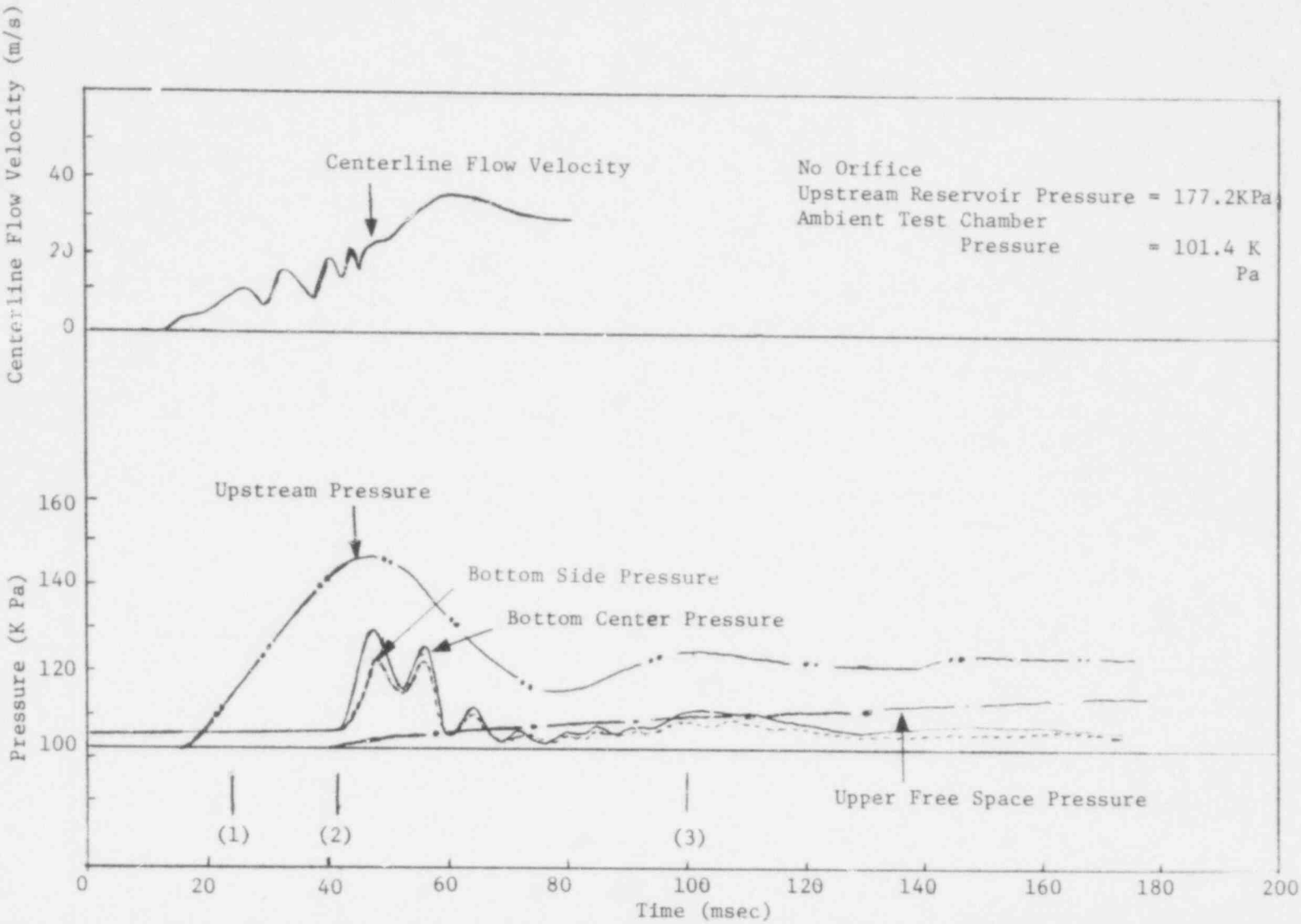

Figure F.1 Flow Rate and Pressure Histories without Orifice and Using Air.

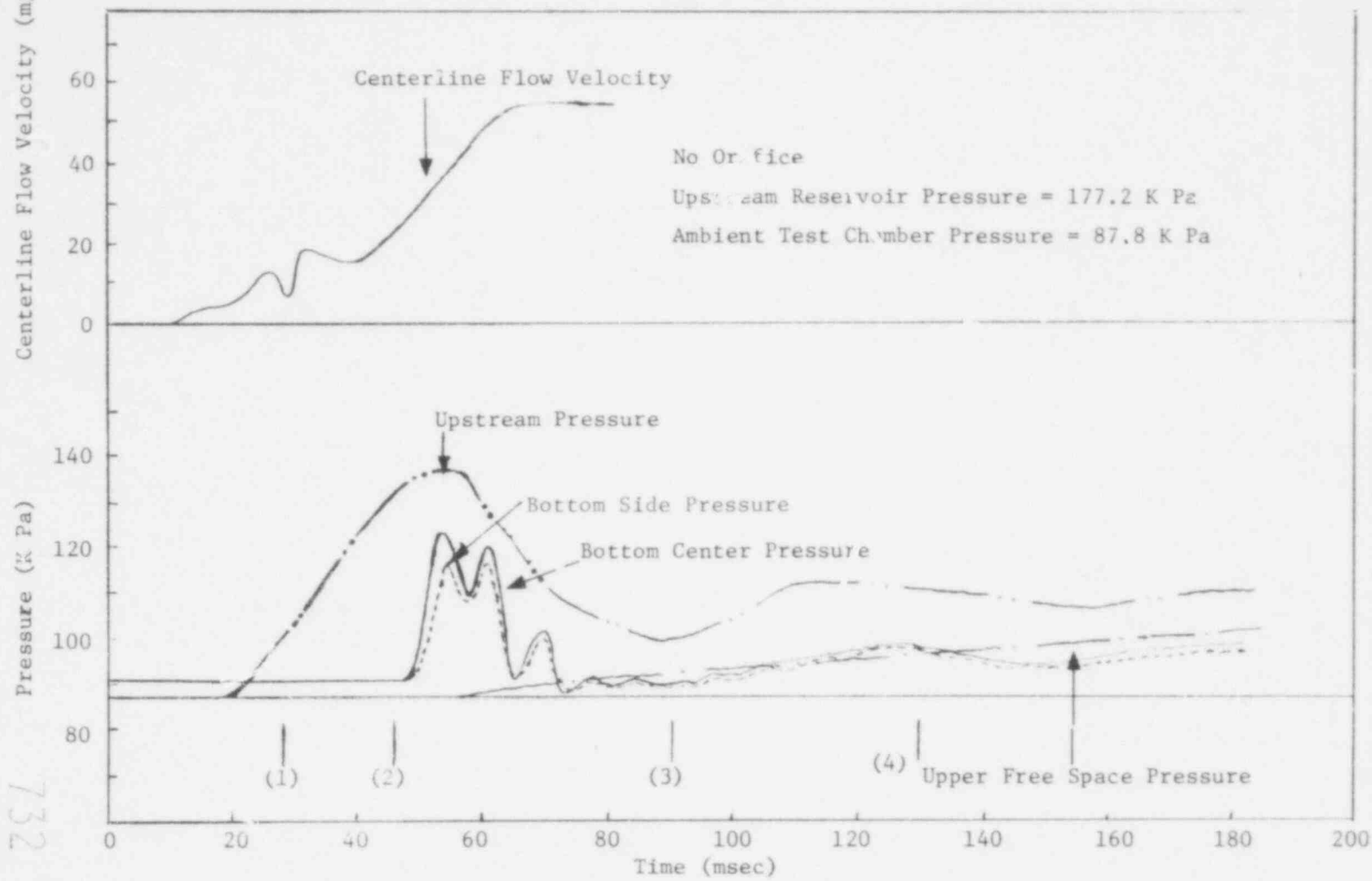

Figure F.2 Flow Rate and Pressure Histories without Orifice and Using Air.

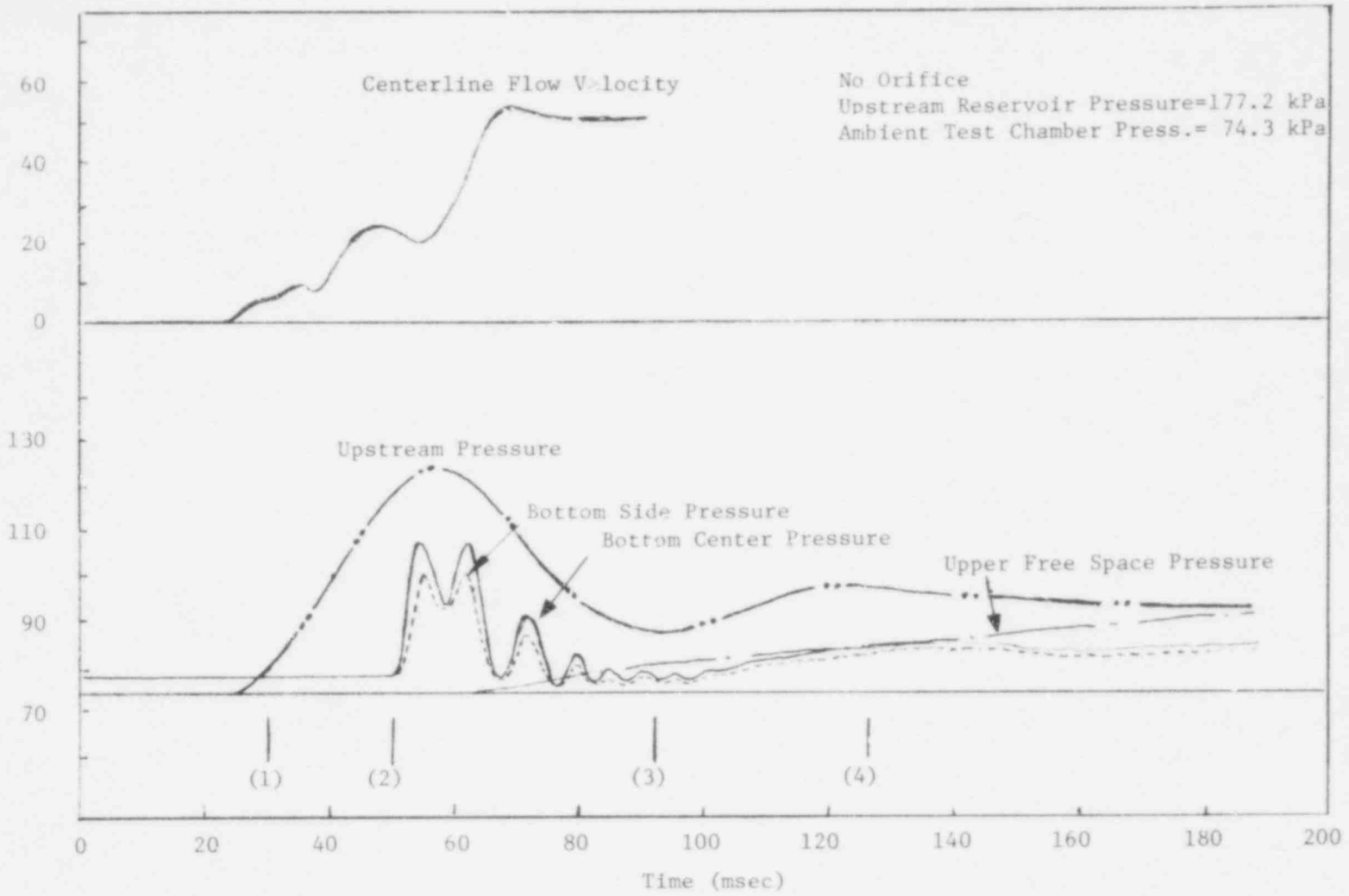

Figure F.3 Flow Rate and Pressure Histories without Orifice and Using Air

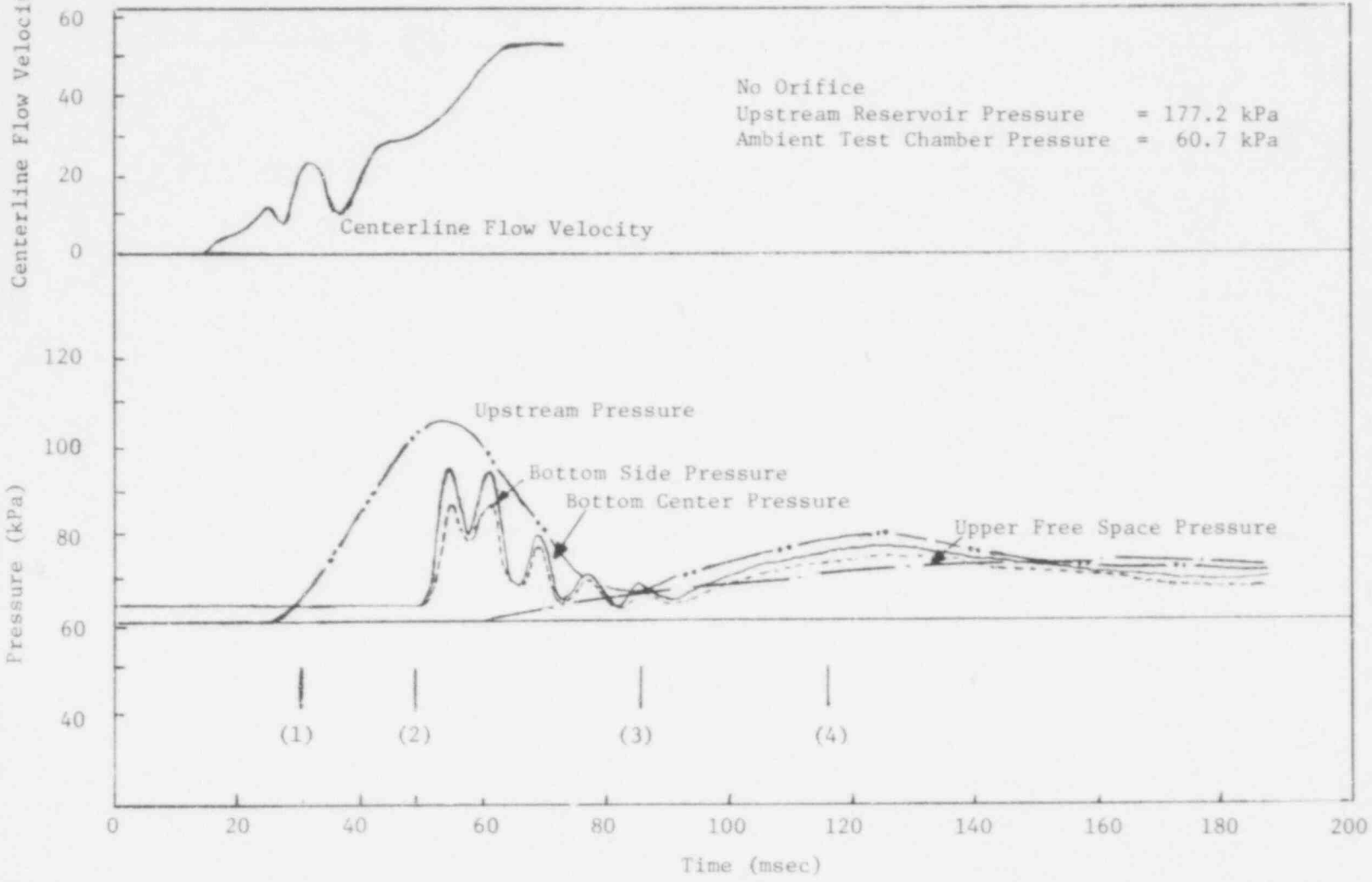

Figure F.4 . Flow Rate and Pressure Histories without Orifice and Using Ai.

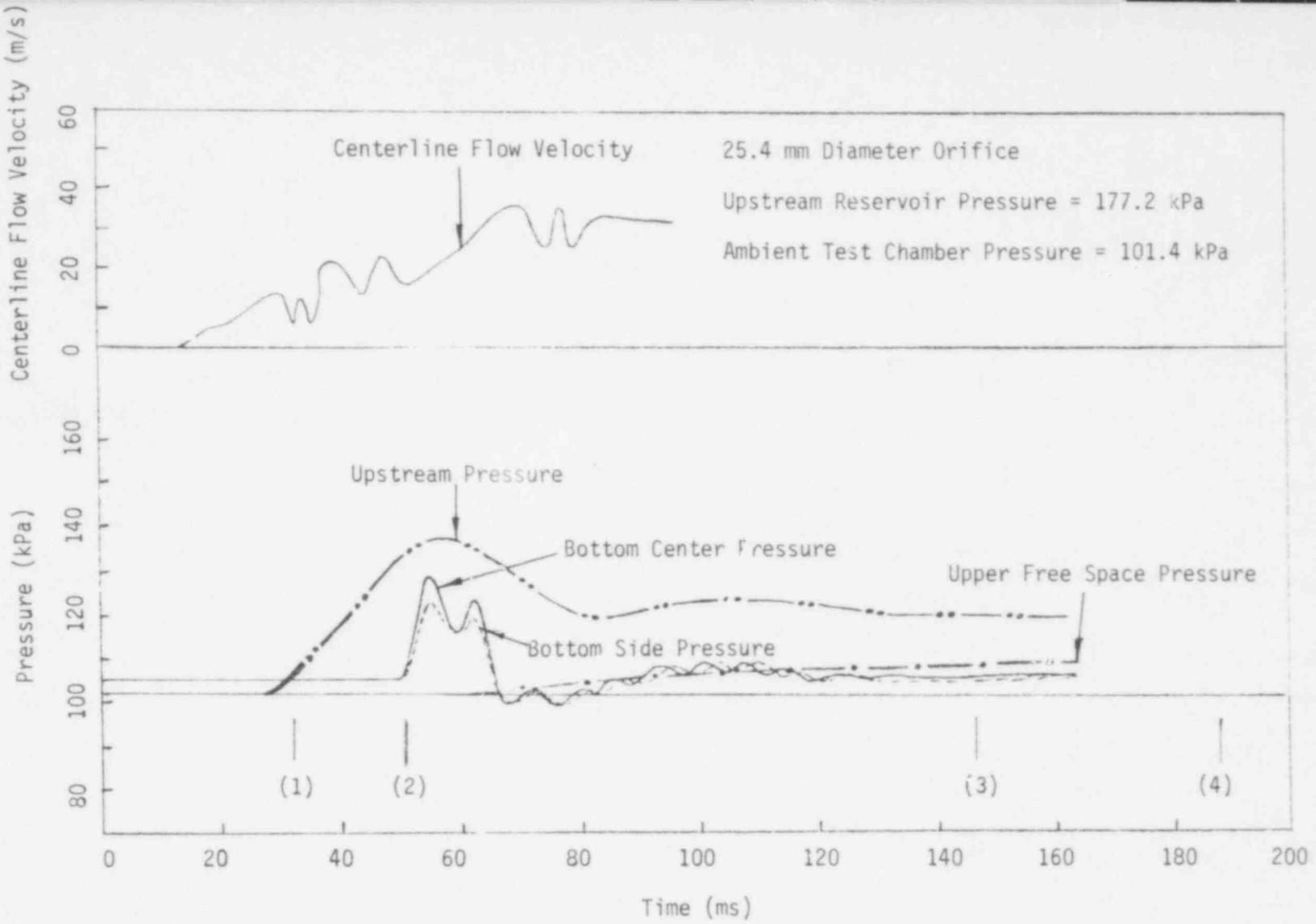

Figure F.5 Flow Rate and Pressure Histories with 25.4 mm Diameter Orifice and Using Air.

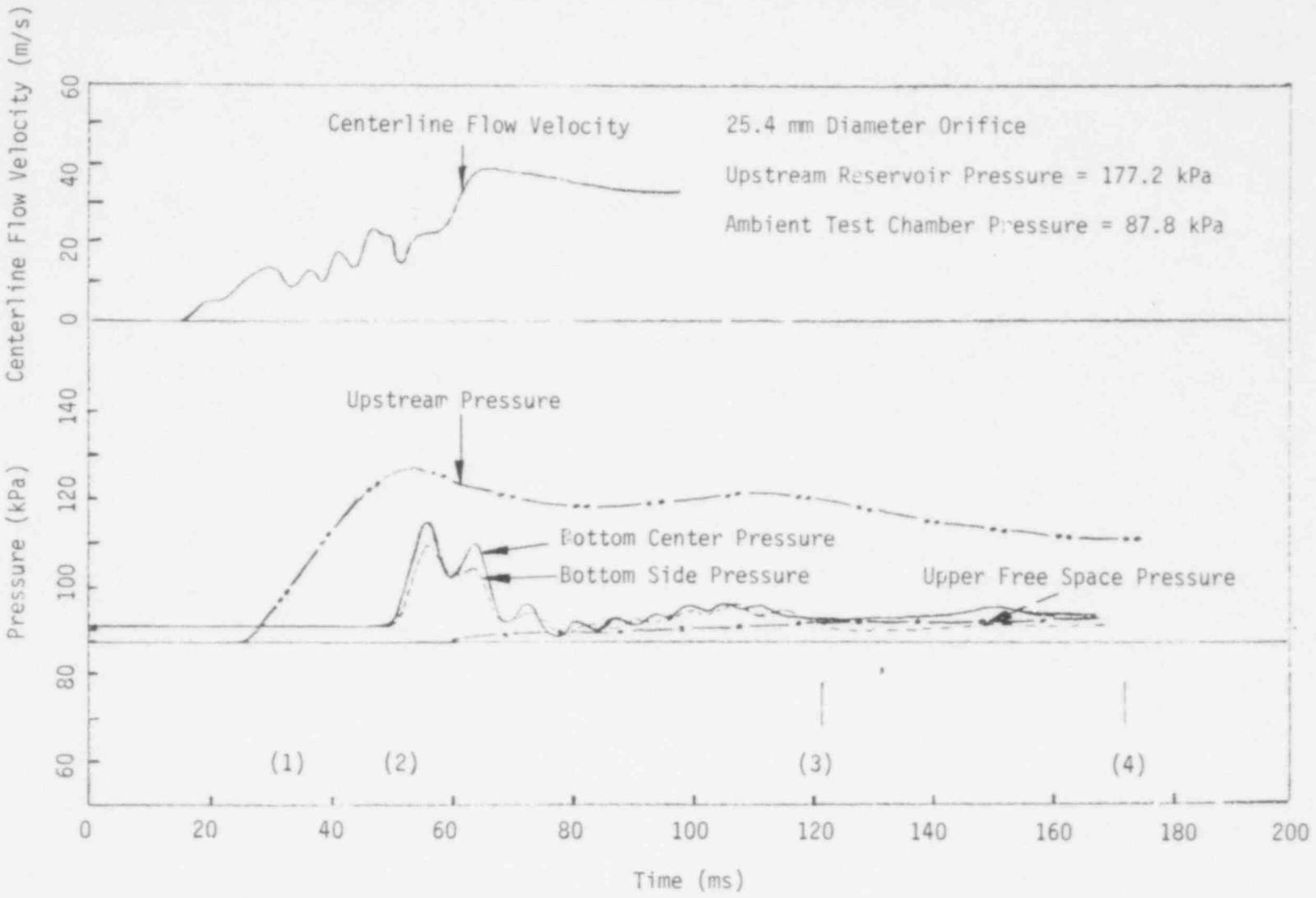

Figure F.6. Flow Rate and Pressure Histories with 25.4 mm Diameter Orifice and Using Air.

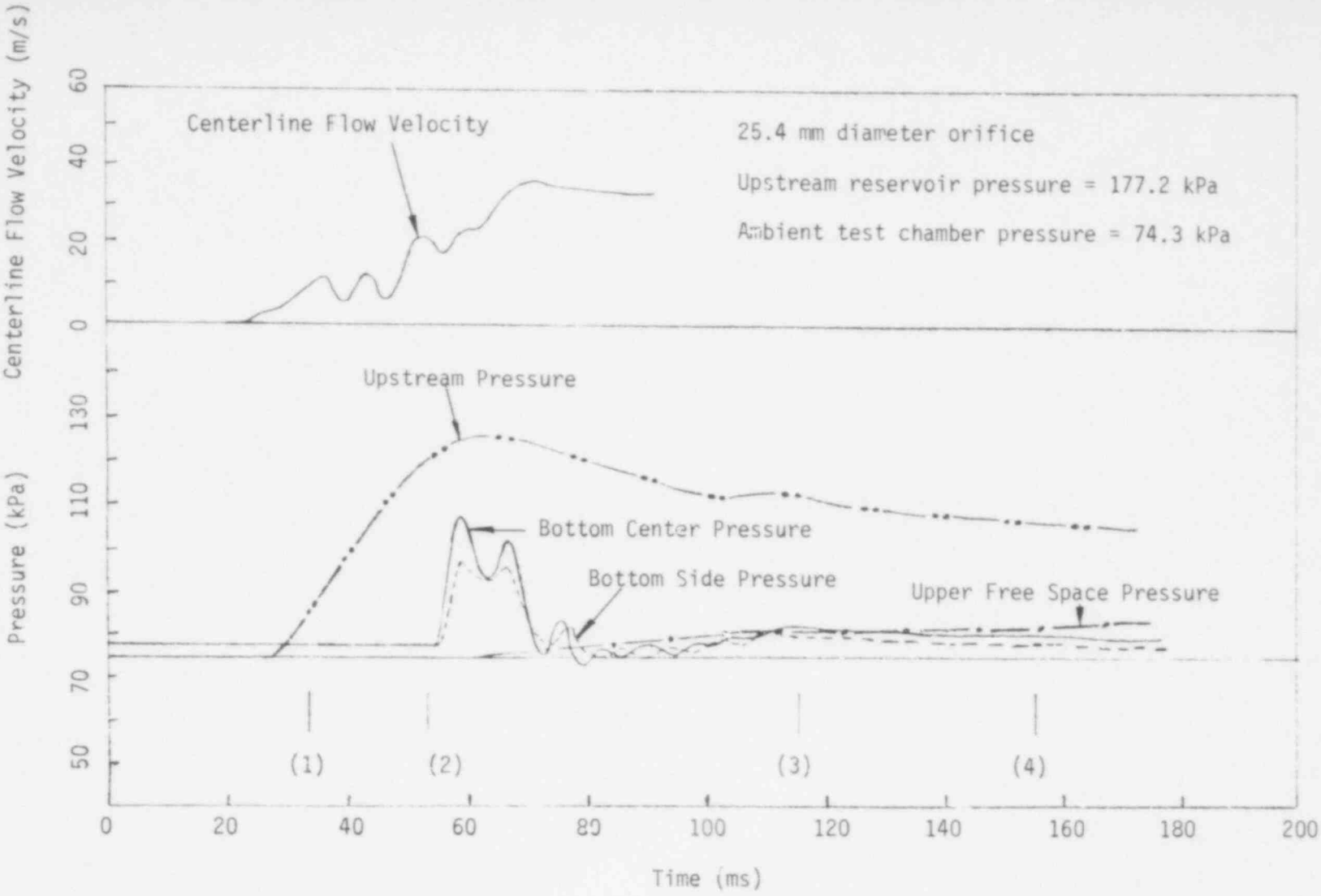

Figure F.7. Flow Rate and Pressure Histories with 25.4 mm Diameter Orifice and Using Air.

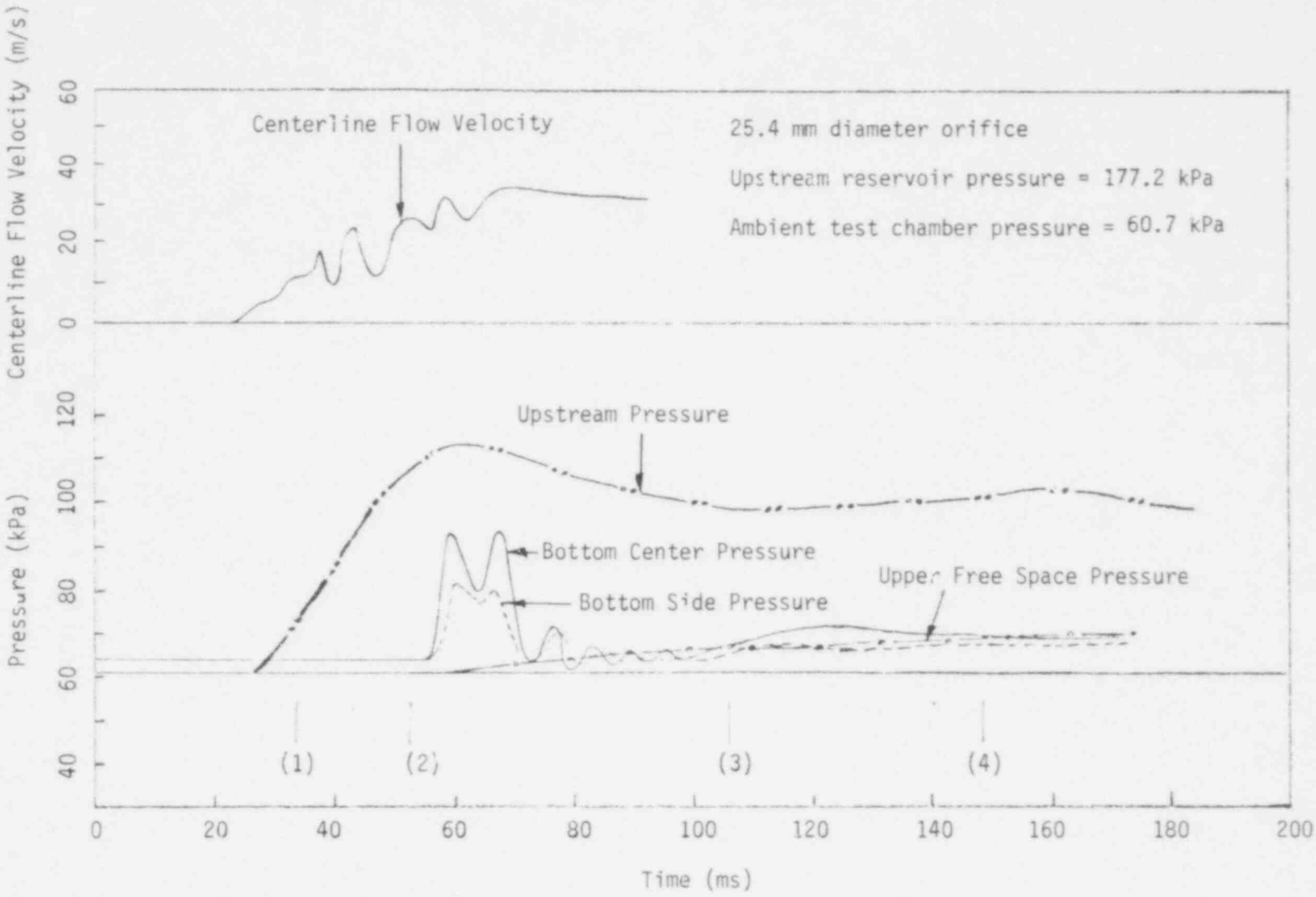

Figure F.3 . Flow Rate and Pressure Histories with 25.4 mm Diameter Orifice and Using Air.

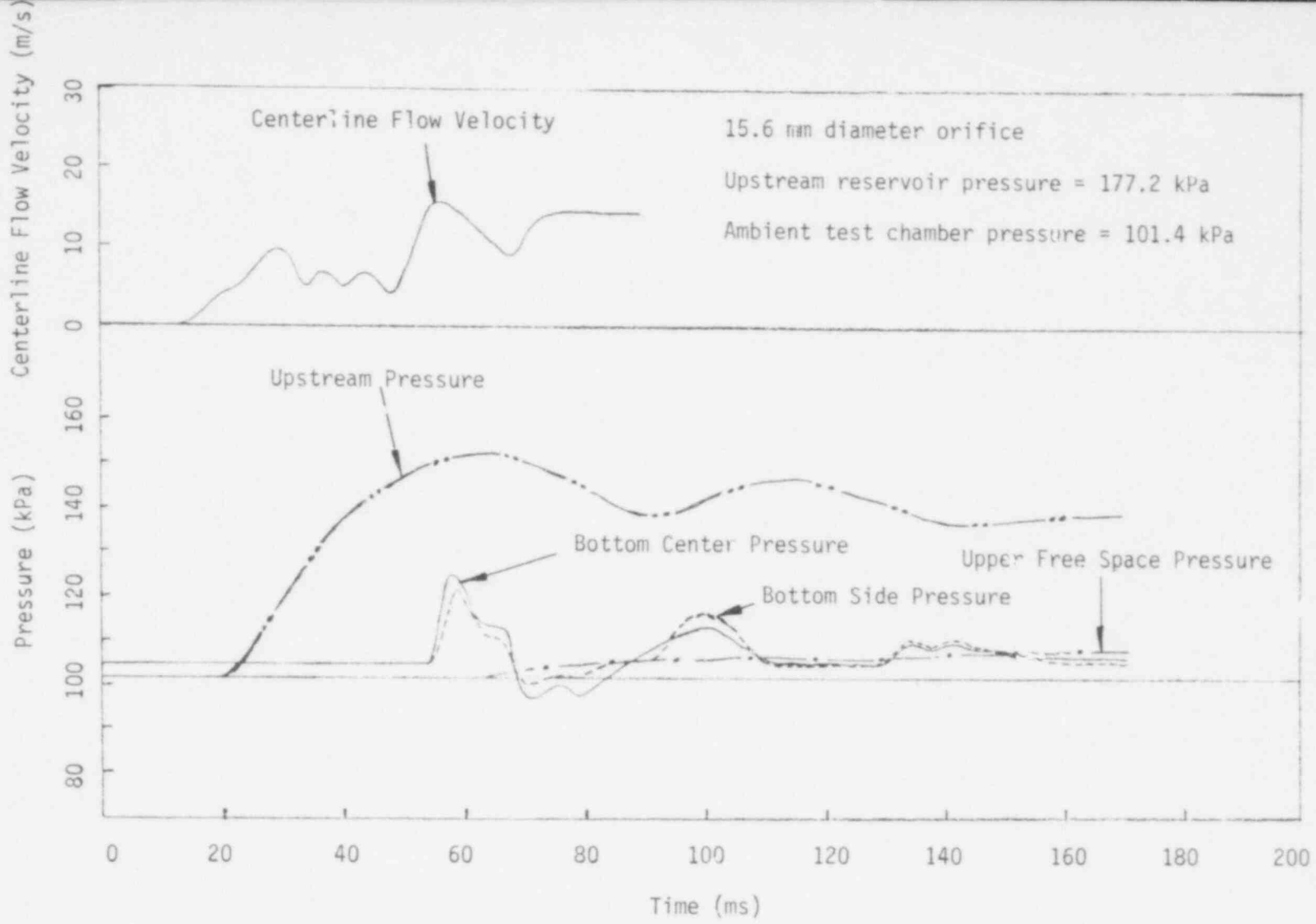

Figure F.9. Flow Rate and Pressure Histories with 15.6 mm Diameter Orifice and Using Air.

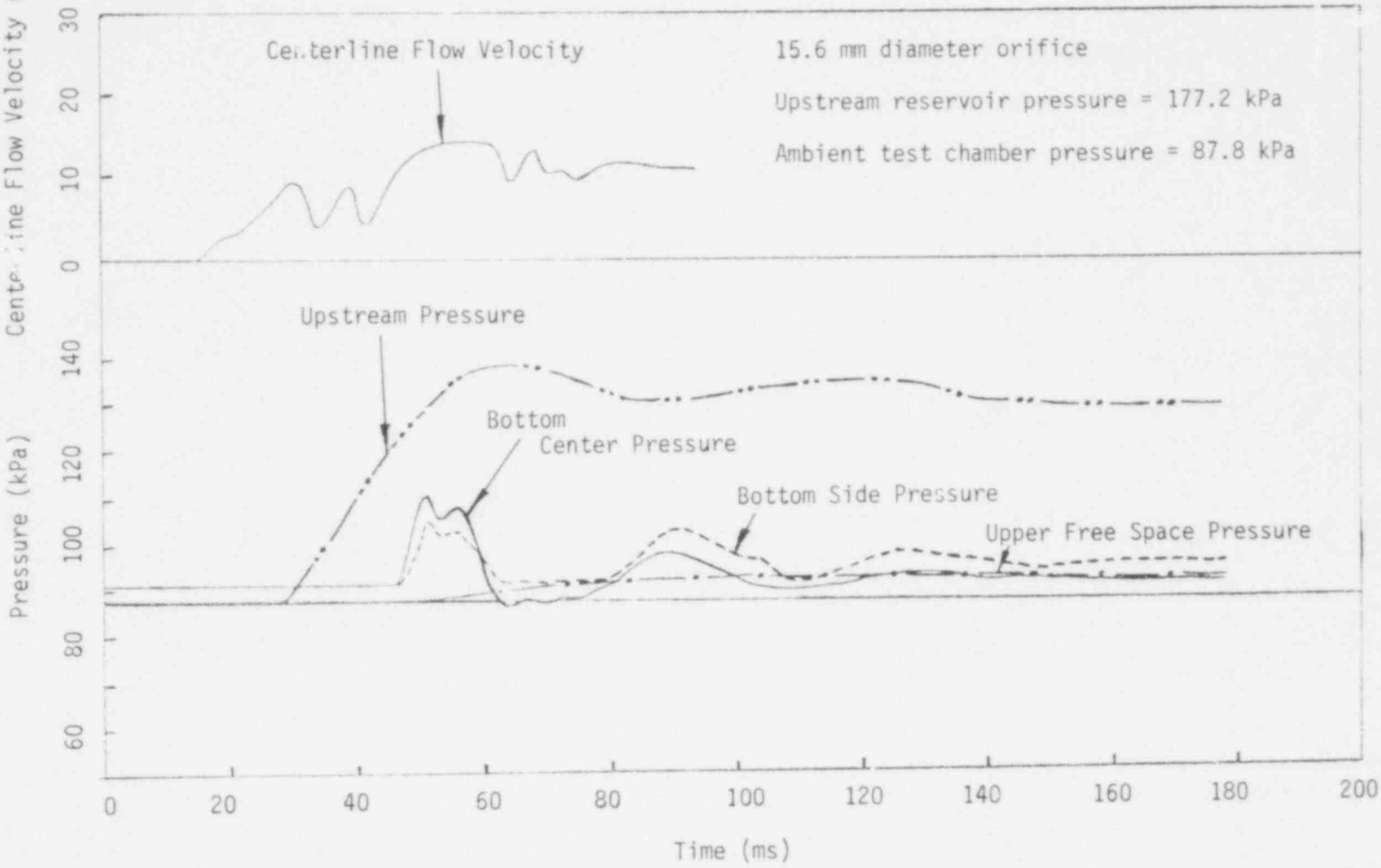

Figure F.10. Flow Rate and Pressure Histories with 15.6 mm Diameter Orifice and Using Air.

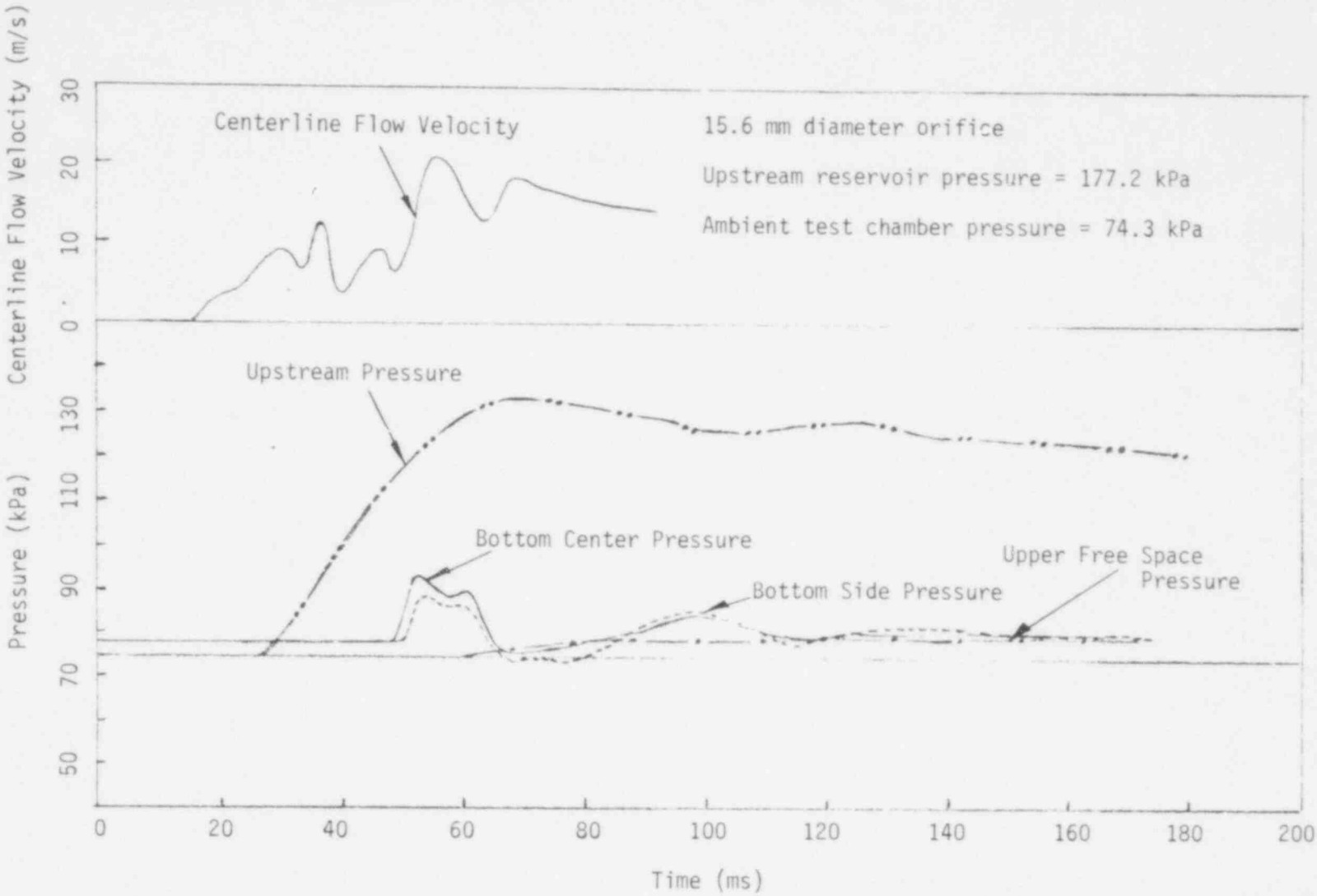

Figure F.11. Flow Rate and Pressure Histories with 15.6 mm Diameter Orifice and Using Air.

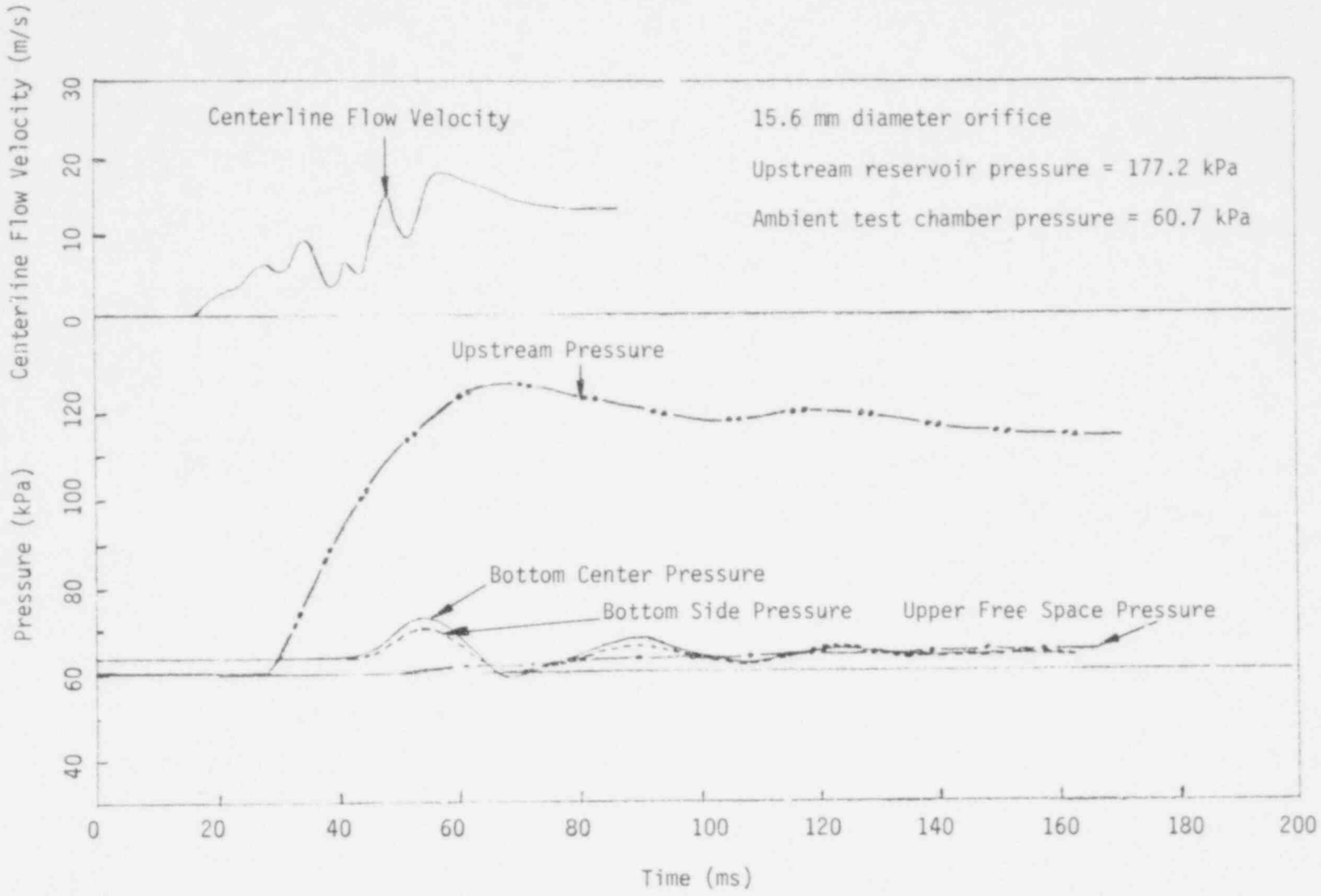

Figure F.12. Flow Rate and Pressure Histories with 15.6 mm Diameter Orifice and Using Air.

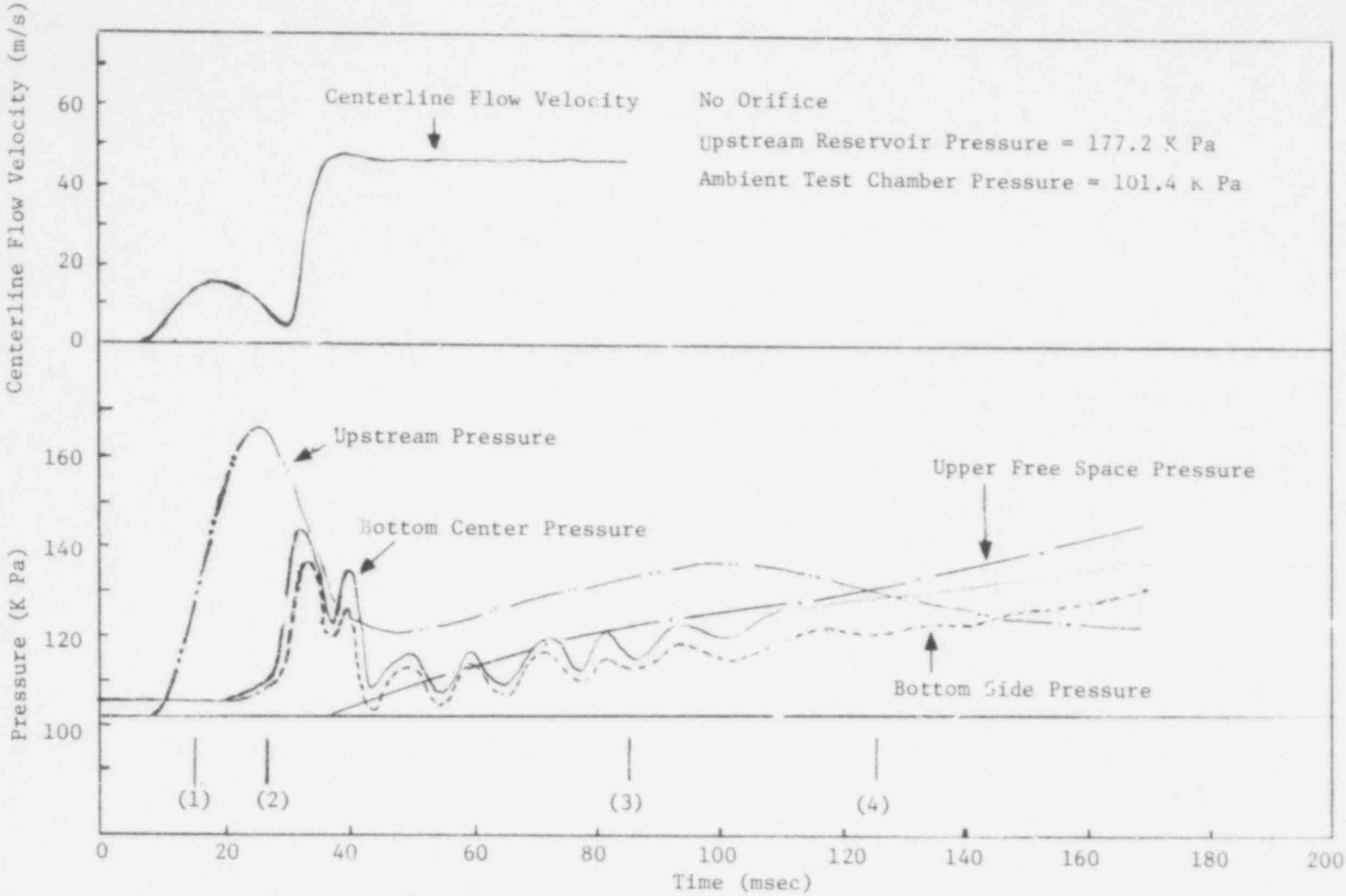

Figure F.13 Flow Rate and Pressure Histories without Orifice and Using Helium Gas.

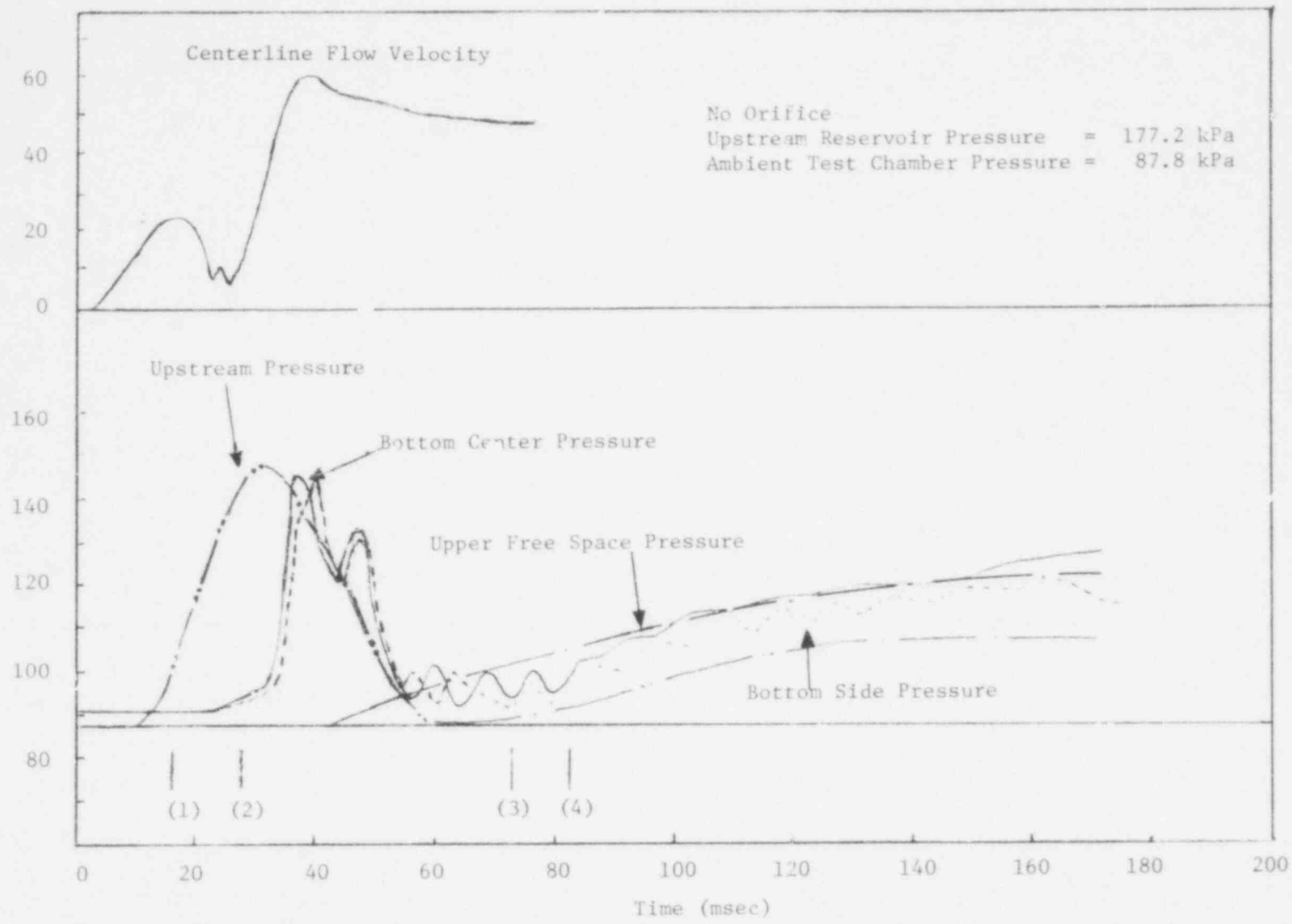

Figure F.14 Flow Rate and Pressure Histories without Orifice and Using Helium Gas

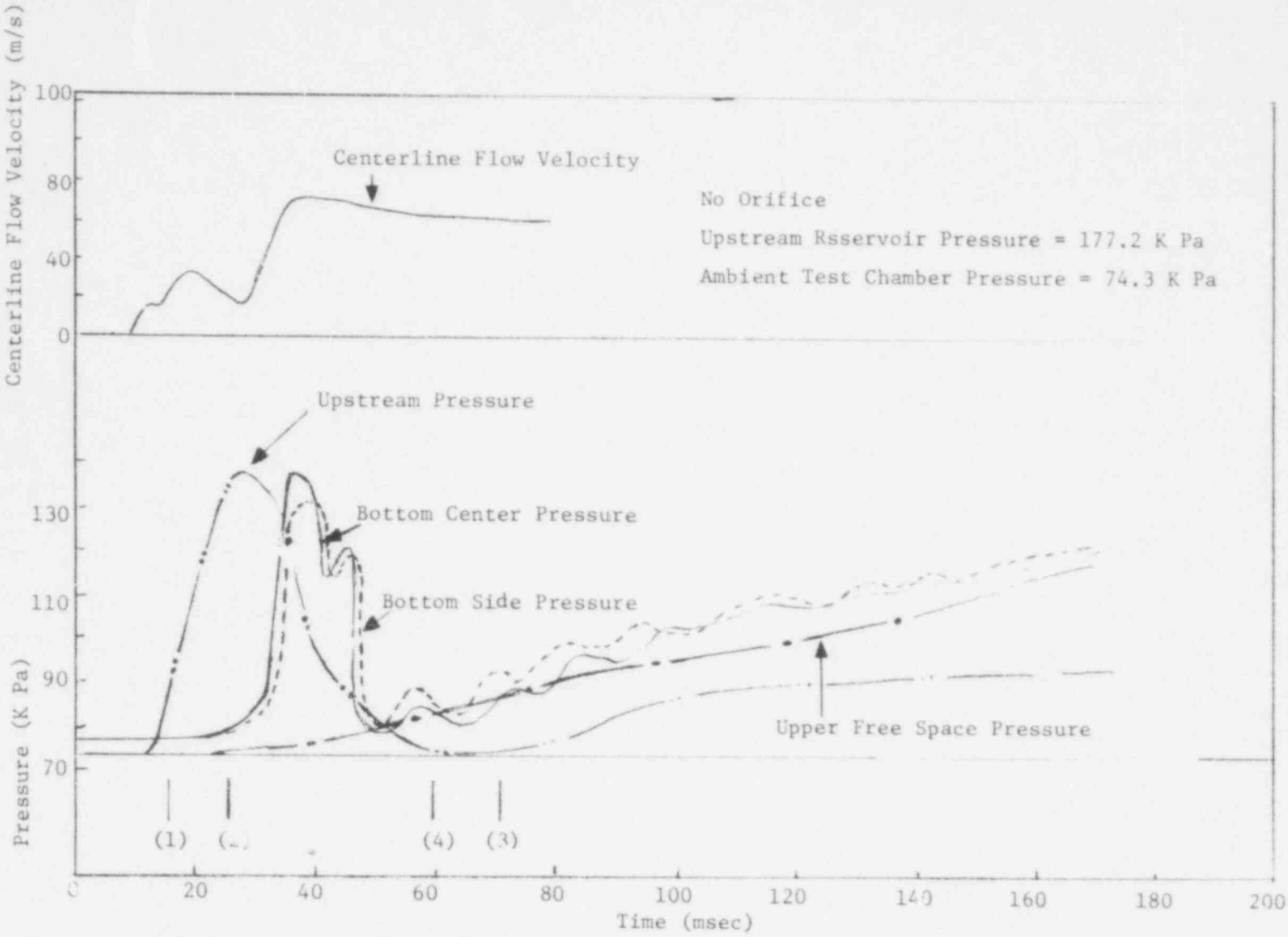

Figure F.15 Flow Rate and Pressure Histories without Orifice and Using Helium Gas.

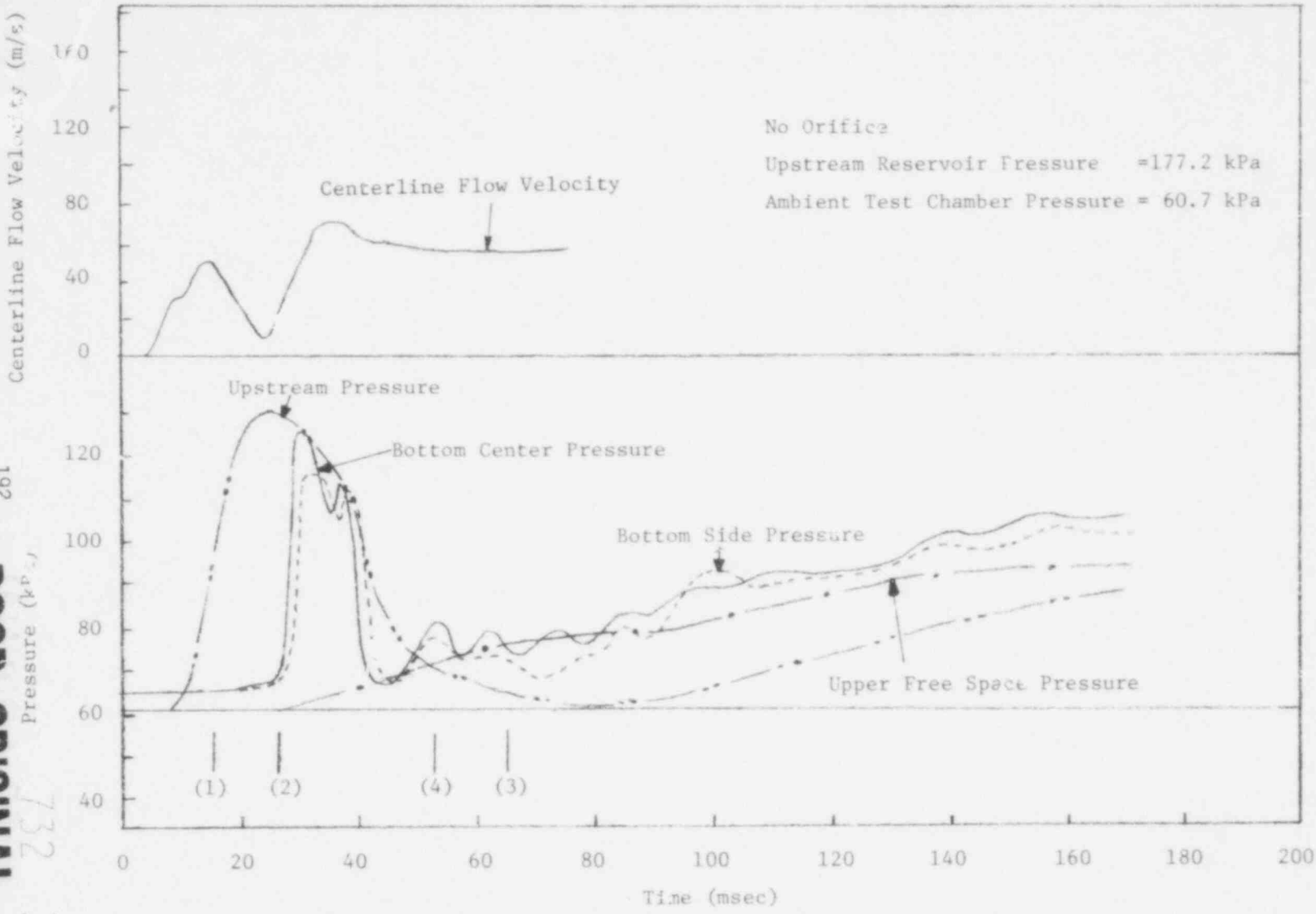

Figure F.16 Flow Rate and Pressure Histories without Orifice and Using Helium

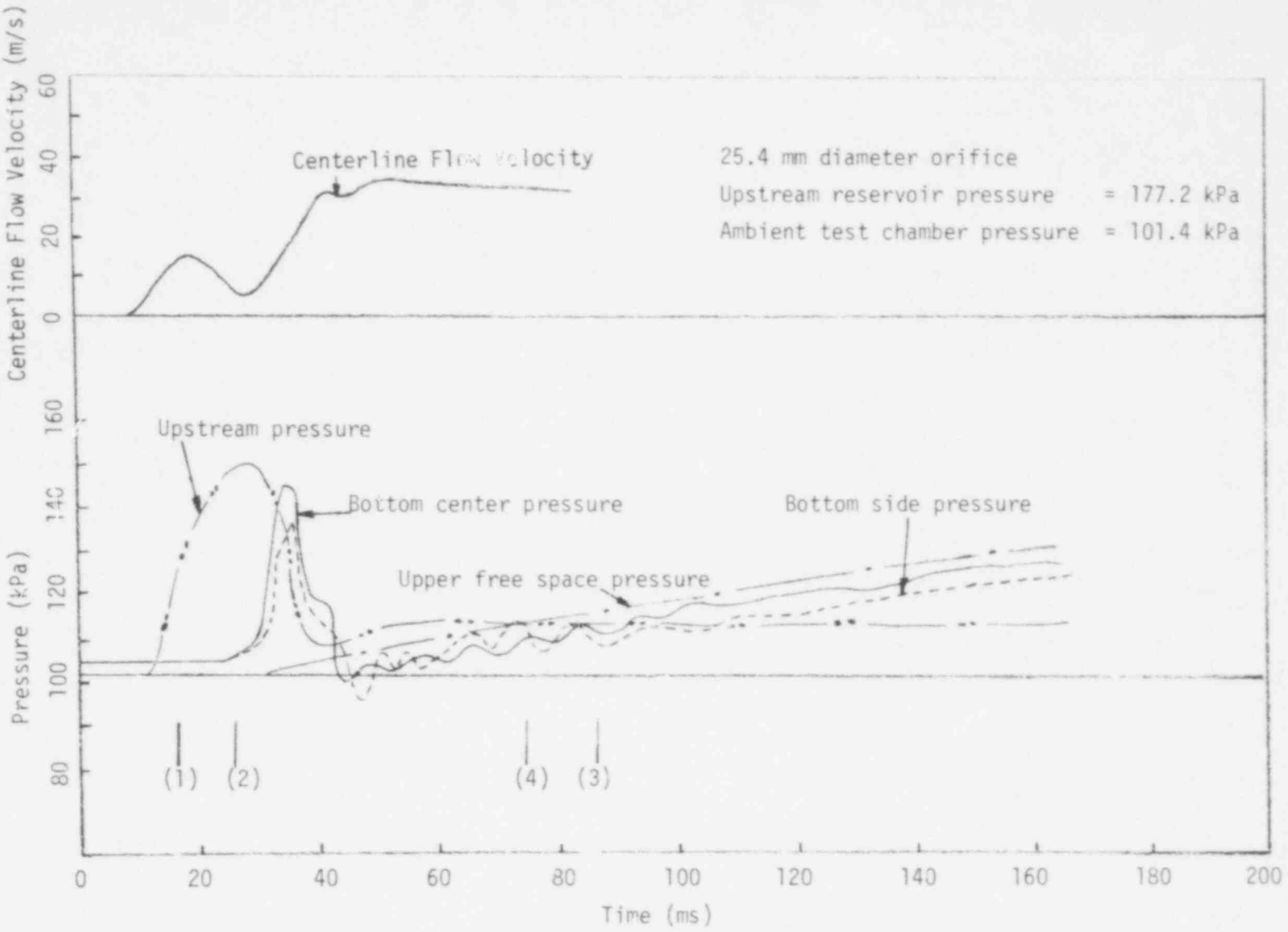

Figure F.17 Flow Rate and Pressure Histories with 25.4 mm Diameter Orifice and Using Helium Gas

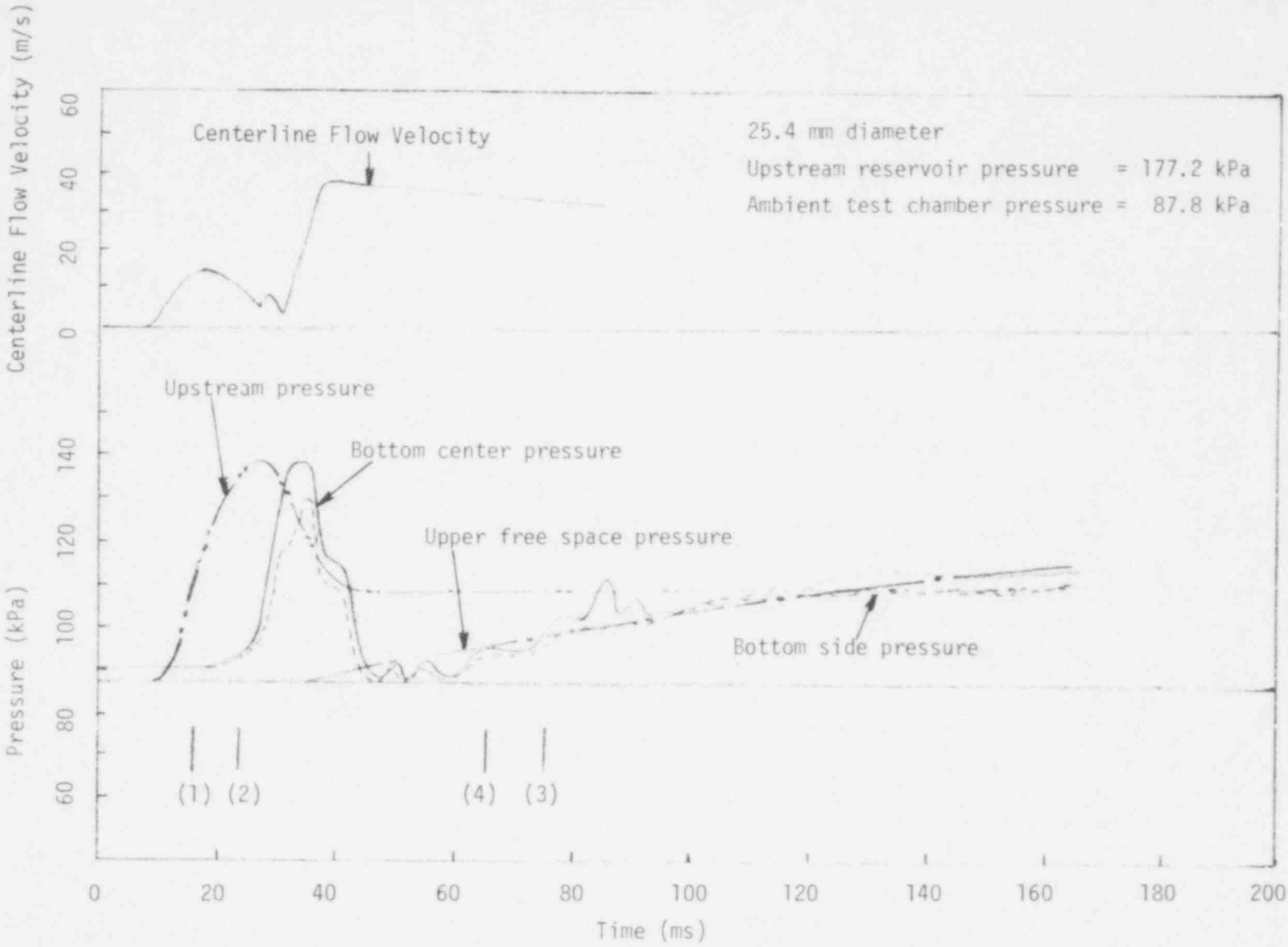

Figure F.18 Flow Rate and Pressure Histories with 25.4 mm Diameter Orifice and Using Helium Gas

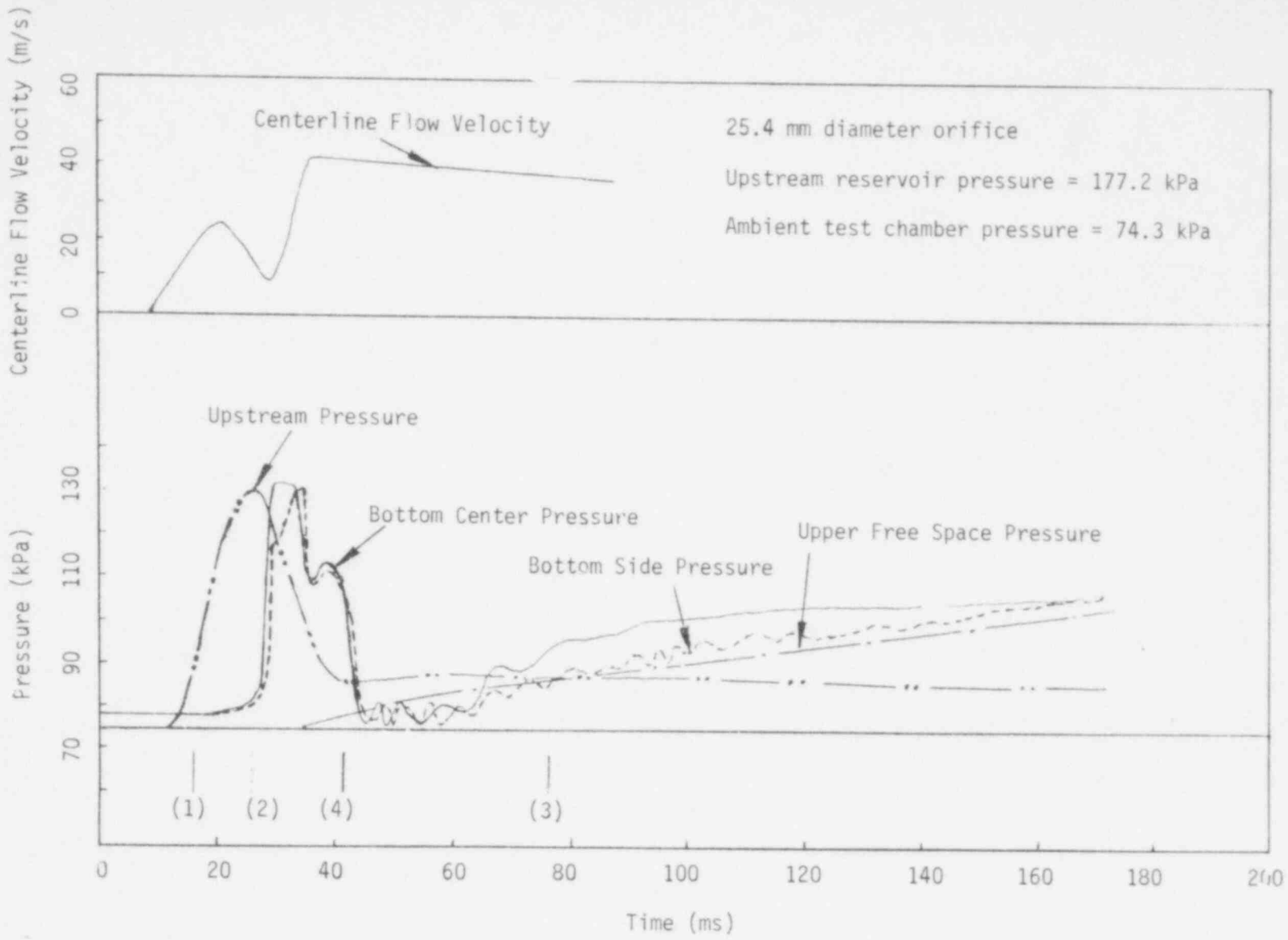

Figure F.19 . Flow Rate and Pressure Histories with 25.4 mm Diameter Orifice and Using Helium Gas.

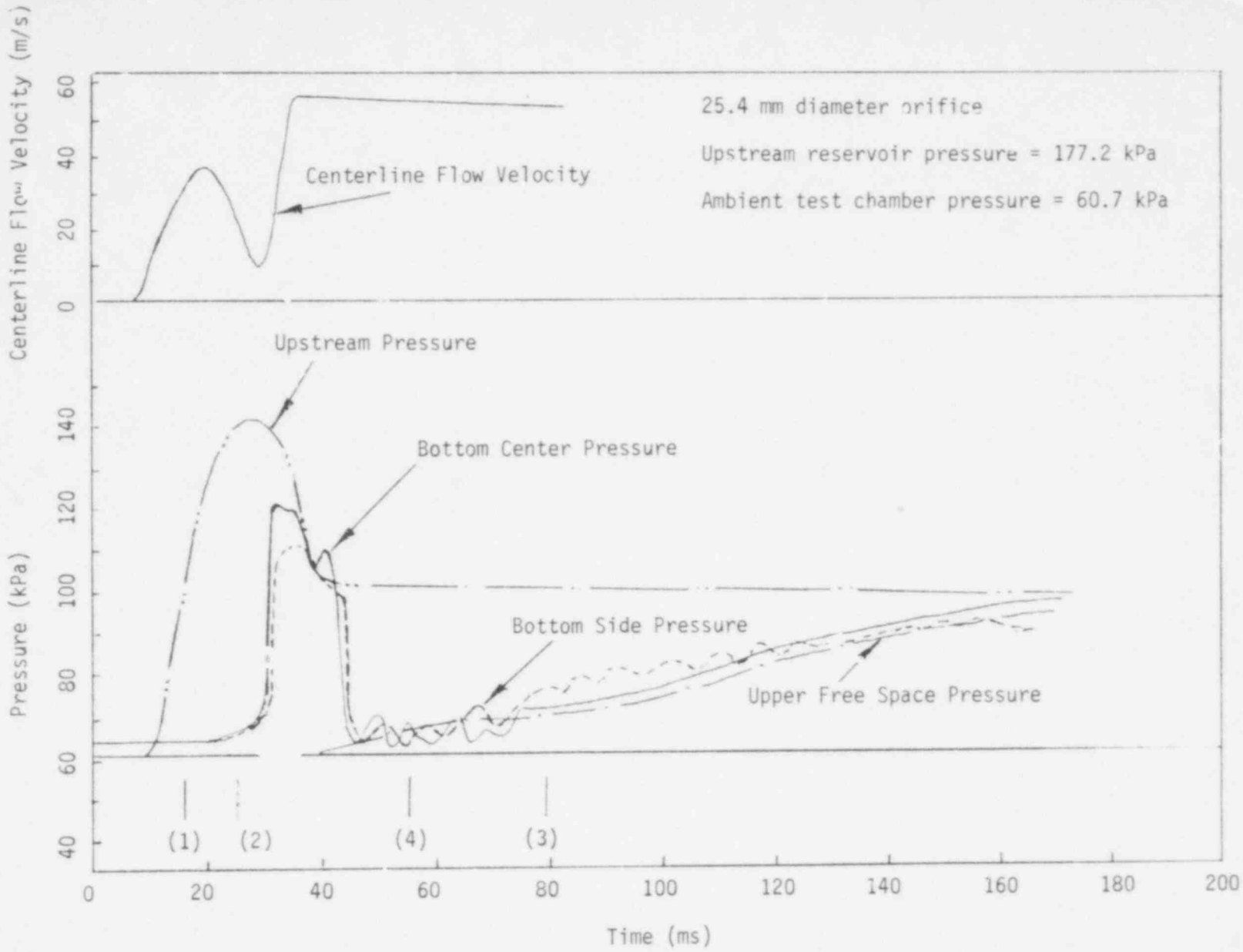

Figure F.20. Flow Rate and Pressure Histories with 25.4 mm Diameter Orifice and Using Helium Gas.

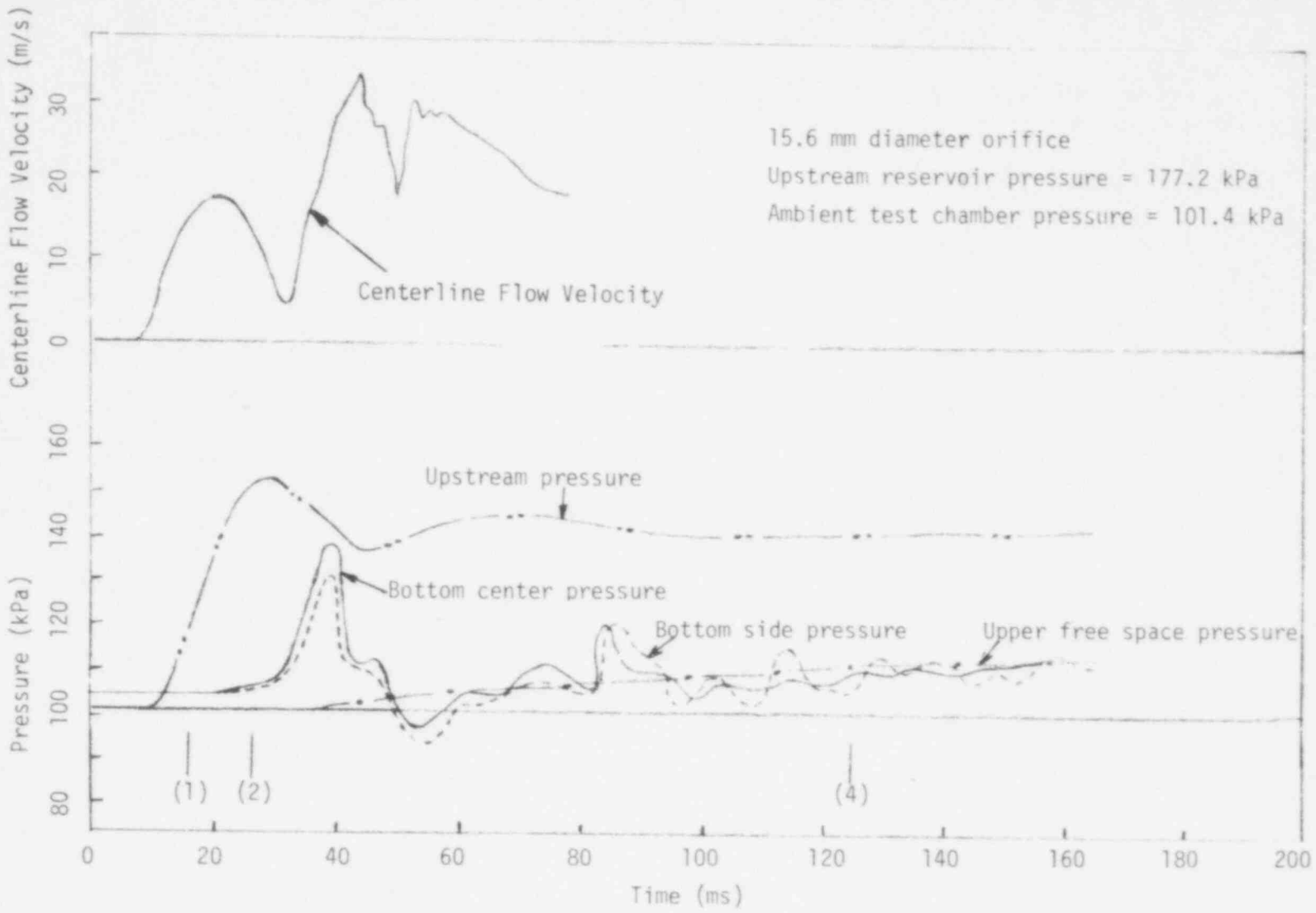

Figure F.21 Flow Rate and Pressure Histories with 15.6 mm Diameter Orifice and Using Helium Gas

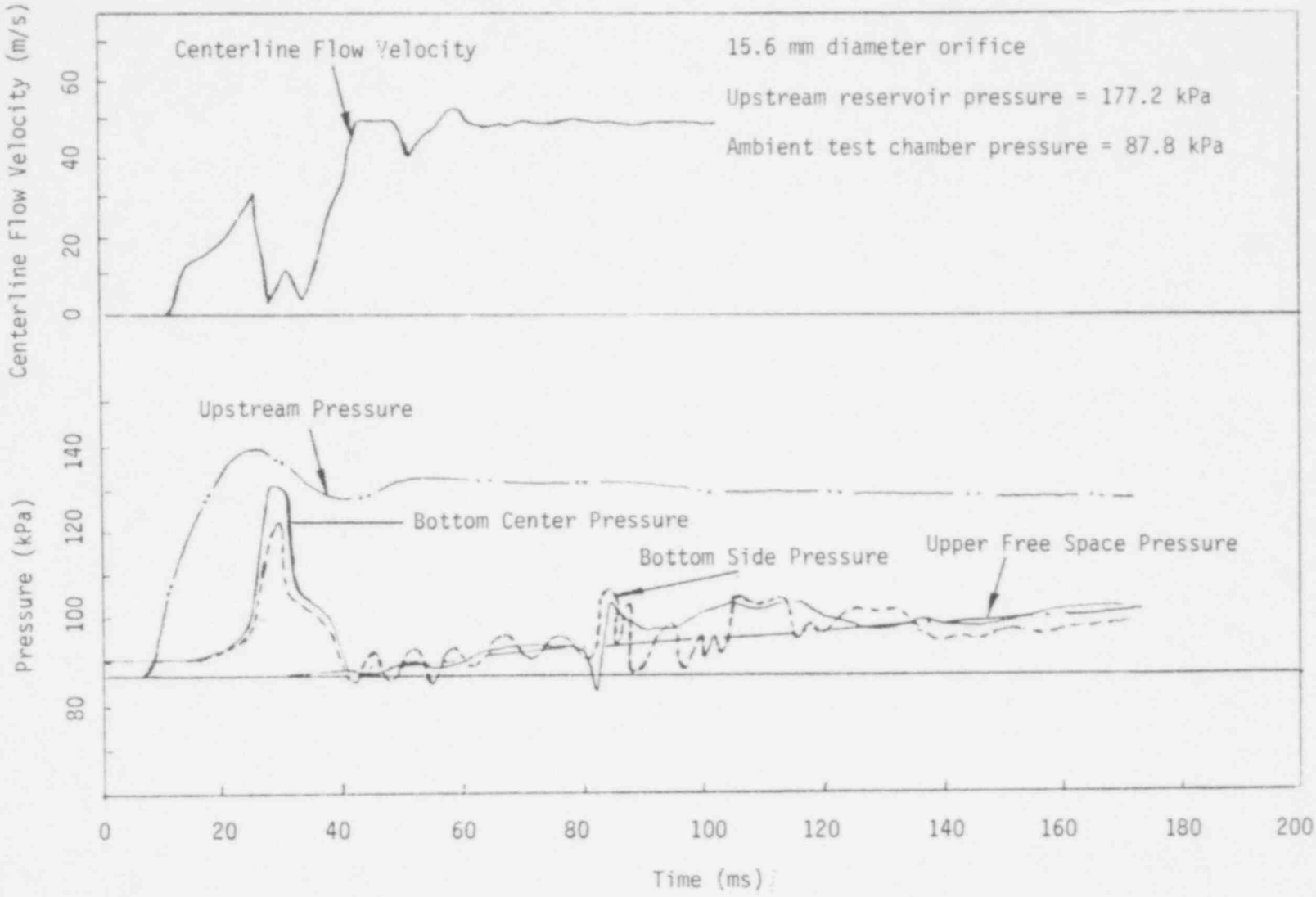

Figure F.22. Flow Rate and Pressure Histories with 15.6 mm Diameter Orifice and Using Helium Gas.

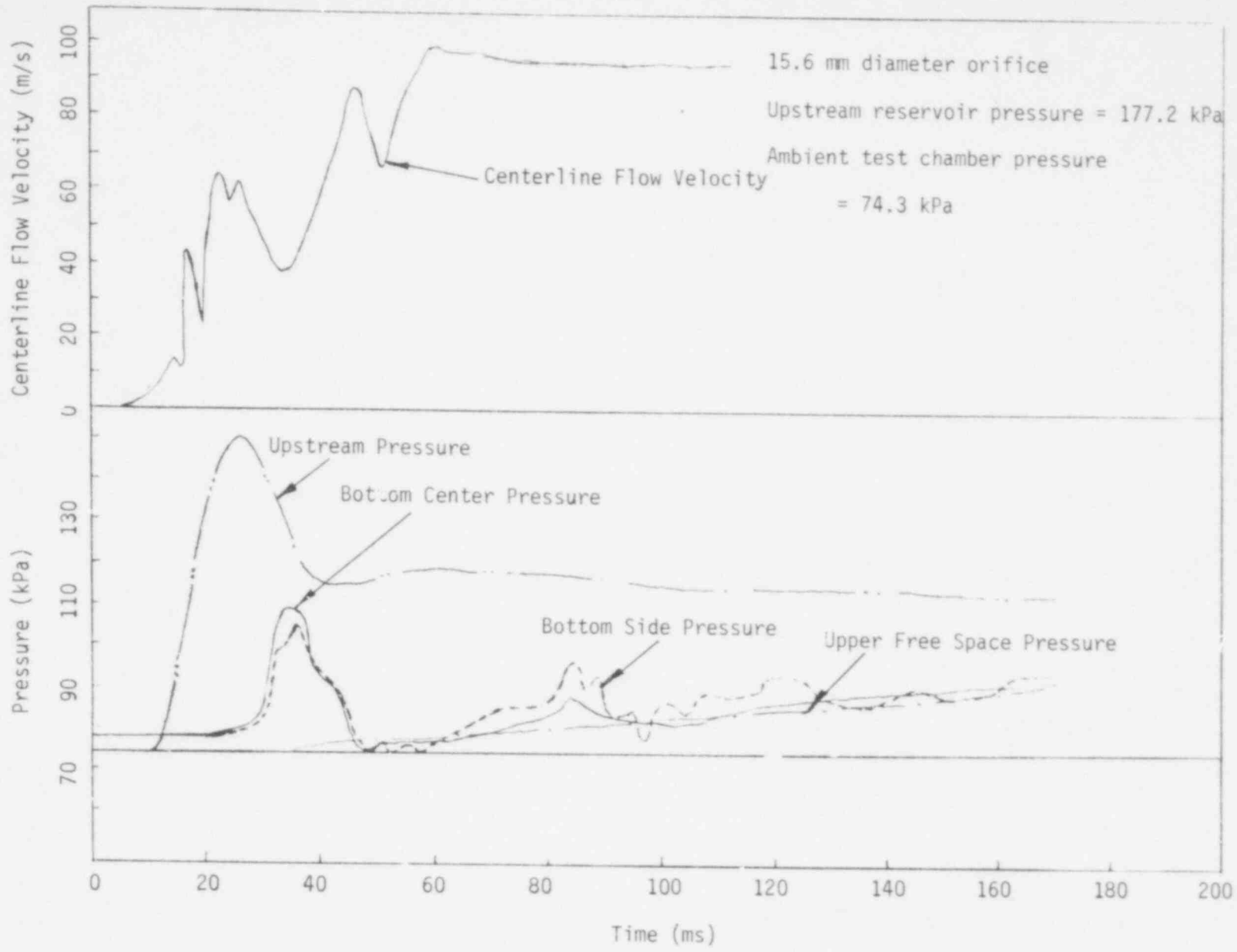

Figure F.23. Flow Rate and Pressure Histories with 15.6 mm Diameter Orifice and Using Helium Gas.

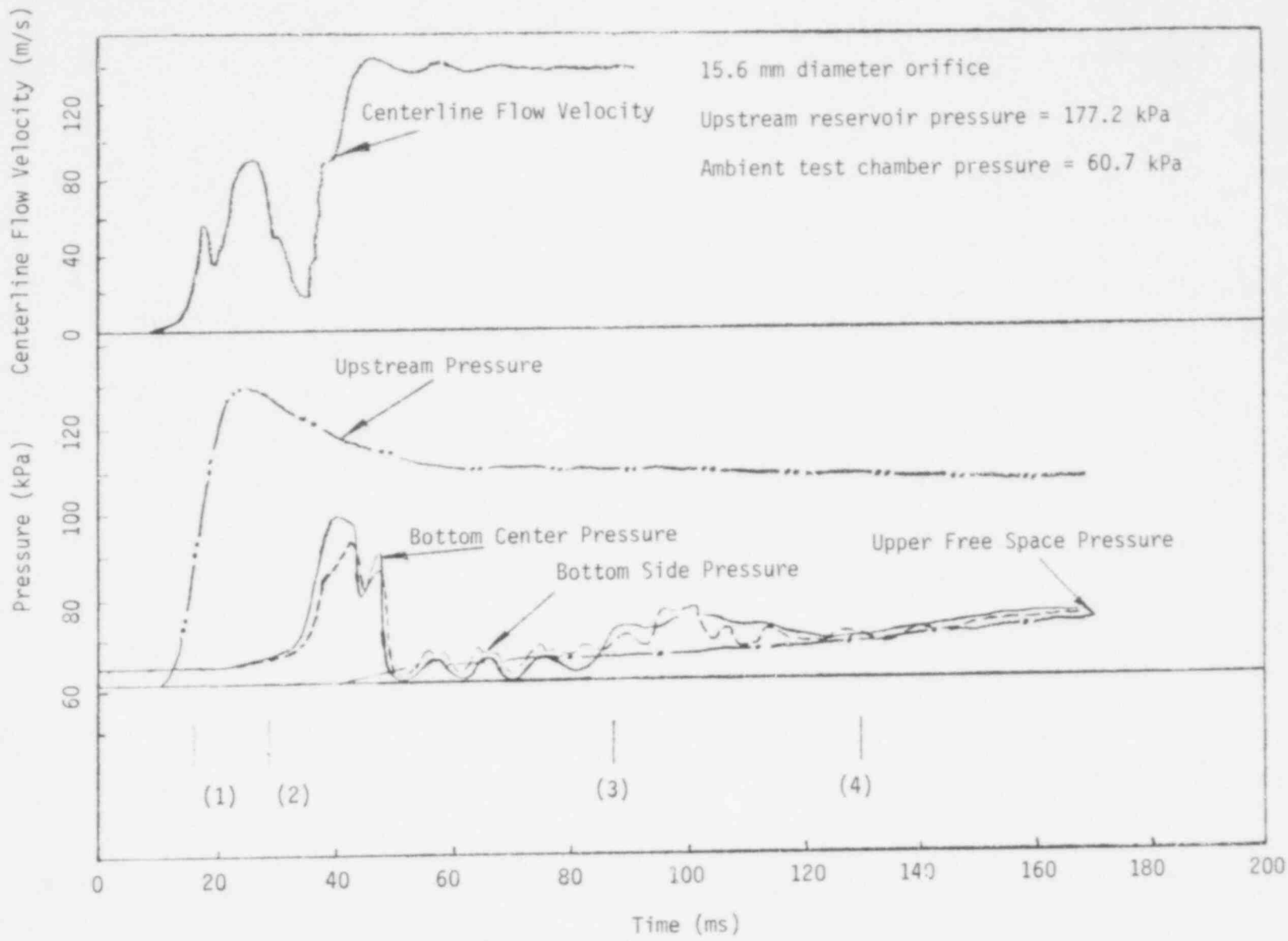

Figure F.24. Flow Rate and Pressure Histories with 15.6 mm Diameter Orifice and Using Helium Gas.

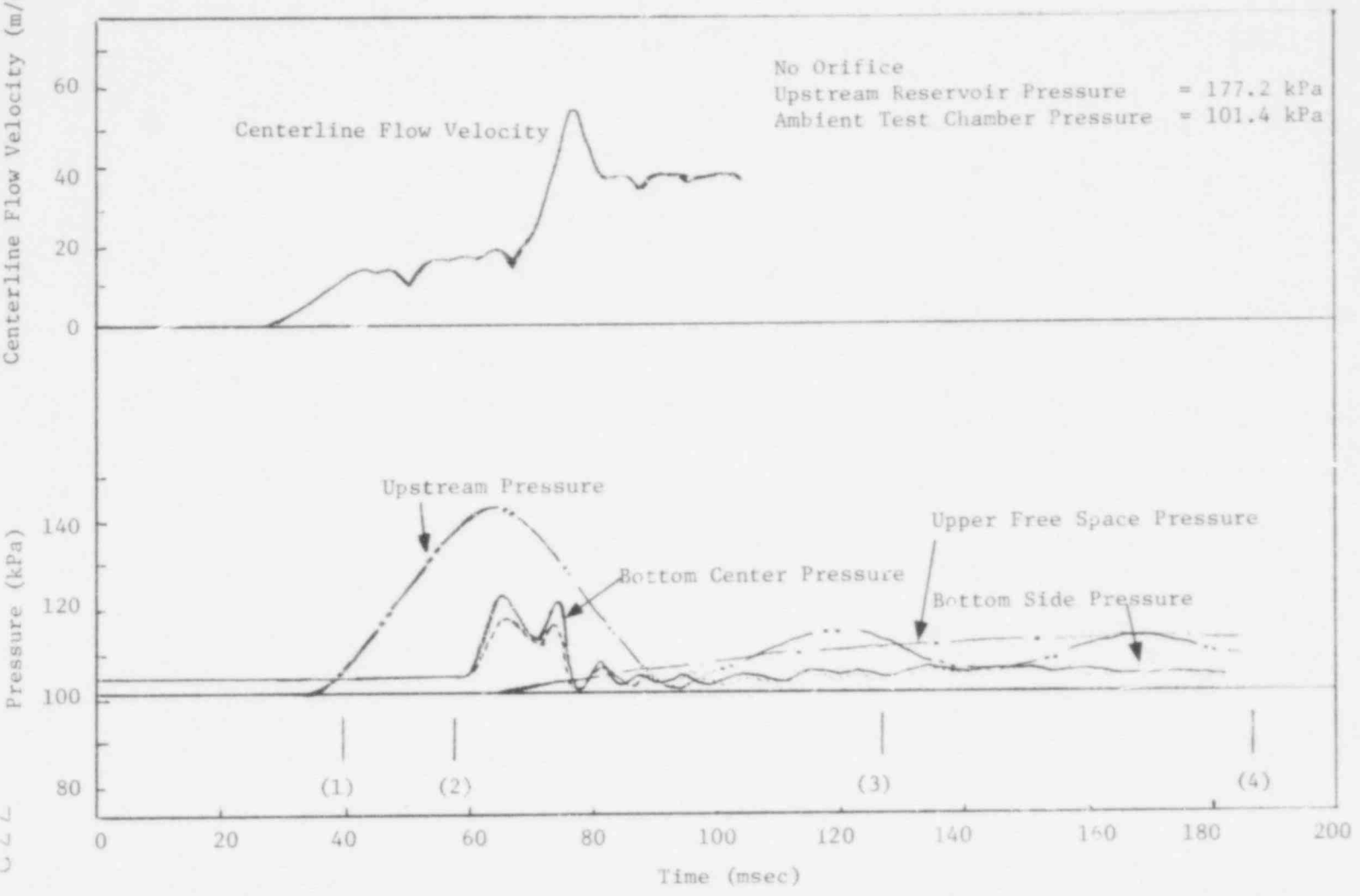

Figure F.25 Flow Rate and Pressure Histories without Orifice and Using Argon Gas

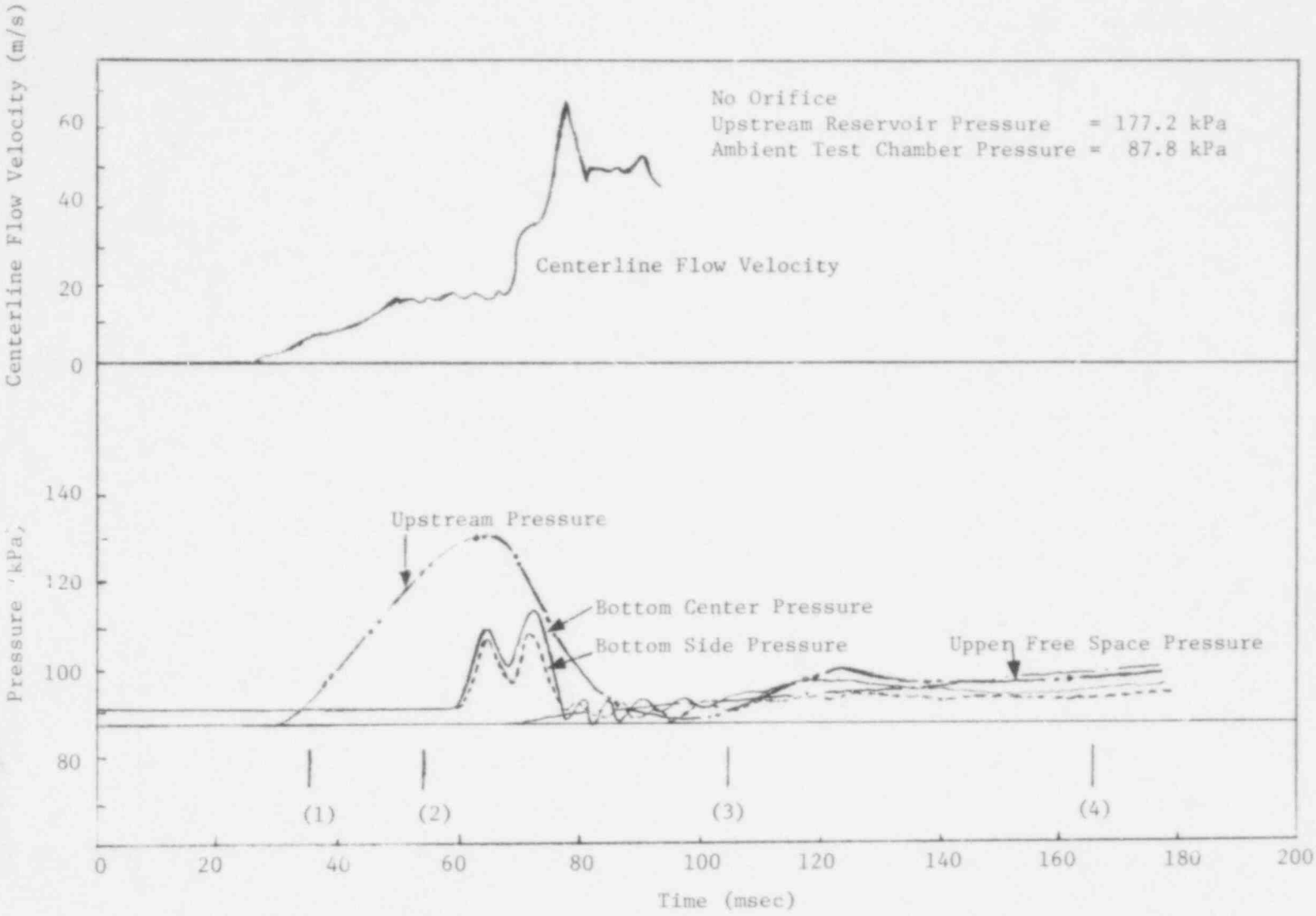

Figure F.26 Flow Rate and Pressure Histories without Orifice and Using Argon Gas

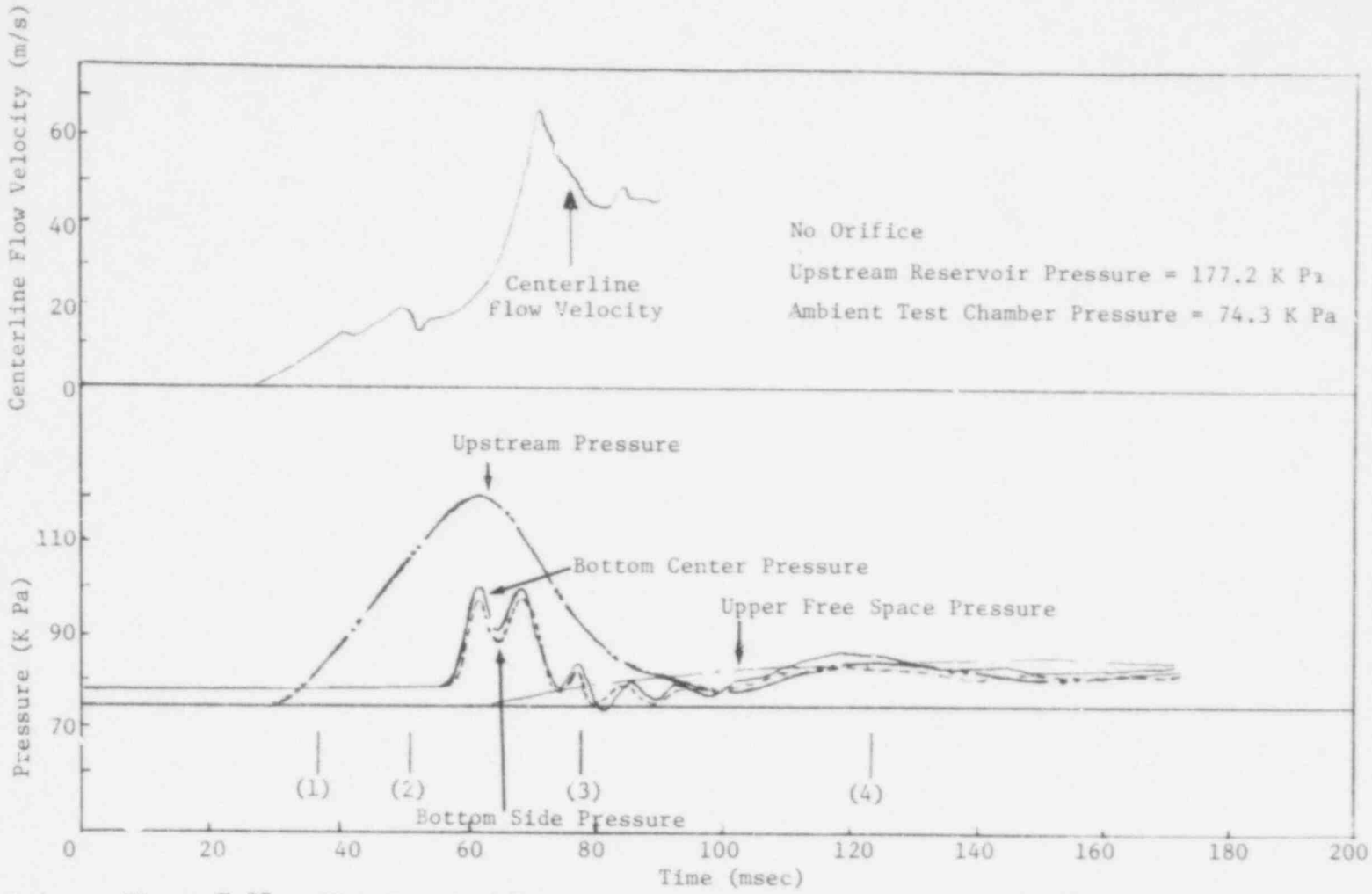

Figure F.27 Flow Rate and Pressure Histories without Orifice and Using Argon Gas.

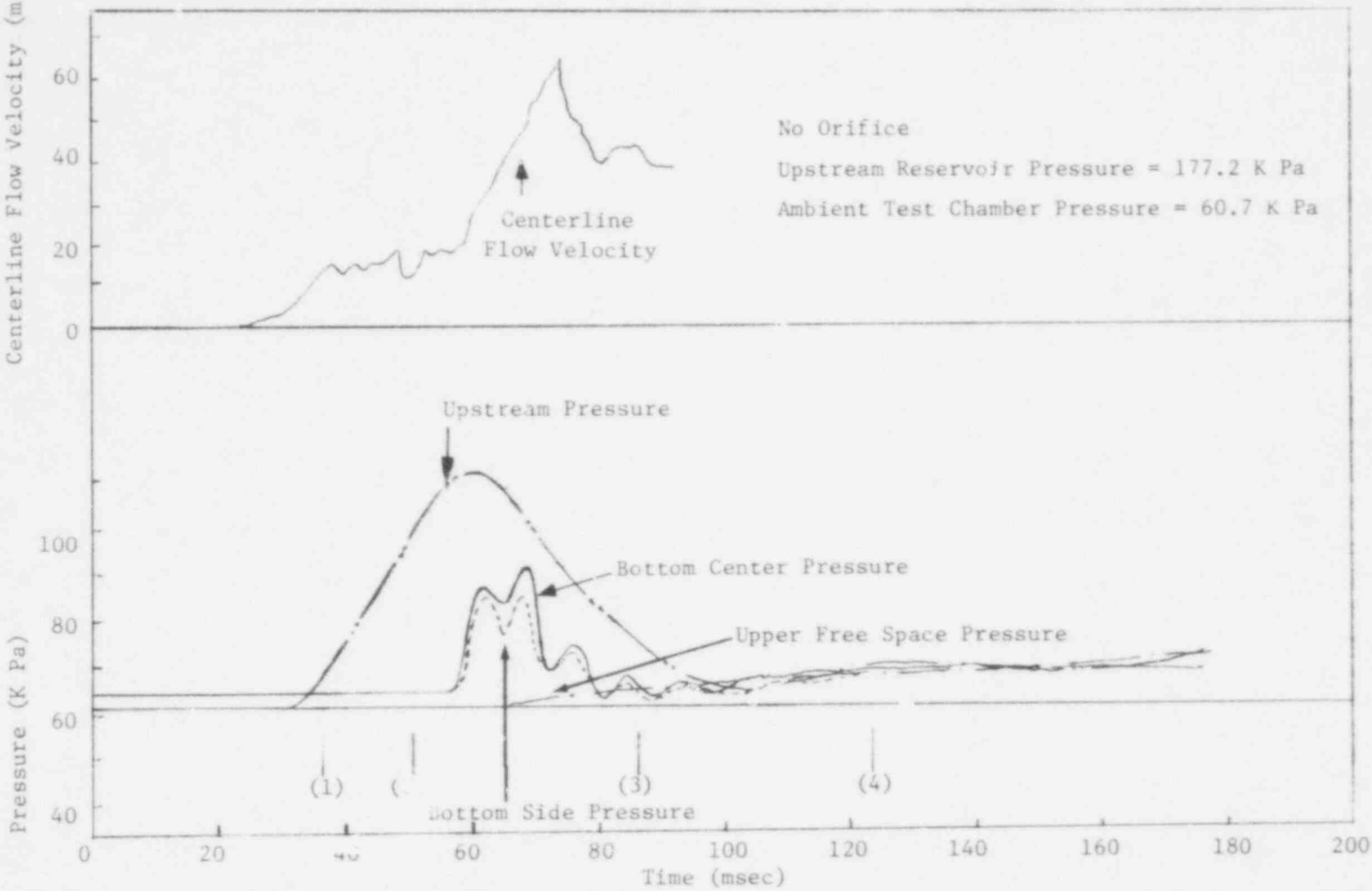

Figure F.28 Flow Rate and Pressure Histories without Orifice and Using Argon Gas

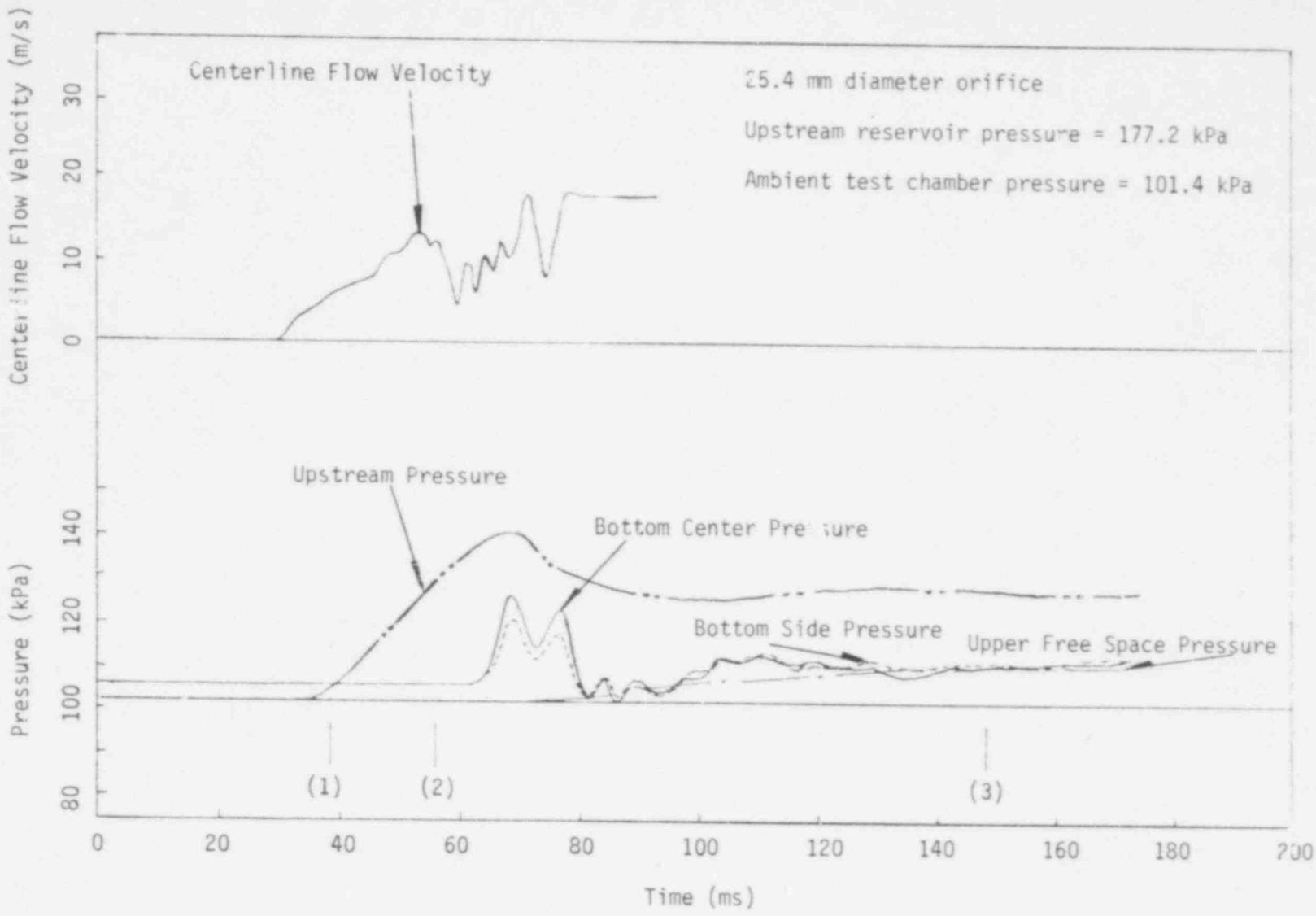

Figure F.29. Flow Rate and Pressure Histories with 25.4 mm Diameter Orifice and Using Argon Gas.

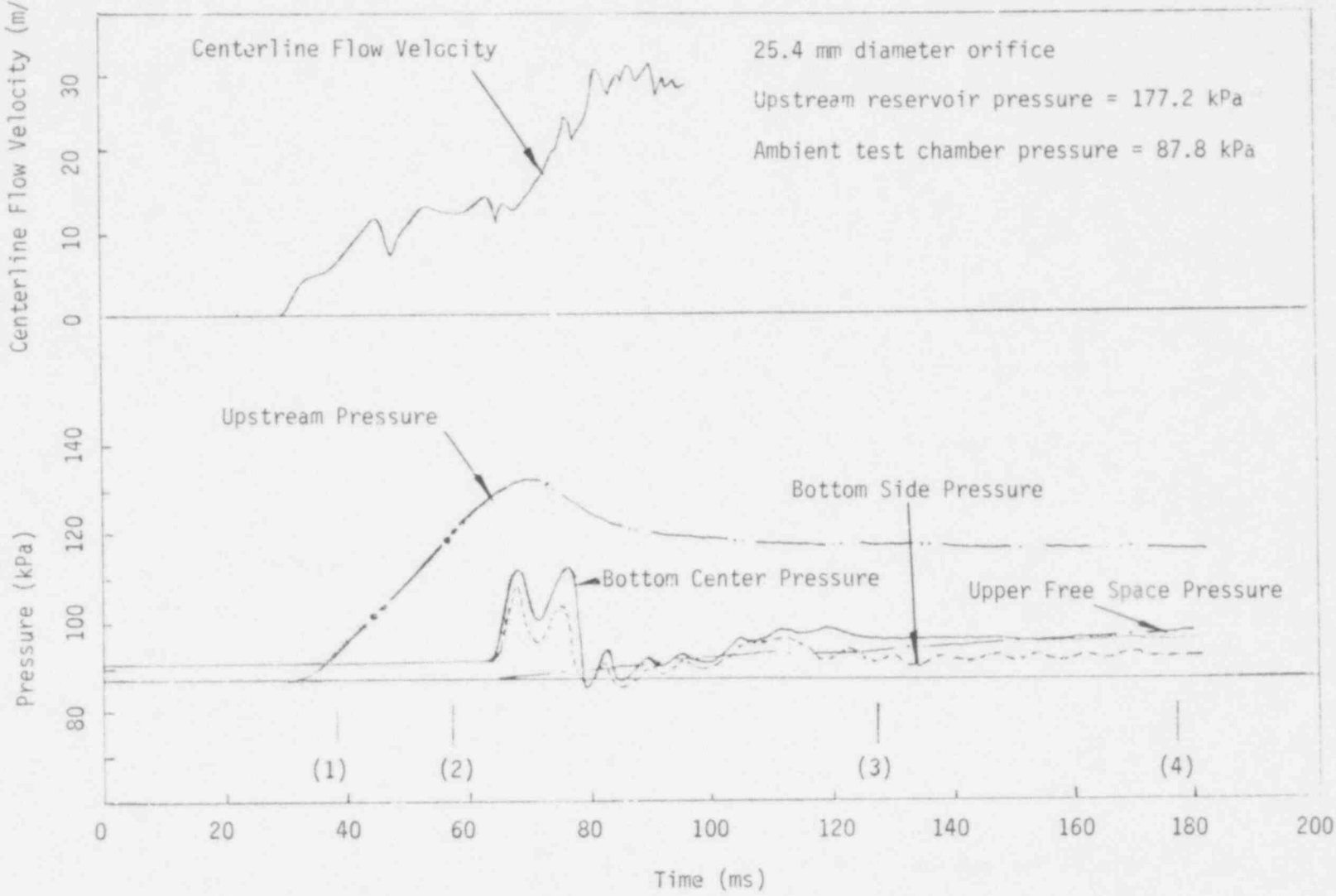

Figure F.30. Flow Rate and Pressure Histories with 25.4 mm Diameter Orifice and Using Argon Gas.

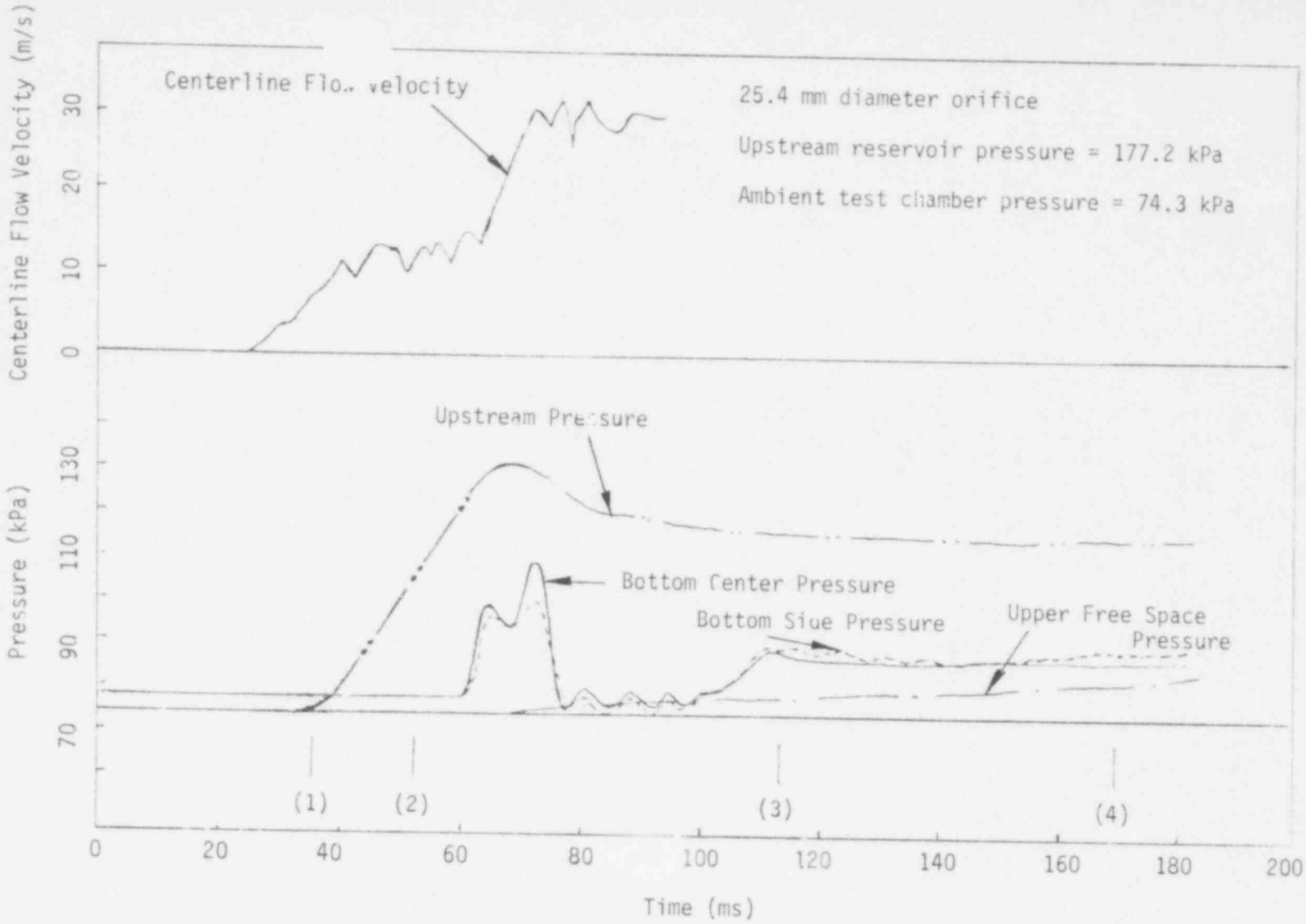

Figure F.31 . Flow Rate and Pressure Histories with 25.4 mm Diameter Orifice and Using Argon Gas.

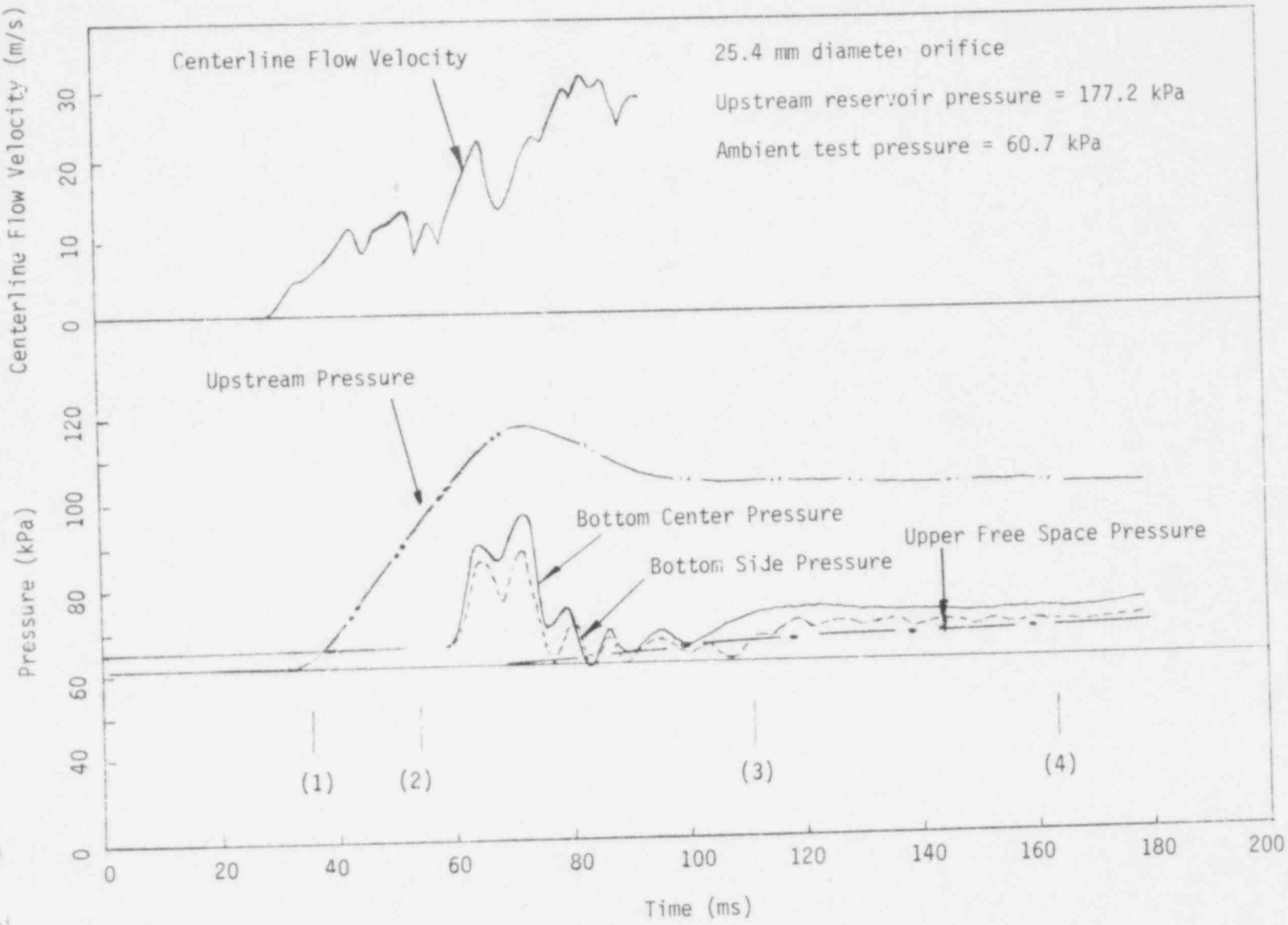

Figure F.32 . Flow Rate and Pressure Histories with 25.4 mm Diameter Orifice and Using Argon Gas.

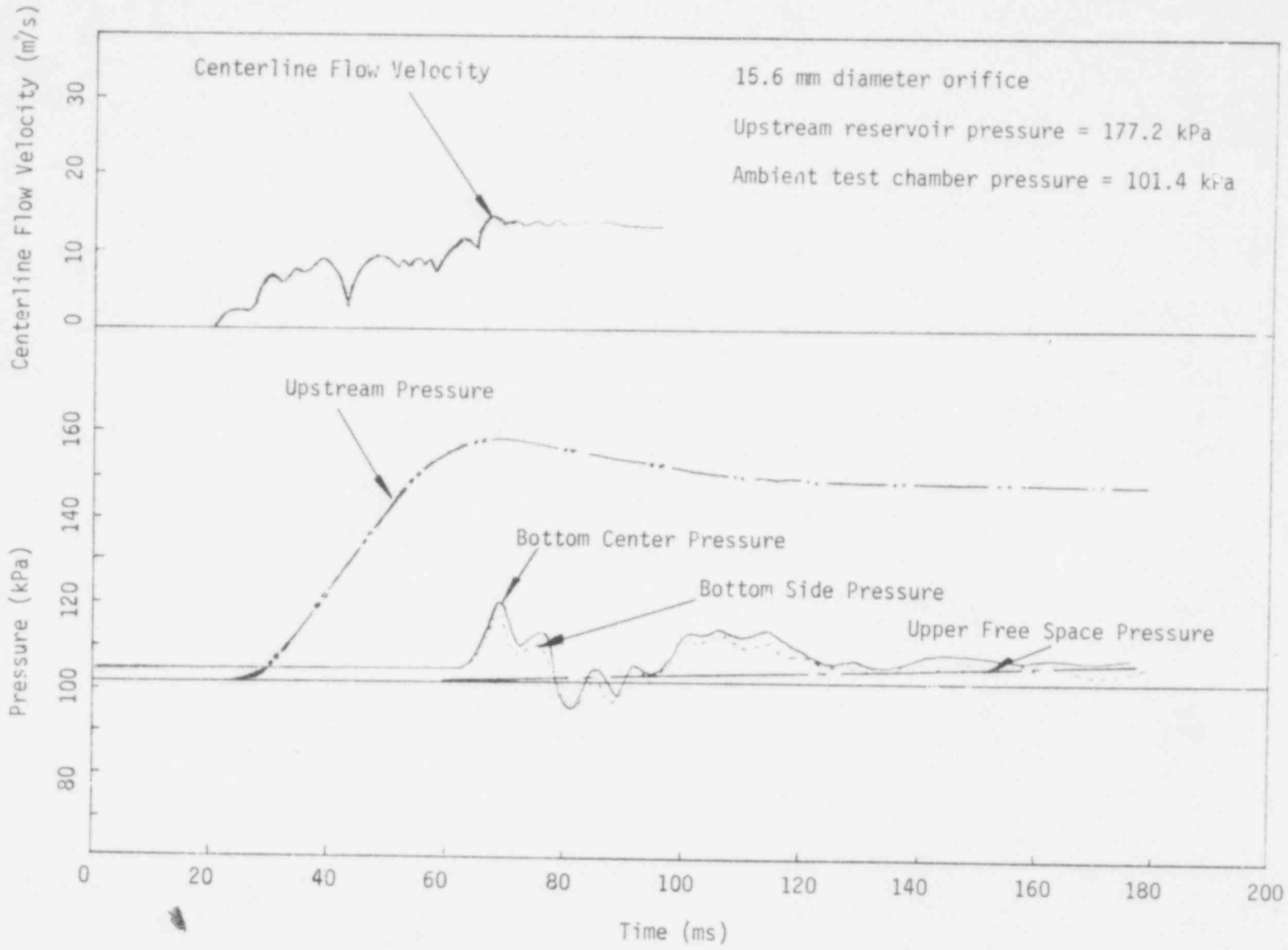

Figure F.33 . Flow Rate and Pressure Histories with 15.6 mm diameter Orifice and Using Argon Gas.

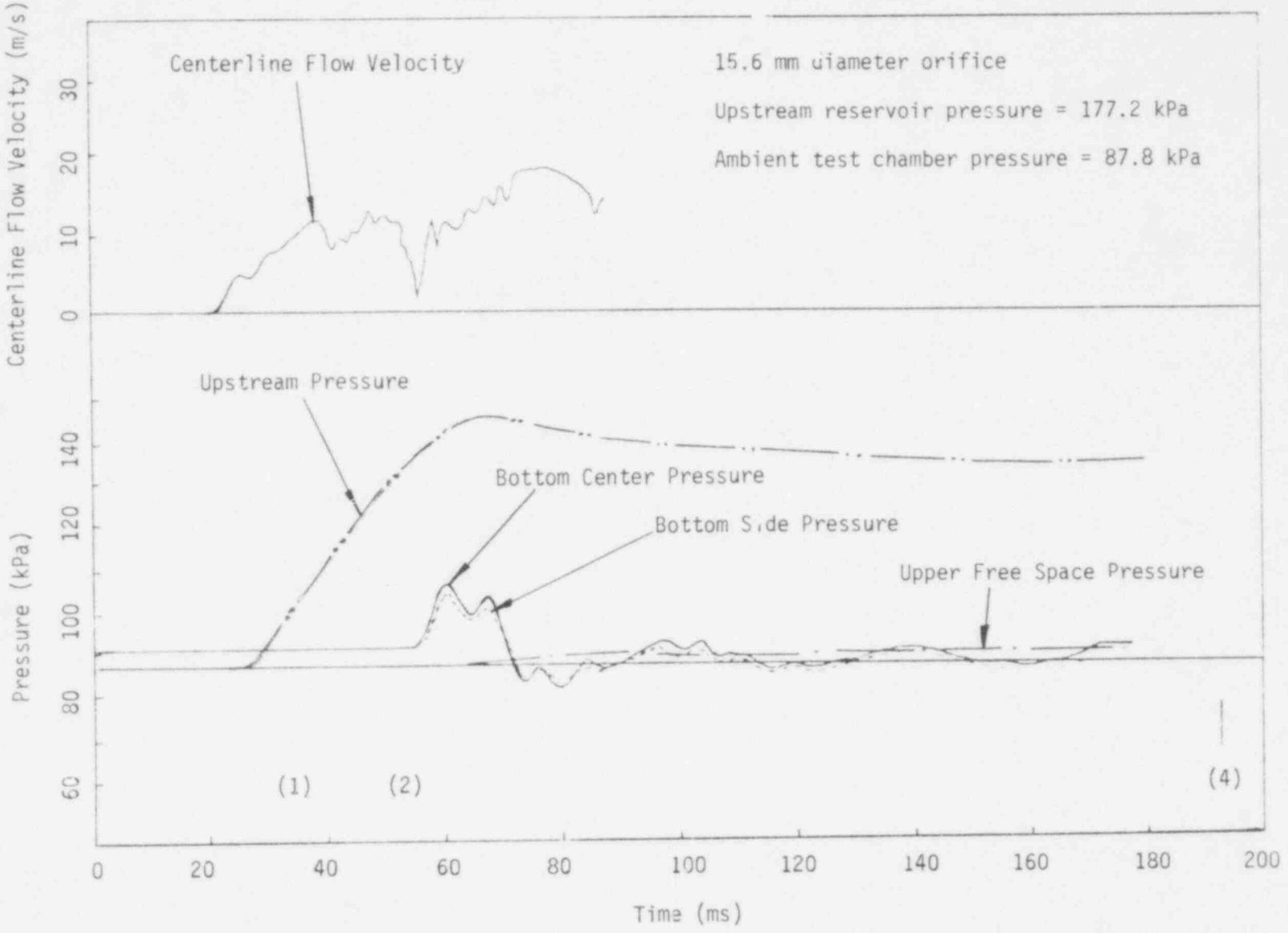

Figure F.34 . Flow Rate and Pressure Histories with 15.6 mm Diameter Orifice and Using Argon Gas.

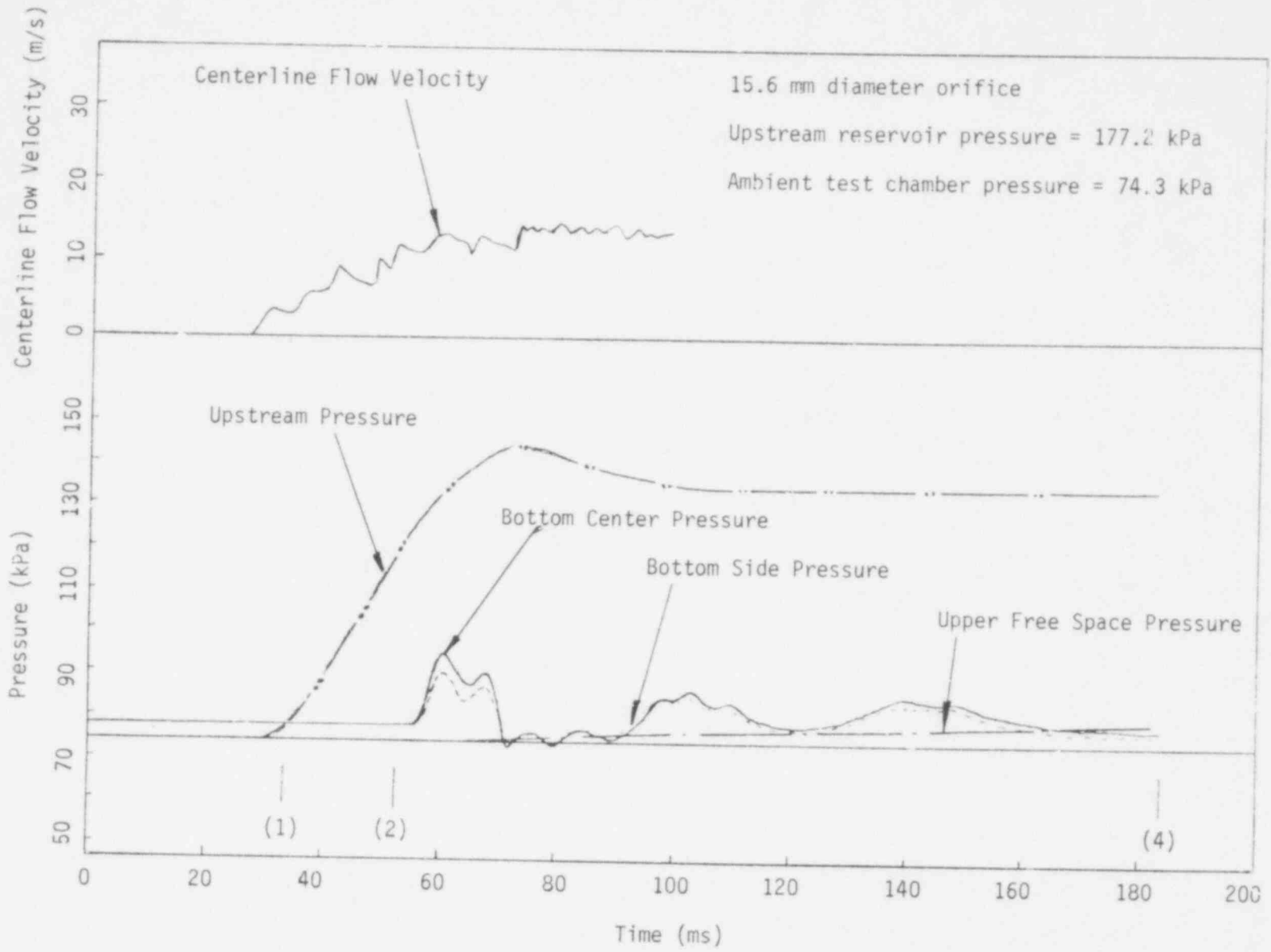

Figure F.35 . Flow Rate and Pressure Histories with 15.6 mm Diameter Orifice and Using Argon Gas.

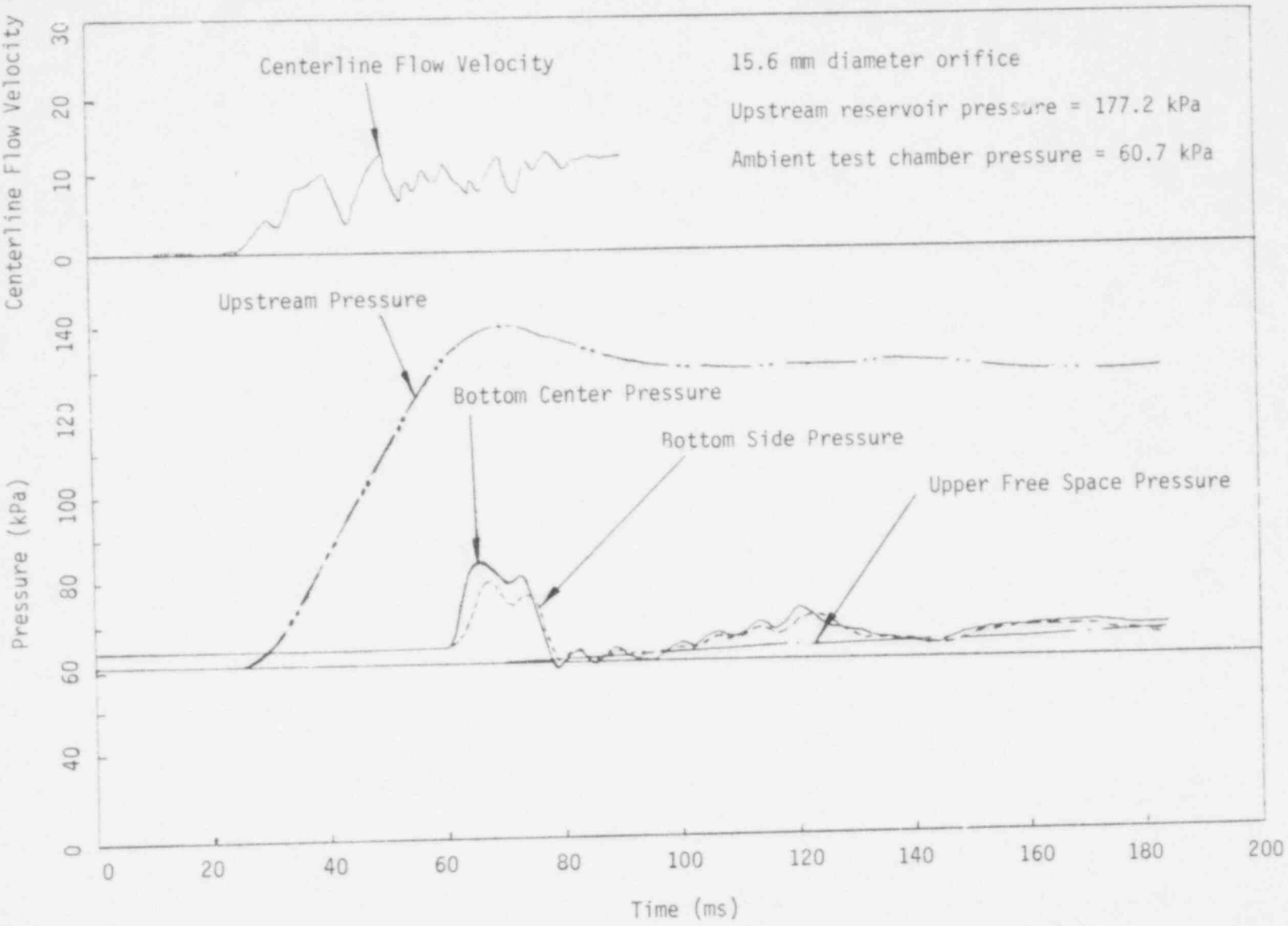

Figure F.36. Flow Rate and Pressure Histories with 15.6 mm Diameter Orifice and Using Argon Gas.

Appendix G. Pool Swelling and Water Splash

This Appendix summarizes the pool swelling height and the water splashing level for different gases and orifices. These data are deduced from the bubble growth pictures presented in Appendix F.

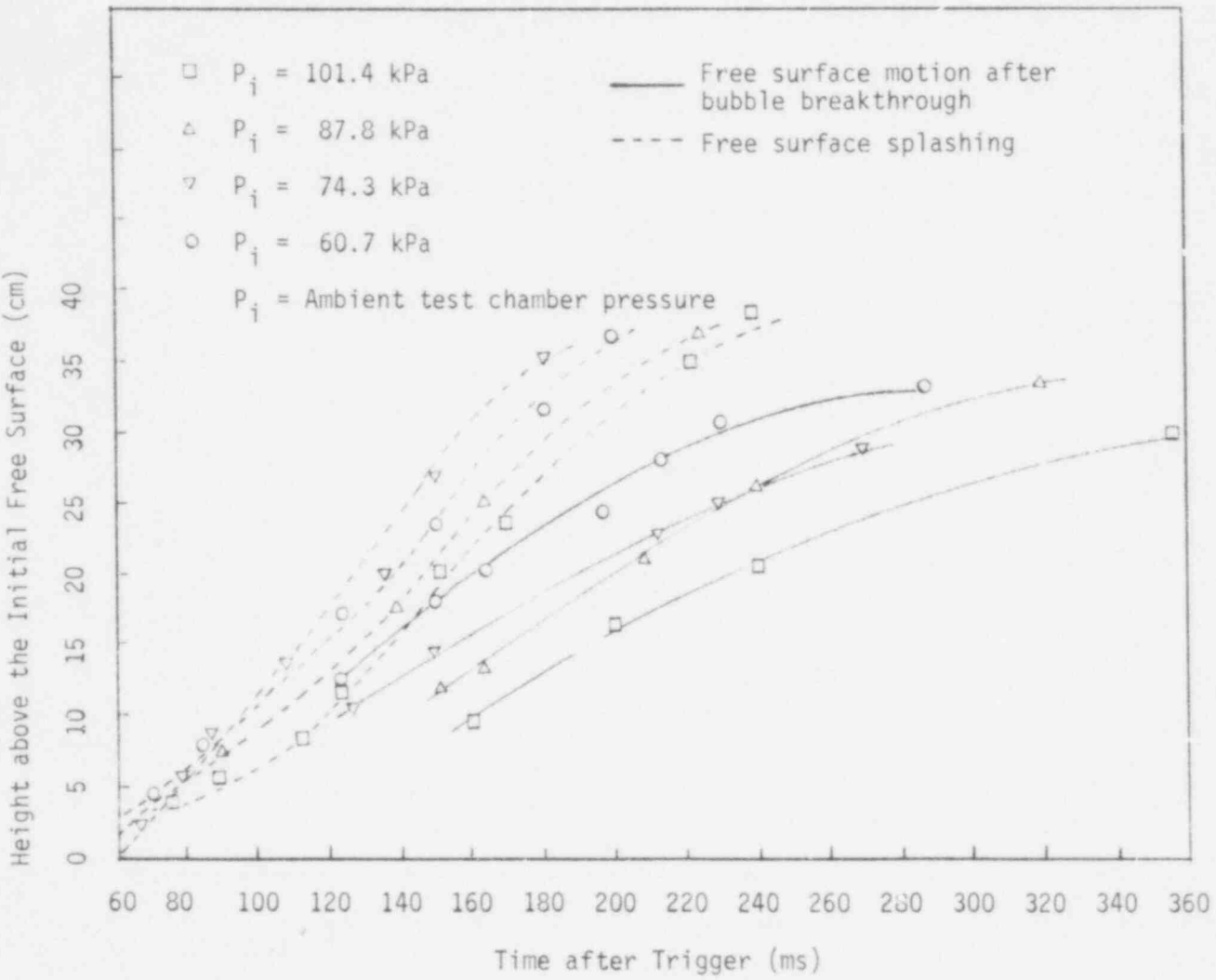

Figure G.1. Pool Swell and Splash Height History for 177.2 kPa Upstream Pressure and 46 mm Diameter Tube in Air Medium without Orifice.

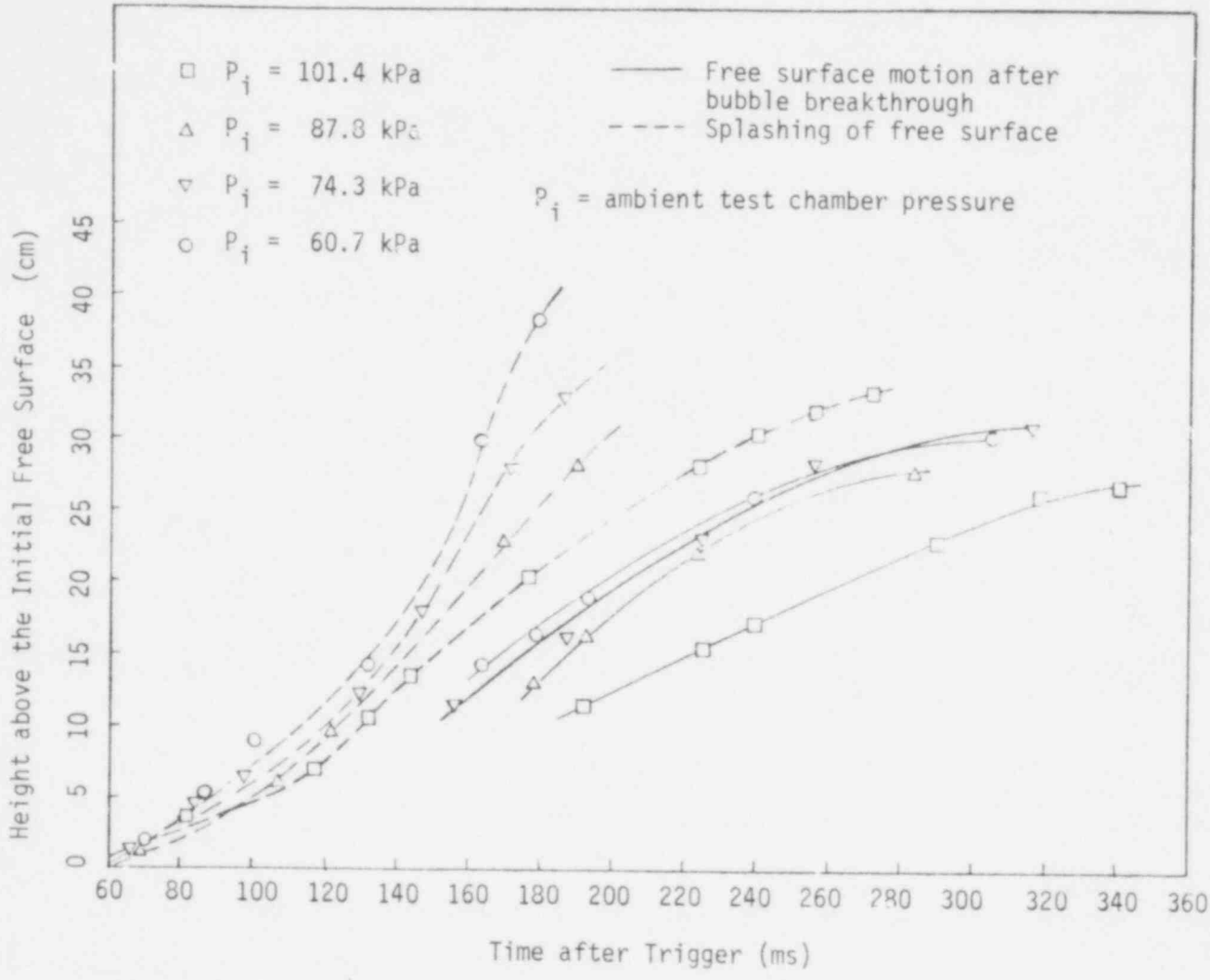

Figure G.2 Pool Swell and Splash Height History for 177.2 kPa Upstream Pressure and 46 mm Diameter Tube in Air Medium with 2.54 cm Diameter Orifice.

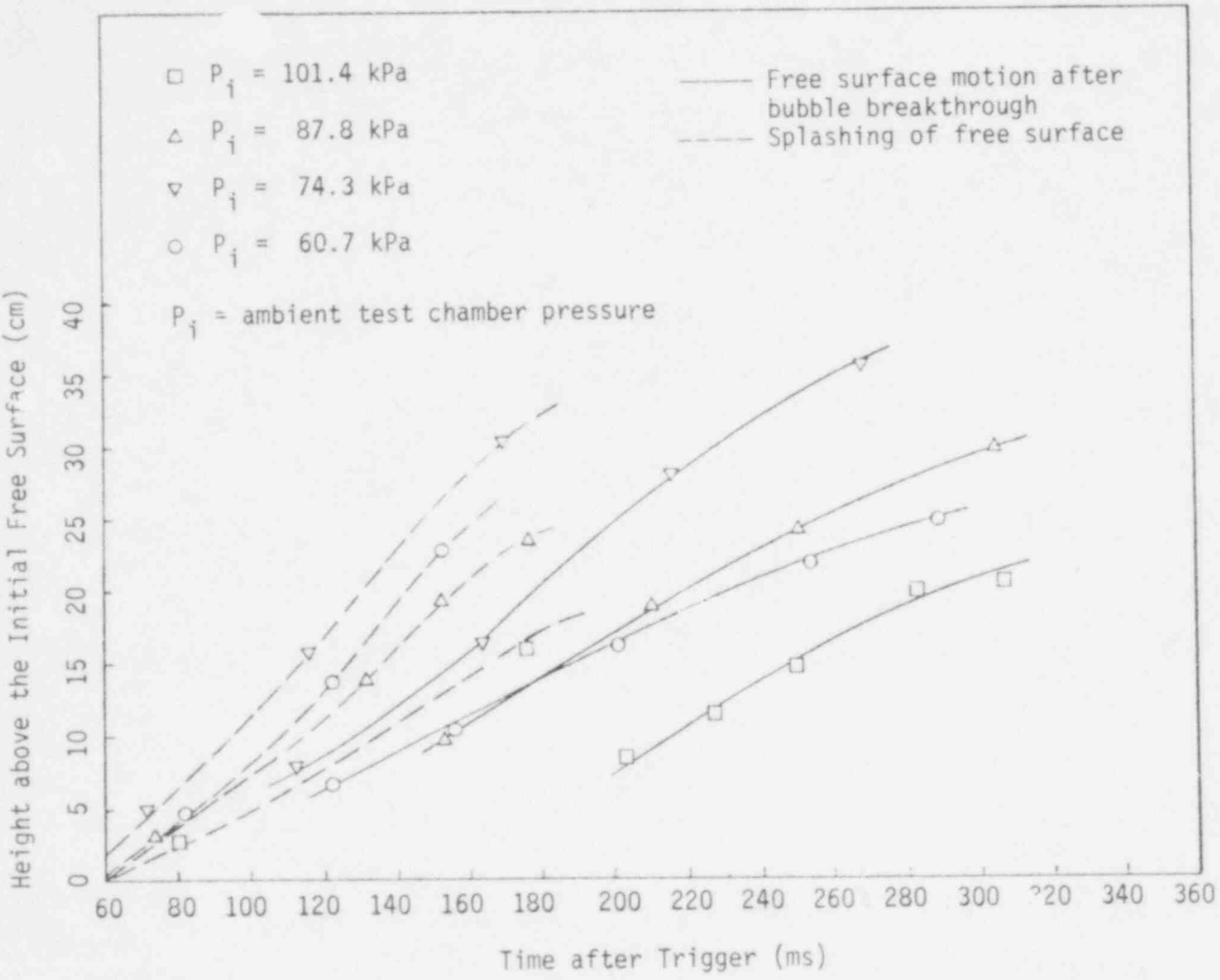

Figure G.3 Pool Swell and Splash Height History for 177.2 kPa Upstream Pressure and 46 mm Diameter Tube in Air Medium with 1.56 cm Diameter Orifice.

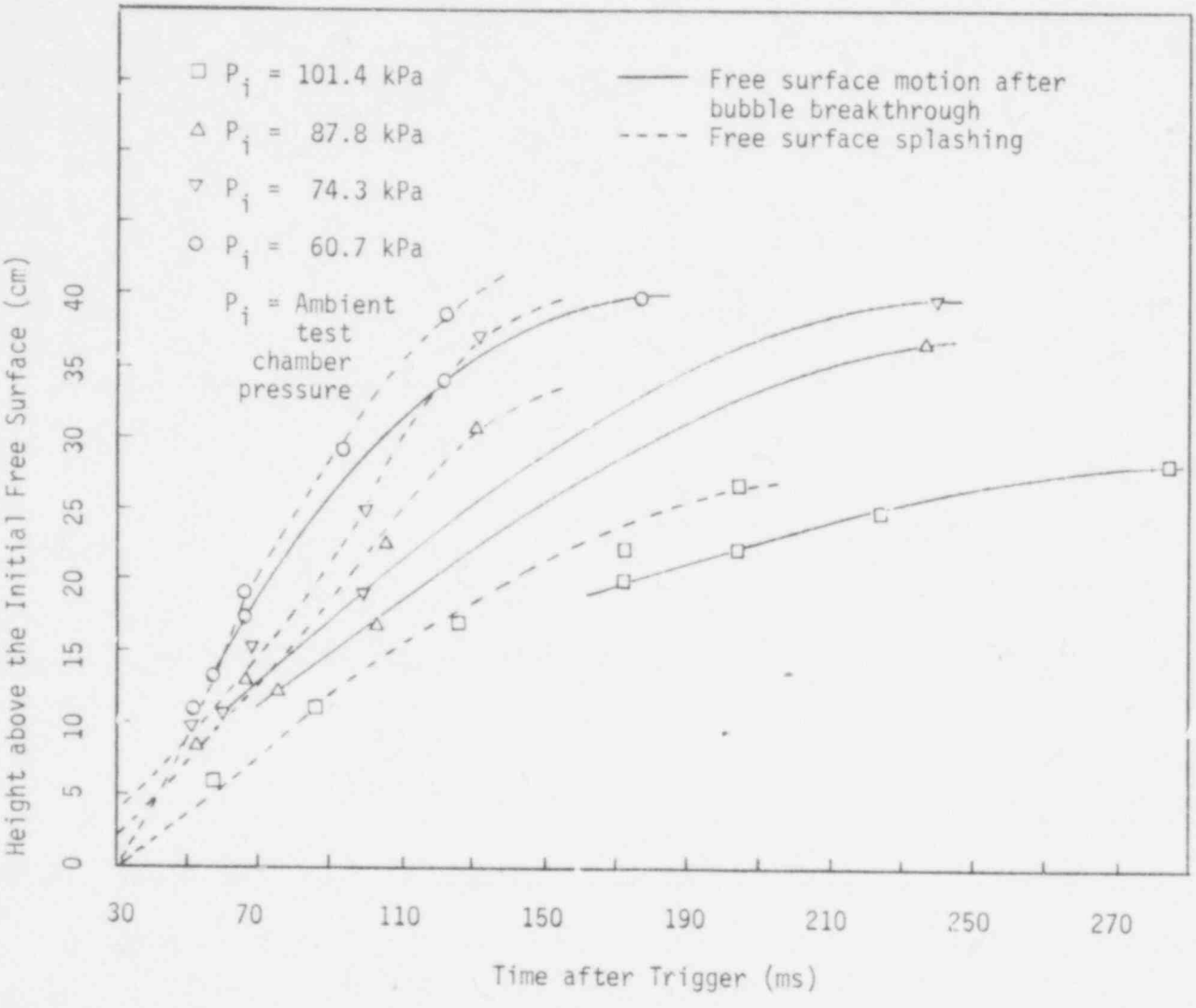

Figure G.4. Pool Swell and Splash Height History for 177.2 kPa Upstream Pressure and 46 mm Diameter Tube in Helium Medium without Orifice.

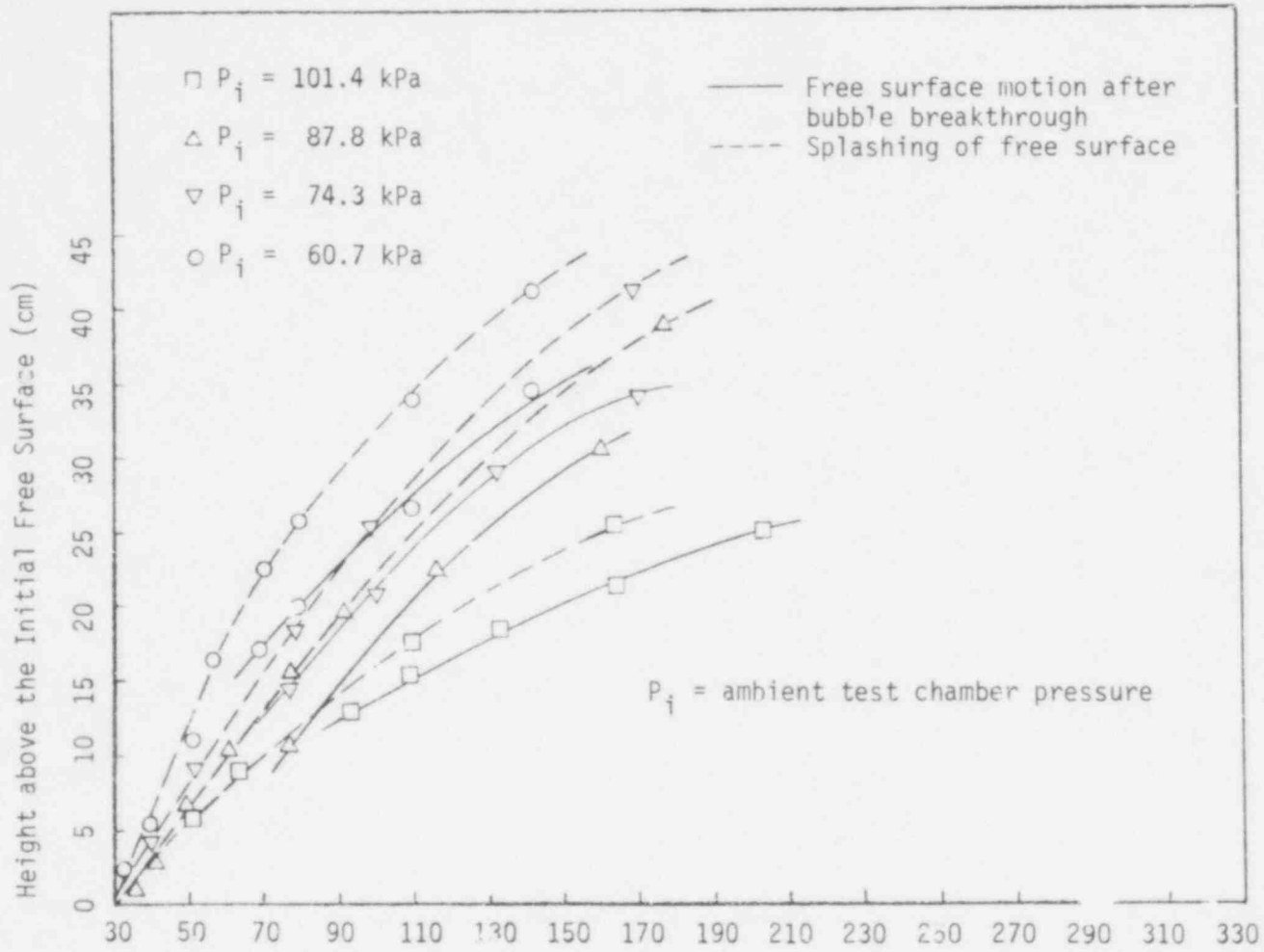

Figure G.[illegible] Pool Swell and Splash Height History for 177.2 kPa Upstream Pressure and 46 mm Diameter Tube in Helium Medium with 2.54 cm Diameter Orifice.

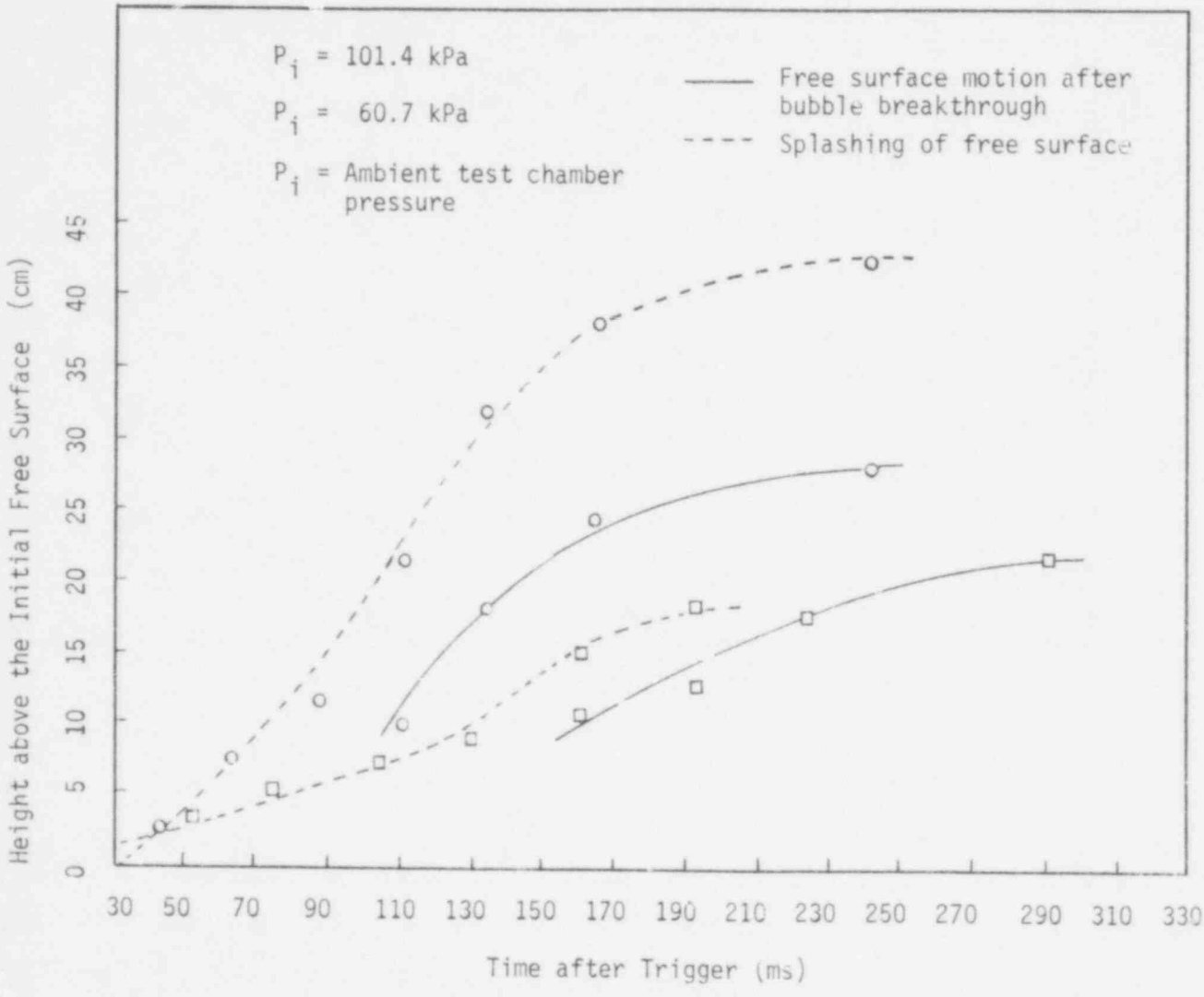

Figure G.6. Pool Swell and Splash Height History for 177.2 kPa Upstream Pressure and 46 mm Diameter Tube in Helium Medium with 1.56 cm Diameter Orifice.

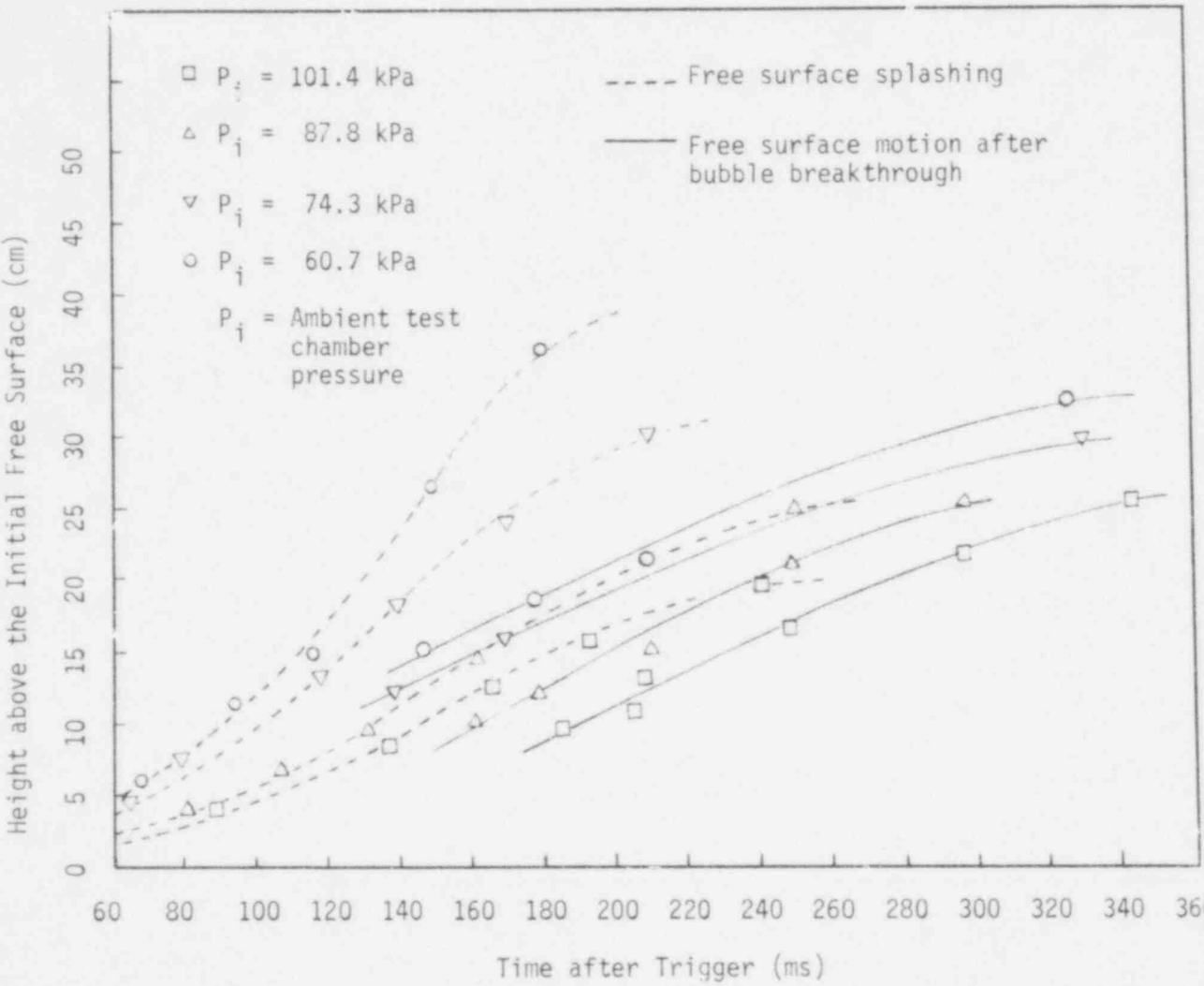

Figure G.7. Pool Swell and Splash Height History for 177.2 kPa Upstream Pressure and 46 mm Diameter Tube in Argon Medium without Orifice.

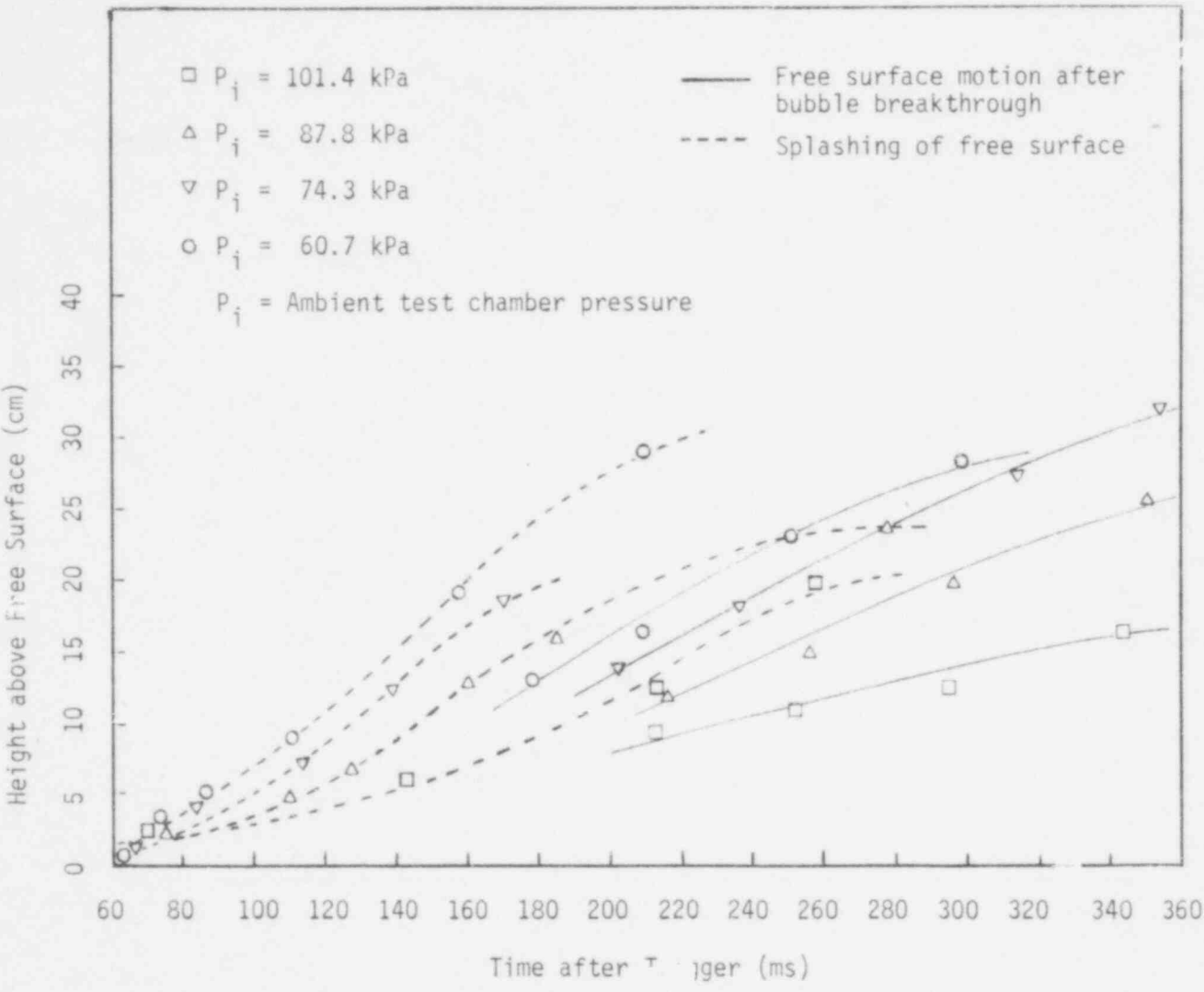

Figure G.8. Pool Swell and Splash Height History for 177.2 kPa Upstream Pressure and 46 mm Diameter Tube in Argon Medium with 2.54 cm Diameter Orifice.

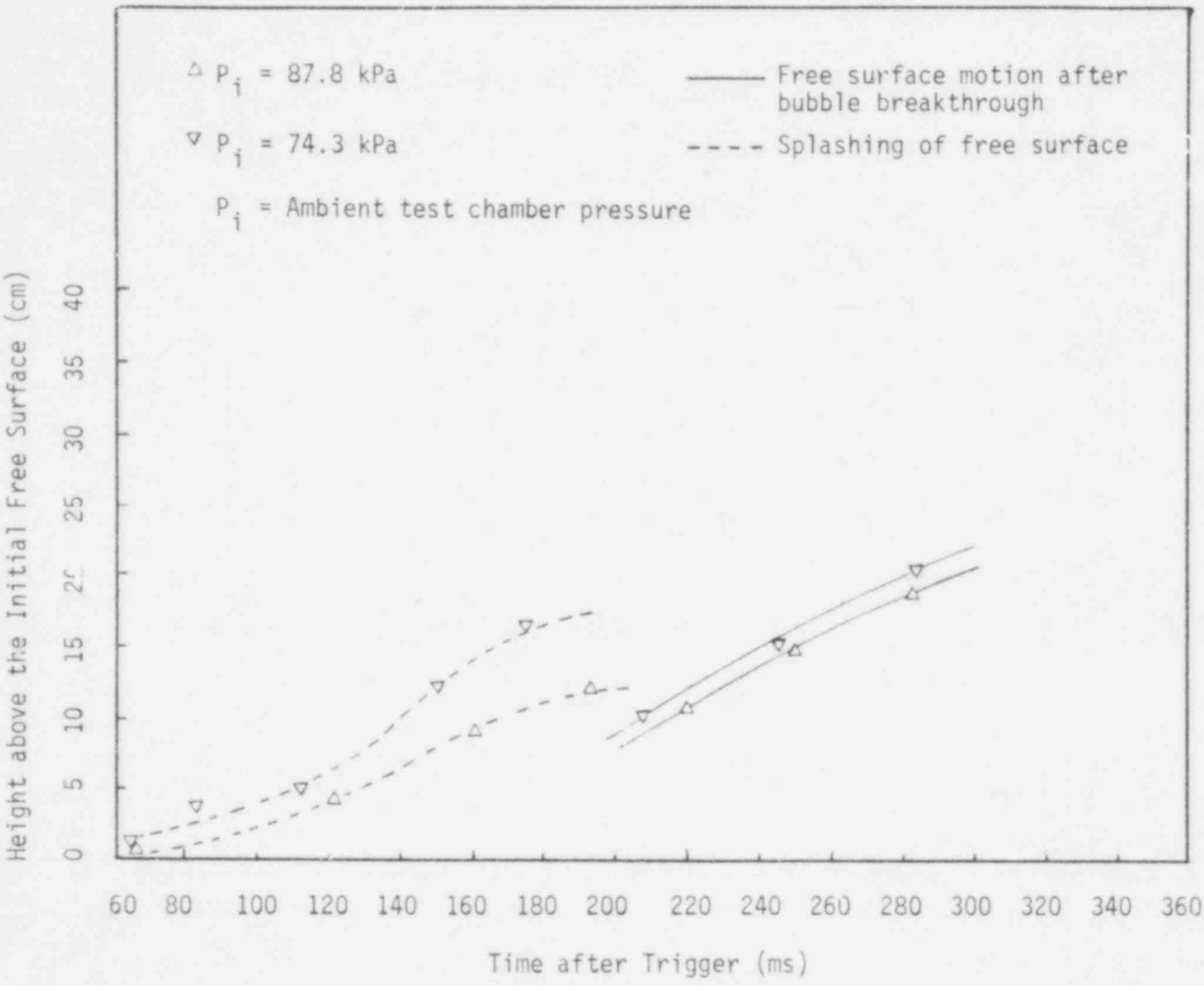

Figure G.9. Pool Swell and Splash Height History for 177.2 kPa Upstream Pressure and 46 mm Diameter Tube in Argon Medium with 1.56 cm Diameter Orifice.

UNITED STATES
NUCLEAR REGULATORY COMMISSION
WASHINGTON, D. C. 20555

OFFICIAL BUSINESS
PENALTY FOR PRIVATE USE, $300

POSTAGE AND FEES PAID
UNITED STATES NUCLEAR
REGULATORY COMMISSION

732 354